EXPERIMENTAL AND FINITE-ELEMENT INVESTIGATION OF FLOW PAST SINGLE AND MULTIPLE CYLINDERS

by

Manoranjan N. Dhaubhadel

Dissertation submitted to the Faculty of the

Virginia Polytechnic Institute and State University

in partial fulfillment of the requirements for the degree of

DOCTOR OF PHILOSOPHY

in

Engineering Mechanics

APPROVED:

Dr. D. P. Telionis, Chairman	Dr. J. N. Reddy
Dr. T. E. Diller	Dr. T. Herbert
Dr. D. T. Mook	Dr. M. S. Cramer

August, 1986

Blacksburg, Virginia

ABSTRACT

EXPERIMENTAL AND FINITE-ELEMENT INVESTIGATION OF FLOW PAST SINGLE AND MULTIPLE CYLINDERS

by

Manoranjan N. Dhaubhadel

Fluid flows past single and multiple cylinders in different configurations are investigated both experimentally and numerically. Three and five in-line cylinders and in-line and staggered bundles of cylinders with different pitch-to-diameter ratios are considered. Experimental work comprises of laser-Doppler velocimetry and flow visualization obtained in a water tunnel and skin friction, pressure, lift, drag and hot-wire measurements obtained in a wind tunnel. Both steady and pulsed flows are considered. Numerical work consists of finite element analysis of Navier-Stokes and energy equations governing viscous fluid flow past single and multiple cylinders. Detailed measurements of the fluid dynamic quantities for flow past cylinders reveal that flow pulsation at frequencies which induce lock-on increases the organization of the flow in gaps between cylinders. A new pattern of flow field is found for flow past a triad and a pentad of cylinders with a pitch-to-diameter ratio of 1.8. The numerical analysis generates important integral characteristics like flow resistance and heat transfer. A staggered square arrangement of finite bundle of cylinders is found to have better heat transfer characteristics compared to the in-line or staggered equilateral-triangular arrangements.

Dedicated to my parents

ACKNOWLEDGEMENTS

I would like to express my sincere appreciation to Dr. D. P. Telionis for his guidance, understanding and encouragement throughout my program of study. I would like to thank him for his continuous support and invaluable suggestions.

I would like to extend my sincere thanks and appreciation to Dr. J. N. Reddy and Dr. T. E. Diller for their constructive input and encouragement in this work. They have followed my work closely and guided me through it. Sincere thanks and appreciation are also extended to Dr. D. T. Mook and Dr. T. Herbert for their guidance and encouragement during the course of my study. Thanks is also extended to Dr. M. S. Cramer for his help as a member of my graduate committee. I would also like to thank Dr. D. Frederick for his help and consideration in my work as an instructor.

The support of this research as part of contract no. DE-A505-82ER 12022 from the Office of Basic Energy Research, Department of Energy, is gratefully acknowledged.

I express my thanks to my fellow colleagues in the ESM Department and ME Department for their friendship and encouragement. Thanks are extended to ESM technical support personnel, Mr. Don Bodnar, Mr. Kenneth McCauley, Mr. Robert Davis and Mr. George Lough for their assistance. Thanks are also

extended to Mrs. Paula Lee, Mrs. Vanessa McCoy and Mrs. Marlene Taylor for their clerical support.

Finally, I would like to express my profound gratitude and appreciation to my family, whose love, support and inspiration helped me finish this work. I thank my wife for her patience and understanding throughout the course of this work.

TABLE OF CONTENTS

LIST OF FIGURES

LIST OF TABLES

CHAPTER I

INTRODUCTION

Flow past a single cylinder is a fundamental problem in aerodynamics and hydrodynamics and has been investigated by numerous researchers for decades. Experimental and numerical investigations of flow past multiple cylinders are of great practical interest, due to the various engineering applications like heat exchangers and nuclear reactors. The problem is complicated by the fact that the wake originating from one or more cylinders interacts with cylinders further downstream. The geometry introduces one more parameter,the pitch-to-diameter ratio, besides the usual fluid dynamic parameters. The complex nature of the flow in cavities between cylinders poses a challenge to today's experimentalists and numerical analysts. This thesis reports both experimental and numerical results obtained in an effort to understand the flow past multiple cylinders. The experimental work consists of laser-Doppler velocimetry (LDV) measurements and flow visualizations performed in a water tunnel and hot-wire anemometry, pressure and skin friction measurements carried out in a wind tunnel. Both steady and pulsed flows are considered for

cylinders in different configurations. The numerical work consists of finite-element solutions of flow past multiple cylinders.

Flow past a single cylinder has been studied by numerous researchers [e.g. Son and Hanratty, 1969; Lebouche and Martin, 1975; Farrel et al., 1977; Bouard and Coutanceau, 1980; West and Apelt, 1982; Brooks and Hughes,1982; Esposito and Labadi, 1983; Kawahara and Hirano, 1983; Kawamura and Kuwahara, 1984; Gresho et al.,1984; Borel et al., 1984; Kim et al., 1984; Andraka and Diller, 1985; VandenBerghe, 1985; Karniadakis et al.,1986 to name just a few]. Flow past multiple cylinders has received much attention in the last few years [Kostic and Oka, 1972; Hiwada et al., 1982, Zdravkovich, 1977; Aiba et al., 1980; Igarashi and Suzuki, 1984; Zukauskas, 1972; Bergelin et al.,1952; VandenBerghe et al., 1985; Fujii et al., 1984; Antonopoulos, 1985; Launder and Massey, 1978]. Experimental results to date include hot-wire and LDV measurements. More and more refined techniques have been developed. The measurements in a cavity region in the multiple cylinder case, however, still pose problems and the flow field in this region is yet to be fully resolved. Hot-wire anemometers used in the complex flow situations may cause problems because of the considerable deviation from the ideal situation for which they are calibrated. Shear stress around a single cylinder has been measured by various investigators but surprisingly shear stress measurements around cylinders for flow across multiple cylinders could not be found in the literature.

A few investigators have analysed the flow across multiple cylinders using finite difference methods [Fujii et al., 1984; LeFeuvre, 1973; Antonopoulos,

1985; Launder and Massey, 1978]. The finite element method has been applied to the classical flow past a single cylinder [Kawahara and Hirano, 1983; Gresho et al., 1984; Brooks and Hughes, 1982]. However, finite element analysis of flow past multiple cylinders is not available in the literature.

The present work reports the results of LDV, hot-wire anemometry, flow visualization and finite element analysis of flow across a single cylinder and multiple cylinders in different configurations. The present investigation differs significantly from the ones available in the literature in that detailed results of flow in cavity regions is furnished. Introduction of LVDT (Linear Variable Differential Transformer) transducers allows accurate traversing of the probe volume. The addition of digital interface modules to the LDV system makes possible accurate measurements in recirculating regions where adequate seeding is often difficult. The effect of freestream pulsation on shear stress and pressure around a cylinder is studied in detail. Results of shear stress around a cylinder for the case of flow past multiple cylinders are also novel. The problem of flows past finite and infinite bundles of cylinders have been solved for the first time by the finite element method. The FEM solution of time-dependent problems of flow past three cylinders in a row and 3-D flow past perpendicular arrangement of cylinders proved to be very expensive and was not completed. Although these problems are of prime importance in heat exchangers, no one seems to have solved them analytically or numerically.

A detailed review of the current state of the literature pertaining to a subject is given at the beginning of each chapter. Laser-Doppler velocimetry and flow

visualization hot-wire anemometry and other instrumentation and data acquisition system is fully automated and has feedback control mechanisms for accurate traversing. These are described in detail in chapter two. In chapter three the experimental work is described.The experimental results are presented and discussed in chapter four. LDV results consist of velocity measurements in the cavity regions between the cylinders. Wind tunnel results include velocity, pressure, shear stress and lift and drag measurements. Flow visualization results show photographs of flow fields with particles and dyes. The finite element method is described in chapter five. Numerical results and discussion of results are covered in chapter six. Conclusions and recommendations are made in chapter seven.

CHAPTER II

EXPERIMENTAL FACILITIES AND EQUIPMENT

2.1 INTRODUCTION

The experimental work is carried out in both a water tunnel and a wind tunnel. Laser-Doppler velocimetry and flow visualization are employed in the water tunnel and hot-wire anemometry is used in the wind tunnel. The advantage of using a water tunnel over wind tunnel lies in the fact that realistic Reynolds numbers and Strouhal numbers can be achieved in water with significantly lower freestream speeds and driving frequencies. Velocity measurements are made in the water tunnel whereas pressure, shear stress, lift, drag and velocity are the quantities measured in the wind tunnel. Laser-Doppler velocimetry in water is more convenient and can generate almost continuous signal. Moreover, flow visualization in water is more effective. On the other hand, a wind tunnel provides easy accessibility of the models and instruments used. Also, use of pressure transducers, shear stress gauges etc. is more convenient. The techniques of measurement and data acquisition systems employed are discussed in the sections that follow.

2.2 WATER TUNNEL

2.2.1 General Description

The water tunnel(see figure 2.1) was constructed by the Engineering Science and Mechanics Department at VPISU in 1976. The polyvinyl chloride and plexiglass construction holds 570 gallons of water. Plexiglass in the test section and lower half of the tunnel allows laser velocimetry measurements and flow visualization. The detailed design of the tunnel is described by Koromilas [1978] and Mezaris [1979]. Since the construction of the tunnel, several modifications were undertaken. Screens and honeycombs were added to improve the quality of the flow. A disturbing mechanism was built to produce periodic pulsation of the mean flow.

2.2.2 Test Section

The test section has a 25 cm × 30 cm cross section and is 183 cm long with three interchangeable sections. To eliminate the end effects in the test section, a set of false inner walls is employed (see figure 2.2). The wall boundary layers are directed behind the false walls and thus the flow past the model is virtually uncontaminated by the boundary layers of the upstream walls. Velocity profiles in the boundary layer on the inside of the false walls and associated turbulence level as measured by Poling [1985] are shown in figures 2.3 and 2.4

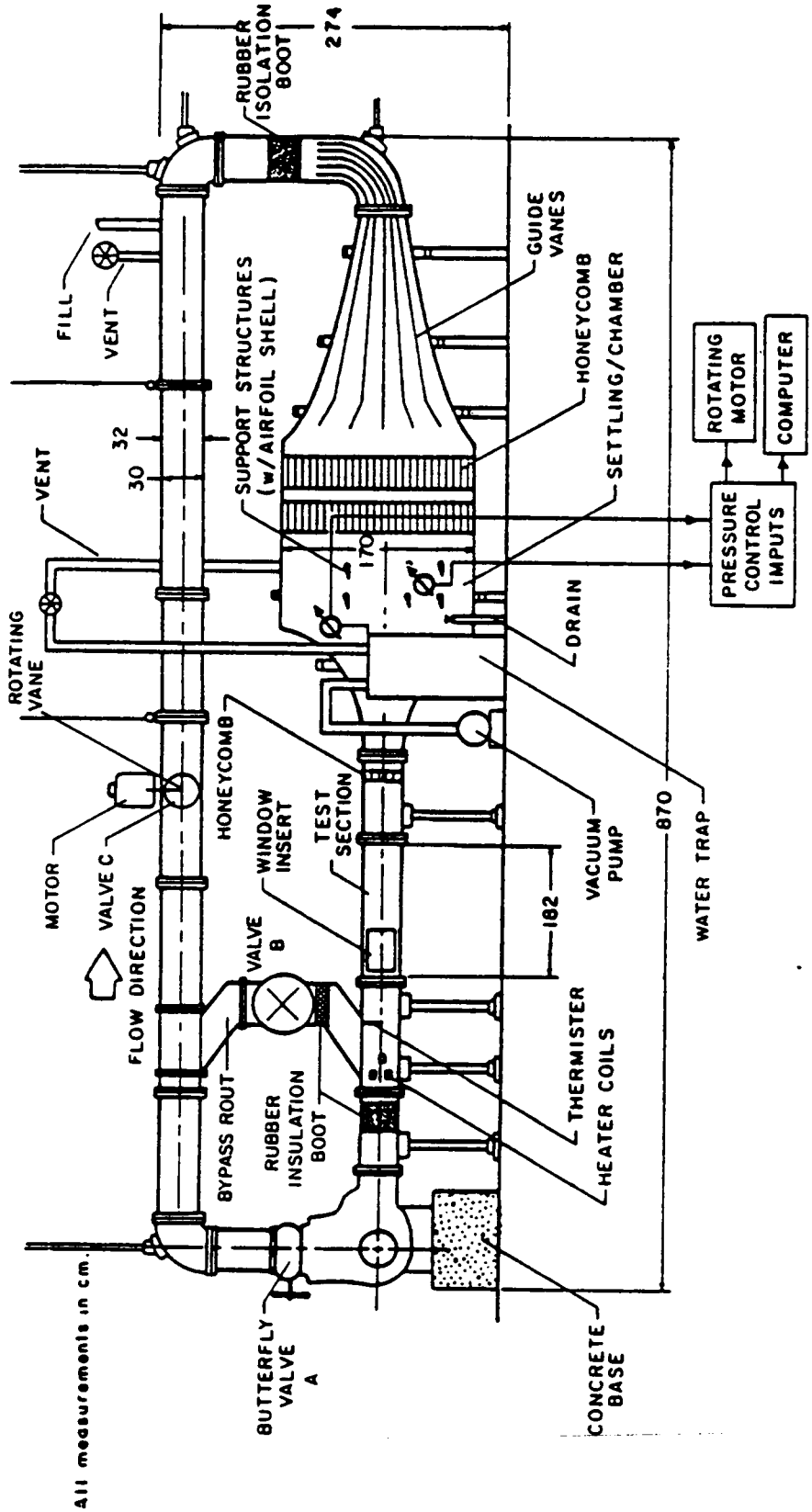

Figure 2.1 Schematic of the water tunnel

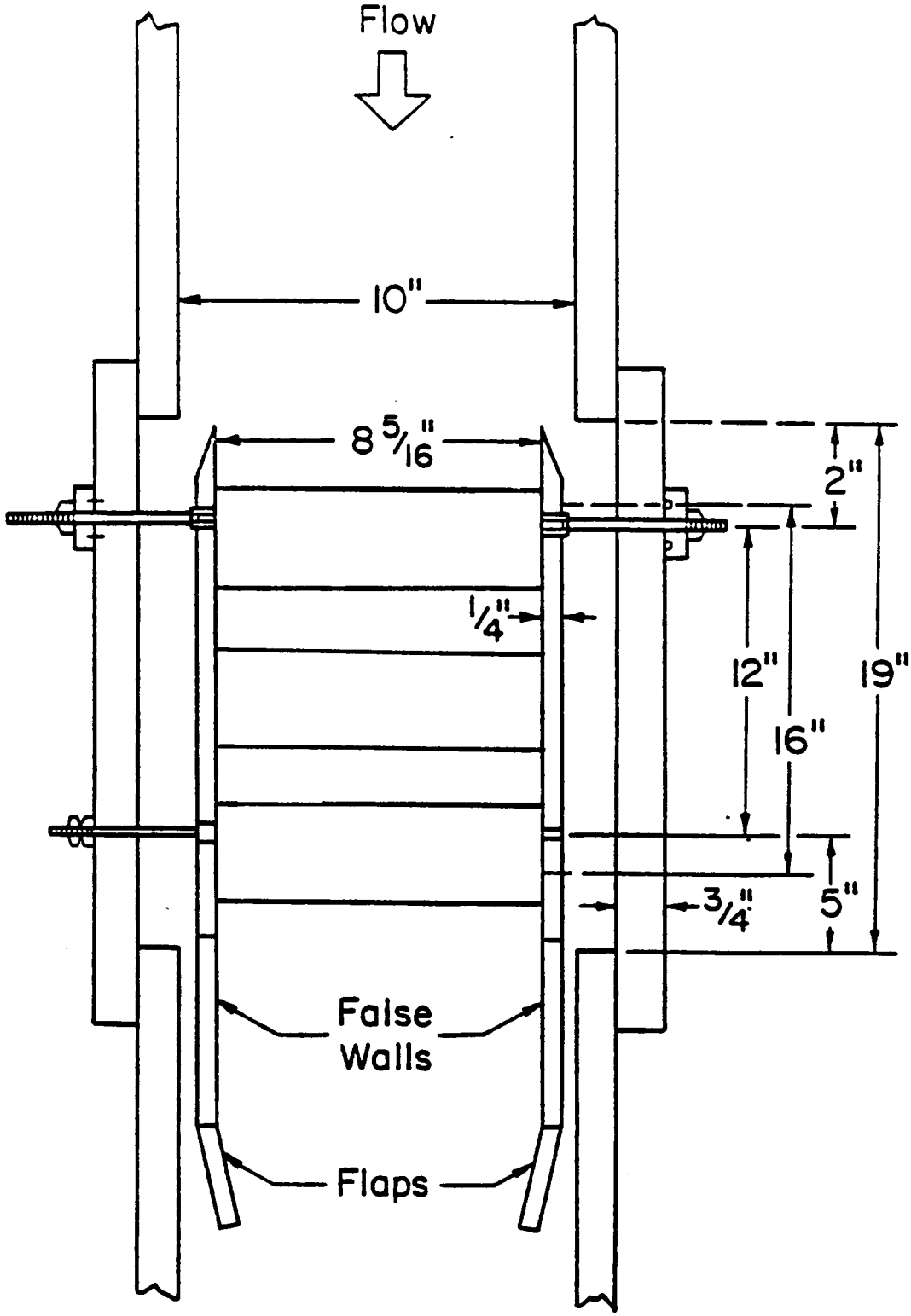

Figure 2.2 Top view of the test section showing the false walls

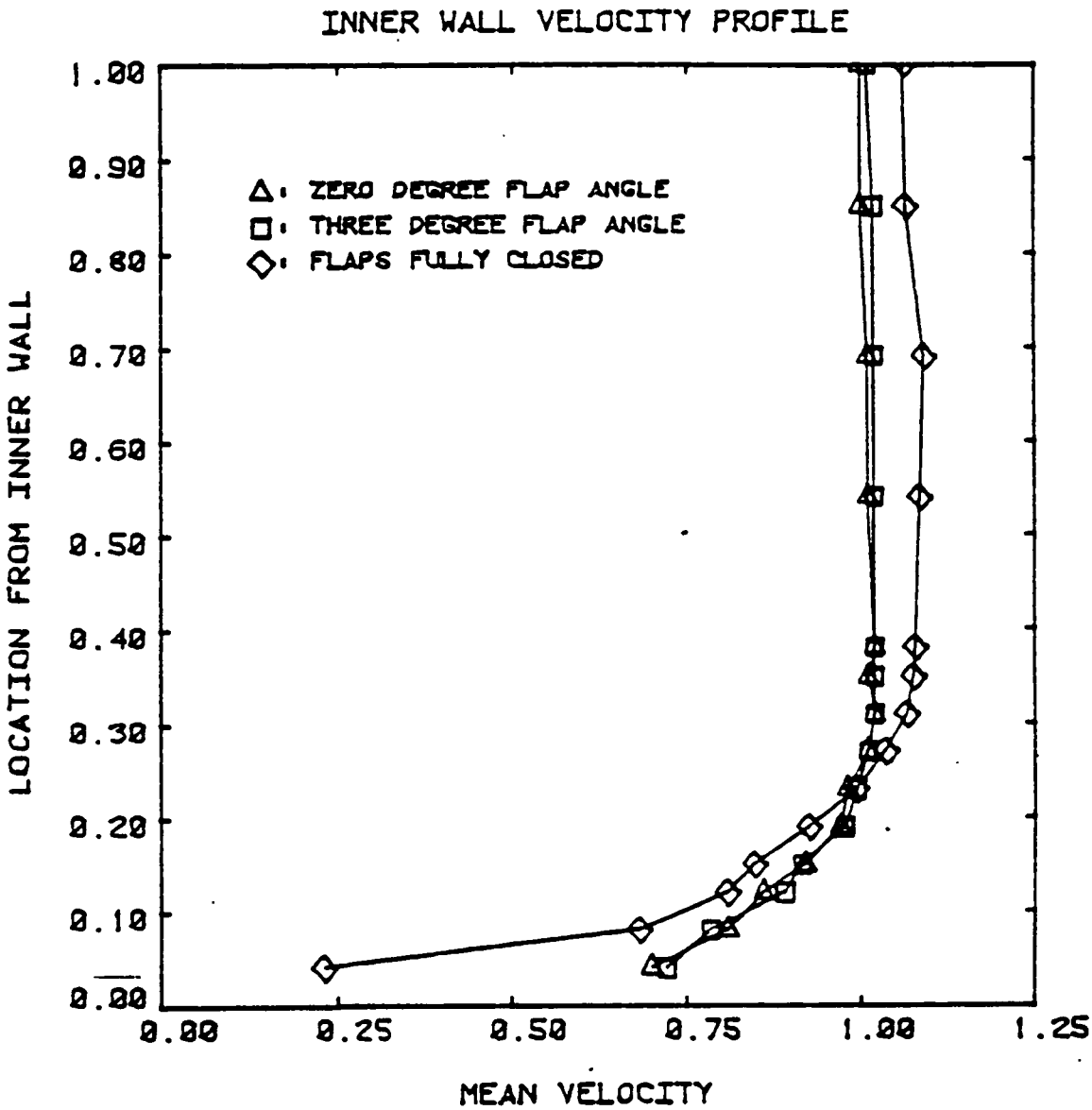

Figure 2.3 Mean velocity profile on the inside of the false wall

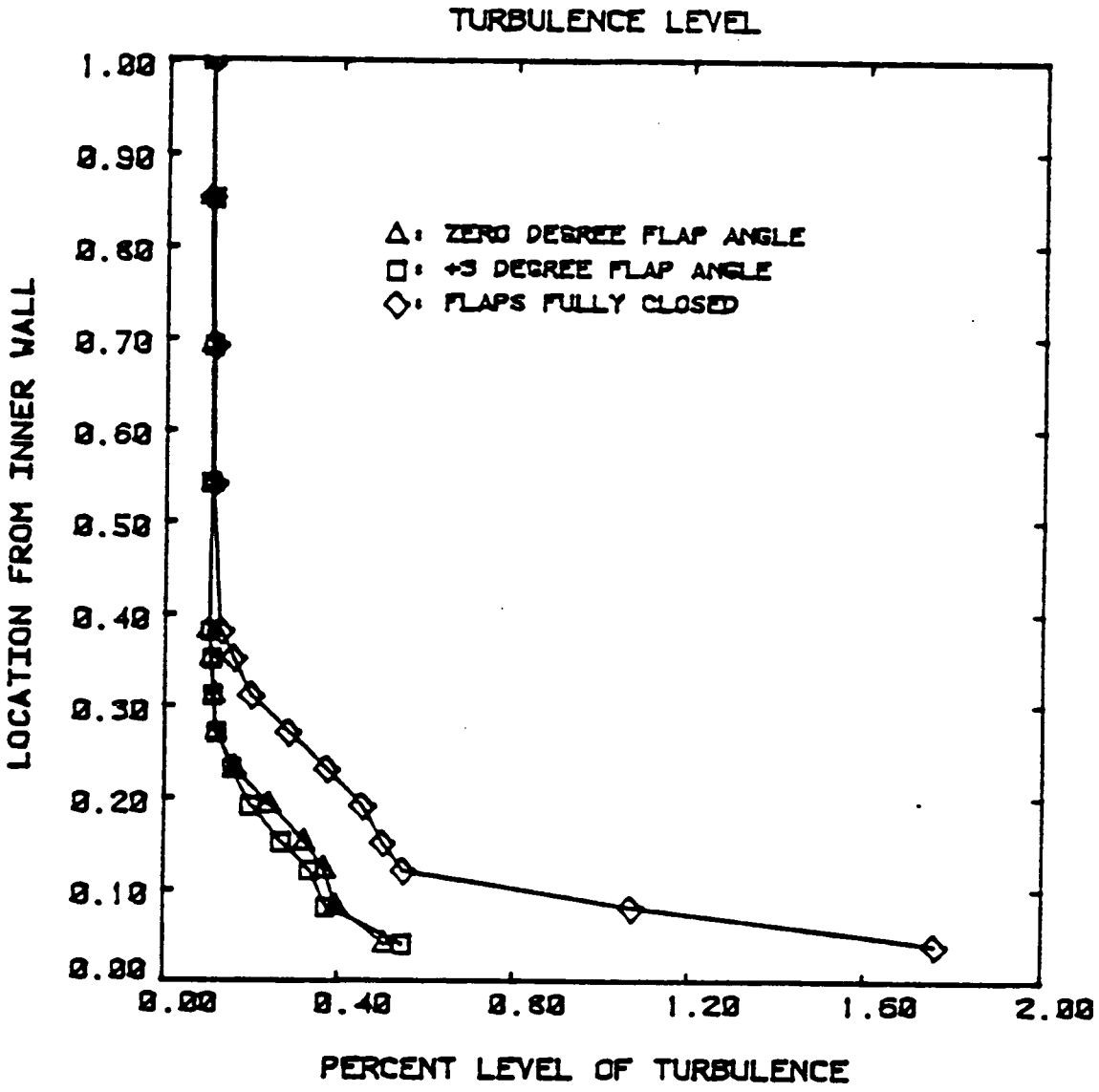

Figure 2.4 Turbulence level on the inside of the false wall

respectively. Flap position at 10 degrees is found to be optimum for minimum side wall boundary layer effect.

2.2.3 Control of Mean Speed, Amplitude and Frequency of Pulsation

A centrifugal pump coupled with a variable speed electric d. c. motor gives freestream velocities up to 5 meters per second. A variable opening by-pass section with butterfly valves allows some control on the amplitude of the pulsation and the turbulence level. A specific freestream speed and pulsation amplitude can be obtained with different settings on the electric motor and the by-pass valve.

A rotating vane installed upstream of the settling chamber (see figure 2.1) generates a nearly sinusoidal disturbance on the mean tunnel speed at the test section. A Heller variable-speed d. c. motor controls the speed of the vane to within 0.5 percent of the set value. The frequency of the freestream disturbance is twice the frequency of the rotating vane. The control unit can be adjusted to get frequencies up to 6 Hertz.

2.2.4 Temperature Control

A temperature control unit employed in the water tunnel can raise the water temperature at 3 degrees centigrade per hour. The unit maintains a fairly constant water temperature (within 0.5 degrees centigrade) in the tunnel and thus the viscosity is essentially kept constant.

2.2.5 Turbulence Level and Calibration

Since the construction of the water tunnel, a lot of attention has been given to turbulence control. Tunnel calibration with two honeycombs installed in the settling chamber [Koromilas, 1978; Mezaris, 1979] indicated freestream turbulence in the range of 0.7 to 1 percent and in some cases greater than 1 percent. Addition of a honeycomb at the end of the converging section later [Jones, 1980] gave turbulence levels of 0.5 to 0.8 percent. Turbulence levels of 0.5 percent and less were achieved several years later [Mathioulakis, 1985] with the addition of a finer honeycomb and three standard mesh window screens. Screens reduce axial turbulence [Scheiman and Brooks, 1980] while honeycombs absorb lateral eddies, thus eliminating large scale vortices and swirling motions. The screens were later removed to enable flow visualization. The tunnel calibration was done with a one component DISA set up. The details of the calibration can be found in Telionis, Mathioulakis, Kim and Jones [1984].

2.2.6 Test Models

Three different configurations of flow past circular cylinders are considered. Four different sets of false walls are prepared to mount respectively a single cylinder, three cylinders in a row and five cylinders in a row. The arrangement of cylinders is schematically shown in figure 2.5.

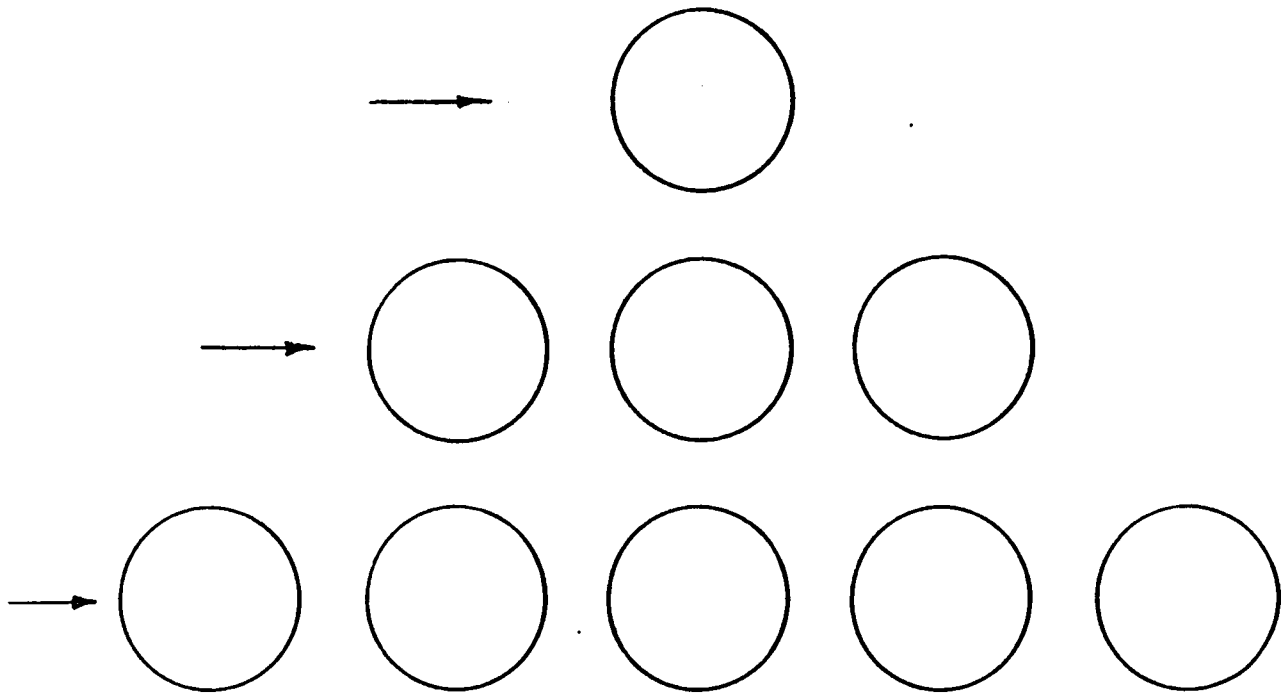

Figure 2.5 Schematic of various arrangements of cylinders

A pitch-to-diameter ratio of 1.8 is employed for the three- and five-cylinder cases. Two of the cylinders are instrumented for dye visualization. Dye can be instantaneously and independently released from four different locations on the instrumented cylinder (see figure 2.6).

2.3 FLOW VISUALIZATION

Extensive flow visualization studies are undertaken with particles, dyes and particles and dyes together. Time exposure of particles generate small segments which are essentially particle paths and therefore nearly parallel to the velocity vectors. The dyes on the other hand generate streaklines. For particle flow visualization Pliolite particles of 0.25 to 0.5 mm diameter, which are neutrally buoyant in water (sp. gr. 1.02) are used. For dye visualization Rhodamine B which is red and Uranine which is green in water are used. With a sheet of light cutting through the flow, the particles shine because of reflection. Dyes are visible due to fluorescence.

In order to pass a uniform sheet of light through the test section both from the top and the bottom, two tungsten-halogen 1000 watt high pressure lamps are used at the top and the bottom of the test section. In addition, cylindrical lenses are used to maximize illumination in the sheet. Any light not passing through the lenses or not contributing to the lighting of the sheet in the test section is covered with black cloth to insure a dark background for

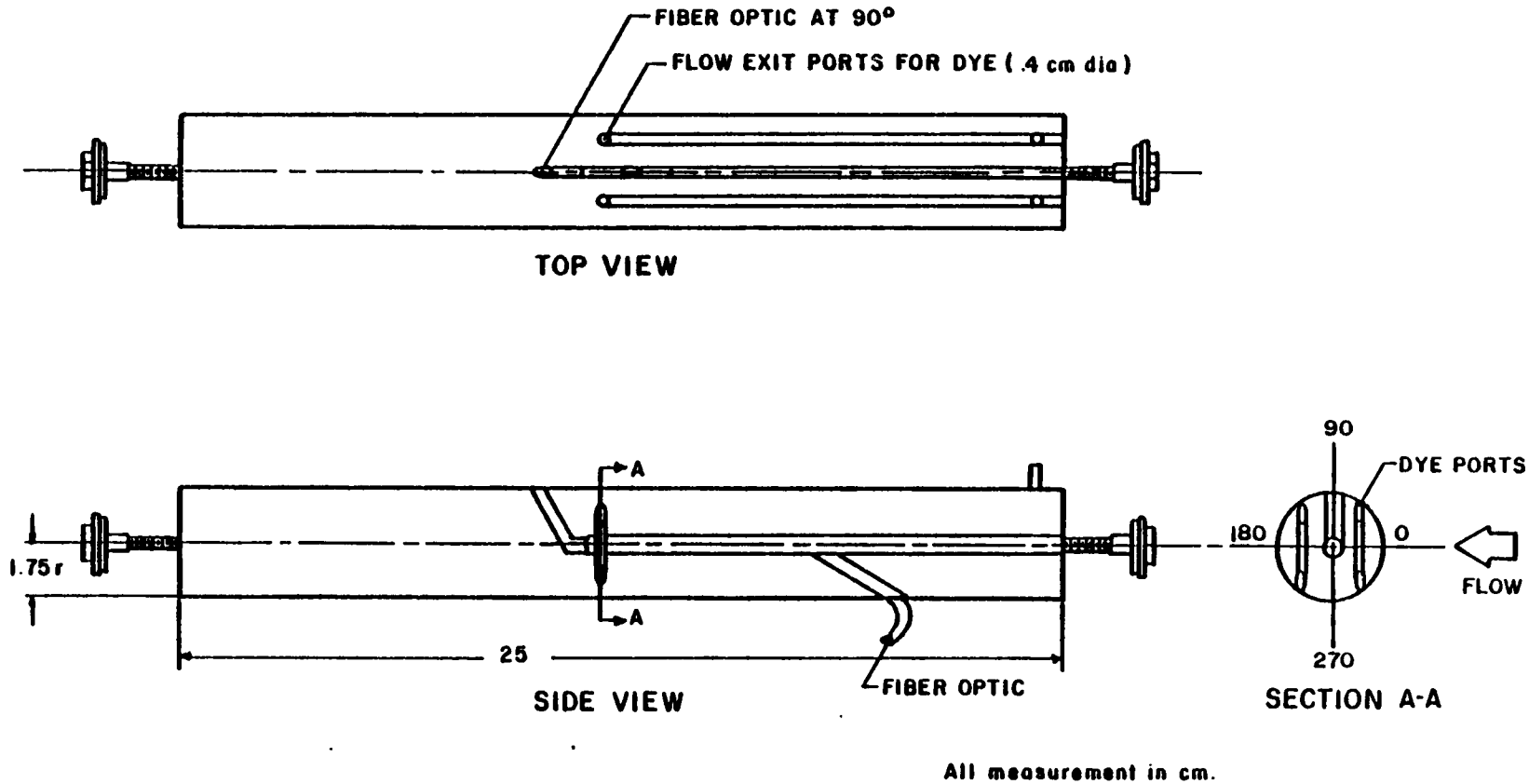

Figure 2.6 Test cylinder for dye visualization

photography. A false wall painted black is employed in the far side of the test section for good background contrast.

To record the time history of particle paths in the cavity regions between cylinders and in the wakes, photographs and movie films are taken. Black and white photographs of particles and color photographs of particles and dyes are obtained using a Nikon 35 mm camera with a f-3.5 macro-lens. A custom-made digital electronic clock is used to indicate the instants when the pictures are taken. The clock is designed to reset to zero when triggered by an external trigger mechanism. In the present study the clock is triggered by the trigger pulse coming from the rotating vane driving the flow.

Exposure and lighting problems are often encountered because of the need for high speed photography while at the same time details of the flow need to be preserved. To obtain a clear recording of particle paths and dye movements, films with different designated speeds are tried. Kodak #2475 high speed recording film (black and white) and Kodachrome ASA 1600 (color) film are found to be suitable with the the lighting arrangement described above. Shutter speeds and apertures are set at 1/15 of a second and f-3.5, respectively. A motor driven clock attached to the Nikon camera allows up to 4.5 frames per second. This kind of speed is needed when studying periodicity in the flow. Moreover, 8mm color movie films are used for movies at speeds ranging from 8 frames a second to 64 frames per second. An ARRIFLEX movie camera gives this range of speeds. ASA 400 rated films are used and pushed up one stage during

developing which essentially changes them to ASA 800 films. In contrast to photographs, movie films make possible the dye visualization from the first release of the dye.

2.4 LASER DOPPLER VELOCIMETRY

Laser-Doppler velocimetry (LDV), also known as laser-Doppler anemometry, (LDA) is used to make flow measurements in the water tunnel. LDV is a technique to measure velocity by determining the Doppler shift of light scattered from moving particles in the fluid. When two laser beams cross, interference fringes are formed due to optical beating. The region where the beams cross, which is referred to as the measuring volume, is full of interference fringes. The light scattered by particles in the measuring volume (see figure 2.7) is received by a photo-detector and then converted to voltage. The modulation of intensity at the detector is due to the variation in the illumination of particles as they cross light and dark fringes. The electric signal from the photo-detector gives the Doppler frequency which is directly proportional to particle velocity.

The Laser velocimetry systems are gaining popularity because of their distinct advantages over other methods of measurements. The chief advantages are

a) They do not disturb the flow.

b) They have high spatial resolution, typically 20 μm to 100 μm.

c) They have a fast response.

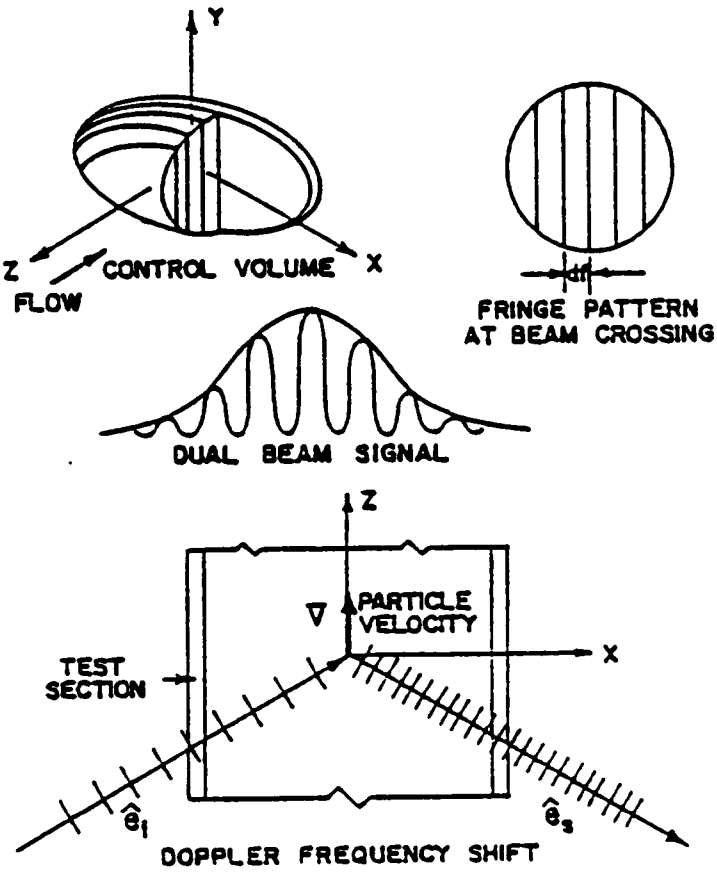

Figure 2.7 Measuring volume

d) The response is linear, frequency output is directly proportional to velocity and hence does not require involved calibration.

e) Directional discrimination is possible with the use of frequency shifting.

f) Temperature changes do not usually affect the operation.

The chief disadvantage of LDV is the need for expensive signal processing equipment. Optical accessibility and the need to add scattering particles may pose problems in some cases.

In the present work, two He-Ne lasers one rated 5 mW and another 15 mW are used in the forward and back scatter modes respectively. The laser in each case has a wavelength of 632.8 nm. Forward scatter is used to monitor the freestream because it does not require traversing, which is difficult in forward-scatter mode. The back-scatter system has an advantage in the ability to traverse but has a greater laser power requirement for acceptable signals. A two-component back-scatter system which is used in the present work for making velocity measurements in complex domains is described in section 2.4. Both TSI and DISA systems are used. The DISA frequency tracker model 55L20 and the TSI counter model 1985 are used to monitor the freestream. TSI counters (TSI 1985 and 1995) with digital interfaces are used for two component velocity measurements. Both systems comprise of sending optics and receiving optics along with signal processing equipment. These are described below.

2.4.1 Optical Components In Forward-Scatter System

The DISA system in forward scatter mode is shown in figure 2.8.

a) Sending Optics

The 5-mw laser beam from a Spectra-Physics He-Ne laser is passed through a DISA 55L01 beam splitter, which splits it into two beams of equal intensity. The two beams go through a 150 mm focal length lens and converge at the measuring volume.

b) Receiving Optics

The light scattered by particles in the measuring volume is received by a DISA 55L10 photomultiplier. The photomultiplier converts the light signal to an electric signal, which is sent to a DISA 55L20 frequency tracker for signal processing. A counter-type signal processor can also be used with the DISA power supply. The crossing angle between the two beams gives the fringe spacing d_f and the Doppler frequency f_d recorded gives the particle velocity, U from the following relations

$$d_f = \frac{\lambda}{2 \sin \theta} \qquad [2.4.1]$$

$$U = f_d \times d_f \qquad [2.4.2]$$

where, λ = wave length of laser light

θ = half angle of beam intersection

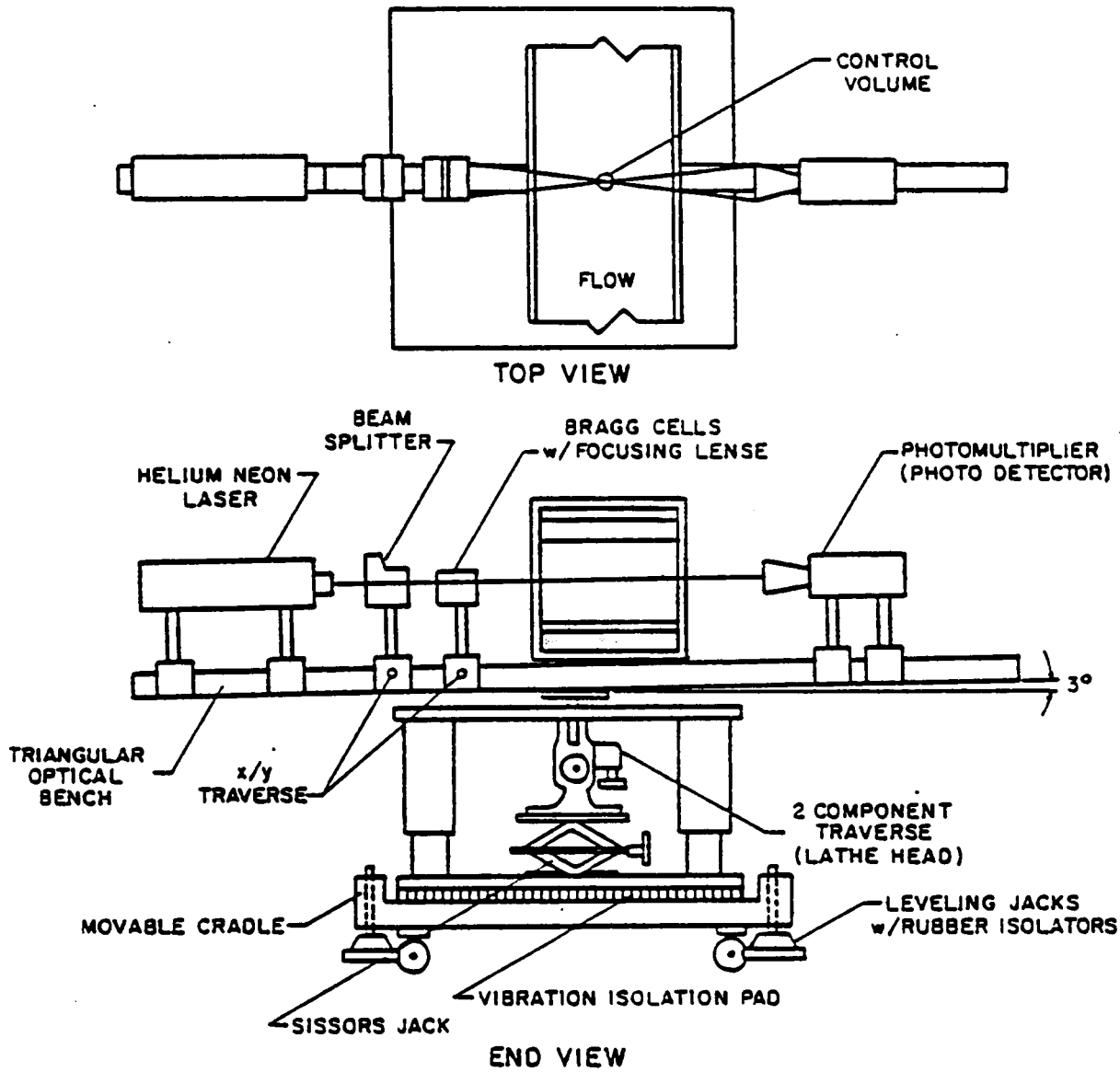

Figure 2.8 DISA system in forward scatter mode

2.4.2 Optical Components In 2-Component Back-Scatter System

a) Sending Optics

The beam from a Spectra-Physics 15 mw He-Ne laser is split into three beams of approximately equal intensity by means of a variable-intensity beam splitter (TSI 9216-2) and an equal-intensity beam splitter (TSI 9115-2). One of the beams which is reflected by the beam splitter (TSI 9115-2) goes through a polarization rotator (TSI 9103-2) which changes its polarity by 45 degrees. The three beams are thus brought to the same polarity. Two of the beams are directed through two bragg cells to shift their frequencies by 40 MHz (TSI 9182-2) and 60 MHz (TSI 1982) respectively. The bragg cells are adjusted so that the shifted beams become the brightest. Shifting the frequency of a beam shifts the frequency corresponding to zero velocity and enables the system to measure both positive and negative velocities. Frequency shifting also allows removal of the pedestal signal easily and at the same time minimizes fringe-biasing error (Seasholtz 1977)

The three parallel beams are passed through the beam spacer (TSI 9114-22) and the beam expander (TSI 9188). This reduces the probe volume by a factor of 2 and consequently, the signal to noise ratio is improved. The dimensions of the measuring volume which is oval in shape are calculated as follows (TSI manual pp.77)

$$d_m = \frac{4\lambda f}{\pi D E} \qquad [2.4.3]$$

$$l_m = \frac{d_m}{\tan\theta} \qquad [2.4.4]$$

where f is the focal length of the lens, D is the diameter of the laser beam, E is the expansion ratio of the beam expander and d_m and $l_m$are the diameter and length of the measuring volume oval respectively. The following are the values of the quantities used in the present research

f=250 mm

$\tan\theta = 25 \times 2/250 = 0.632$ μm

D=1 mm

E=2.27 (TSI 1988 Expander)

These values result in the following

$d_m = 0.088mm$

$l_m = 1.24mm$

$d_f = 4.47\mu m$

obtained via equations 2.4.3, 2.4.4 and 2.4.1 respectively.

Light is scattered by particles in the flow according to the Mie diagram and its power fluctuates with the Doppler frequency. The quality of the signal depends very much on the particles in the flow. In the present work silicon carbide seeding with a particle diameter of 1.5 μm is employed to obtain the correct amount of seeding.

Figure 2.9 shows the crossing of the three beams. Plane D represents the plane of the focussing lens. The beams meet plane D at points A, C and B which form a right triangle. The two Bragg cells in the transmitting optics allow the

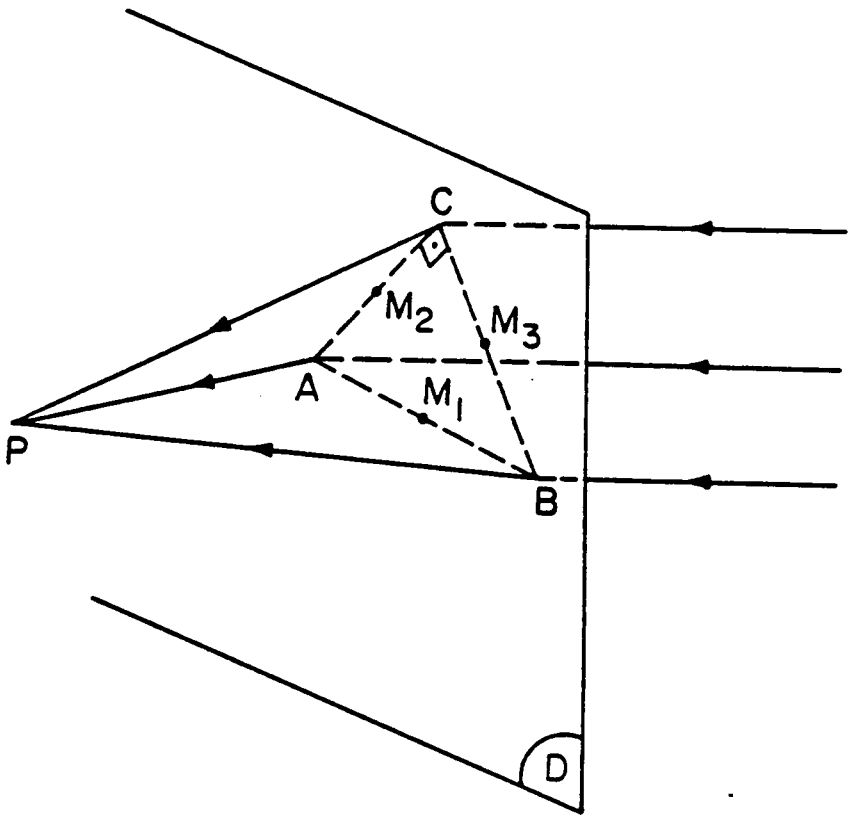

Figure 2.9 Crossing of the three beams

shifting of frequency of the two beams CP and BP by 40 MHz and 60 MHz respectively. The fringes generated by any two beams are parallel to their bisector. Three sets of fringes exist for the three beam case and correspondingly, three velocity components normal to the fringes are available from processing of the light scattered from the particles in the measuring volume. The three signals are centered around 40 MHz, 20 MHz and 60 MHz corresponding to velocity components parallel to AC, BC and AB respectively. Only two of the three components are linearly independent. b) Receiving Optics

Scattered light from the measuring volume is collected by the photo-detector (TSI 9162) mounted on the receiving assembly (TSI 9140). The receiving assembly is mounted on the same side as the sending assembly (back-scatter mode) as shown in figure 2.10. The entire alignment and focussing of the beams and clean optical components are essential for the generation of a good signal. The backscatter mode allows easy traverse of the probe volume. Also the entire train of optics can be rotated about an axis parallel to the beam by two rotating mounts (TSI 9178-2 and TSI 9179). This enables the system to make measurements in the vicinity of curved surfaces. The signal from the photo-detector, which carries information on the three velocity components, is fed to a signal processing system.

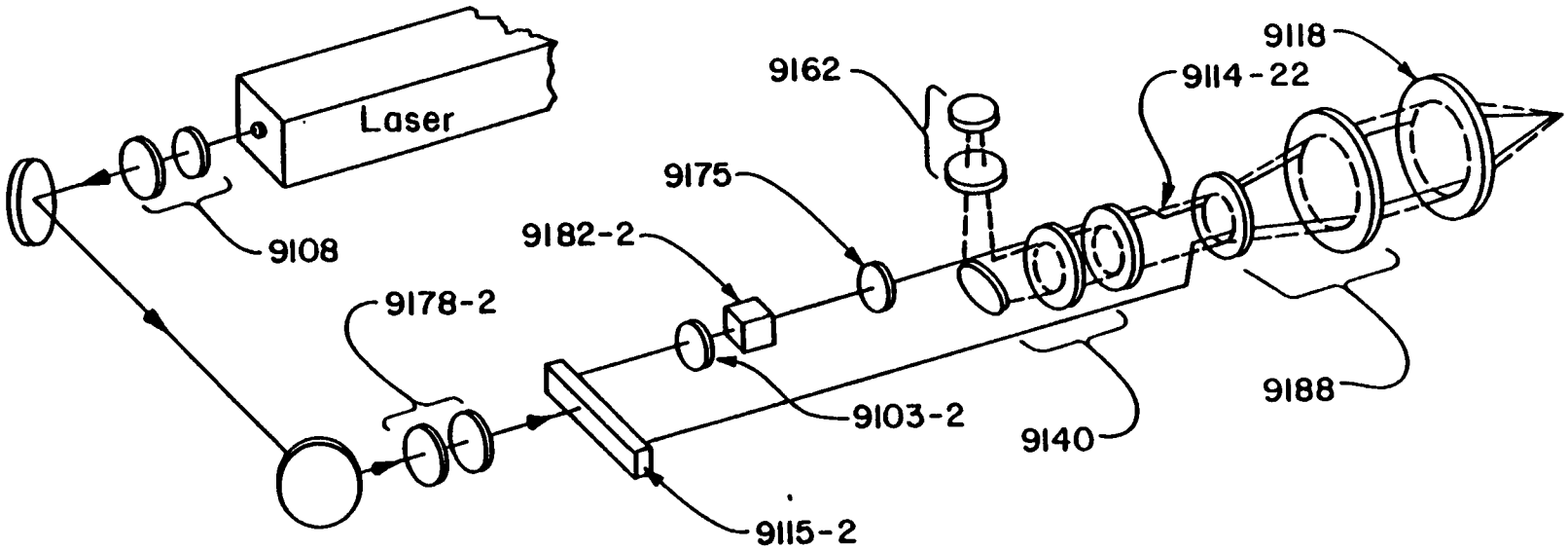

9118	Achromatic lens with focal length 250 mm
9188	Beam expander
9114-22	Beam spacer
9140	Receiving assembly
9162	Photodetector
9175	Beam Steering module
9182-2	Bragg-cell of 40 MHz
9103-2	Polarization rotator
9115-2	Beam splitter of equal intensity
9178-2	Rotating mount
9108	Collimator

Figure 2.10 TSI LDV system in back scatter

2.4.3 Traversing Mechanism and Feed-back Control

Displacement of the measuring volume in any direction within a vertical plane is carried out by a sophisticated traversing system. A major improvement is the addition of LVDT transducers enabling feedback control of the vertical and the horizontal traverse of the measuring volume. Accuracy in traverse of the order of 10 μm is obtainable with the present system.

The laser and the entire train of optics are mounted on a sliding table which is attached to a movable cradle (see figure 2.8). The table is carefully insulated against floor vibrations. The slider can be displaced horizontally. A mirror tower with two mirrors allows translation of the measuring volume in the vertical direction. The lower mirror is fixed and the upper mirror including the lens can be moved up or down, thus displacing the measuring volume. Figure 2.11 shows the details of the mirror tower. It is essential that the lower mirror be adjusted such that the reflected beams emerge vertically. This will ensure movement of the measuring volume in the vertical direction and more importantly, the beams then remain crossed after large vertical displacements.

The horizontal and vertical displacements are carried out by two stepping motors (SLO-SYN) which are controlled by the laboratory minicomputer (MINC-11). Schematic of the traversing mechanism is shown in figure 2.12. A pulse sent from the d/a converter of the MINC to a resistor activates one motor at a time. The horizontal lead screw requires 250 pulses sent from the digital out

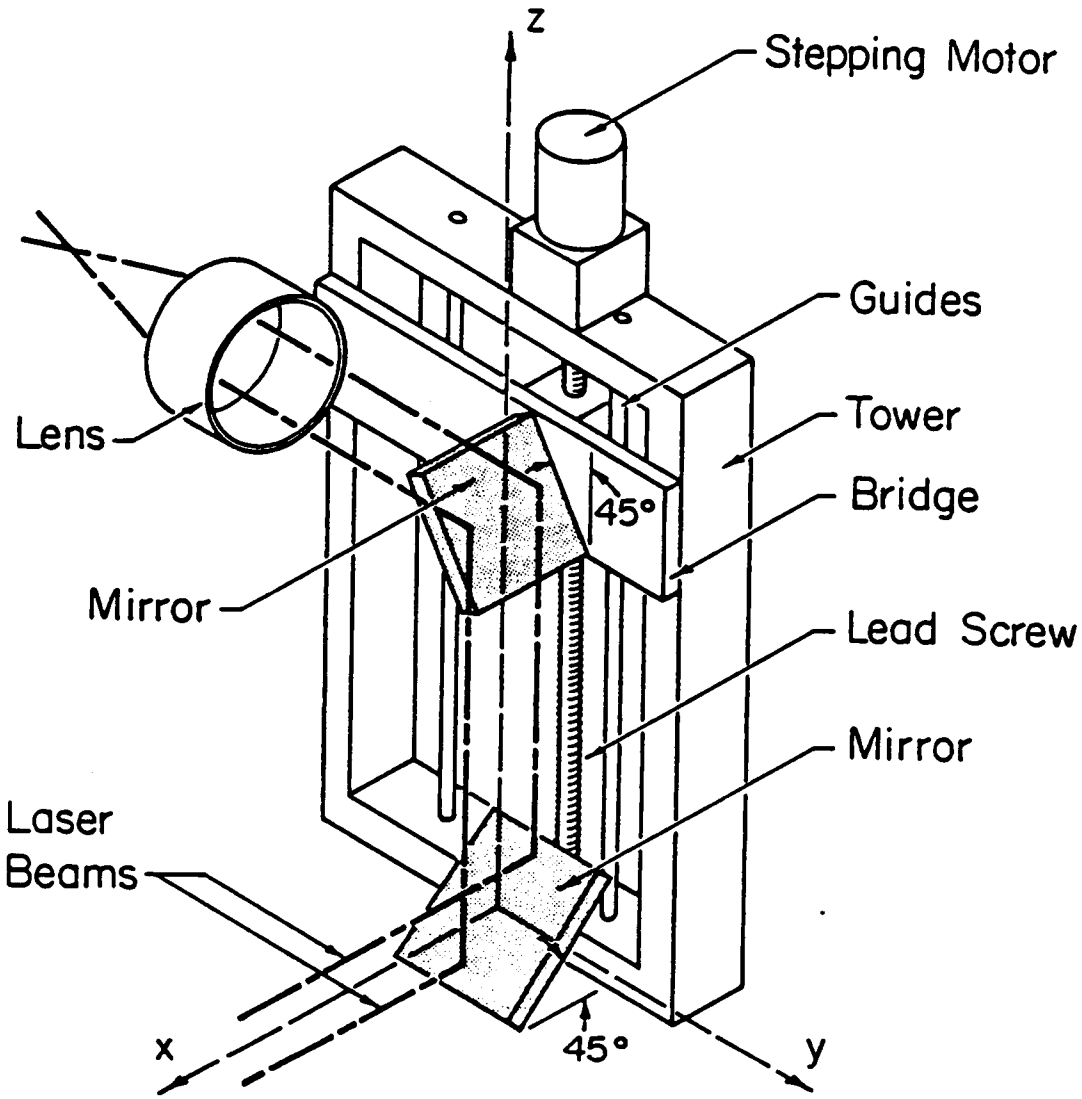

Figure 2.11 Sketch of the Mirror Tower

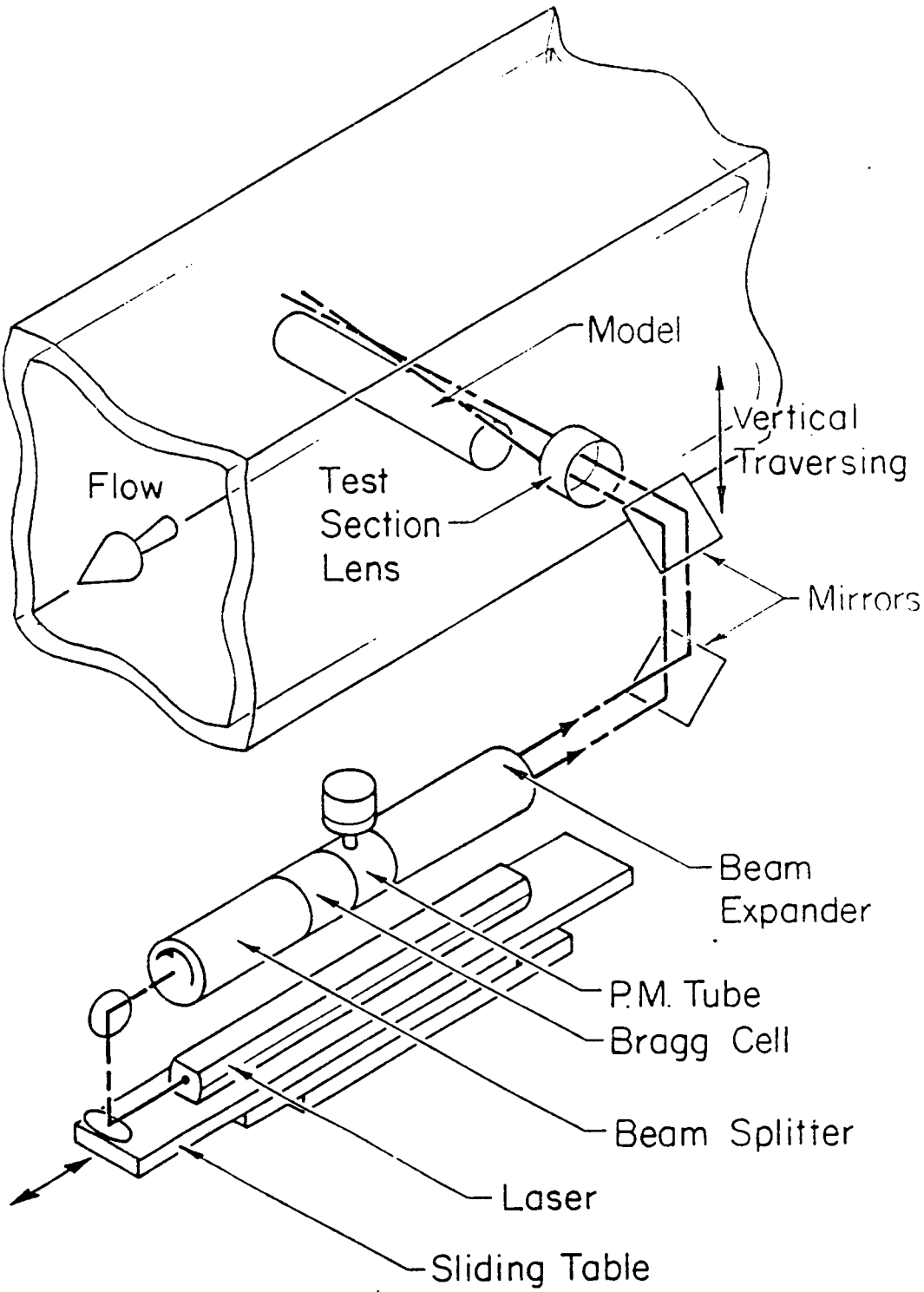

Figure 2.12 Traversing mechanism

module of the MINC for 1 mm of displacement. The vertical lead screw takes 80 pulses for 1 mm of displacement.

A significant improvement in the system is achieved through the addition of feedback control mechanisms. Miropositioning feedback is available for both the vertical and the horizontal directions. LVDT transducers (figure 2.13) produce electrical outputs proportional to the spatial position of the measuring volume. Output voltage for either vertical displacement or horizontal displacement is recorded by the MINC and checked against the correct value for a preassigned location. If the two do not check within 10 μm , the computer programme computes the difference and executes the movement in the proper direction by sending the required number of pulses through the stepping motor. The correction continues until the displacement is obtained within the preset accuracy of 10 μm. This feedback control allows measurements inside boundary layers and in wake regions with much improved accuracy. This is especially important when a large number of small displacements are to be undertaken and large errors could accumulate in the absence of the feedback control.

Subroutines are written to execute data acquisition in either rectangular grids in cavity regions or along radial lines around a cylinder. The data acquisition system is fully automated. Once the program is started, the computer takes over and data is acquired and stored for all the programmed grid points in the flow region.

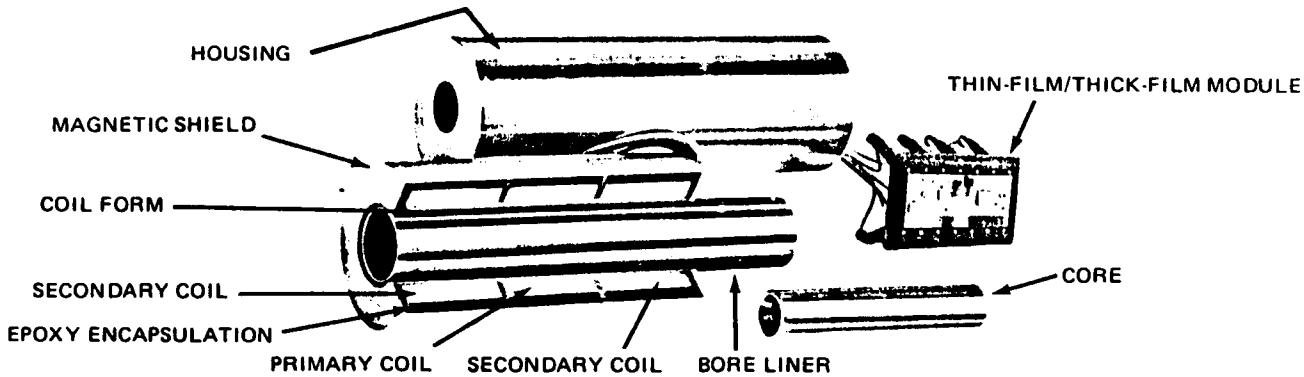

Figure 2.13 Schematic of LVDT transducer

2.5 WIND TUNNEL

A low speed pulsating wind tunnel (figure 2.14) is used for flow investigation by hot-wire anemometry. The tunnel design is based on a smaller, blower-type tunnel designed by Tavakoli et al. [1983]. The size of the test section is 124 × 74.1 × 52.9 cm. The settling chamber consists of a honeycomb and six screens. The contraction through the settling chamber outlet is made of steel and has a contraction ratio of 6:1. Pulsation of the mean flow is effected by six rotating vanes mounted on parallel shafts in the settling chamber. The vanes are gear-driven by a 2 hp. variable speed dc HELLER electric motor. Tunnel speeds of up to 33 meters per second can be generated. The turbulence level is below 0.5 percent and amplitudes of velocity fluctuation up to 25 percent are obtainable (Andraka, 1985).

2.5.1 Wind Tunnel Models

Three test cases of flows past a single cylinder, three cylinders and five cylinders in a row are undertaken. The cylinders are made of acrylic and have an outside diameter of 8.9 cm and a wall thickness of 5 mm. One of the cylinders is instrumented to measure pressure and skin friction around it. The end mounts on the cylinder can be replaced by another set to accomodate the balance system for lift and drag measurement. Pitch to diameter ratios of 1.1 and 1.8 are considered in the multiple cylinder cases.

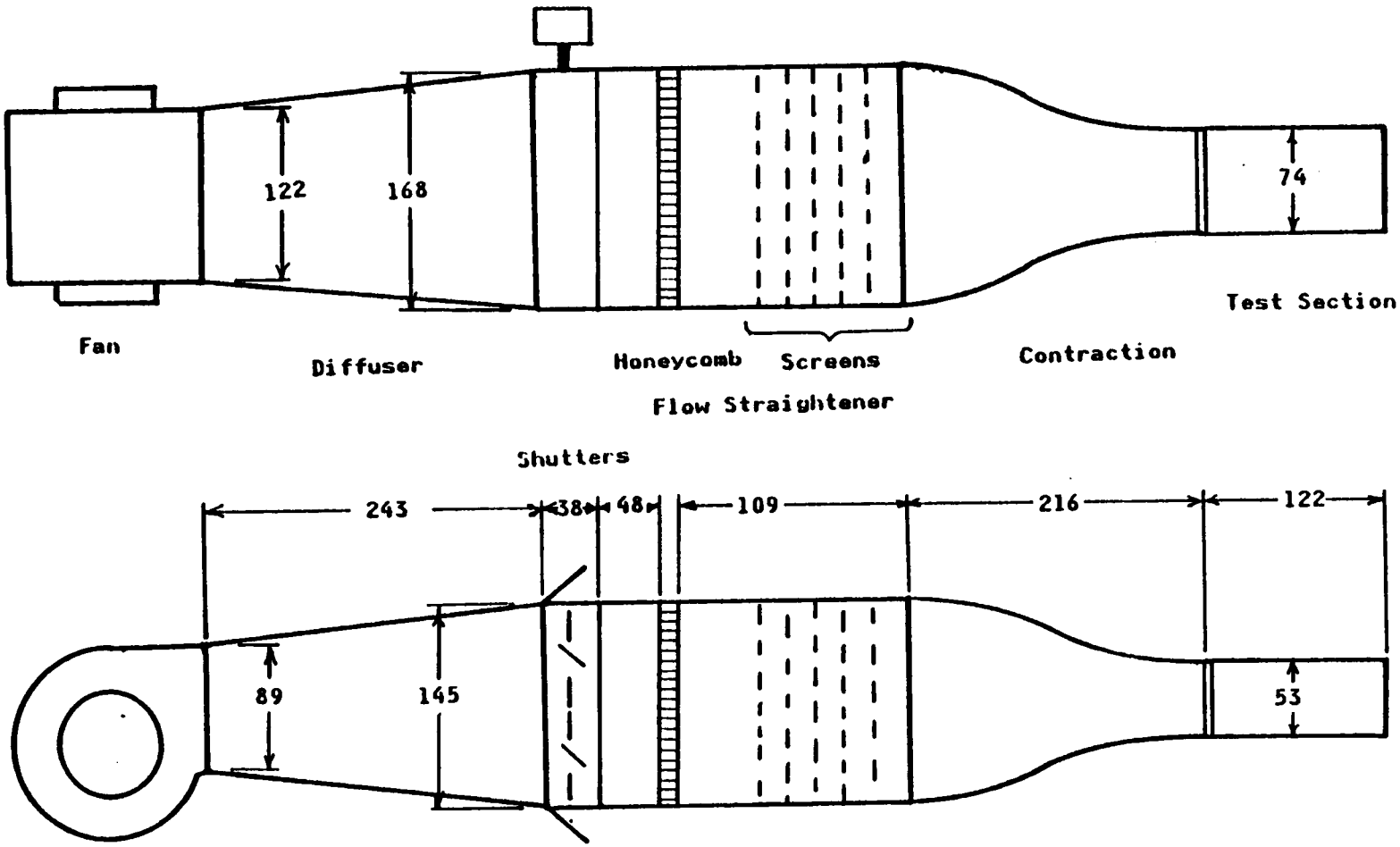

Figure 2.14 Schematic of the wind tunnel

2.5.2 Instrumentation for Data Acquisition

The data acquisition system comprises of hot-wire anemometers, a pressure transducer, a shear stress gauge, a balance system for lift and drag measurement and a minicomputer which controls the collection and on-line processing of data. The computer also executes the rotation of the instrumented cylinder thus allowing measurement of pressure and shear stress around the cylinder with only one pressure transducer and one shear stress gauge mounted on the cylinder.

Two brands of hot-wire anemometers, both constant temperature type are employed. The DISA system consists of a DISA 55D01 anemometer and a DISA 55D10 linearizer. A schematic of this equipment is shown in figure 2.15. The TSI system consists of an IFA 100 flow analyser and a model 1073 output linearizer. The DISA hot-wire probe is used with the DISA system and the TSI model 1210 hot film probe is used with the

Traversing of the hot-wire probe is done by a scale which allows vertical motion of the probe. Horizontal traverse is not possible with the present set up. Rotation of the instrumented cylinder is carried out by means of a stepping motor which is controlled by a minicomputer. This allows accurate positioning of the microphone or the shear stress gauge at any location around the circle with respect to the freestream direction.

The data acquisition system consists of a TRS80 minicomputer, a HP5420 signal analyser and a SLUMBERGER rms meter. Digital data stored on floppy

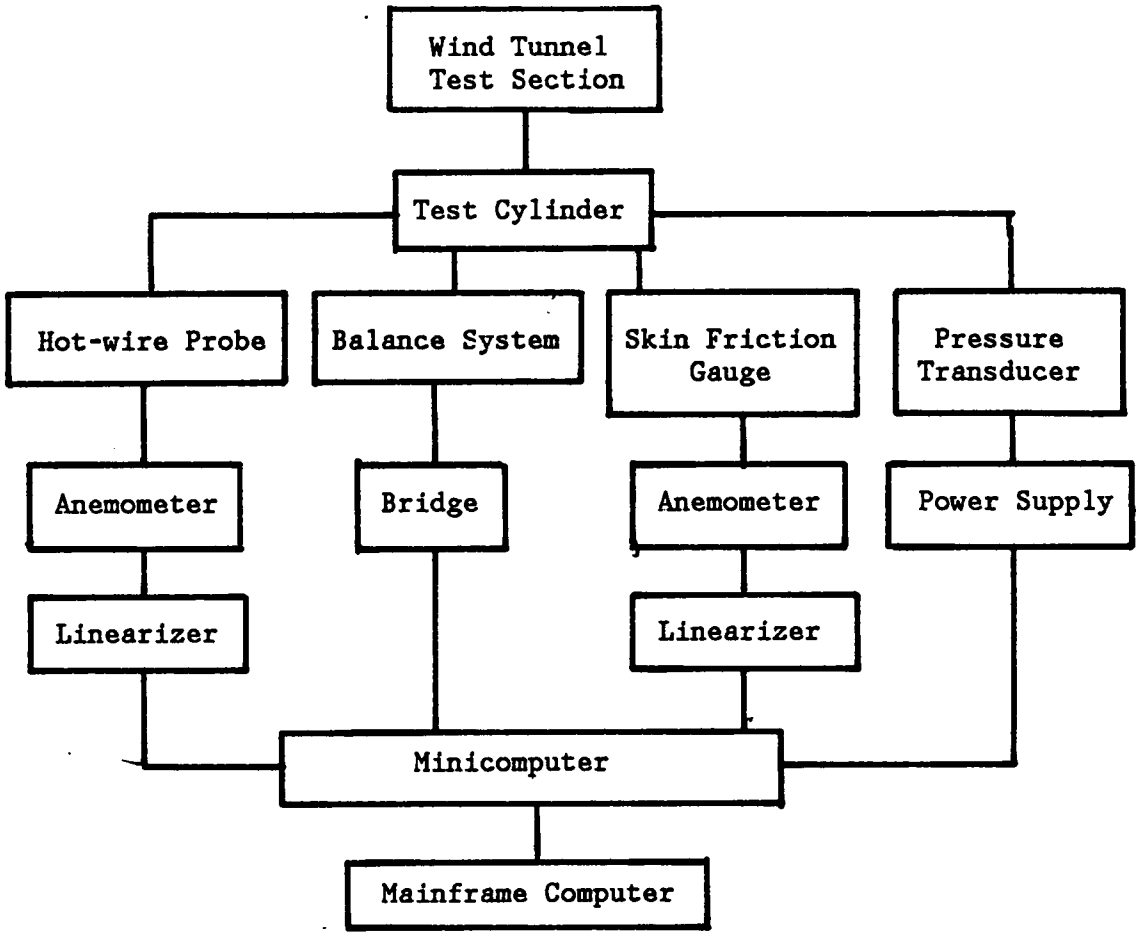

Figure 2.15 Data acquisition system in the wind tunnel

disks are transferred to the main frame computer for processing. Frequency-domain and time-domain data acquired by the HP5420 signal analyser are stored in HP tapes for later use.

2.6 COMPUTATIONAL FACILITIES

Computers employed for the work in this thesis range from micro to supercomputers. For data acquisition in the wind tunnel and the water tunnel laboratory minicomputers namely DEC MINC-11, MASSCOMP 560, TRS 80 and HP 5420A Digital Signal Analyzer were employed. The MINC and HP 5420A were extensively used for sampling and on-line processing of data. The main frame computer IBM 3084 was used for additional processing and plotting. Numerical analysis was performed mainly on CRAY-XMP supercomputer. CRAY-2, CRAY-1 and IBM 3090 were occassionally used. An IBM PC was used mostly as a dummy terminal to access the supercomputers located in Livermore, California. Brief descriptions of these computer facilities are given in appendix C.

CHAPTER III

EXPERIMENTAL WORK

3.1 INTRODUCTION

The experimental investigation of steady and pulsed flows across single and multiple cylinders is discussed in this chapter. Experimental facilities comprise of a water tunnel and a wind tunnel. Laser-Doppler velocimetry is conducted in the water tunnel for flow past three and five cylinders in a row. Emphasis is placed on measurements in the cavity regions between cylinders. Freestream velocities with different amplitudes and frequencies of oscillation are employed. Power spectra at various points in the cavity regions and outside are obtained. This enables identification of different frequencies of oscillation, both natural and forced. Lock-on studies are also carried out by taking power spectra at different driving frequencies. Flow visualizations are obtained in the water tunnel for the cases of flows past three and five cylinders. The photographs and films taken serve well in understanding the flow in different regions.

Experimental work in the wind tunnel provides velocity, pressure, shear stress and lift and drag measurements. Steady and pulsed flow across a single

cylinder, three cylinders and five cylinders are considered. Pressure, shear stress, lift and drag forces can not be measured directly in the water tunnel. The flow field indicated by the different fluid dynamic quantities mentioned above is then compared with that obtained from LDV measurements in the water tunnel. The following subsection presents a survey of literature pertaining to the experimental work reported in this chapter.

3.2 LITERATURE REVIEW

Numerous experimental works involving LDV, hot-wire anemometry and flow visualization can be found in the literature. During the recent years an extensive number of papers on laser-Doppler velocimetry has been published. Basics of LDV are provided in texts and reports like Durst, Melling and White [1976], Drain [1980]. A good bibliography can be found in Durst [1977] and, Pfeifer [1981]. Hot-wire anemometry can be found treated in numerous publications as well. Lomas [1986], Comte-Bellot [1975] are two examples. Brunn [1977] and Comte-Bellot [1976] give good reviews of hot-wire anemometry works.

During the past several years an extensive number of investigations have been reported on cross flow past cylinders. Experimental works in this area can be divided into three categories. The first is the fundamental problem of flow past a single cylinder. The second is the flow across tandem arrangement of multiple cylinders and the third is the flow around a bundle of cylinders. Flow around a

single cylinder in steady cross flow has been studied for decades and is now fairly well understood. Some of these studies [Morgan, 1975; Kestin et al., 1969] also deal with the effect of free stream turbulence on flow and heat transfer characteristics. The flow can be divided into three characteristic regions: the outer flow which is practically inviscid, the boundary layer where the flow is inherently viscous and the wake which is more or less inviscid but rotational. The boundary layer grows with distance downstream, reaching its maximum thickness near the point of separation. A laminar boundary layer in the subcritical Reynold's number range of 500 to 200,000 separates from the body surface at around 82 degrees from the front stagnation point to form a free shear layer. Vortices are shed alternately from the top and the bottom of the cylinder at the Strouhal frequency, forming a Karman vortex street behind the cylinder. More recently, three distinct regions in the separated flow have been identified [Lebouche and Martin, 1975] as shown in figure 3.1. Beyond a Reynold's number of 200,000 in the transition range the Karman vortex street is not regular. In the supercritical range, when the Reynolds number is beyond 4,000,000 a regular vortex pattern is seen again. Transition can occur at lower Reynolds numbers in the presence of significant freestream turbulence.

The effect of organized flow pulsations on flow past cylinders has received some attention lately. Pulsation of the freestream changes the flow characteristics which in turn alters the heat transfer characteristics of a flow system. The effects of organized freestream pulsations on flow past a single cylinder have been measured by several investigators [Lebouche and Martin; 1975, Andraka and

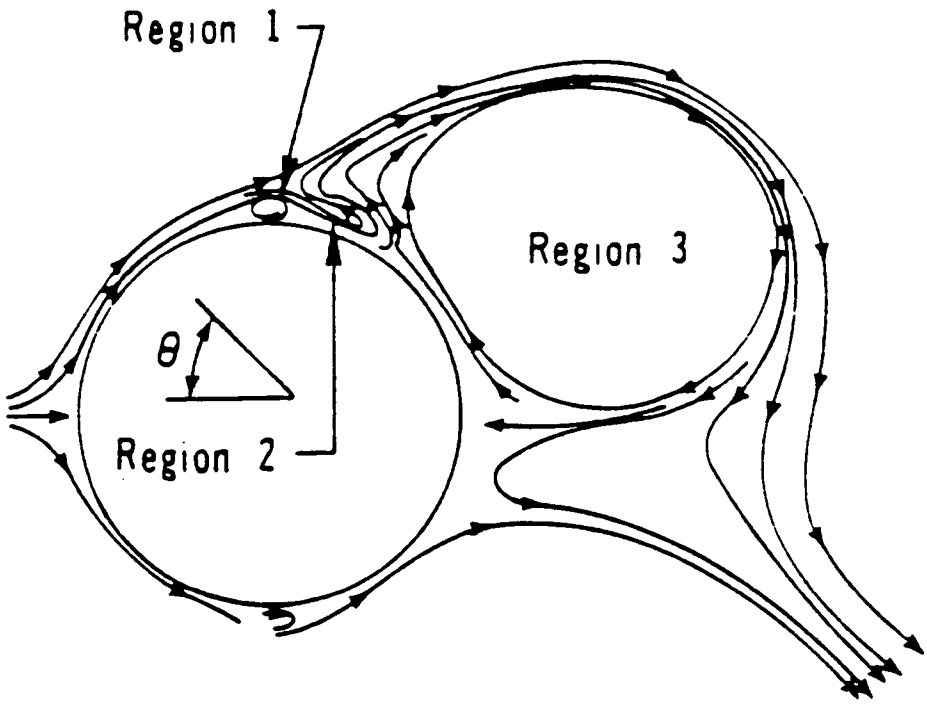

Figure 3.1 Three distinct regions in the flow past a single cylinder (Lebouche and Martin, 1975)

Diller, 1984; VandenBerghe, 1985; Saxena and Laird, 1978]. Lebouche and Martin [1975] and Andraka and Diller [1985] found no change in the time averaged heat transfer in the stagnation region due to freestream pulsation at low turbulence level. On the other hand, Lebouche and Martin [1986] as well as VandenBerghe [1985] found increases up to 12 percent in heat transfer at the back of the cylinder due to freestream pulsation. The mean surface pressure distribution around a circular cylinder has been measured by various investigators [Roshko, 1961; Achenbach, 1968; West and Apelt, 1982; Borell et al., 1984; Meier et al., 1981] for a wide range of Reynolds numbers. The coefficient of pressure on the back of the cylinder has been found to be lower for pulsed freestream by Borell et al. [1984]. Shear stress around a single cylinder in steady cross flow has been studied by several investigators [Achenbach, 1968; Son and Hanratty, 1969; Meir et al. 1981]. Shear stresses under pulsatile cross flow have been studied by Bellhouse and Schultz [1966]. They found a relationship between the fluctuating heat transfer from the gauge and the fluctuating skin friction. In most of these investigations, one or at most two measuring devices are employed. In the present work, a complete picture of the flow oscillations based on the measurements of all the fluid dynamic quantities obtained in the same tunnel and employing the same model at identical conditions is provided.

Flow across multiple cylinders is very much of interest because of their direct application to heat exchangers. Several investigators [Zukauskas et al., 1983; Achenbach, 1981; Aiba et al., 1982; Bergelin et al., 1952; Antonopoulos,

1978] have recently studied the problem of flow past a finite number of cylinders in a row. Kostic and Oka [1972] investigated the flow around a tandem arrangement of two cylinders. They suggest two flow patterns depending on the pitch-to-diameter ratio (figure 3.2). The laminar boundary layer on the first cylinder separates at around 82 degrees from the front stagnation point for all pitch-to-diameter ratios. SL and ST in the figure denote separation point laminar and separation point turbulent respectively. At pitch-to-diameter ratios greater than 3.8, the second cylinder has no influence on the flow developing around the first and the wake pattern is the same for both the cylinders. The flow around the first cylinder is similar to laminar flow around a single cylinder and the flow around the second seems like turbulent flow around a single cylinder. The width of wake from the second cylinder is narrower indicating lower form drag. For smaller pitch-to-diameter ratios, a closed quasi-steady vortex region or cavity is formed between the cylinders. The patterns of the flow were found to remain unchanged for Reynolds numbers in the range of 12,000 to 40,000.

Hiwada et al. [1982] obtained measurements of flow past two cylinders in a row. They disagree with Kostic and Oka in their interpretation of the flow phenomena and suggest that the flow pattern is more complicated. They also indicate a discontinuity in Strouhal number at pitch-to-diameter ratio of 3.8 where closed vortex formation region starts to occur.

Zdravkovich [1977] gave a review on results from a number of investigations on flow across two circular cylinders. His conclusion is that there is no vortex shedding behind the first cylinder at pitch-to-diameter ratios less

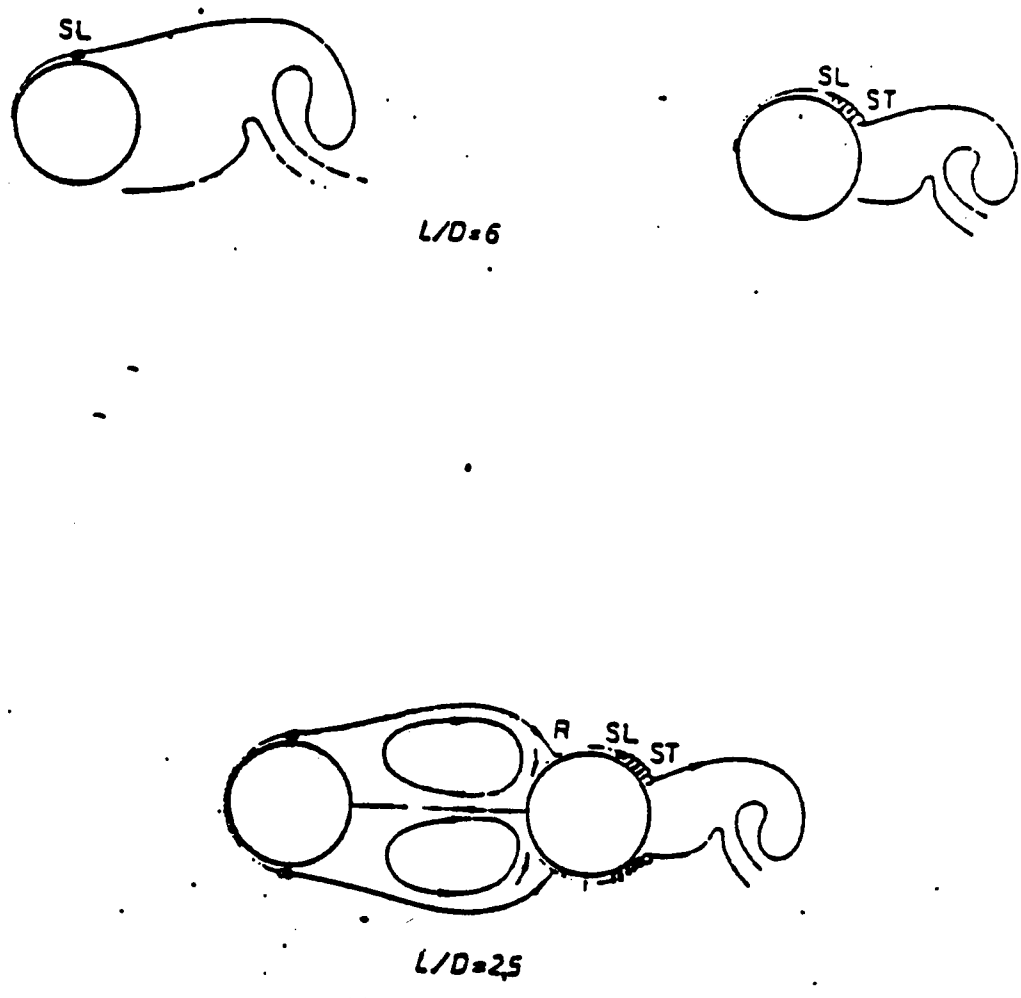

Figure 3.2 Patterns of flow for flow across two cylinders (Kostic and Oka, 1972)

than 3.8. There is a jump in the Strouhal number at pitch-to-diameter ratio (P/D) of 3.8 and two Strouhal frequencies exist intermittently. Up to the critical spacing of P/D of 3.8, the shear layer separating from the upstream cylinder reattaches onto the downstream cylinder forming the quasi-stationary cavity. Beyond the critical spacing, the shear layer rolls up in front of the second cylinder and vortex shedding is observed from both the cylinders.

Igarashi [1984] also carried out investigations on the flow around two circular cylinders arranged in tandem. He classified the flow into various patterns according to the Reynolds number and the pitch-to-diameter ratio as shown in figure 3.3. A peculiar phenomenon of decrease of Strouhal number with increase of Reynolds number in the range 25,000 to 64,000 was observed.

Aiba et al. [1980] made an experimental investigation on fluid flow and heat transfer around the second cylinder of three cylinders in a row. Heat transfer rate is generally found to improve with the decrease of the width of the wake from the first cylinder and with the increase of the oncoming flow velocity. When the boundary layer on the first cylinder is tripped with a wire, the jump phenomenon or the discontinuity in Strouhal number is found to occur at a pitch-to-diameter ratio of 2.8. The pressure drag coefficient decreases with reduced spacing between cylinders for Reynolds numbers greater than 48,000. Aiba et al. also investigated the flow around an in-line arrangement of four cylinders. The jump phenomenon was observed for a spacing smaller than pitch to diameter of 3.8.

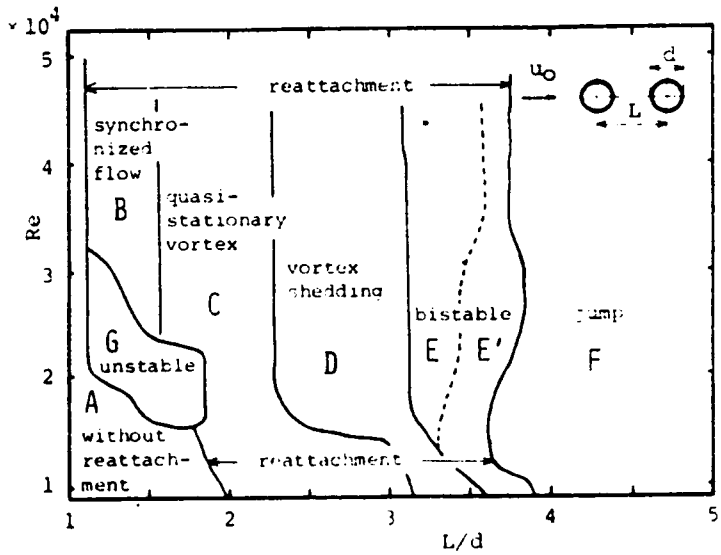

Figure 3.3 Patterns of flow for flow across three cylinders (Igarashi, 1984)

For flow past three cylinders in a row, Igarashi and Suzuki [1984] suggest six different flow patterns as shown in table 3.1 They base this on instantaneous and time averaged flow visualizations along with pressure, velocity and shedding frequency measurements. For a Reynolds number less than the critical value Re_c , vortex shedding occurs only behind the third cylinder and is designated pattern A. Free shear layers separated from the first cylinder do not reattach to either of the two downstream cylinders. For $Re = Re_c$ and $P/D = 1.32$, the pattern B′ is bistable. The free shear layers either remain unattached or alternately reattach to the second and the third cylinders. Two Strouhal numbers of 0.23 and 0.09 exist intermittently. At $Re > Re_c$ and $P/D < 2.21$, pattern B exists whereby the free shear layers reattach onto the downstream cylinders. In pattern C ($Re > Re_c$ and $2.21 < P/D < 3.25$) one free shear layer from the first cylinder reattaches to the second and the other shear layer rolls up and forms a vortex between the second and the third cylinders. This is different from the results of earlier investigations [Kostic and Oka, 1972; Hiwada et al.,1982] with a pair of in-line cylinders which suggest that vortex shedding occurs behind the first cylinder only at $P/D \geq 3.8$. Pattern E is bistable and indicates Strouhal number discontinuity at $P/D = 3.24$. The free shear layer either reattaches to the second cylinder, or rolls up forming a vortex between the downstream cylinders. In pattern D ($P/D > 3.24$) vortices are shed from all three cylinders and Strouhal number lies between 0.16 and 0.18.

Pulsed flow across three cylinders in tandem arrangement has recently been studied also by VandenBerghe et al. [1985]. For P/D of 1.8, the region between

Table 3.1 Flow patterns for flow past a triad of cylinders
(Igarashi and Suzuki, 1984)

Flow Pattern	Shear Layer	Range	S	$C_{D'}$	$\overline{C_D}$
A	(W,W)	$Re < Re_c$	0.23 ~ 0.24	-0.6	0.16
B'	(W,W) & (W,R)	$Re = Re_c$, L/d = 1.32	bistable, hysteresis		
B	(R,R)	$Re \geq Re_c$, L/d < 2.21	0.09 ~ 0.13	-0.4 ~ -0.3	0.3 ~ 0.4
C	(R,J)	2.21 ≦ L/d < 3.24	0.13	-0.3 ~ -0.1	0.4 ~ 0.5
E	(R,J) & (J,J)	L/d = 3.24	bistable : Jump C → D and D → C		
D	(J,J)	L/d > 3.24	0.16 ~ 0.18	0.35 ~ 0.42	0.6 ~ 0.7

the first and the second cylinders contains two standing vortices resembling a cavity flow and violent vortex shedding occurs over the second cylinder. The details will be included in the experimental results to follow.

Flow around five cylinders in a row has been investigated by Ishigai and Nishikawa [1975]. They concluded that for P/D up to 1.5, only the last cylinder sheds vortices while for P/D of 2 or more, vortices are shed from all of the five cylinders. In the present study, it is found that the first cylinder does not shed vortices for P/D up to 1.8. The present findings are therefore in agreement with those of Ishigai and Nishikawa. Investigations on the effect of pulsation of freestream on flow across five in-line cylinders are not available in the literature. The present study deals with both steady and unsteady pulsed flow past five cylinders.

Cross flow past a bundle of cylinders has been investigated by many researchers. Zukauskas [1972] has presented a review of works on fluid flow and heat transfer across cylinder bundles. Savkar [1976] has investigated the effect of transverse pitch-to-diameter ratio on flow measurements for bundle of cylinders. The investigations by Bergelin et al. [1952] covers in-line and staggered bundles of different configurations at low Reynolds numbers. Since flows across in-line and staggered bundles of cylinders are investigated numerically for this thesis, the related works are referenced again in later chapters.

The current experimental investigation considers the effect of organized flow pulsations on flow characteristics for flow over a single cylinder and across in-line arrangements of three and five cylinders.

3.3 LDV SIGNAL PROCESSING AND DATA ACQUISITION

The two signals, which are shifted by 40 MHz and 20 MHz from the Doppler frequencies, are passed through two band-pass filters (TSI 1985-3) with band widths of 12-28 MHz and 32-48 MHz, respectively. The two frequencies containing information on the two components of velocity are thus separated. These signals are then fed to separate frequency mixers, namely, the 20 MHz+ signal to the TSI 9186A-20 and the 40 MHz+ signal to the TSI 9186. The frequency mixers are set to a predetermined down or upshift frequency, usually termed the 'zero frequency'. This shifted frequency corresponds to zero velocity. The frequency mixers output frequencies corresponding to the two components of fluid velocity. Thus the frequency output from the mixer is given by

$$f_s = f_0 + f_d \qquad [2.4.5]$$

where f_s is the signal frequency, f_0 is the zero frequency and f_d is the Doppler frequency

The signal outputs from the mixers are then fed to signal processors (TSI 1990, TSI 1980 counters) which generate voltages corresponding to the signal frequencies. A schematic of the frequency shift system is shown in figure 3.4. The

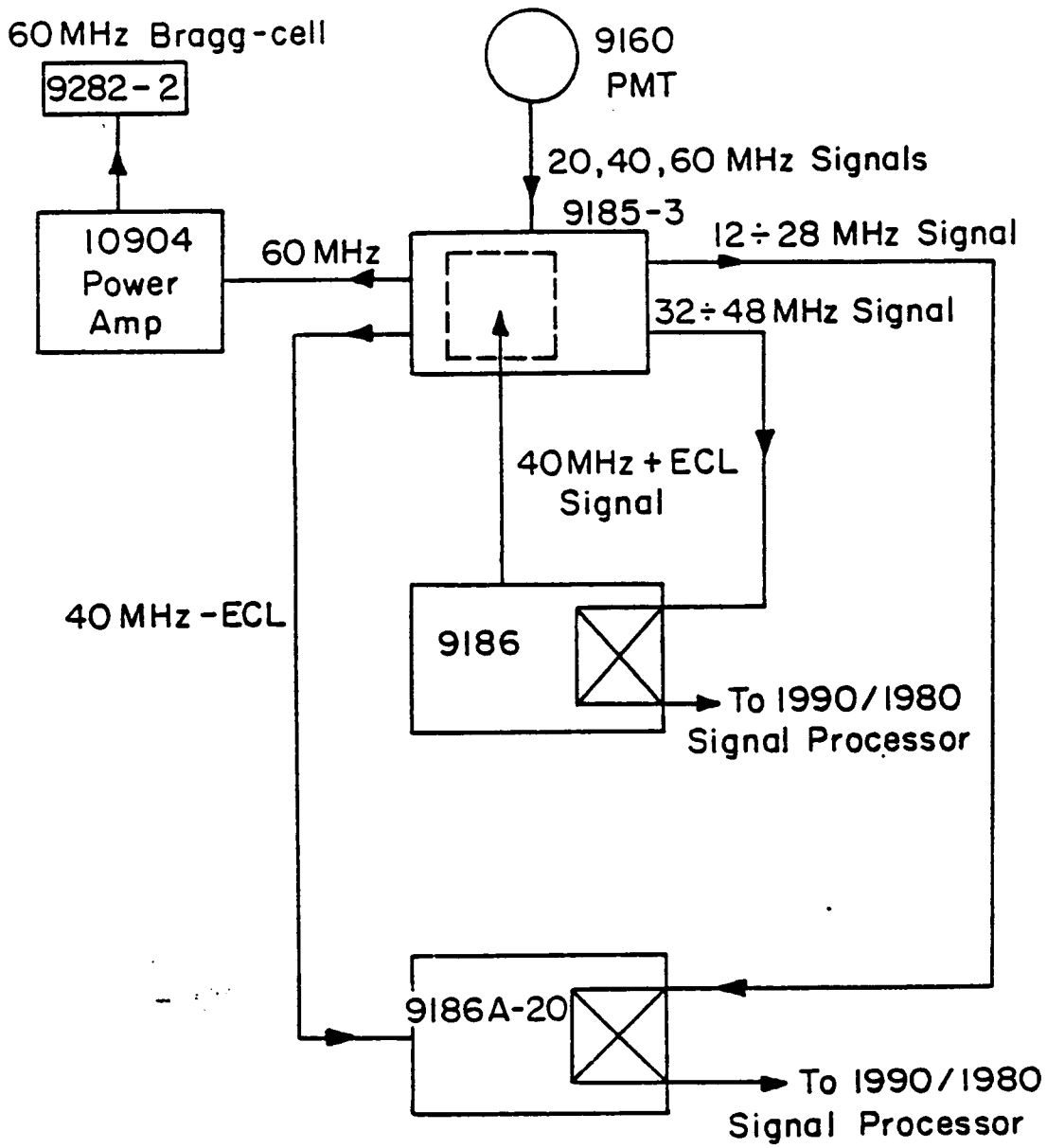

Figure 3.4 Schematic of the frequency shift system

voltage, V_d corresponding to the velocity component under consideration is given by

$$V_d = V_s - V_0 \qquad [2.4.6]$$

where V_s is the signal voltage, V_0 is the voltage corresponding to f_0 The frequencies are related to the output voltages through the transfer function, X as indicated below

$f_d = X \times V_d$

$f_s = X \times V_s$

$f_0 = X \times V_0$

The transfer function is determined by the exponent setting on the counter. The exponent setting is selected so that the signal voltage lies within 5V, which is the maximum that can be fed to the minicomputer (DEC MINC-11). Input conditioner (TSI 1994B) and Timer (TSI 1995B) modules in the counter allow adjustments in the band pass filter, gain and comparison settings for optimum signal output.

With the latest addition of a digital interface (master interface and slave interface) to the counters, both analog and digital data acquisition are possible. In the analog data acquisition, output from the analog module (TSI 1988) is digitized by the d/a converter of the MINC and stored for analysis. The digital interface allows digital data to be stored through the DMA driver in the preassigned addresses without having to go through the CPU of the minicomputer. This leaves the CPU available for other purposes while the data

is being acquired. Also it is believed that the digital data thus obtained through the digital interface will represent the flow better than digitized analog data, especially in the case of signals with low data density. Figure 3.5 shows the schematic of the data acquisition system.

To monitor the freestream, the output from a DISA photomultiplier is connected through a DISA power supply to a third TSI counter (TSI 1980). A counter is used instead of a tracker for uniformity. The spatial and time variations of the two velocity components and time variation of the freestream are recorded and stored on floppy disks. The Fortran programs used for digital and analog data acquisition including the traversing are listed in appendix A. The present data acquisition system also comprises of a two channel HP-5420 signal analyser for time domain and frequency domain data analysis and a Schlumberger digital voltmeter for measuring rms of velocity fluctuations. The data stored on floppy disks are transfered to the main frame computer for further processing.

3.4 CLIBRATION OF GAUGES AND WIND TUNNEL MEASUREMENTS

Calibration of the anemometers is done with measurements recorded via a pitot tube. An electronic manometer employed for the purpose allows measurements to an accuracy of 0.08 mm of water head difference between the static and the dynamic pressures. In pulsed flows the accuracy goes down to 0.3 mm of water at driving frequencies less than 5 Hz.

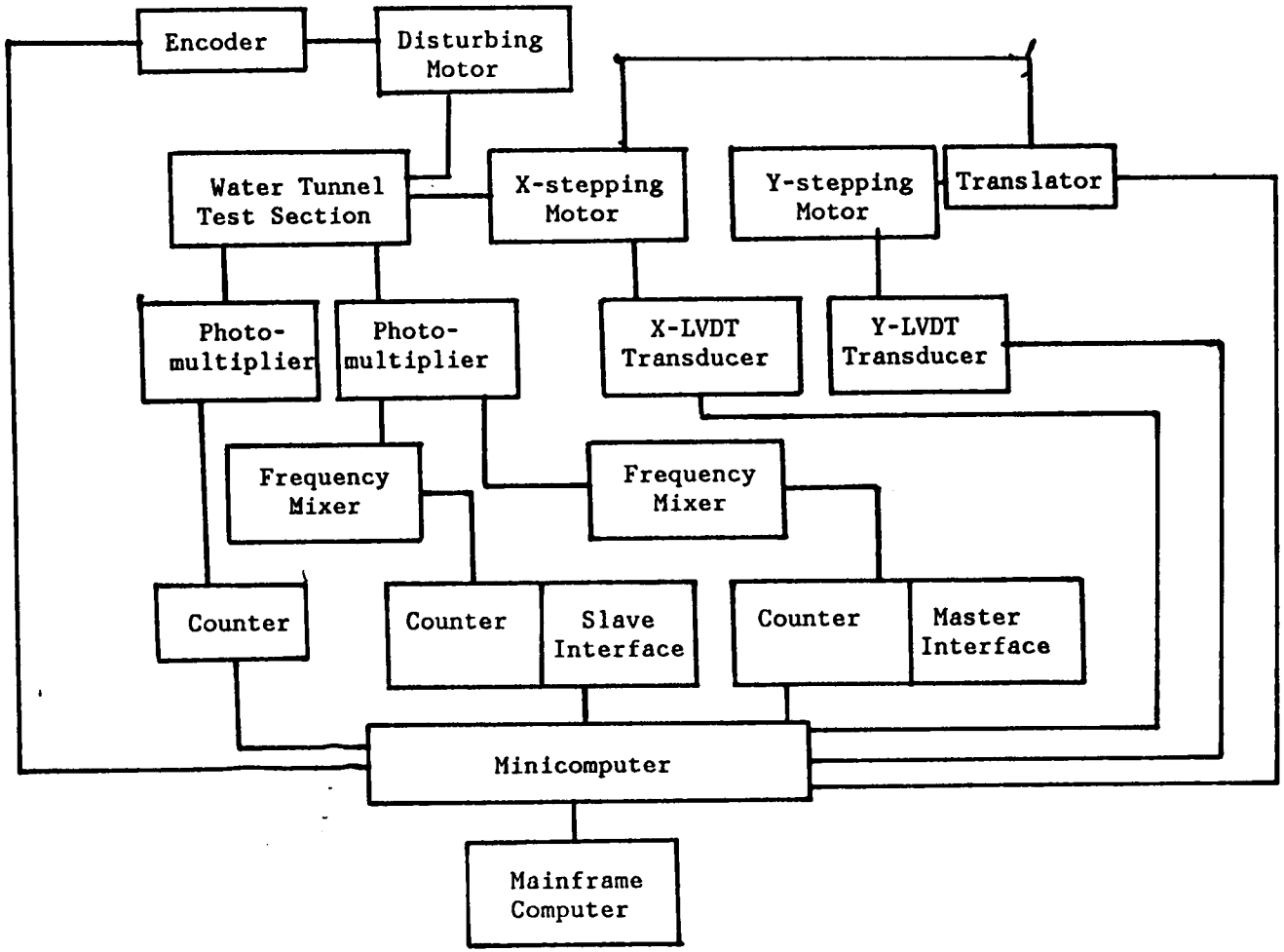

Figure 3.5 Layout of the LDV data acquisition system

The calibration of the hot-wire (or hot film) is done by recording velocity and voltage-output. The velocity-voltage relationship is given by King's law

$$E^2 = A + BV^n \qquad [2.4.7]$$

where E is the output voltage, V is the flow velocity and A, B and n are constants The linearizer is an electronic device whose transfer function, k is related by

$$V_{out} = k(V_{in}^2 - V_{in0}^2)^m \qquad [2.4.8]$$

where k, V_{in0} and m are constants and V_{in} and V_{out} are the input and output voltages, respectively. By letting $V_{in} = V$ and $V_{in0}^2 = A$ and m = 1/n, the linearizer output voltage becomes linearly proportional to velocity as shown below:

$$V_{out} = k(A + BU^n - V_{in0}^2)^m = kBU \qquad [2.4.9]$$

In the present study, hot-wire anemometers are employed to measure velocity in the freestream and around the cylinders including the wake.

Pressure on the surface of the cylinder is measured by a Bruel and Kjaer 4133 condenser microphone mounted on the test cylinder. The microphone is connected to a model 2619 preamplifier and a model 2801 power supply. The cylinder is rotated by a motor which is driven by a minicomputer (TRS 80). This allows pressure measurements along the entire periphery of the cylinder. Digital calculations are done using a modified version of the data acquisition program used by Andraka [1985] and VandenBerghe [1986]. The program listing is given

in appendix B. Final statistical calculations are made using a HP5420 signal analyser.

Skin friction around the cylinder is measured by means of a TSI flush-mounted hot film gage. The gage is mounted so that the circular surface containing the film is flush with the cylinder wall on which shear stress is to be measured. The sensor is operated by the IFA 100 in the same way as for velocity measurement. Voltage output, E from the anemometer is related to the wall shear stress τ_w [Bellhouse and Schultz, 1966] by

$$\tau_w^{1/3} = AE^2 + B \qquad [2.4.10]$$

where A and B are constants to be determined from calibration. B represents the heat lost to the substrate. The shear stress τ_w depends on the sixth power of E and extreme care must be taken during calibration. A few researchers have proposed different methods of calibration of the skin friction gauge [e.g. Ramaprian and Tu, 1982]. In the present study, bridge voltages from the IFA 100 corresponding to skin friction at 10 and 30 degrees on the cylinder for different Reynolds numbers are used for calibration. Using the known Reynolds number and values of the coefficient of skin friction (C_f) taken from Achenbach [1968] at 10 and 30 degrees, the skin friction τ_w at each data point is obtained

$$\tau_w = C_f \rho U_\infty^2 / Re^{0.5} \qquad [2.4.11]$$

where ρ is the density of the air, U_∞ is the freestream velocity and Re is the Reynolds number. A fourth degree polynomial curve fit determines the constants for use in a TSI 1073 linearizer with a transfer function given by

$$V_{out} = AE + BE^2 + CE^3 + DE^4 = k\tau_w \qquad [2.4.12]$$

where, V_{out} is the linearizer output, A, B, C and D are the linearizer constants, E is the anemometer bridge output and k is a constant linearly relating τ_w and V_{out}.

The calibration is checked by comparing the values of C_f obtained from the linearizer output at different points around the cylinder with the corresponding values from the Achenbach curve. A calibration producing an error of less than five percent is considered acceptable.

A significant influence of the freestream temperature on the linearizer output is noticeable during the actual calibration. The freestream temperature T_∞ directly affects the overheat $(T - T_\infty)$, which in turn depends on the bridge voltage. The gauge temperature T varies directly with the power dissipated (E^2/R) across the bridge. The bridge voltage E and the gauge overheat can be adjusted by varying the gauge's operating resistance in the IFA 100 circuitry. To obtain an overheat equal to that of the calibration run, the operating resistance is adjusted so that the bridge voltage is equal to that obtained for a known velocity used during the calibration. With equal overheat and equal bridge voltage, the calibration results in a repeatable and reliable linearized output for the shear stress.

Lift and drag measurements are made using a balance system shown in figure 3.6. This system was designed, constructed and calibrated especially for this project. The strain gauges bonded to the balance arms, as shown, react to the lift and drag loads. The deflection of the frame due to lift and drag induces strains in the gauges which correspond to the magnitude of the lift and drag forces on the cylinder. The strain gauges are connected to a full bridge and a power supply. Strain changes the resistance of the sensor, which in turn is a function of temperature. The voltage applied across the bridge for null position or constant resistance is thus a measure of the force. The balance system is designed so that the arms do not touch the walls of the tunnel and thus avoid vibrations of the tunnel structure. Wooden posts and vibration absorbers are used to minimize transmission of any vibration from the floor.

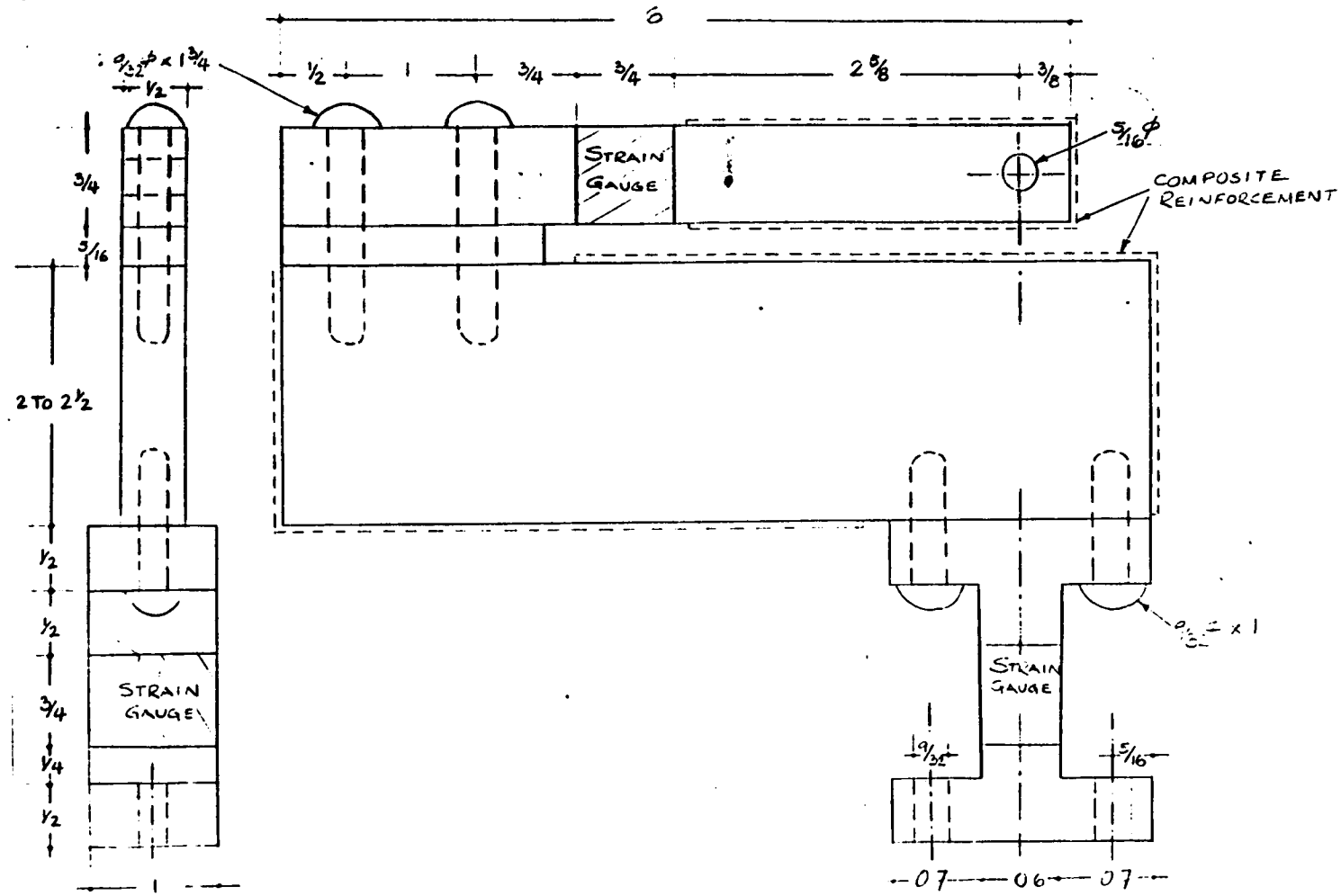

Figure 3.6 Balance system for lift and drag

CHAPTER IV

EXPERIMENTAL RESULTS AND DISCUSSION

4.1 INTRODUCTION

The experimental results discussed below are divided into three sections. The first covers experimental data obtained for flow past a single cylinder. The second section deals with the results obtained for flow past three in-line cylinders and the third provides results of flow measurements around five in-line cylinders. Skin friction, pressure, lift, drag and hot-wire results are presented. The measurements on a single cylinder have been extended to new areas, e.g. simultaneous measurements of skin friction and pressure in separated regions and detailed study of flow organization after separation. The flow field is examined both for steady and pulsed freestream across the cylinder.

Results on flow past a triad of cylinders and five in-line cylinders consist of LDV, flow visualization, skin friction and pressure data. Steady flow results are compared with other available experimental data. Instantaneous velocity data are obtained for these flows for the first time. Skin friction data also could not be found in the literature for comparison. The effect of pulsation on the fluid

mechanics of these flows is studied for the first time. The fluid flow quantities are compared with the respective steady flow counterparts.

4.2 FLOW PAST A SINGLE CYLINDER

Figure 4.1 shows a typical waveform and power spectrum of the freestream velocity in the wind tunnel at a Reynolds number of 23,000 and driven at 18.15 Hz. The waveforms are nearly sinusoidal with the fundamental frequencies carrying about 97 percent of the total wave energy. Turbulence level is below 0.45 percent for all the tests conducted. The amplitudes of fluctuation range from 6 to 25 percent peak to peak.

Figure 4.2 shows the power spectra of skin friction at 40 degrees from the front stagnation point on the cylinder with and without a splitter plate. Introduction of a splitter plate at the back of the cylinder suppreses the shedding frequency completely as can be seen in the figure. Figure 4.3 shows a typical plot of output voltage squared (E^2) versus the angular position on the cylinder, with a splitter plate behind it. This plot could be used for the calibration of the shear stress gauge by assuming E^2 to be proportional to $\tau_w^{1/3}$. But, as mentioned earlier, the calibration is carried out from the actual bridge voltage and C_f data obtained from Achenbach [1968] at 10 and 30 degrees for different Reynolds numbers. The output from the shear stress gauge is linearized by fitting a fourth degree polynomial and setting the coefficients in the TSI linearizer.

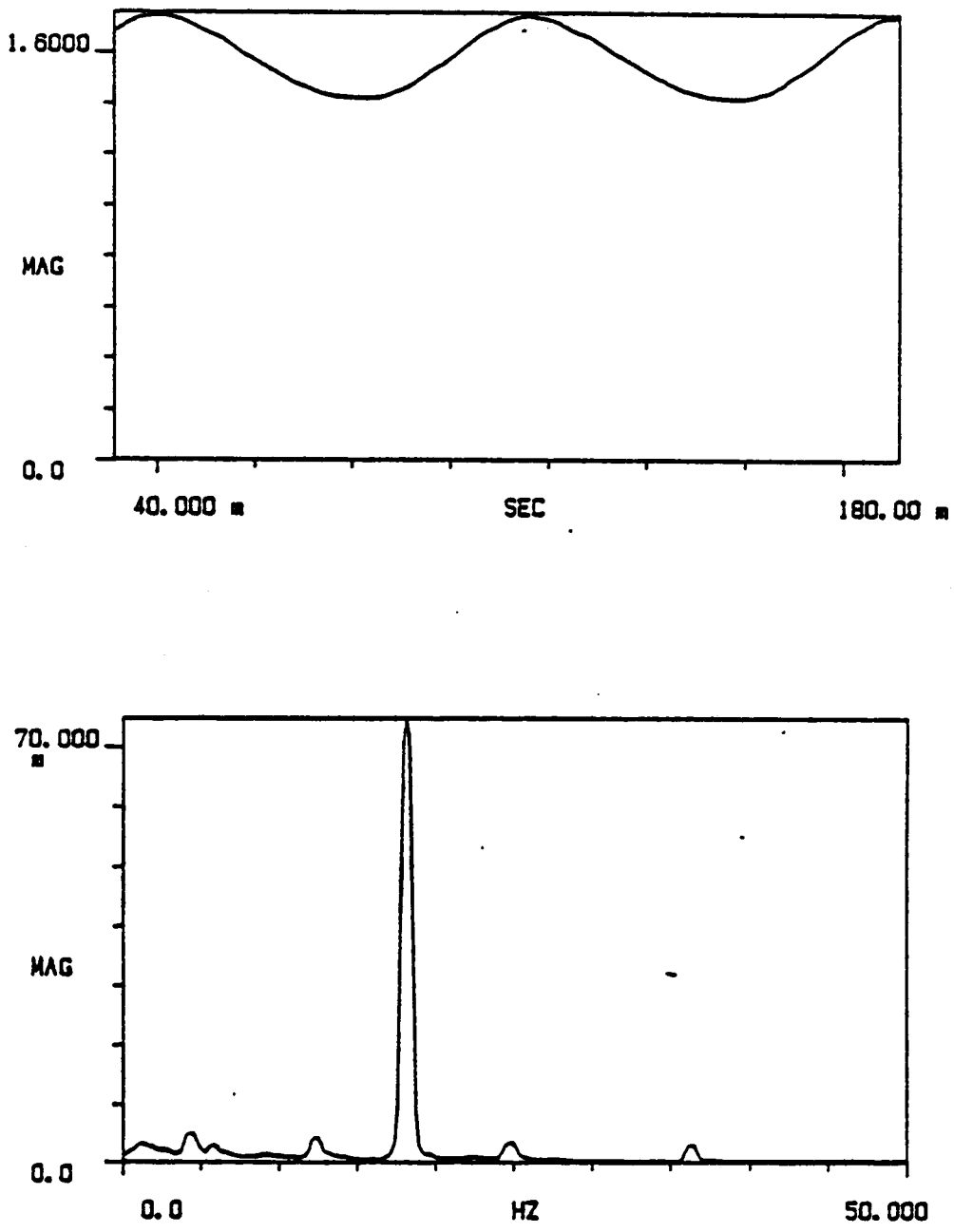

Figure 4.1 A typical time and frequency domain record of freestream in the wind tunnel

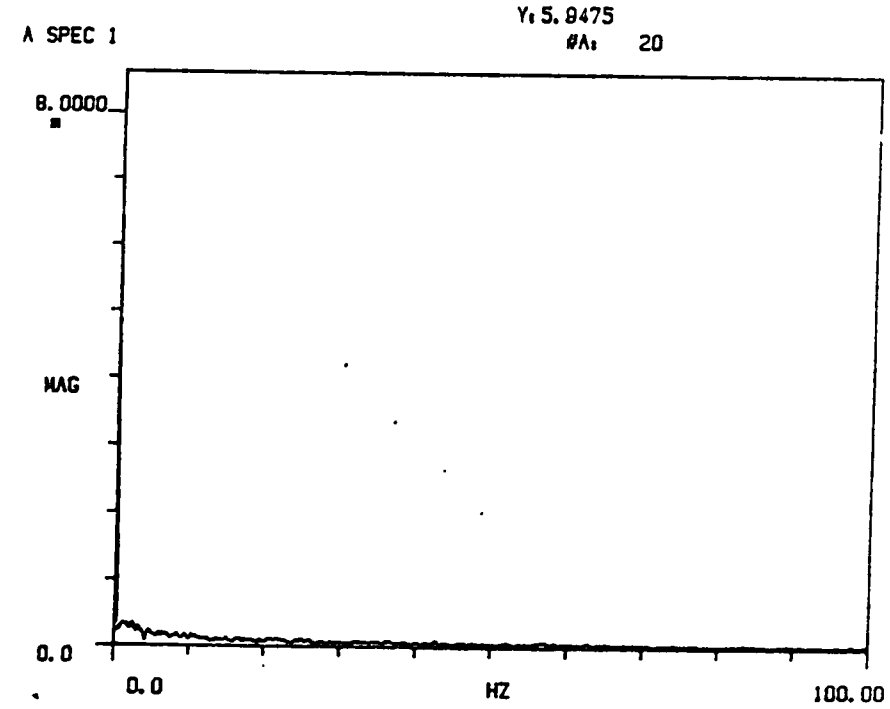

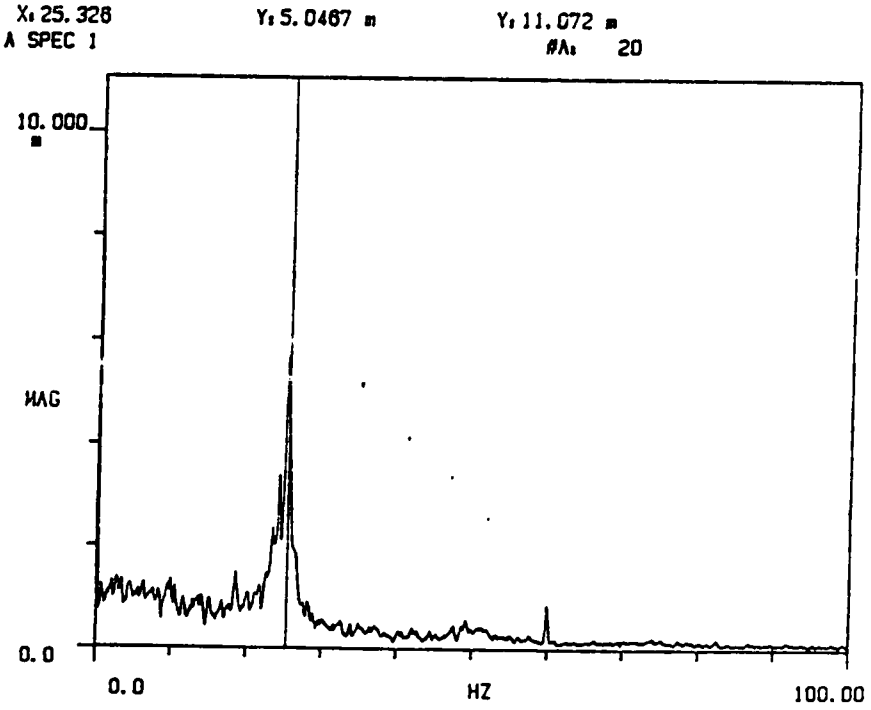

Figure 4.2 Power spectra of skin-friction with and without splitter plate

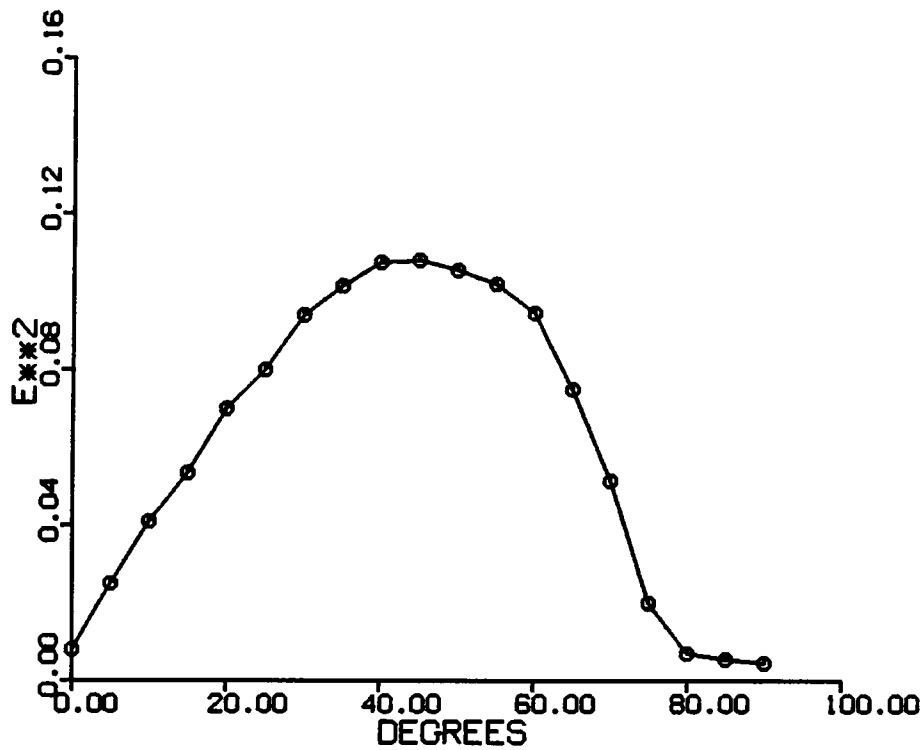

Figure 4.3 Shear stress gauge output squared at different locations around the cylinder

Steady freestream tests are conducted with a single cylinder. In such tests the shedding frequency is practically inescapable, regardless of the sensing device employed. Figure 4.4 displays a dominant frequency indicated by a hot-wire measurement away from the boundary layer. This indicates a flowfield characterized by shedding of vortices at the Strouhal frequency. The Strouhal number is known to remain almost constant and equal to 0.2 for laminar flows.

Power spectra of skin friction at points around the cylinder from 90 degrees to 180 degrees from the stagnation point are shown in figure 4.5. It is observed that skin friction shows a well defined organization at the shedding frequency from 120 to 130 degrees and then again from 150 degrees up to 180 degrees. Skin friction varies in phase with heat transfer in the attached flow region. It is believed, and our work has demonstrated, that the skin friction organization and the magnitude of amplitude variations are similar to those of heat transfer in the separated flow region [Gundappa, 1986]. If increased organization can be achieved in some way, e.g. by pulsation of the freestream, it may be possible to increase the heat transfer considerably. Figure 4.6 shows a comparison of time record of skin friction with and without organization. Figure 4.6a is the time record of the freestream employed in each case. Figure 4.6b is the time record of the skin friction on the cylinder at 120 degrees position where no organization in seen and figure 4.6c is the time records of skin friction at 160 degrees position where skin friction is organized.

Mean shear stresses around the cylinder for steady flow with Re = 50,000 and at different driving frequencies are shown in figure 4.7a. The skin friction

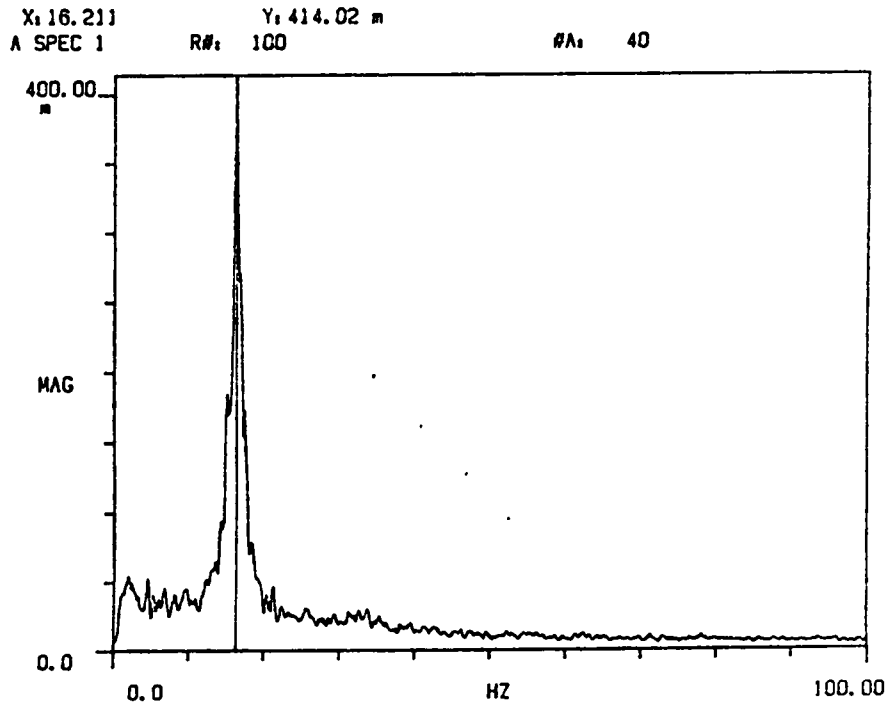

Figure 4.4 Power spectrum showing dominant frequency outside the boundary layer

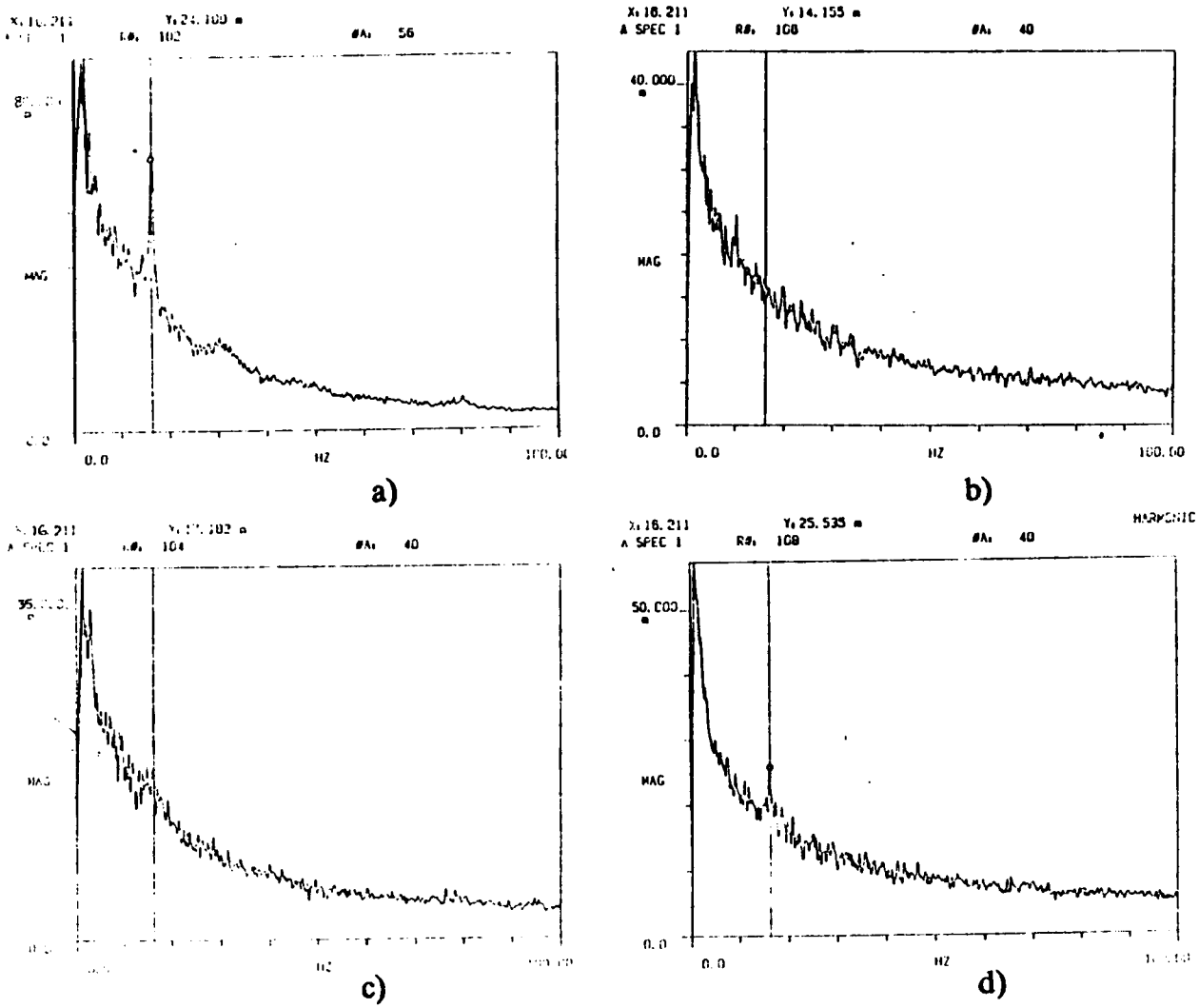

Figure 4.5a Power spectra of skin friction at different locations around the cylinder
a) 90 b) 100 c) 110 and d) 120 degrees

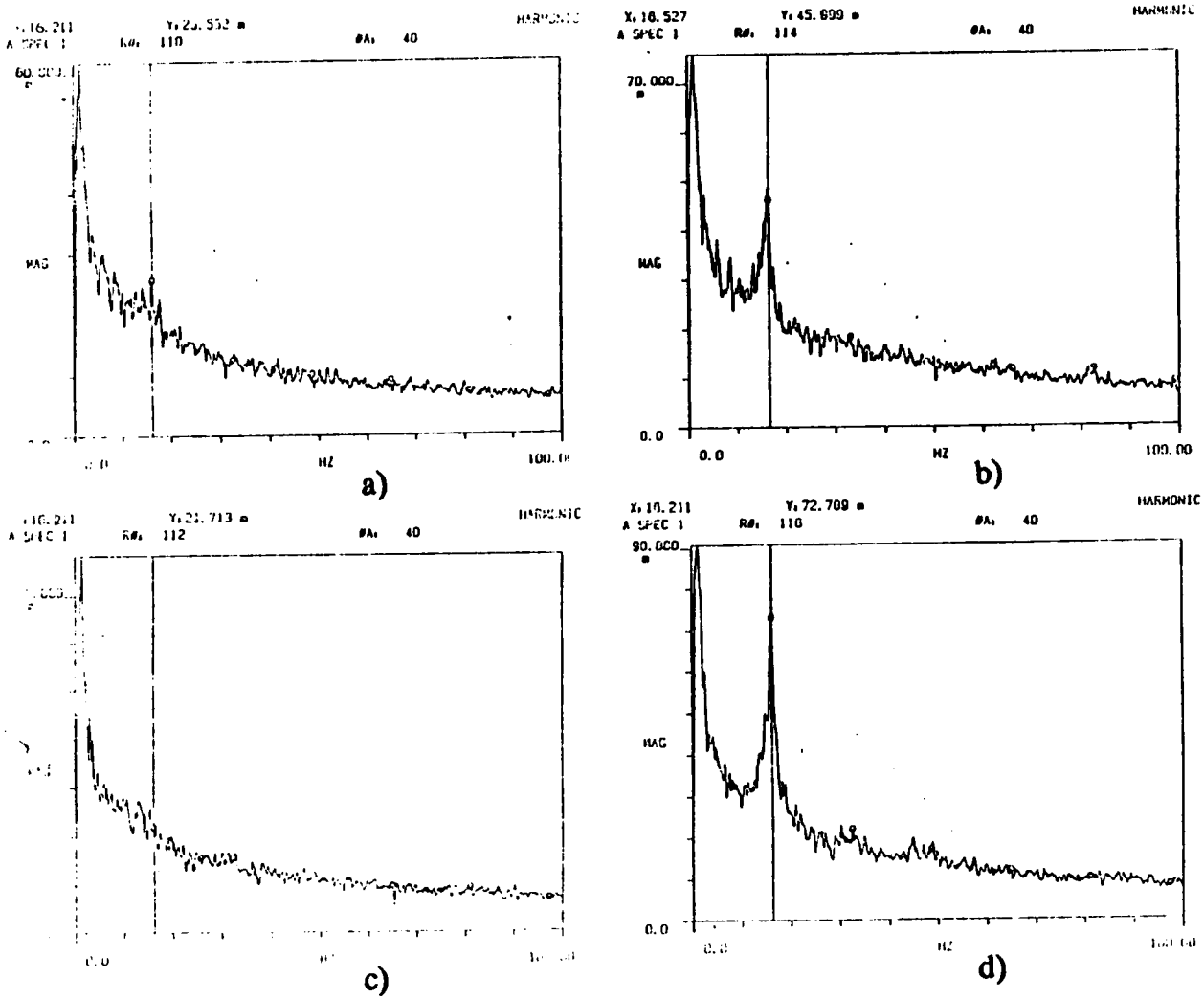

Figure 4.5b Power spectra of skin friction at different locations around the cylinder
a) 130 b) 140 c) 150 and d) 160 degrees

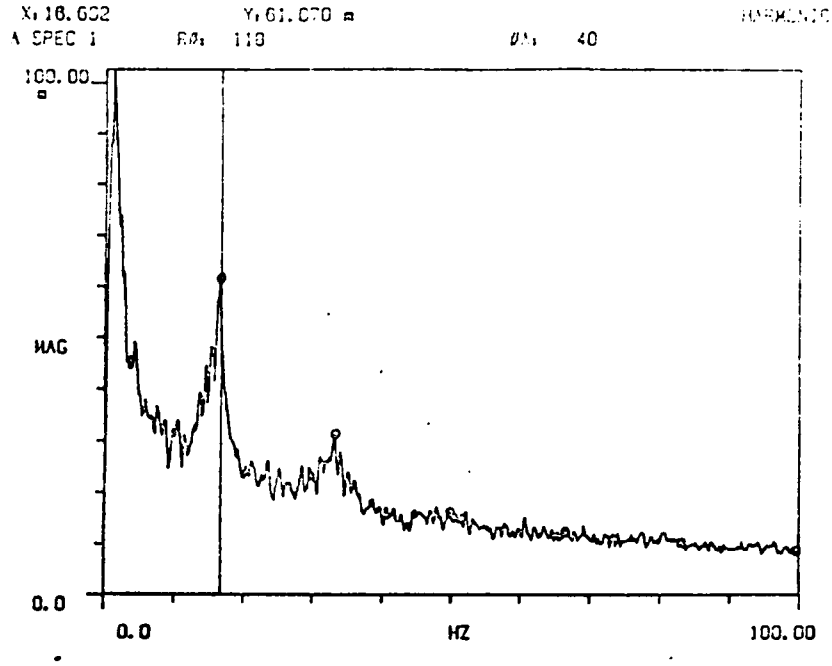

a)

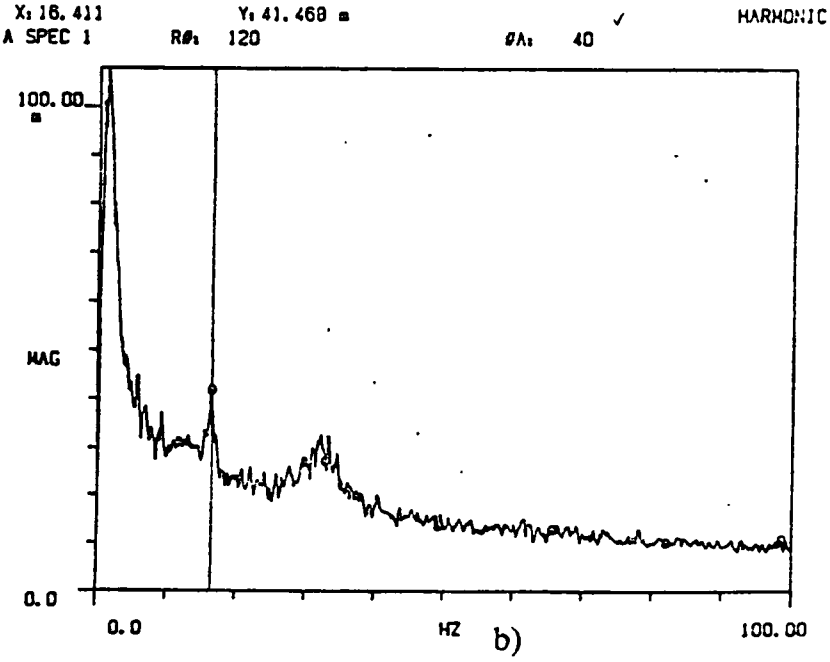

b)

Figure 4.5c Power spectra of skin friction at different locations around the cylinder
a) 170 b) 180 degrees

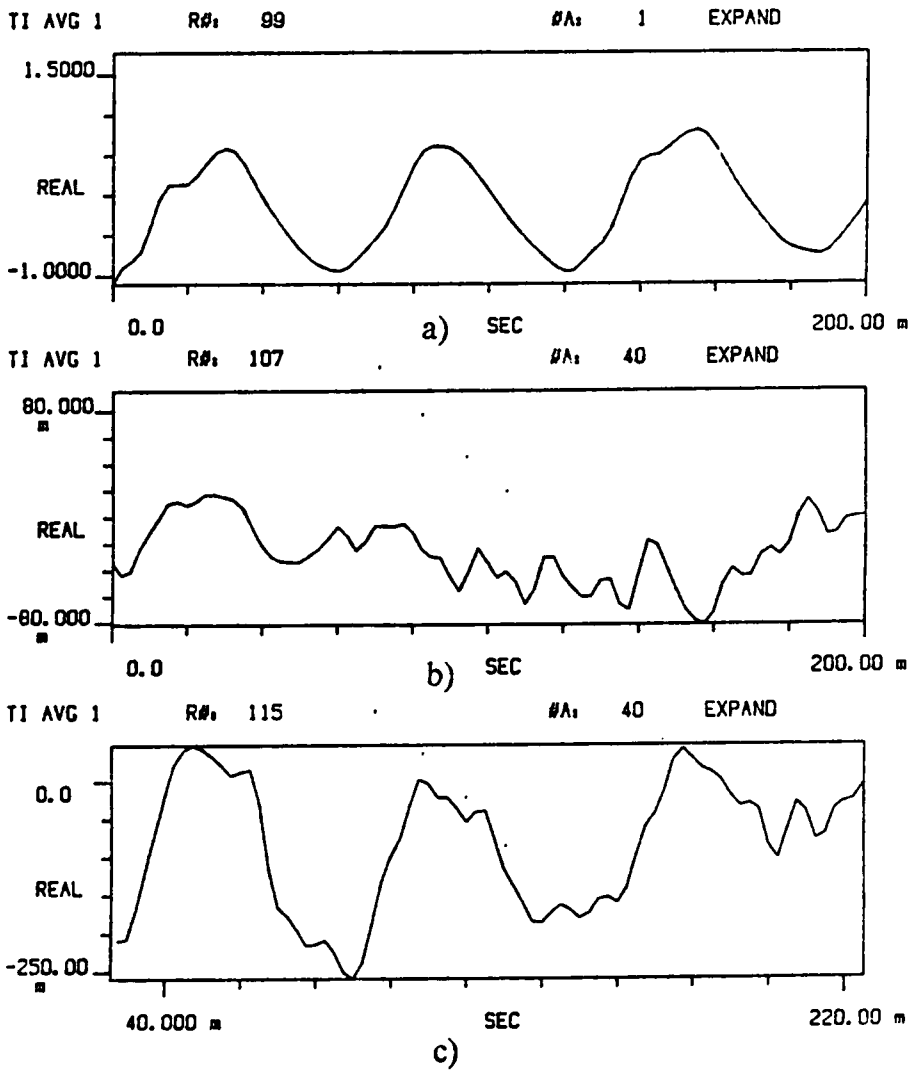

Figure 4.6 Skin friction with and without organization
a) Time record of freestream
b) Time record of skin friction at 120 degrees (without organization)
c) Time record of skin friction at 160 degrees (with organization)

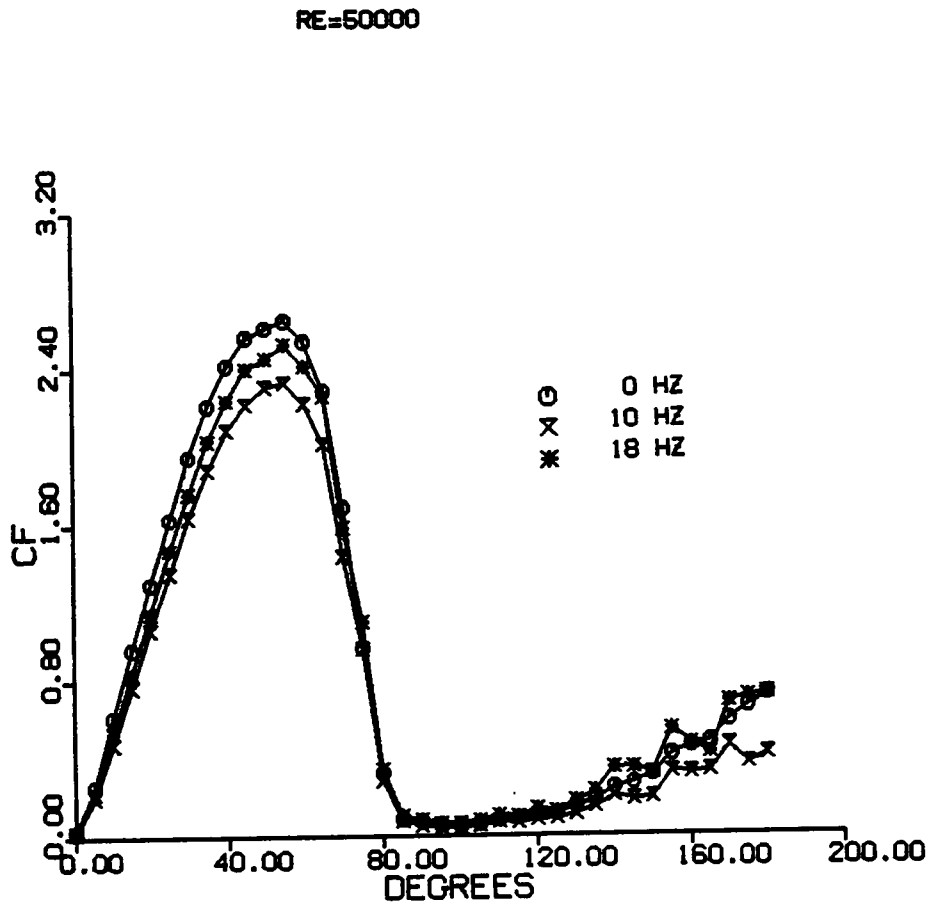

Figure 4.7a Distribution of skin friction at different driving frequencies

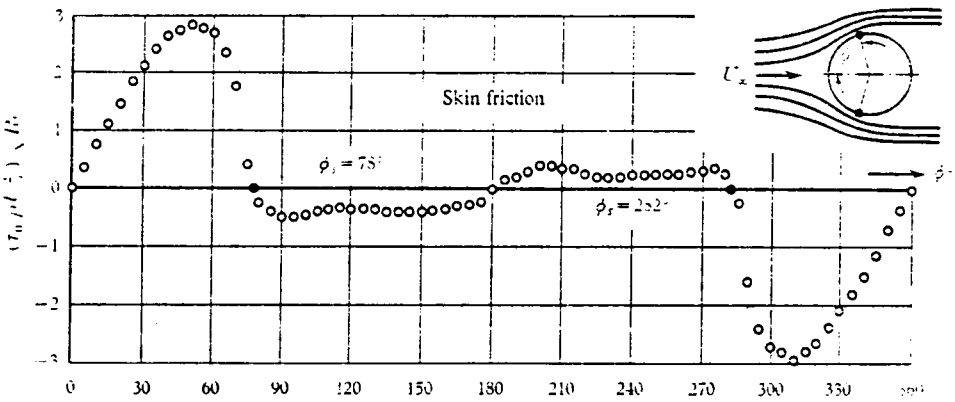

Figure 4.7b Distribution of skin friction for steady flow Re = 100,000 (Achenbach, 1969)

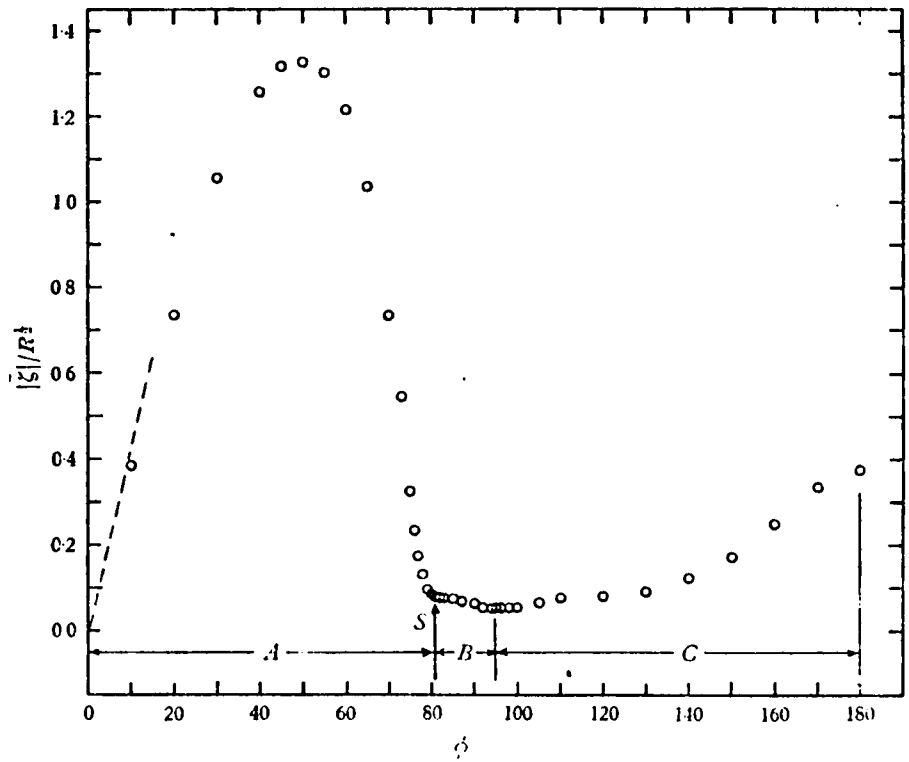

Figure 4.7c Distribution of wall velocity gradient
Re = 50,000 (Son and Hanratty, 1969)

coefficient is defined as shear stress on the wall multiplied by the square root of the Reynolds number and normalized with ρU_∞^2 . The steady values are comparable to the results of Son and Hanratty [1969] and Achenbach [1969] (see figures 4.7b and 4.7c). The ordinate in Son and Hanratty's curve is obtained by normalizing the gradient with half the diameter of the cylinder and hence is half as small as the ordinates in figures 4.7a and 4.7c. The blockage ratio in the present case is 1.58 percent. The point of separation is at around 84 degrees for all three cases considered. The absolute value at a point is frequency dependent and does not show any definite trend with the increase of driving frequency. Figure 4.8 shows the root mean square (rms) of skin-friction coefficient fluctuations around the cylinder at different driving frequencies. Although the rms of skin friction appears to be mostly higher for the case of driving frequency of 18 Hz, there is again no set pattern observed.

The time-averaged pressure distribution is shown in figure 4.9 for steady flow and for flows with driving frequencies of 10 and 18 Hz and a Reynolds number of 50,000. The steady flow curve compares well with the results of West and Apelt [1982] for Re = 30,000 and a blockage of 15.2 percent and Borell et al. [1984] for Re = 36,000. Unlike the results obtained by Borell et al. for Re = 36,000 the pressure distributions for pulsed flows at Re = 50,000 indicates higher than steady flow values on the back of the cylinder. This may be because of different Reynolds numbers and possibly also different amplitudes involved. The amplitude used for the present case is 10.5 percent zero to peak. The amplitude data for the results of Borell et al. is not available. The fluctuating

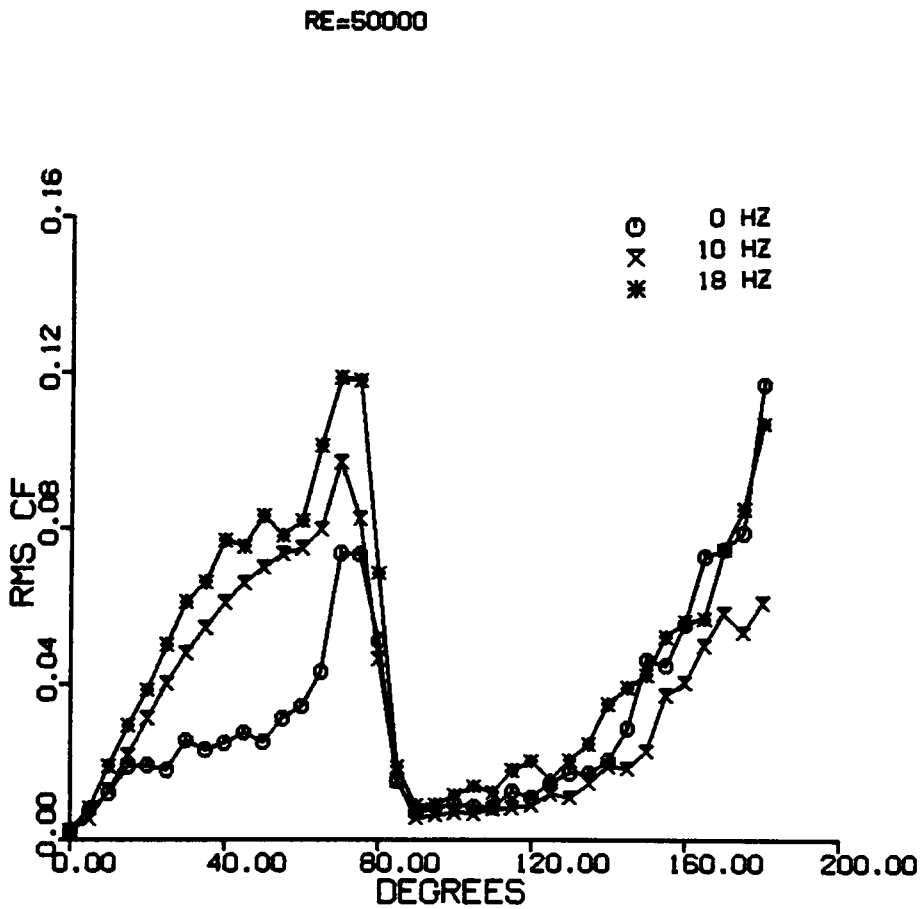

Figure 4.8 Distribution of rms of skin friction at different driving frequencies

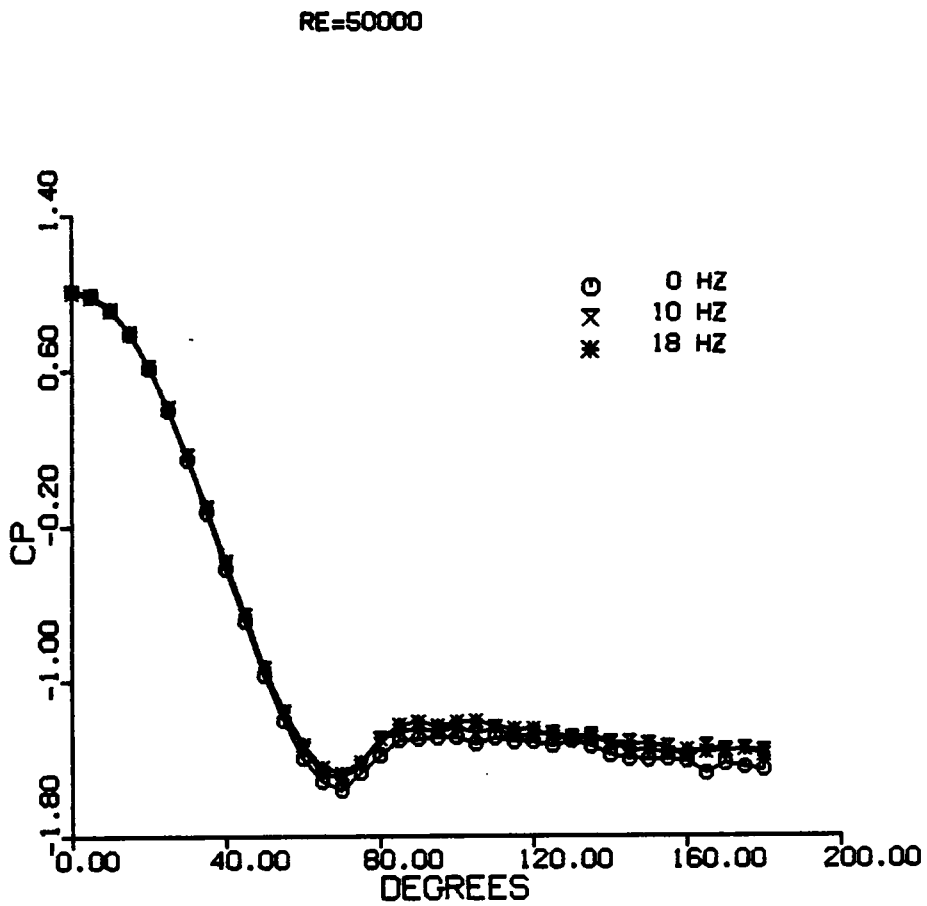

Figure 4.9 Distribution of pressure at different driving frequencies

component of the static pressure on the cylinder is shown in figure 4.10 for different conditions of freestream pulsation. The ordinate represents the nondimensionalized rms of pressure fluctuation and the abscissa represents the angular position on the cylinder. The fluctuating pressure in steady flow has a maximum value near the point of separation. This is in agreement with the results of Arie et al. [1983], Meier et al. [1981] and Borell et al. [1984]. Pressure fluctuations are found to increase considerably when the freestream is pulsed. The amplitude of pressure fluctuation is increased with increased driving frequency. The absolute values of rms of pressure fluctuations again do not agree well with those of Borell et al. for the reasons already mentioned.

Figure 4.11 shows the power spectra of skin friction and pressure at 50, 80, 110 and 160 degrees around the cylinder at a driving frequency of 7 Hz and a Reynolds number of 25,000. The shedding frequency of 16 Hz can be seen in all the spectra for skin friction except in the one for 110 degree position. Figure 4.12 shows power spectra of skin friction and pressure at driving frequency of 18.5 Hz and Reynolds number of 50,000. Here again it is observed that the shedding frequency of 23 Hz is suppressed in the spectrum for skin friction at 110 degrees from the stagnation point. This disappearance of the dominant frequency in the spectrum for skin friction at 110 degree location is also seen in figure 4.13, when the flow is driven at the natural shedding frequency of 23 Hz. It was observed that the skin friction variations are well organized all round the cylinder except from the point of separation to around 130 degrees from the stagnation point

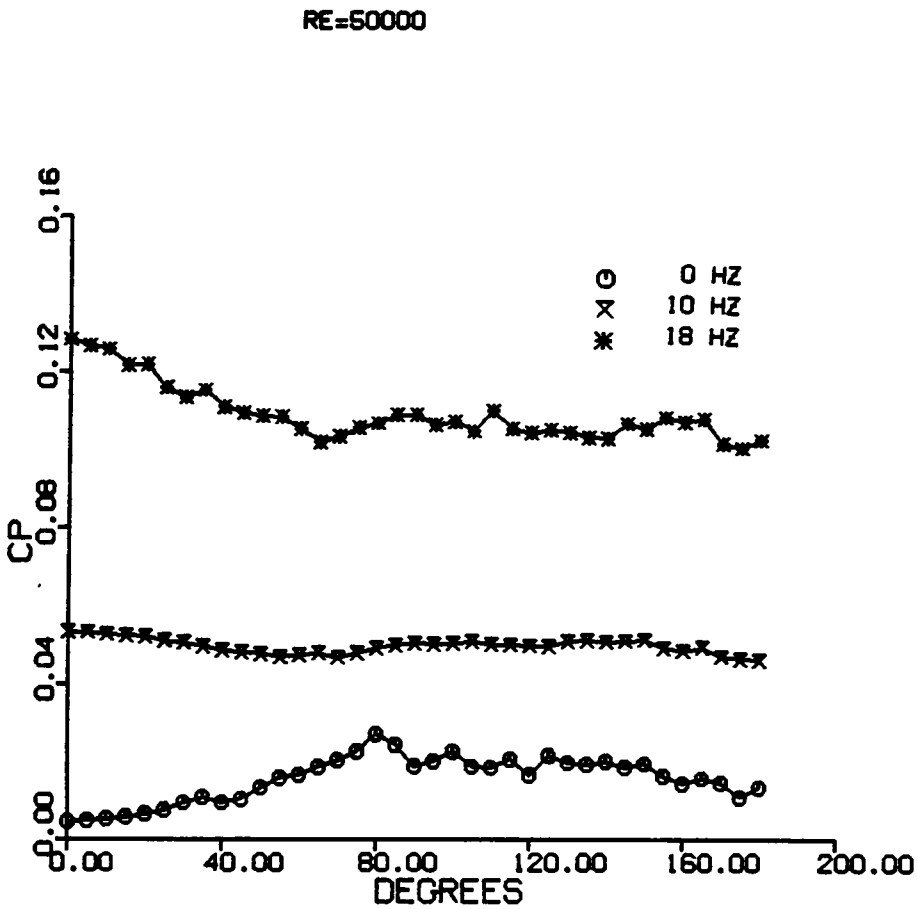

Figure 4.10 Distribution of rms of pressure at different driving frequencies

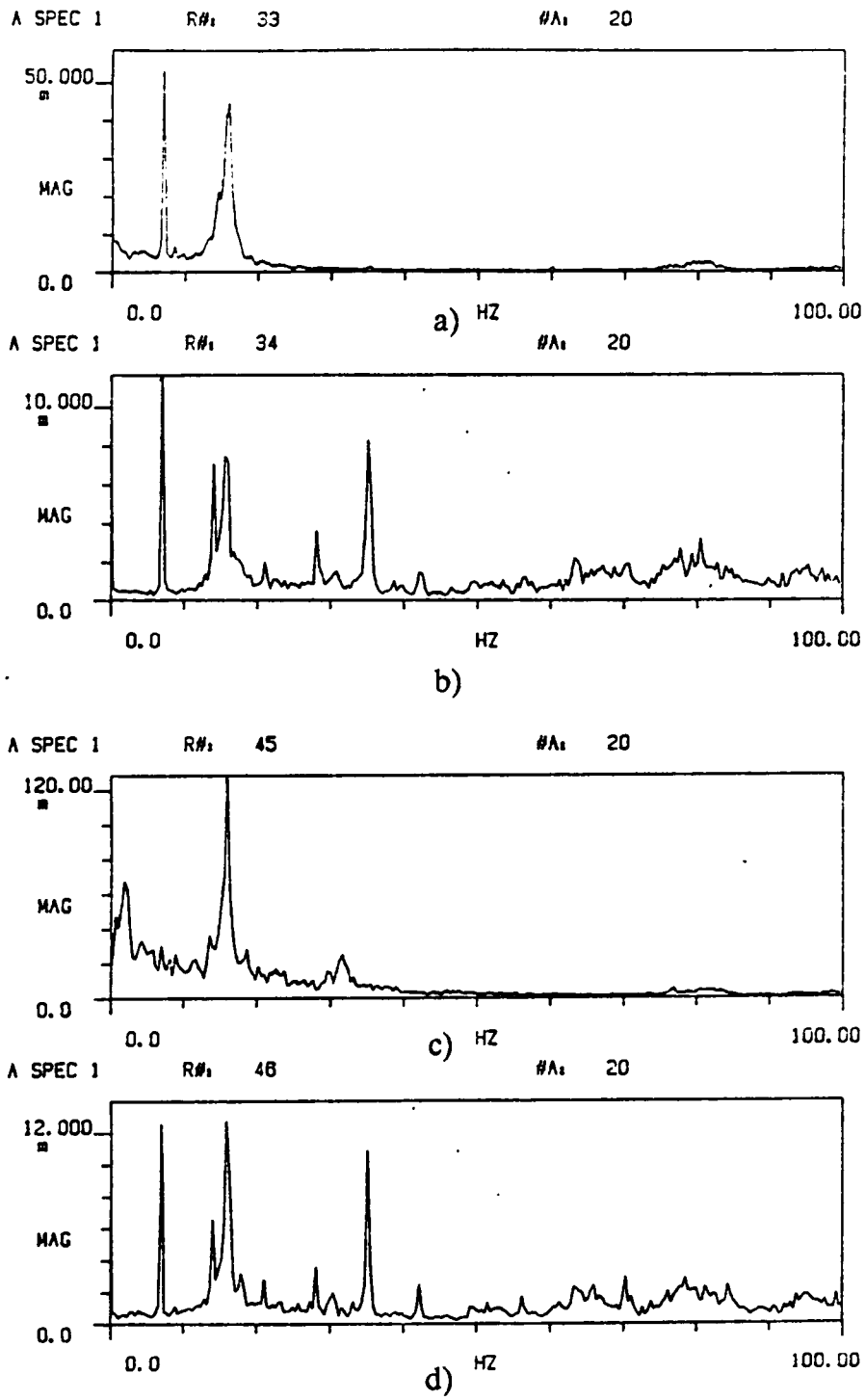

Figure 4.11a Spectra of skin friction and pressure at driving frequency of 7 Hz and Re = 50,000 a) τ_{50} b) p_{50} c) τ_{80} d) p_{80}

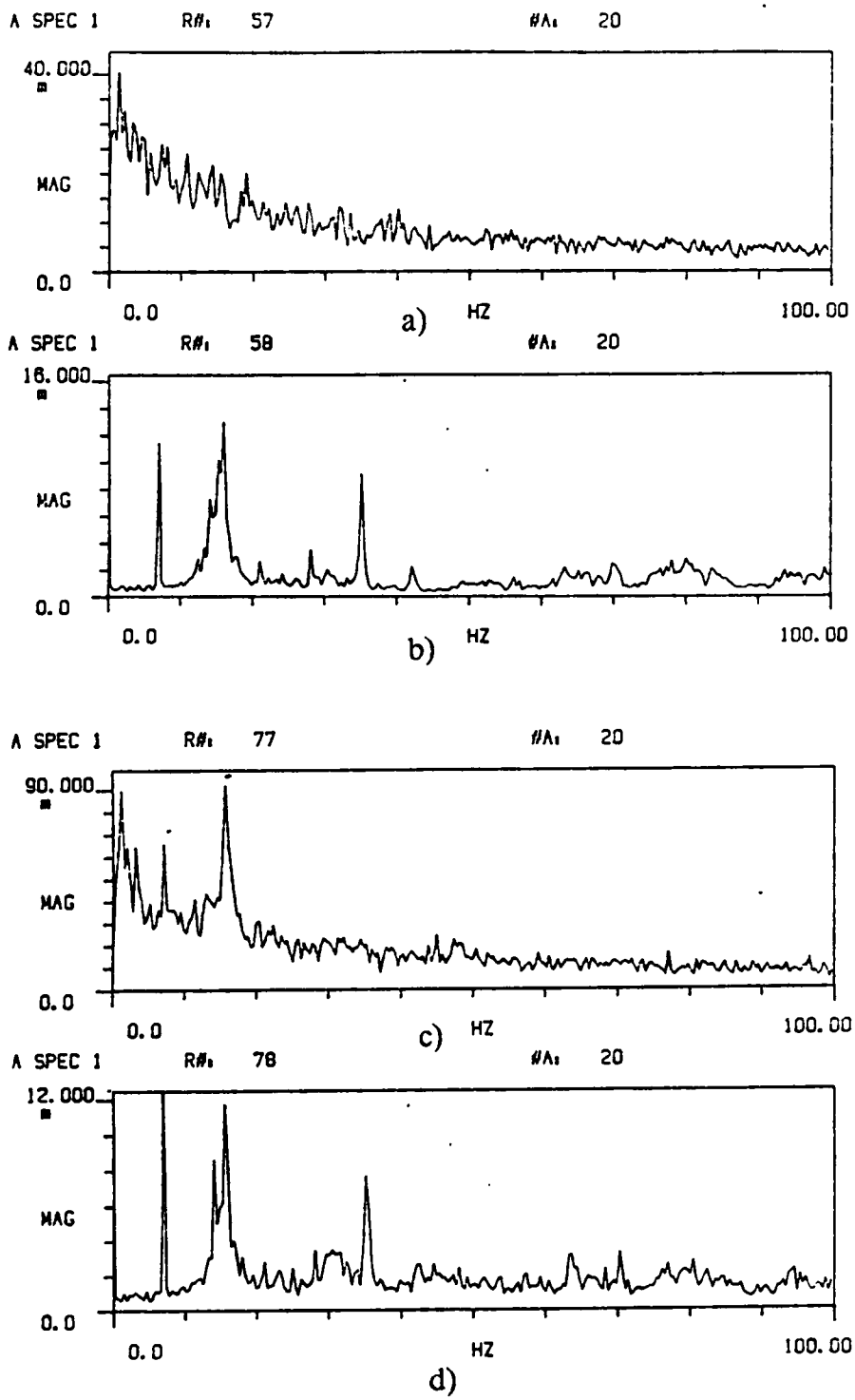

Figure 4.11b Spectra of skin friction and pressure at driving frequency of 7 Hz and Re = 50,000 a) τ_{110} b) p_{110} c) τ_{160} d) p_{160}

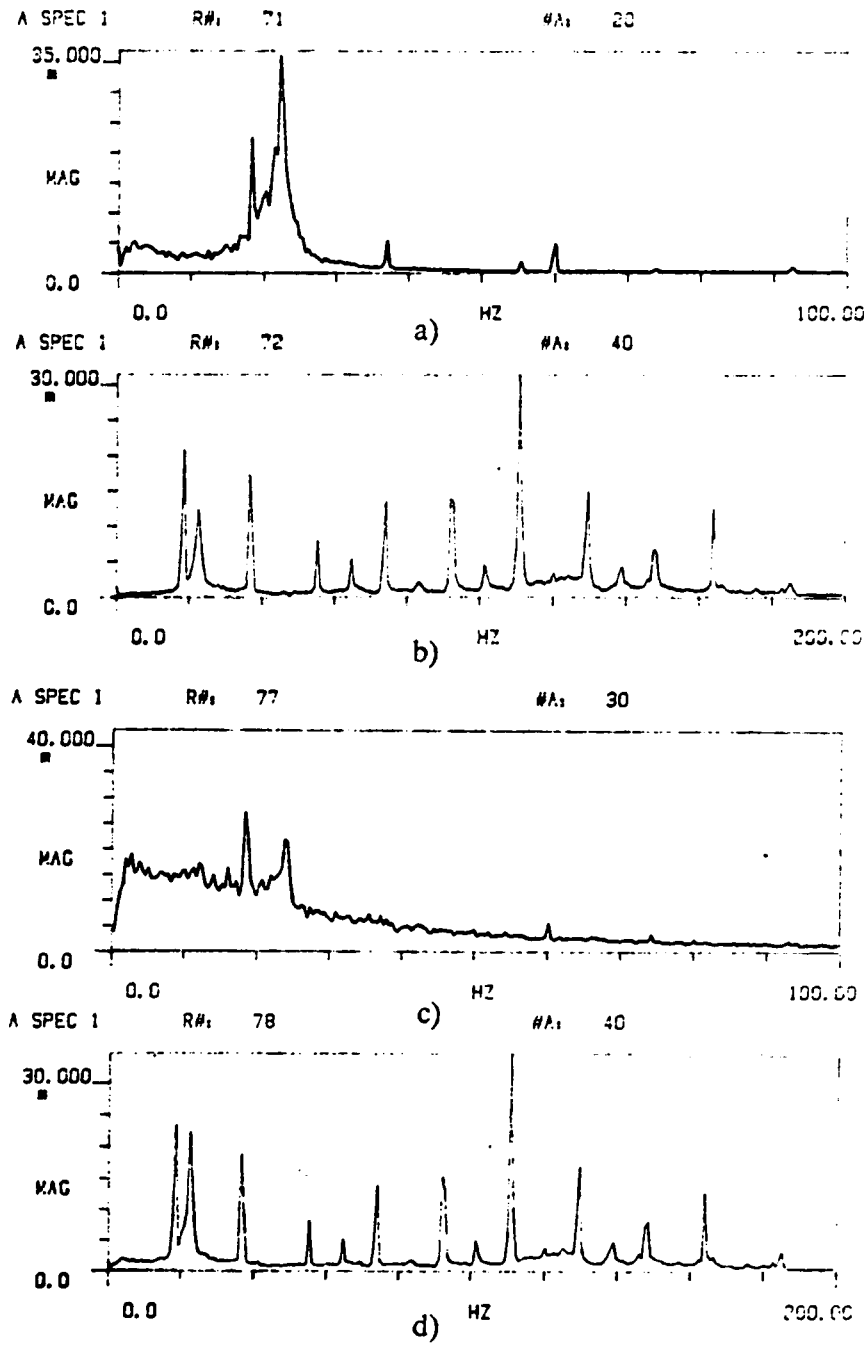

Figure 4.12a Spectra of skin friction and pressure at driving frequency of 18.5 Hz and Re = 50,000 a) τ_{50} b) p_{50} c) τ_{80} d) p_{80}

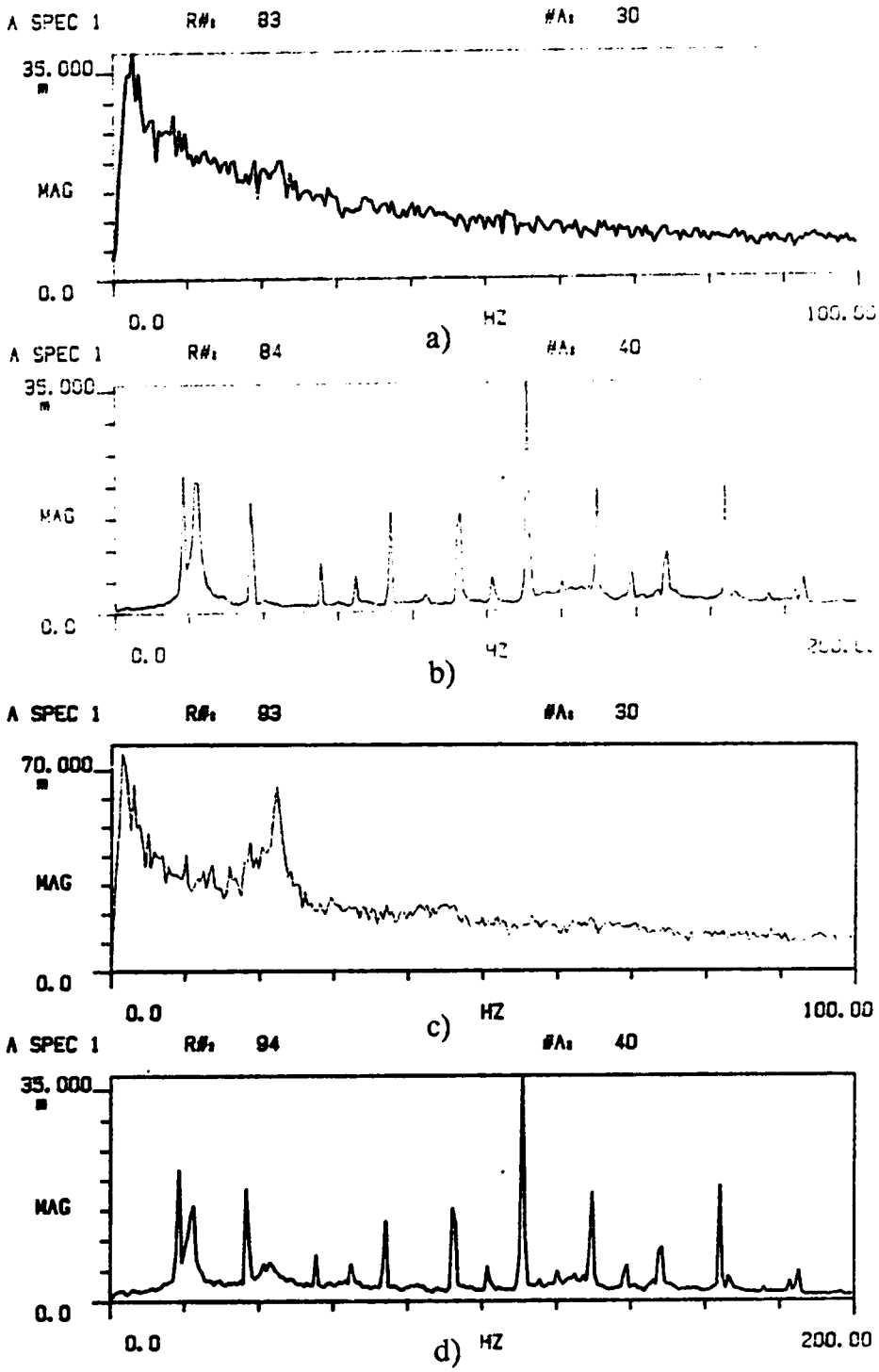

Figure 4.12 b Spectra of skin friction and pressure at driving frequency of 18.5 Hz and Re = 50,000 a) τ_{110} b) p_{110} c) τ_{160} d) p_{160}

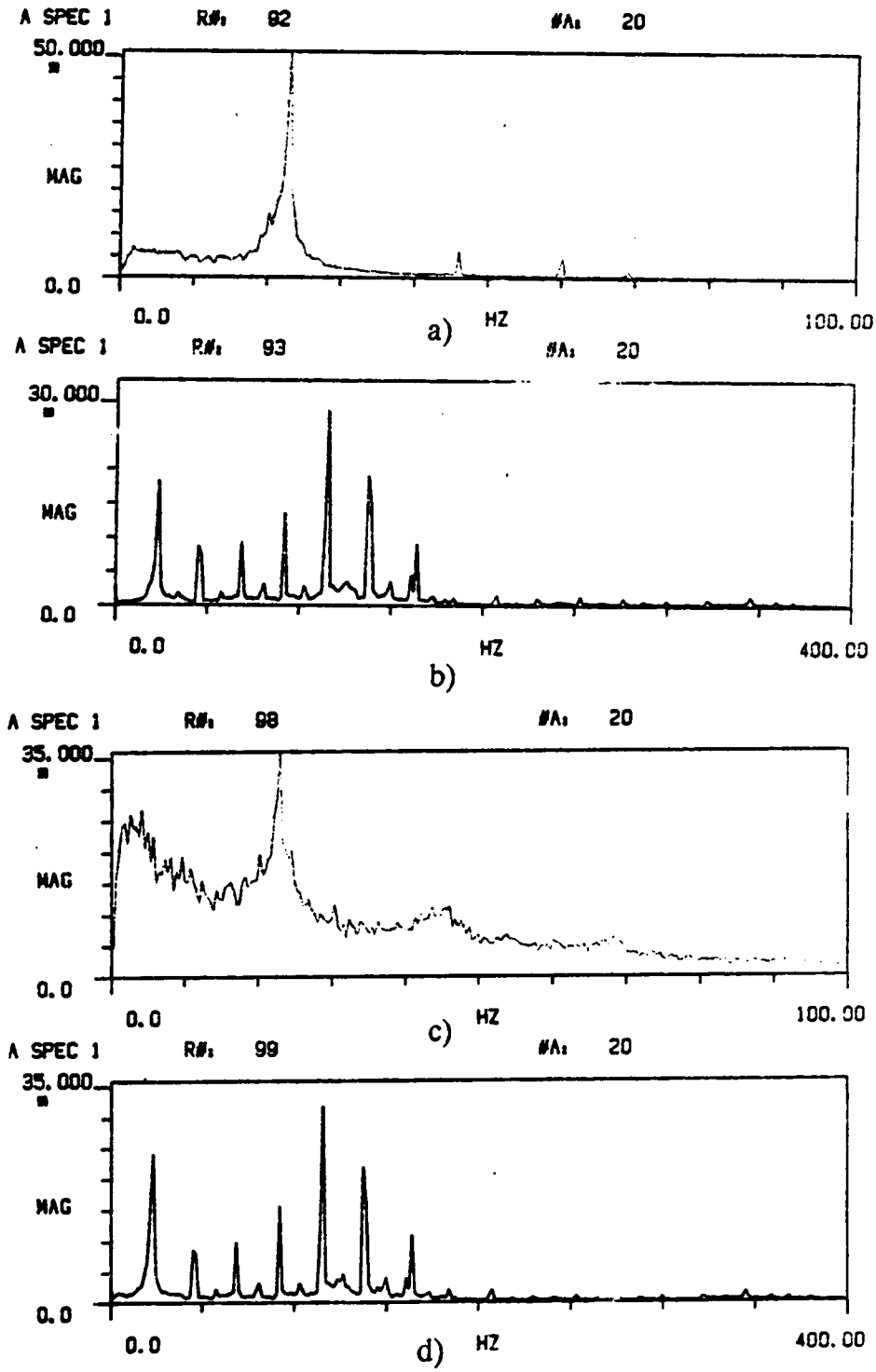

Figure 4.13a Spectra of skin friction and pressure at driving frequency of 23 Hz and Re = 50,000 a) τ_{50} b) p_{50} c) τ_{80} d) p_{80}

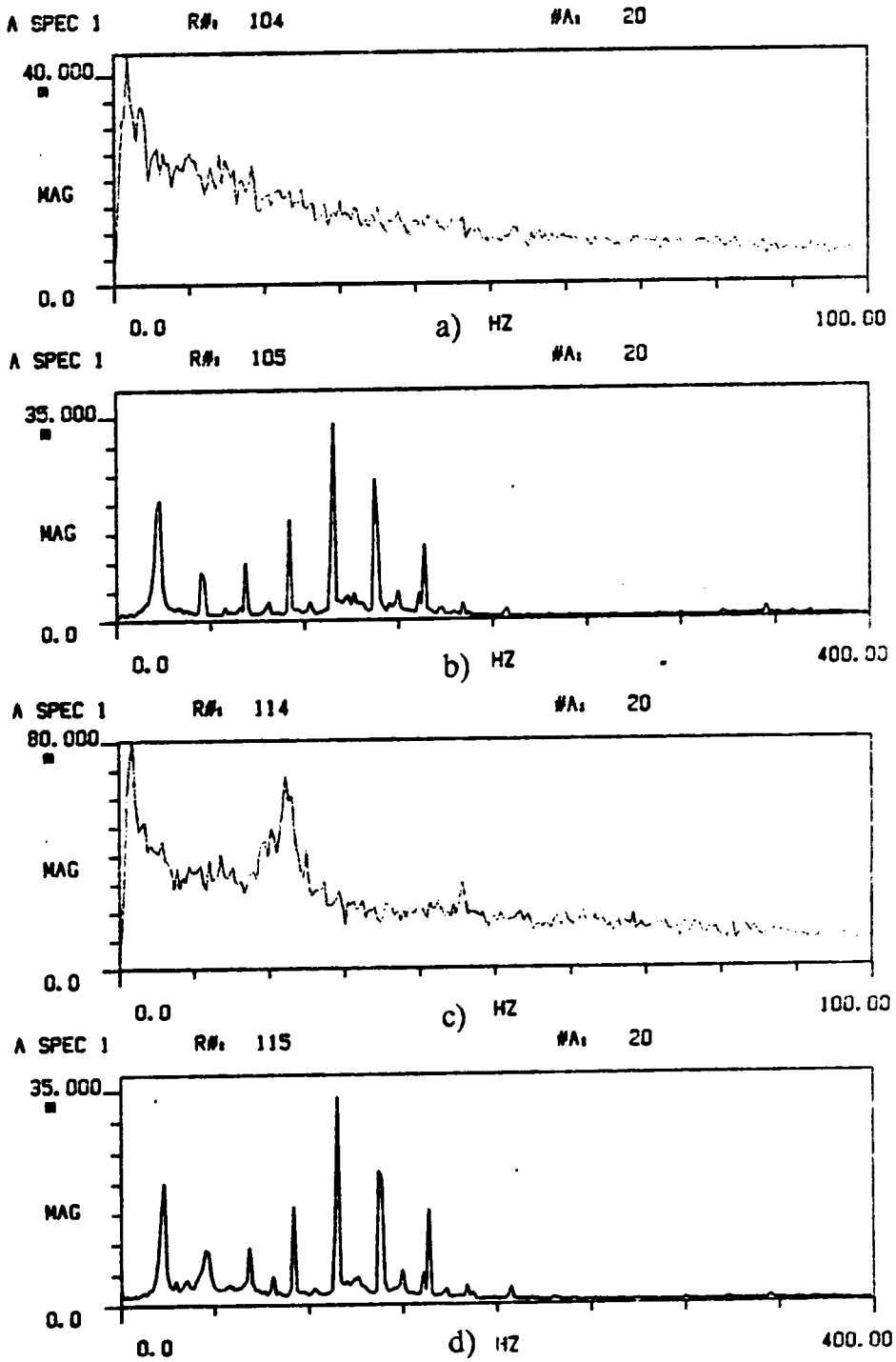

Figure 4.13b Spectra of skin friction and pressure at driving frequency of 23 Hz and Re = 50,000 a) τ_{110} b) p_{110} c) τ_{160} d) p_{160}

both for steady and pulsed flows. This indicates a somewhat inactive region in the separated flow which resembles region 2 in figure 3.1.

Figure 4.14 shows spectra of skin friction and pressure at 0, 45, 84, 140 and 180 degrees around the cylinder for a Reynolds number of 23,000. Steady flow and pulsed flow with driving frequencies equal to and twice the shedding frequency are considered. The shedding frequency is observed to lock on the subharmonic of the driving frequency. Figure 4.15 shows the time record of skin friction and pressure at 0, 45, 140 and 180 degrees from the stagnation point with steady freestream at Reynolds number of 23,000.

Figure 4.16 shows the calibration plots for the strain gauges used in the balance system (figure 2.19) to measure lift and drag. Table 4.1 shows lift, drag, rms of lift fluctuations and rms of drag fluctuations for flow past a cylinder at a Reynolds number of 50,000 and at different driving frequencies. Figure 4.17 shows the time records and the frequency contents of lift and drag for steady flow. The lift has a fundamental frequency of 7.5 Hz at Re = 55,000. and drag has a fundamental frequency of 12.5 Hz at Re = 50,000. For a particular Reynolds number, the fundamental frequency of drag would equal twice the fundamental frequency of lift. Figure 4.18 shows time records and power spectra for lift and drag for the same Reynolds number but now driven at 21 Hz. The shedding is attracted towards the driving frequency in both cases. Figure 4.19 shows the time and frequency domain data on lift and drag when locked on at the driving frequency of 22.65 Hz.

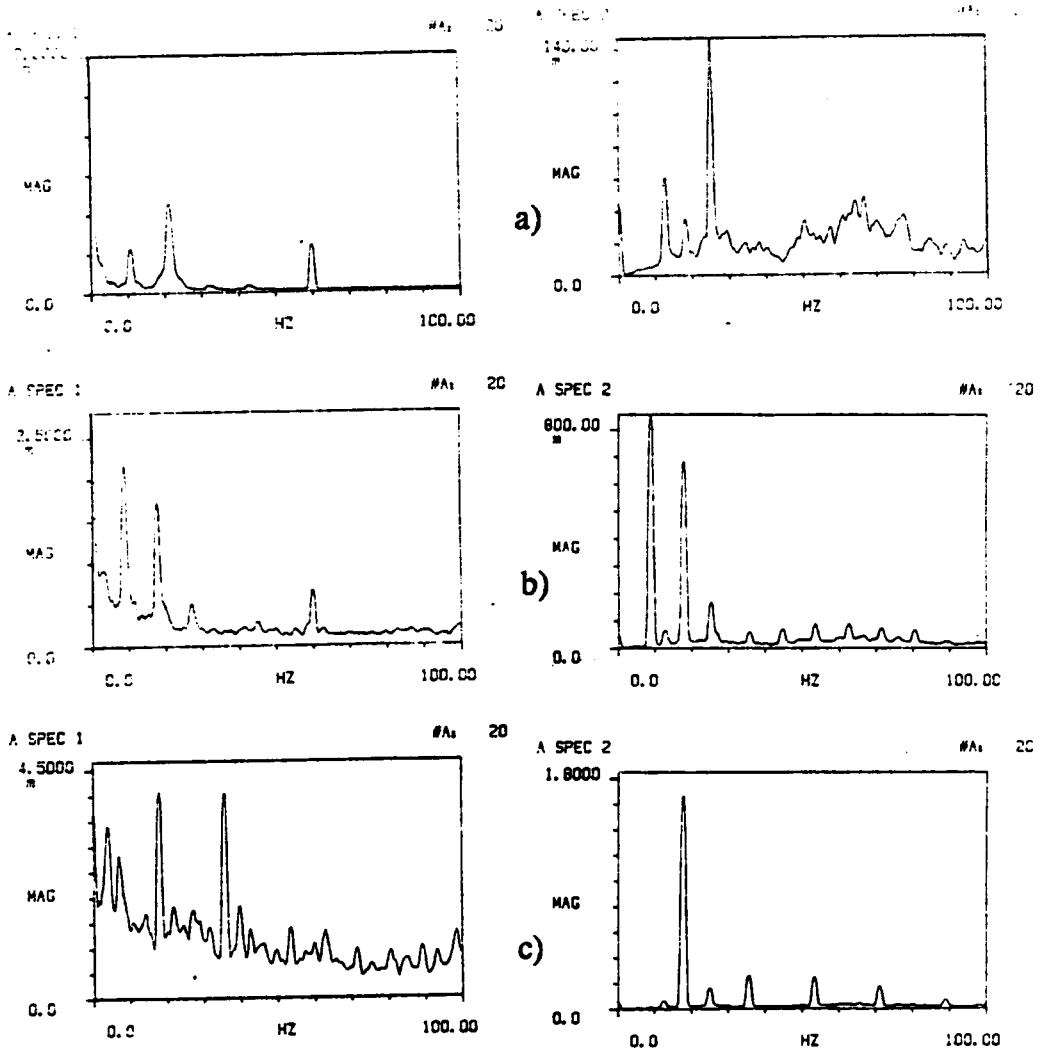

Figure 4.14a Spectra of skin friction and pressure at 0°
for Re = 23,000
and different driving frequencies
a) 0 Hz b) 9 Hz c) 18 Hz

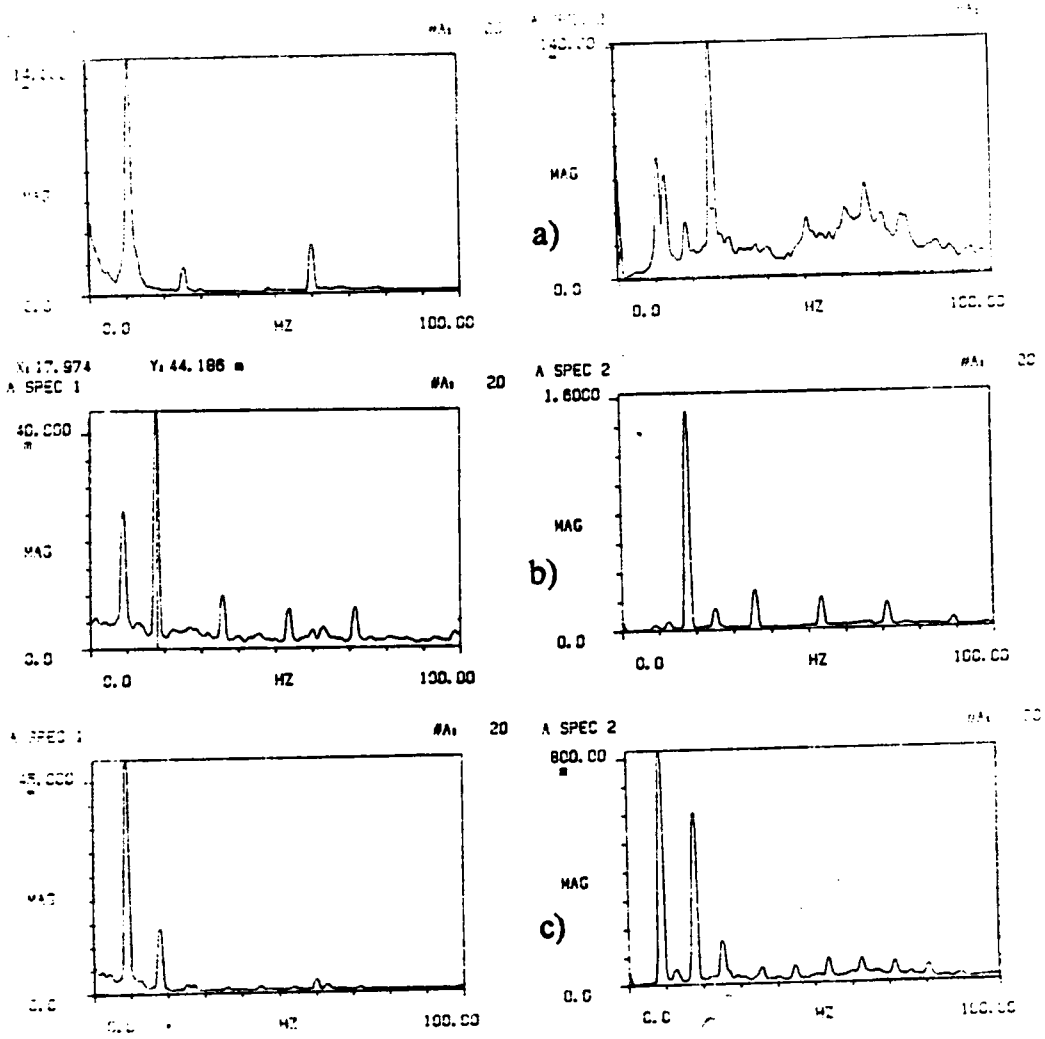

Figure 4.14b Spectra of skin friction and pressure at 45°
for Re = 23,000
and different driving frequencies
a) 0 Hz b) 9 Hz c) 18 Hz

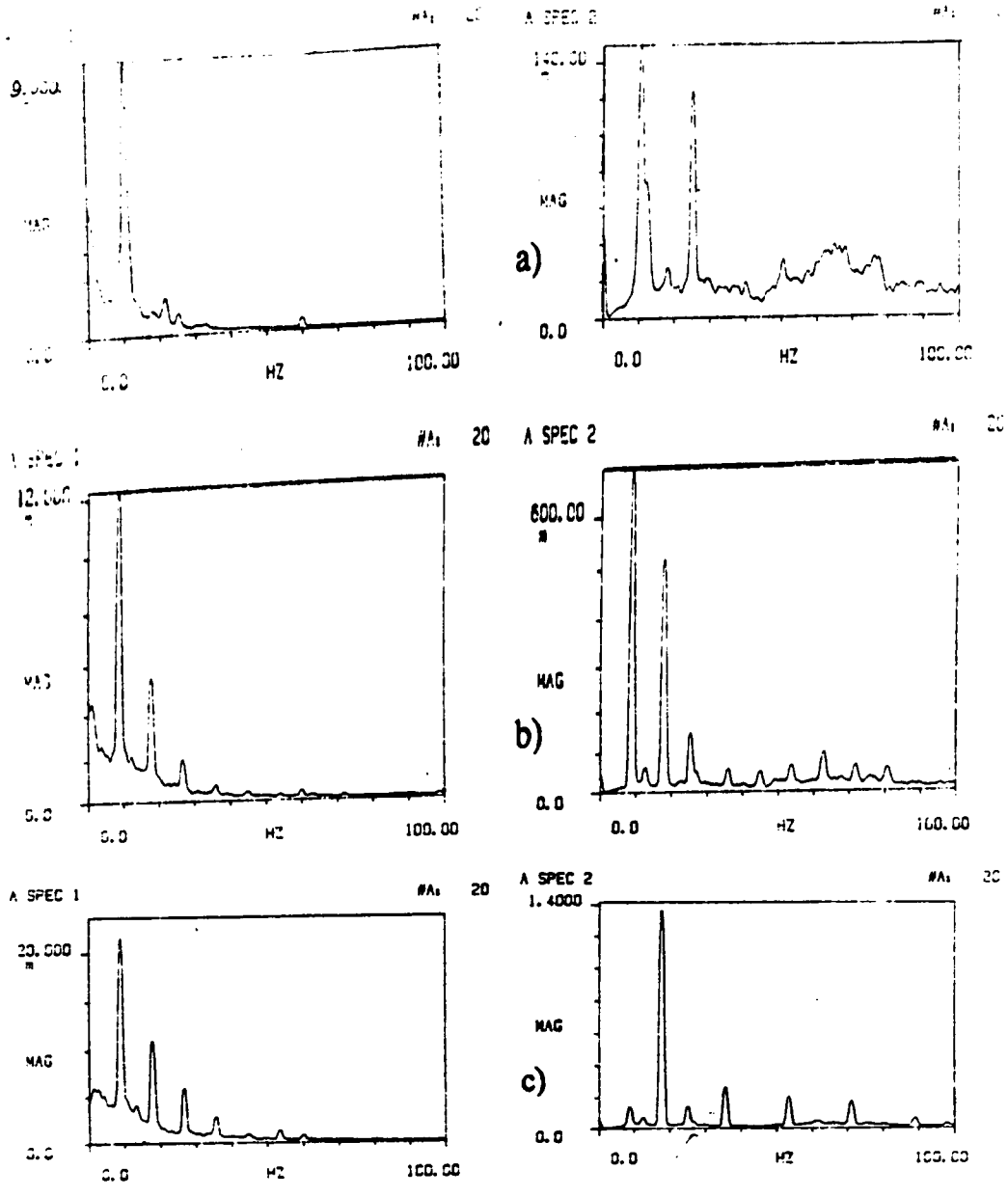

Figure 4.14c Spectra of skin friction and pressure at 84°
for Re = 23,000
and different driving frequencies
a) 0 Hz b) 9 Hz c) 18 Hz

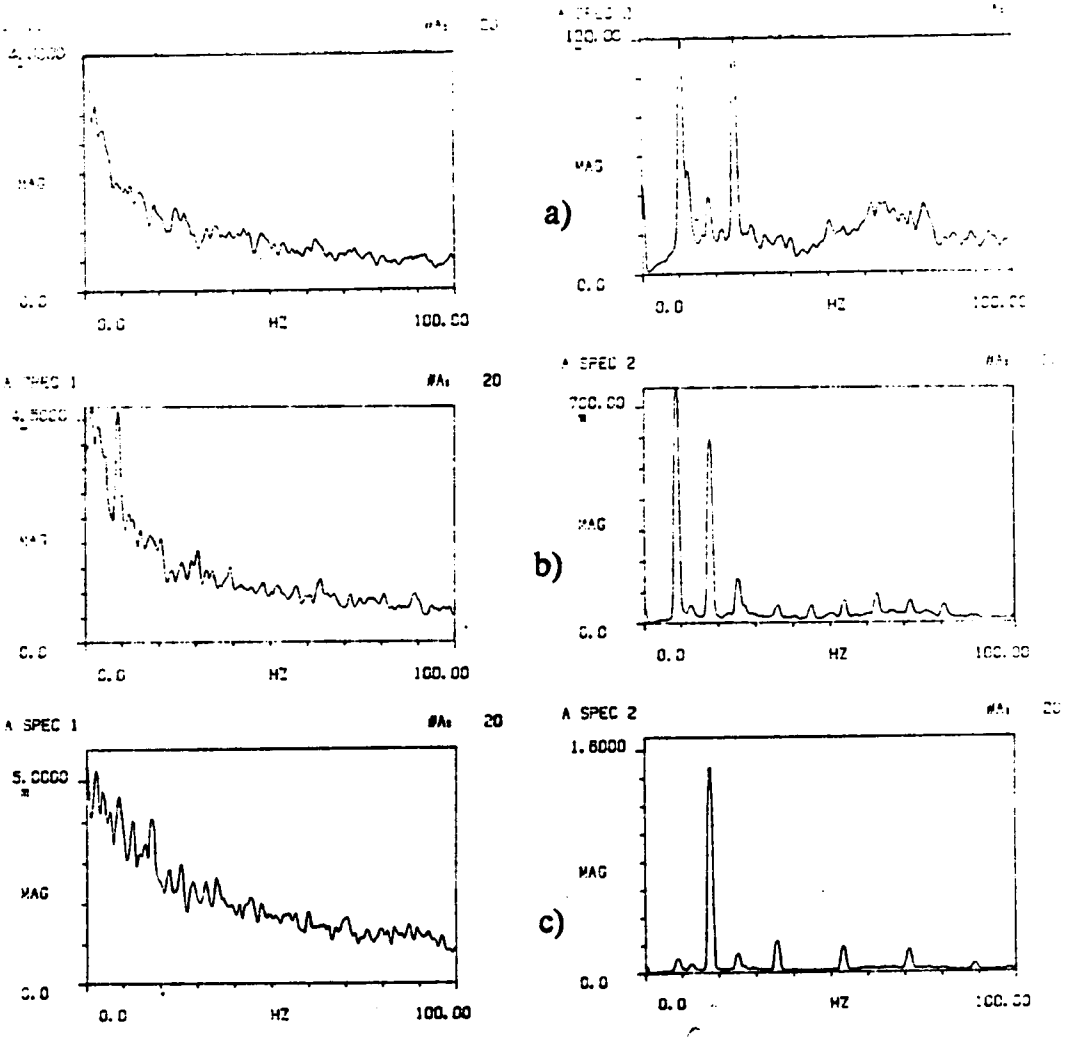

Figure 4.14d Spectra of skin friction and pressure at 140° for Re = 23,000 and different driving frequencies a) 0 Hz b) 9 Hz c) 18 Hz

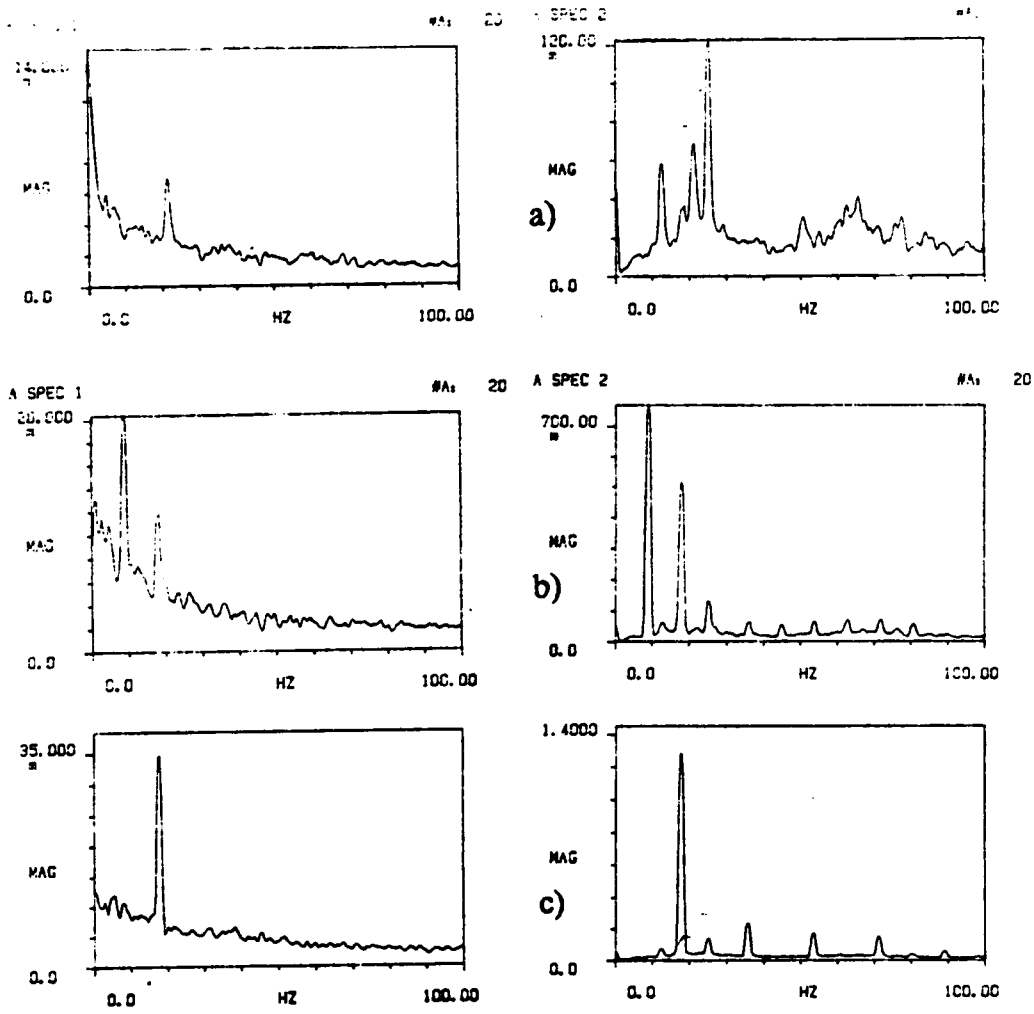

Figure 4.14e Spectra of skin friction and pressure at 180°
for Re = 23,000
and different driving frequencies
a) 0 Hz b) 9 Hz c) 18 Hz

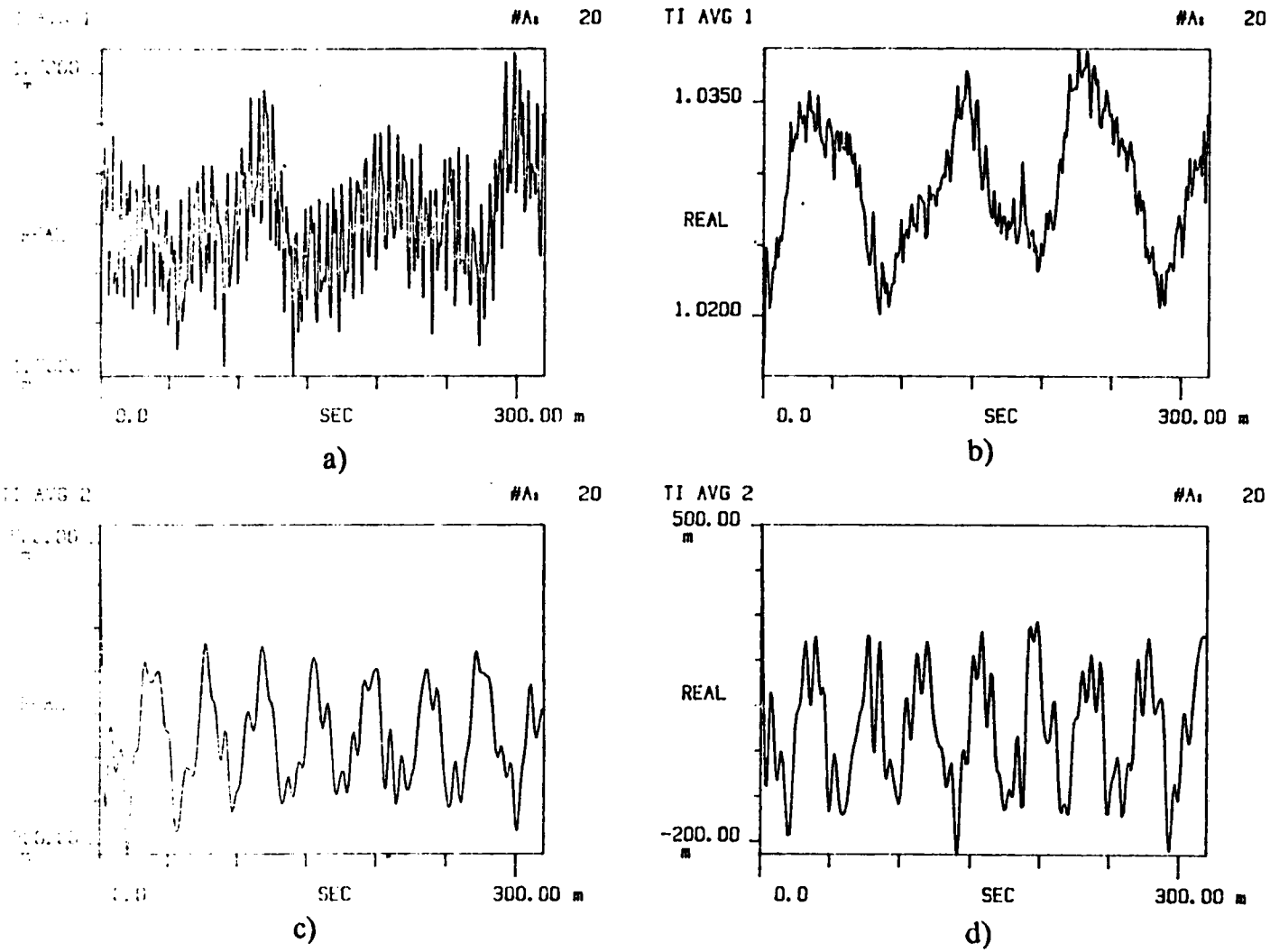

Figure 4.15a Time record of skin friction and pressure for Re = 23,000
a) τ_0 b) τ_{45} c) p_0 d) p_{45}

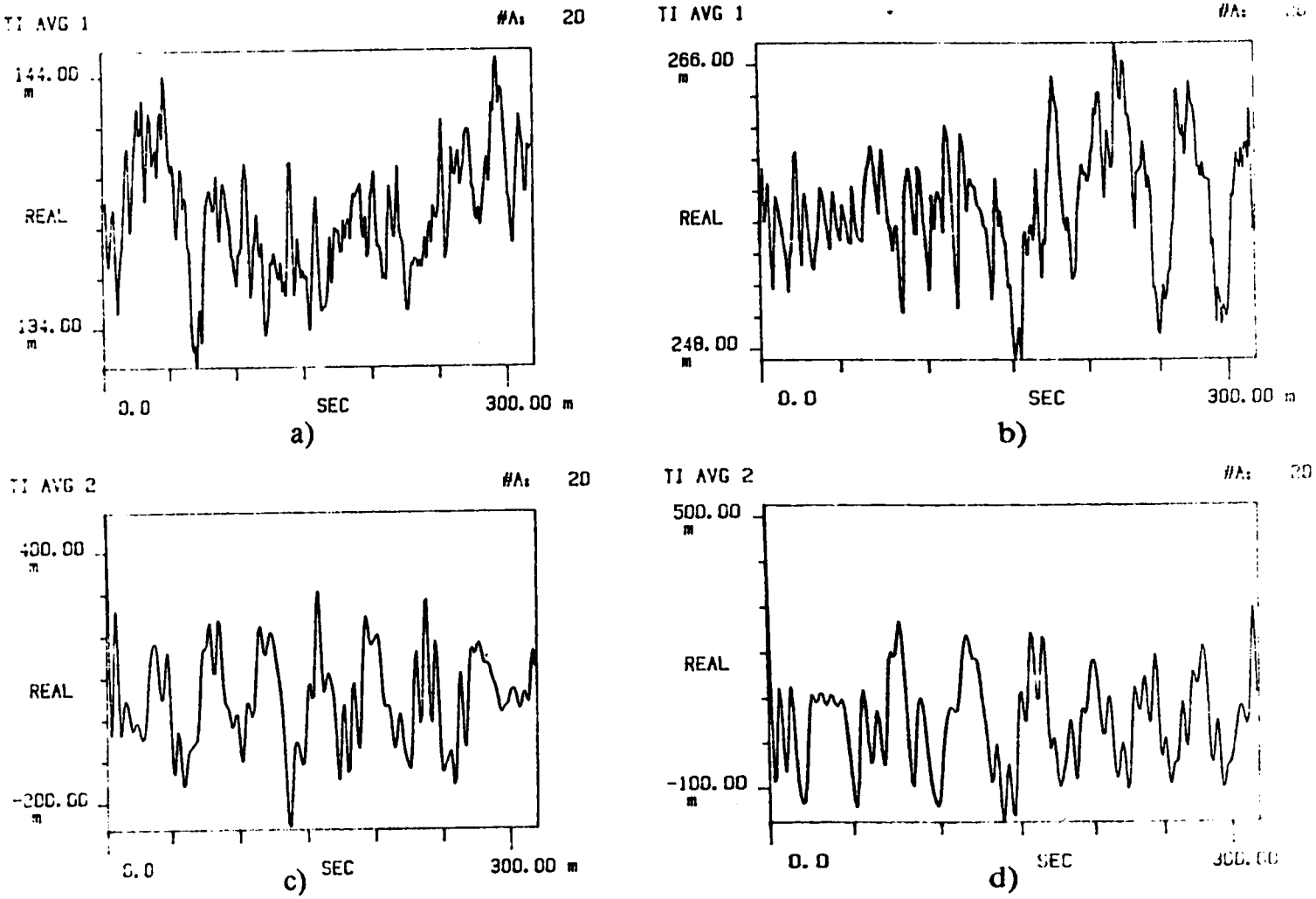

Figure 4.15b Time record of skin friction and pressure for Re = 23,000
a) τ_{140} b) τ_{180} c) p_{140} d) p_{180}

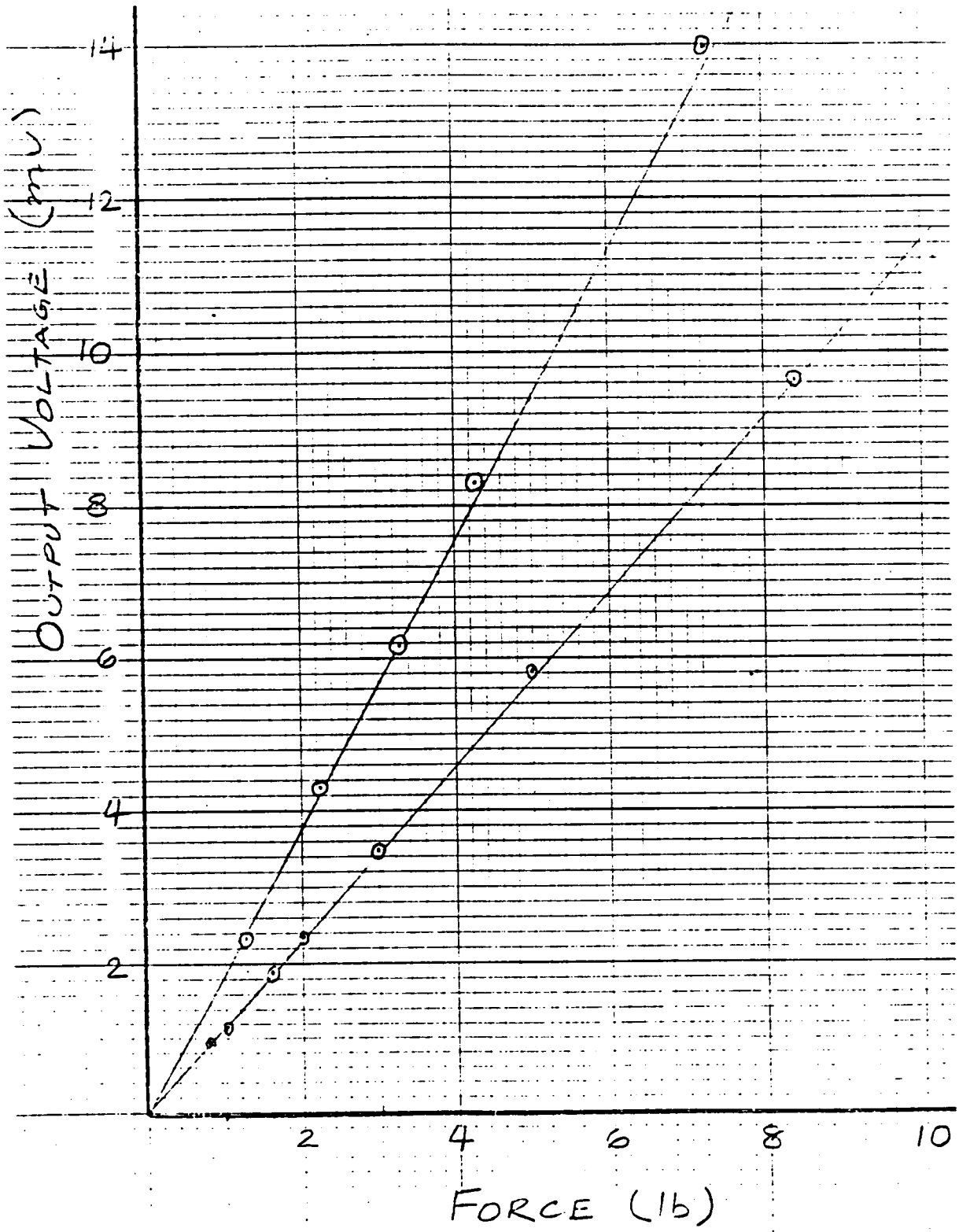

Figure 4.16 Calibration curves for lift and drag

Table 4.1 Lift and drag on a single cylinder, Re=50,000

Driving Frequency (Hz)	Shedding Frequency (Hz)	Amplitude (percent)	Lift (mV)	RMS Lift (mV)	Drag (mV)	RMS Drag (mV)
0.0	22.5	0.0	-0.36	0.33	1.12	0.16
18.2	21.1	11.0	0.54	0.54	1.20	0.72
22.6	22.6	5.2	0.53	0.55	1.25	0.65

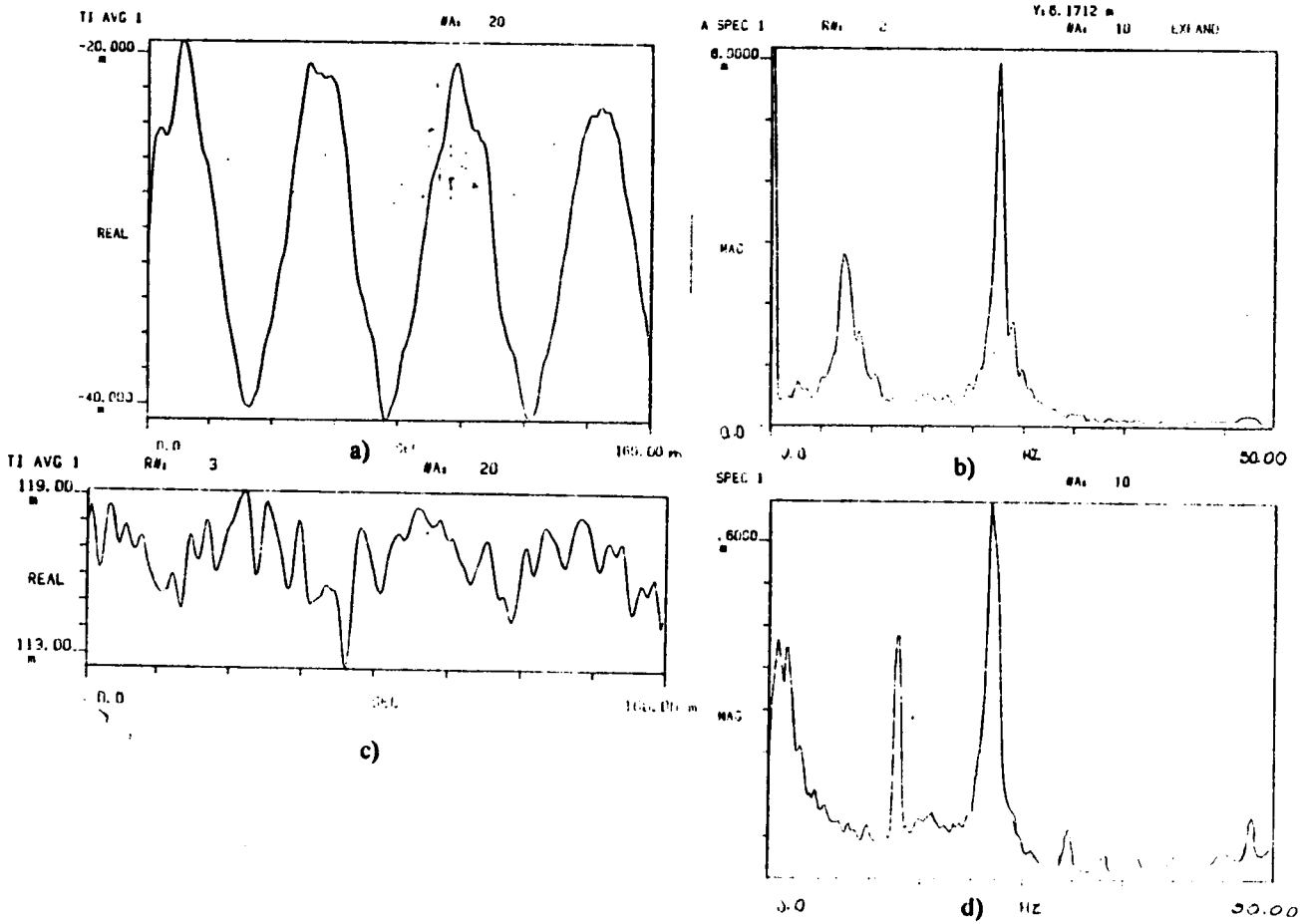

Figure 4.17 Time records and power spectra of lift (Re = 55,000) and drag (Re = 50,000) for steady flow
a) Time record of lift b) Power spectrum of lift
c) Time record of drag b) Power spectrum of drag

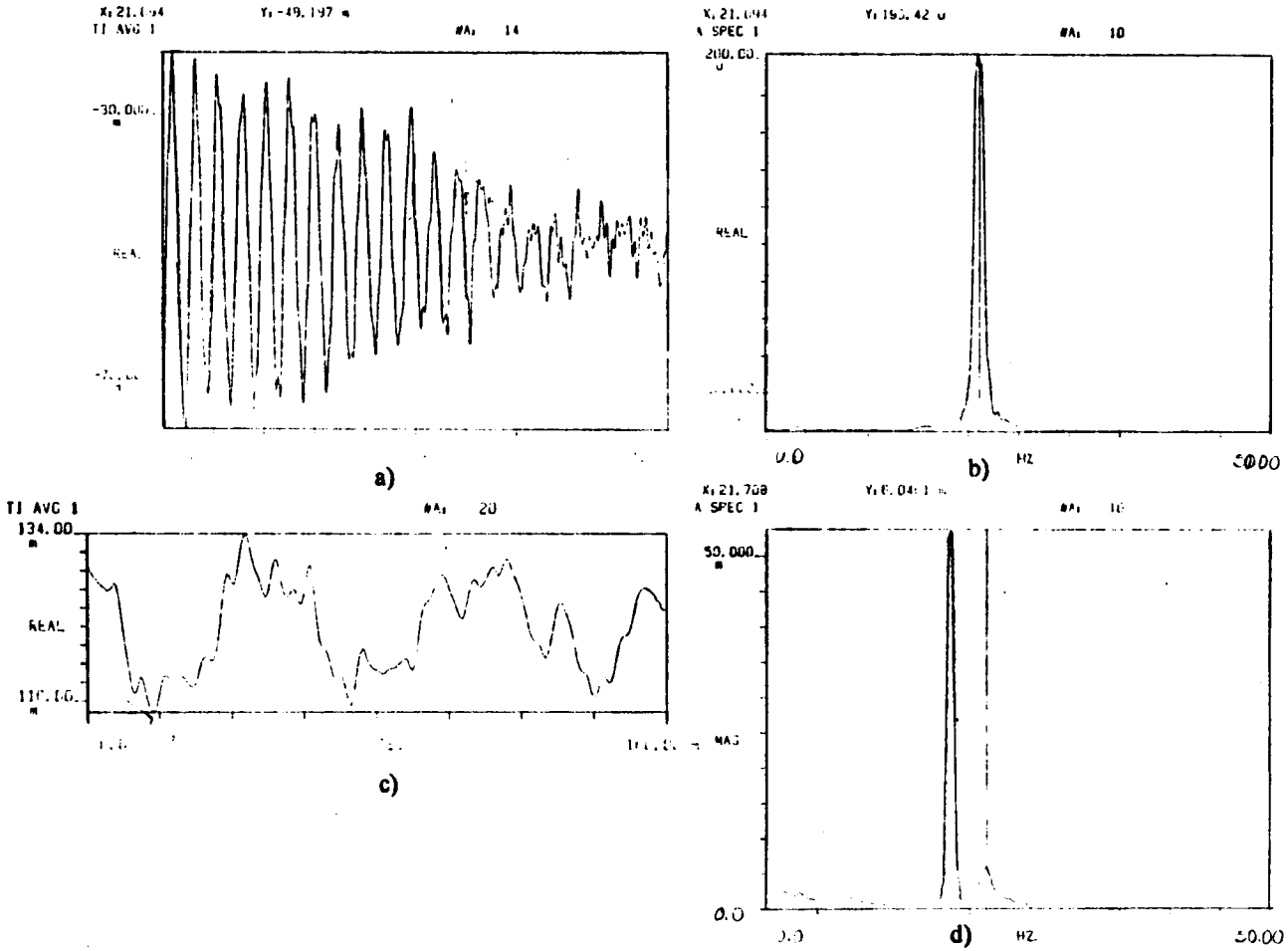

Figure 4.18 Time records and power spectra of lift and drag for pulsed flow at 21 Hz and Re = 50,000 a) Time record of lift b) Power spectrum of lift c) Time record of drag d) Power spectrum of drag

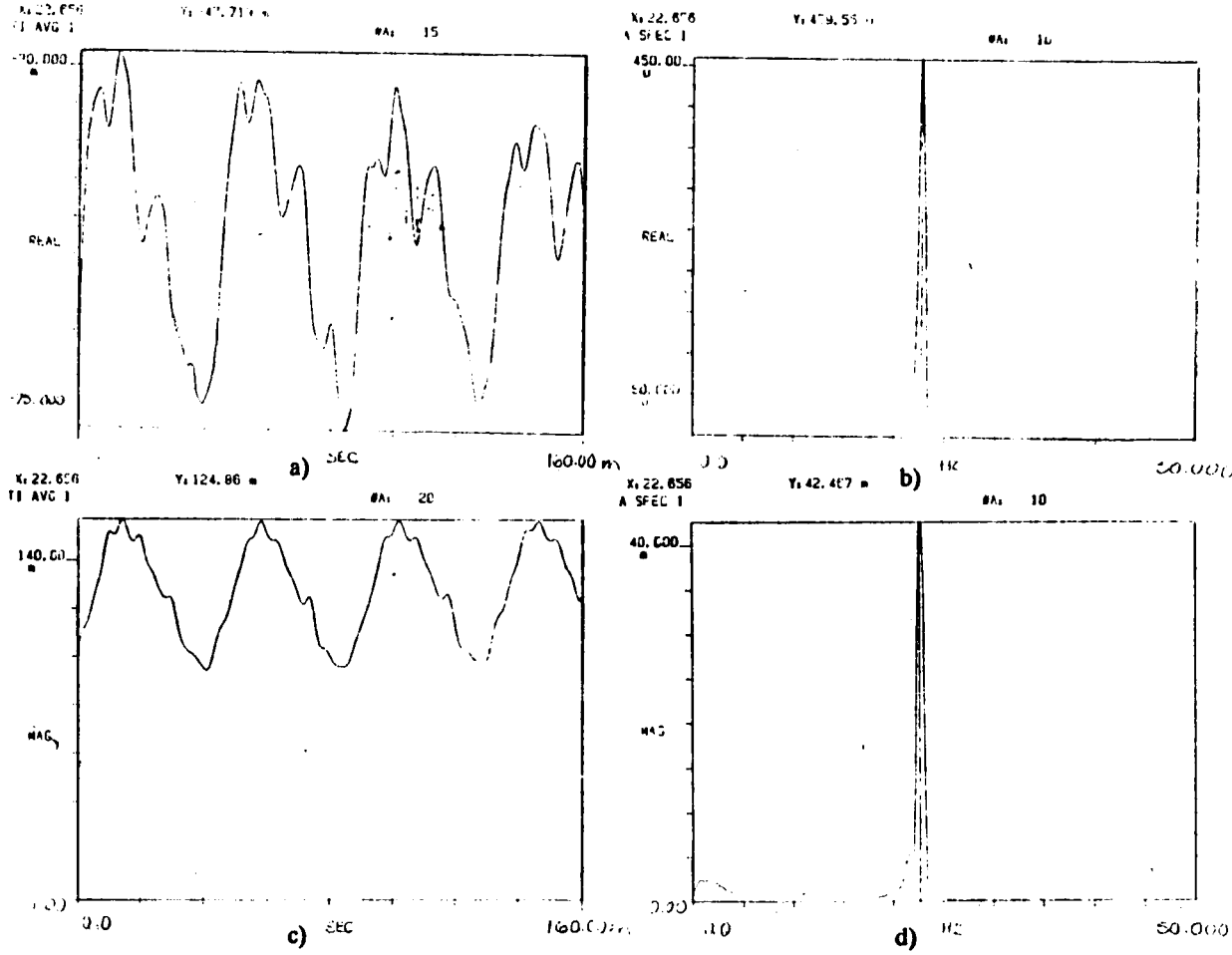

Figure 4.19 Time records and power spectra of lift and drag when locked on at 22.65 Hz and Re = 50,000 a) Time record of lift b) Power spectrum of lift c) Time record of drag d) Power spectrum of drag

4.3 FLOW PAST A TRIAD OF CYLINDERS

In all the tests conducted in the water tunnel the pitch-to-diameter ratio was kept at 1.8. The turbulence level varied between 0.5 and 0.8 percent. Figure 4.20 and figure 4.21 show typical time record and frequency spectrum respectively for a pulsed freestream in the water tunnel at a Reynolds number of 17,200. Figure 4.22 shows the shedding frequency observed above the second cylinder for a Reynolds number of 17,200. This frequency is different from the Strouhal frequency in the case of a single cylinder. The Strouhal number in the present case is equal to 0.16.

Figure 4.23 shows the instantaneous velocity vectors along a vertical line through the top of the second cylinder for a Reynolds number of 17,200 and driven at the shedding frequency. A reduction in the velocity near the boundary layer is seen.

Figure 4.24 shows the power spectrum of LDV signal in the second gap which is between the second and the third cylinders at a distance of one diameter above the center line of the cylinders. The dominant frequency is the same as for the point directly above the center of the second cylinder shown in figure 4.23. The instantaneous velocity vectors along the vertical line through the center of the second gap for a Reynolds number of 17,200 are shown in figure 4.25. The instantaneous velocity near the center of the gap changes direction randomly indicating a chaotic or turbulent region. The velocity spectra in this region do not show any dominant frequency (see figure 4.26). Above the top level of the

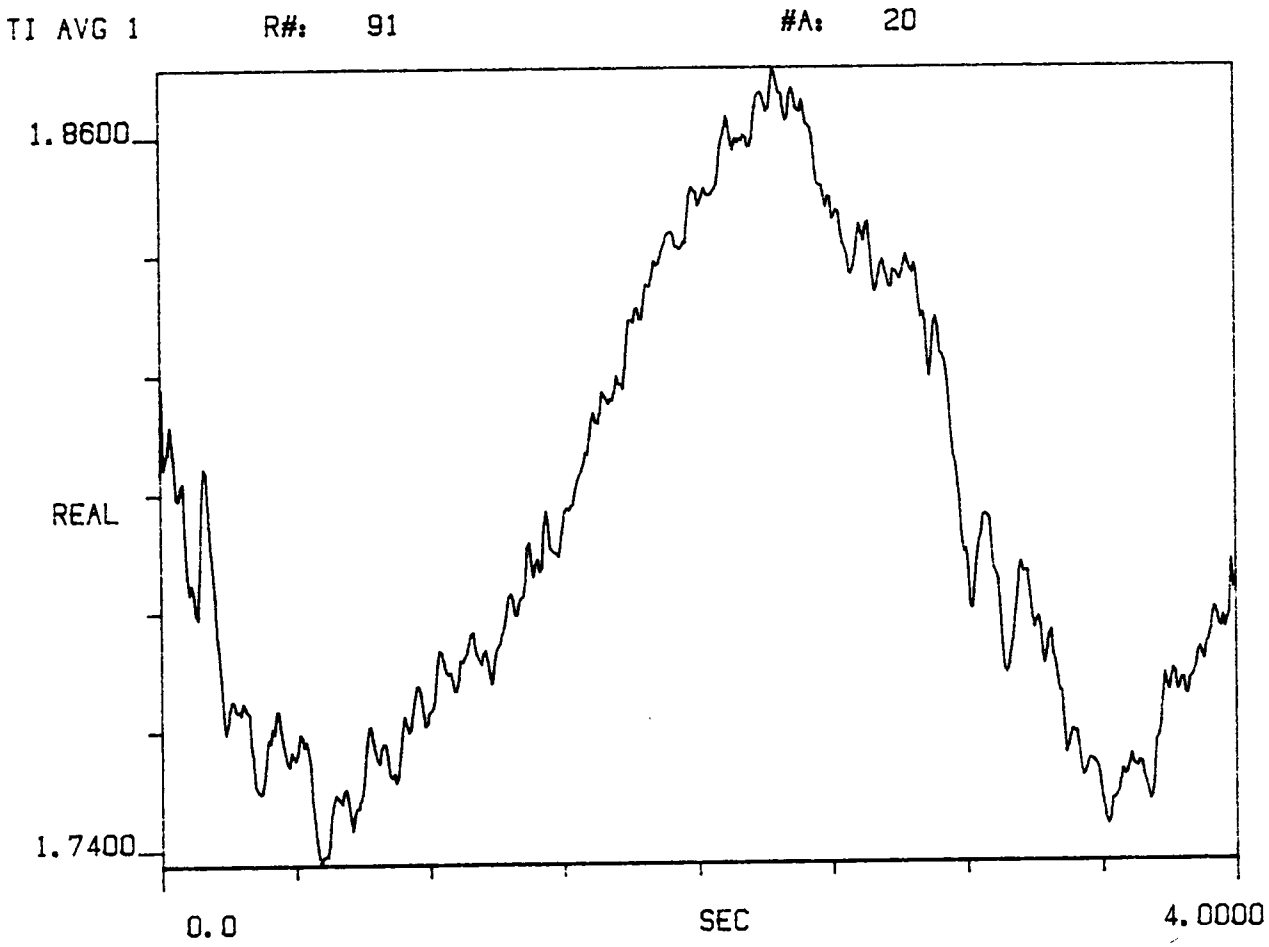

Figure 4.20 A typical time record of free stream velocity in the water tunnel

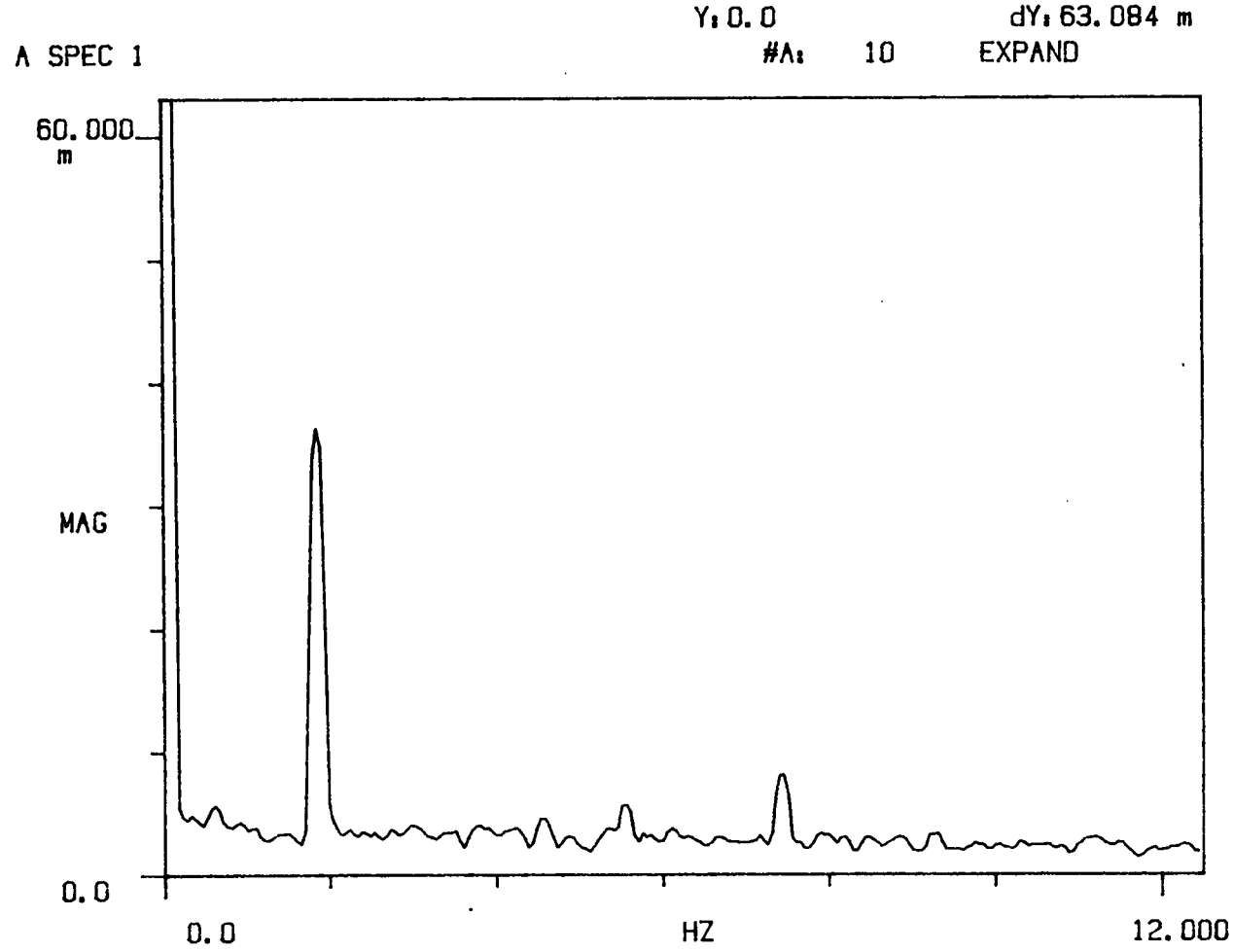

Figure 4.21 Frequency content of the free stream

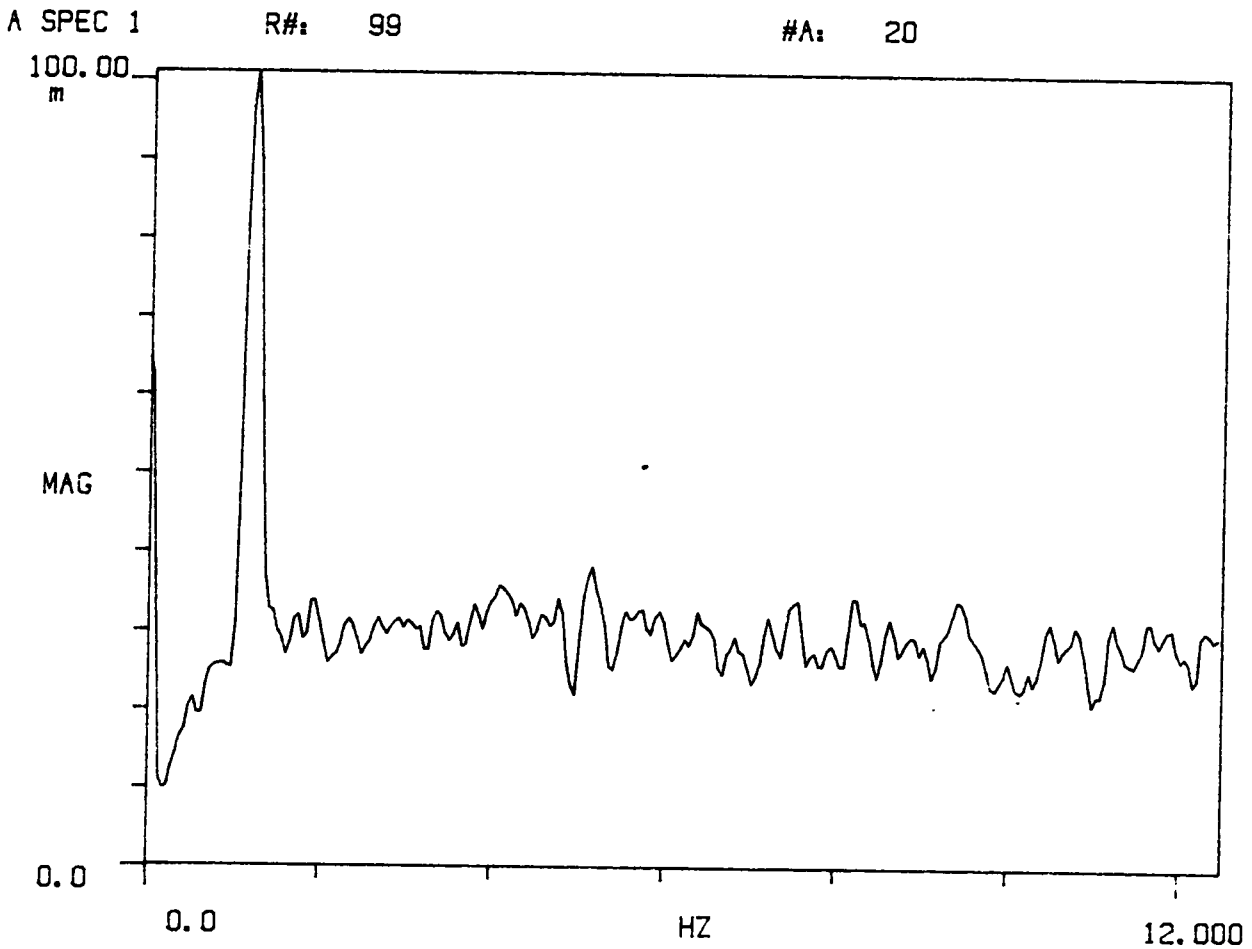

Figure 4.22 Shedding frequency above the second cylinder

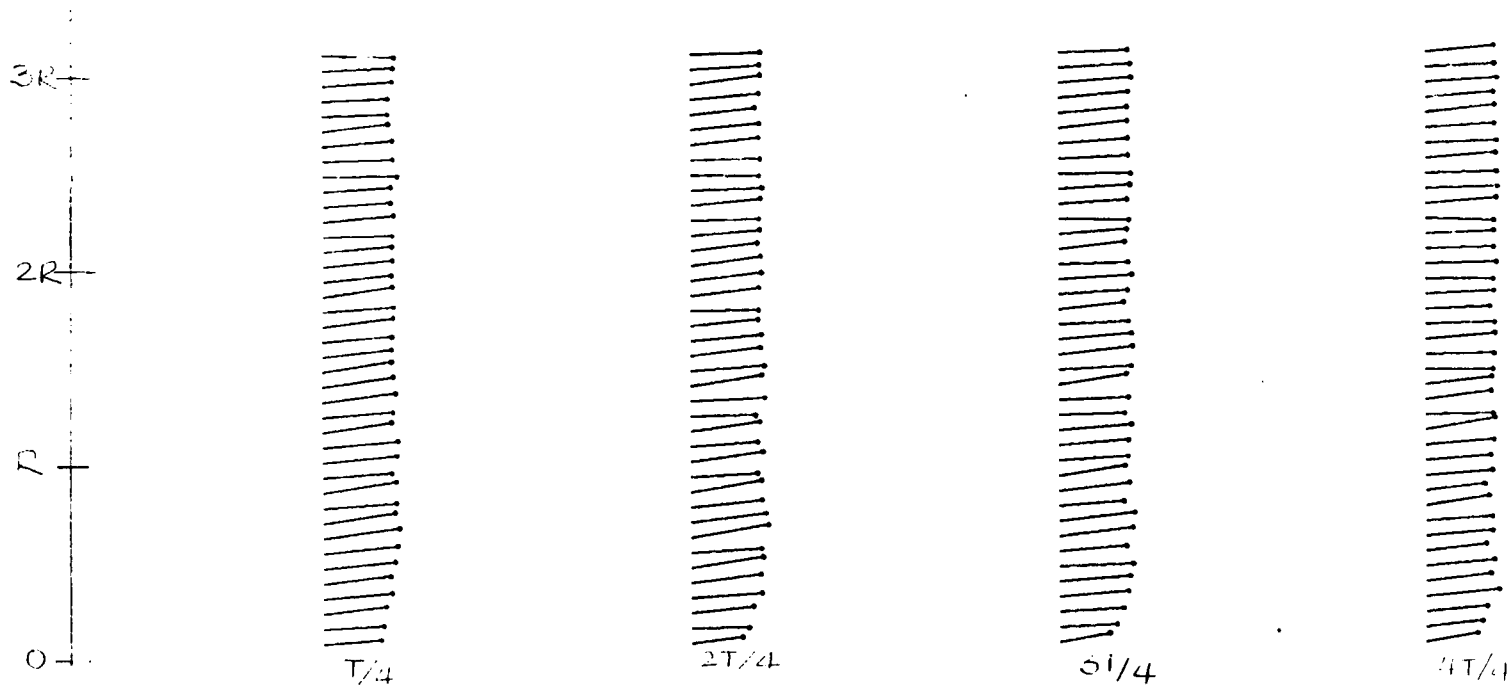

Figure 4.23 Instantaneous velocity vectors along the vertical through the middle cylinder

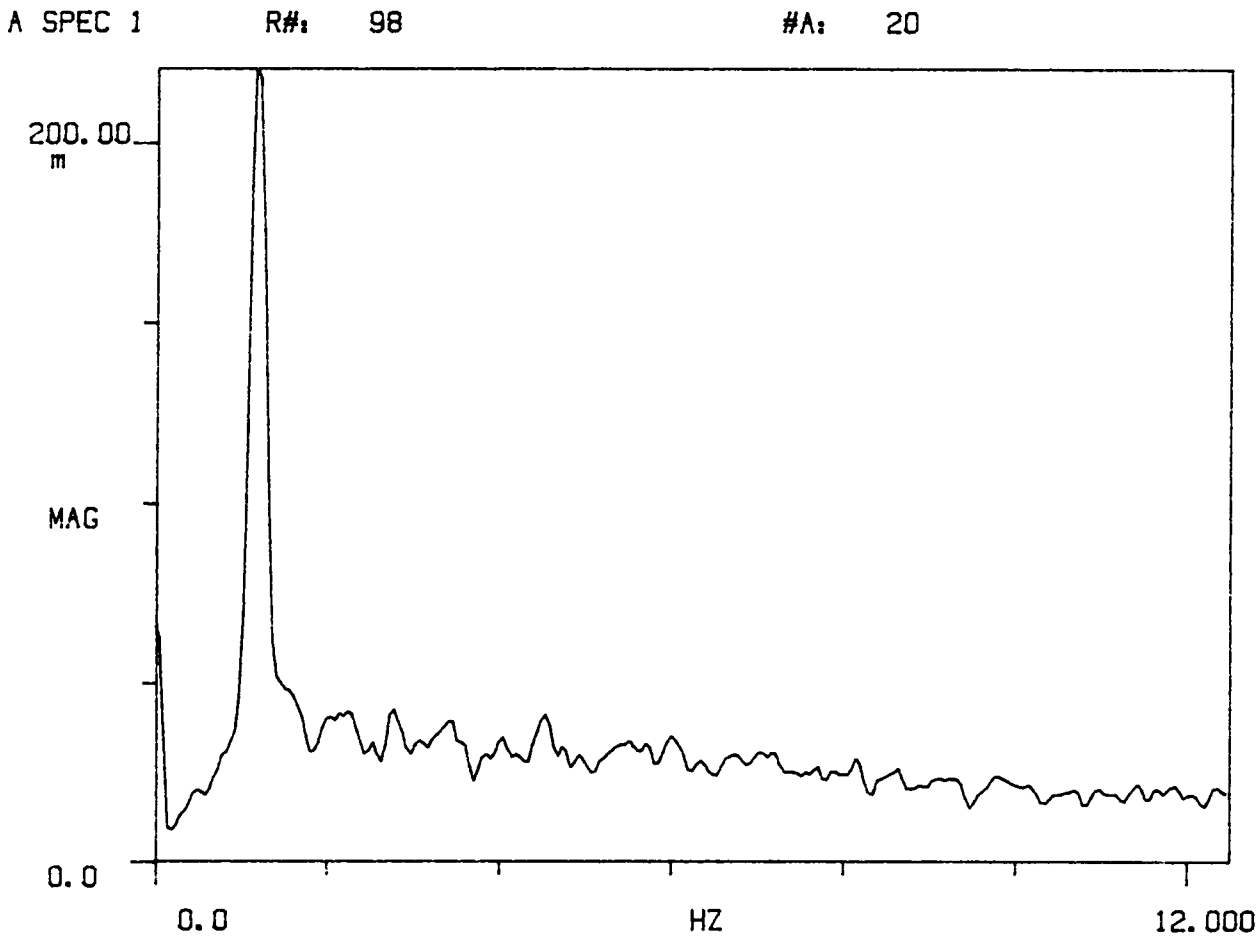

Figure 4.24 Velocity power spectrum in the second gap

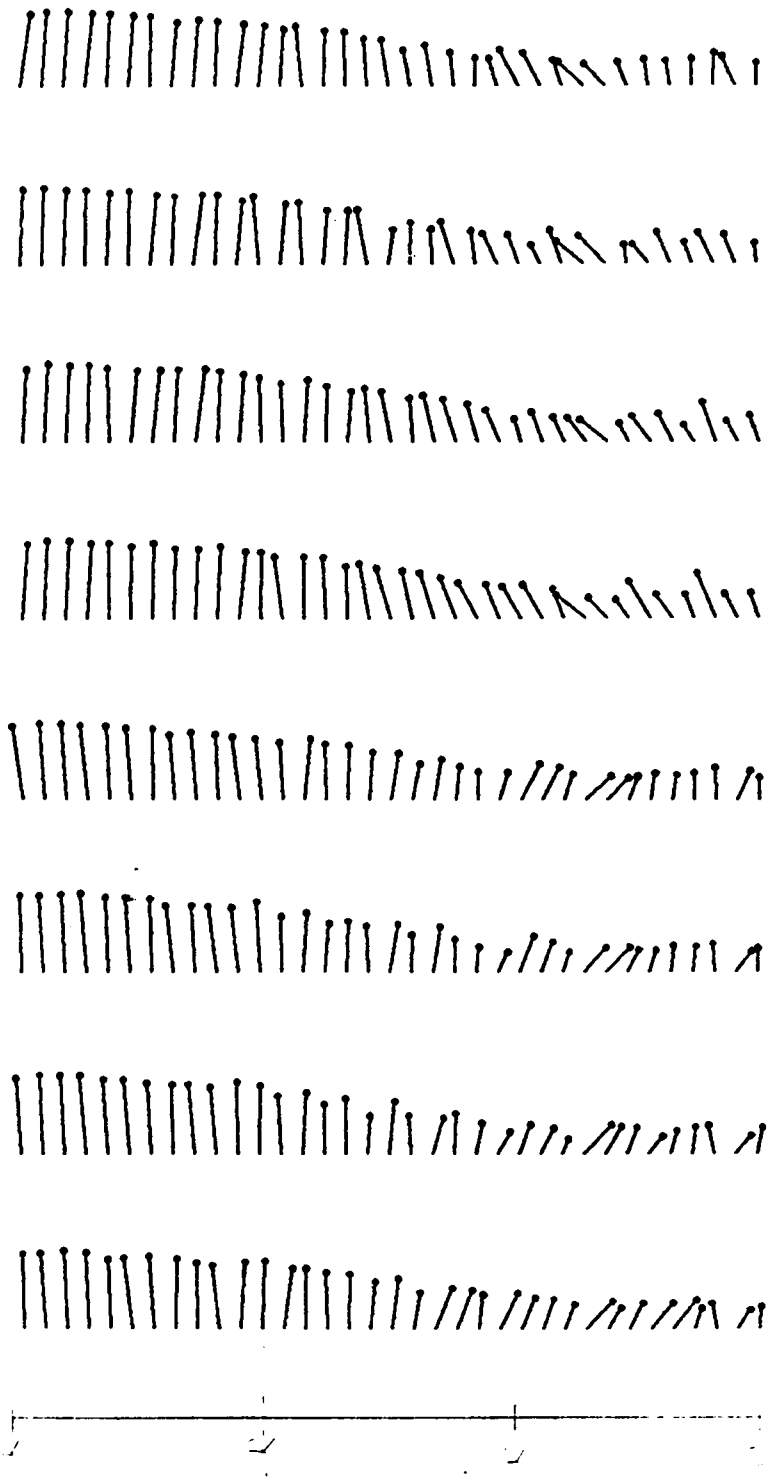

Figure 4.25 Instantaneous velocity vectors along the vertical through the center of the second gap

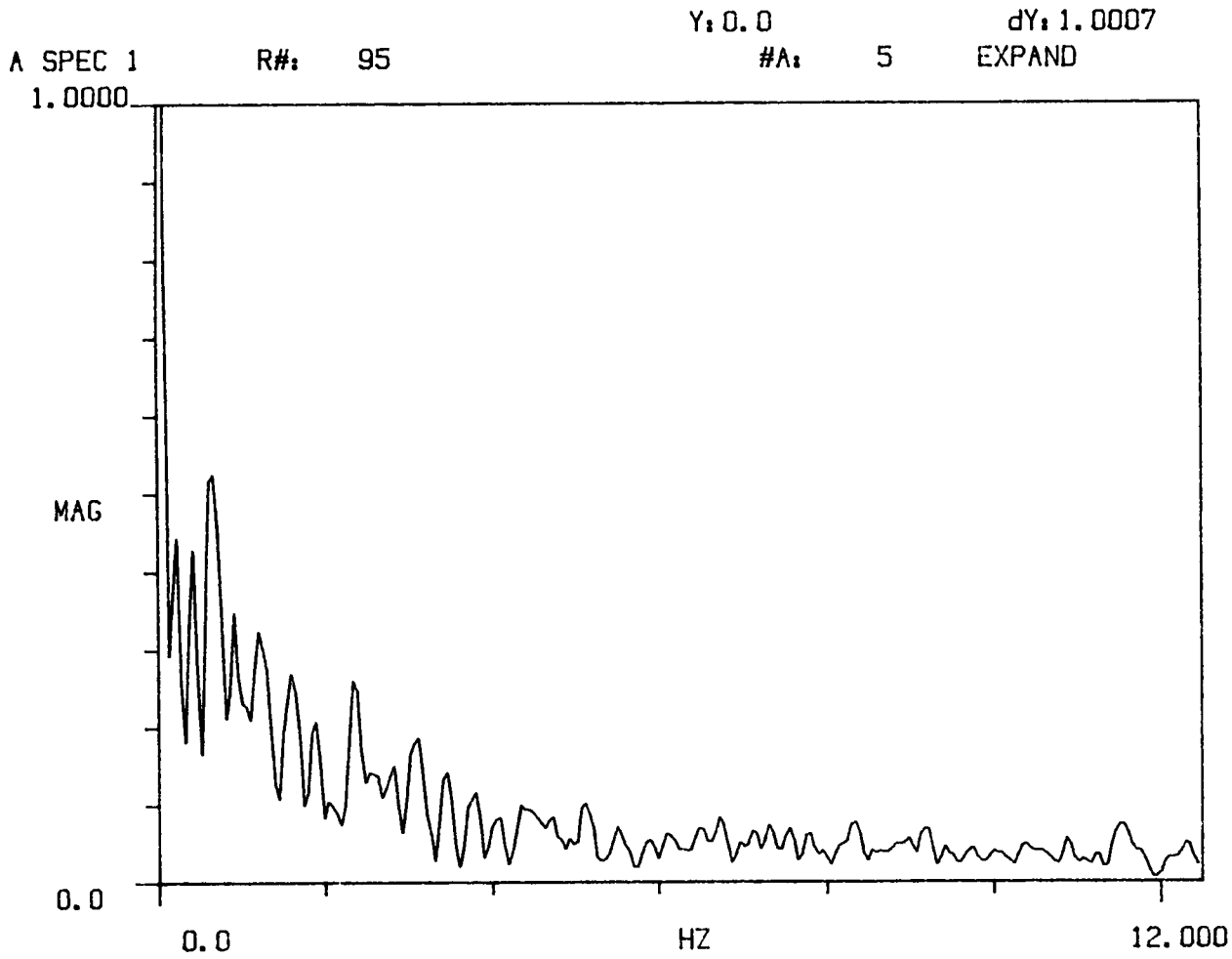

Figure 4.26 Velocity spectrum in the center of the second gap

cylinders the flow behaves in a periodic fashion, as indicated by the velocity spectrum in figure 4.24. No such information is available in the literature for comparison.

Extensive flow visualization studies are conducted in the water tunnel. Flow is visualized in terms of particles, dyes and a combination of both particles and dyes. Color and black and white photographs as well as movie films at different shutter speeds are obtained for various Reynolds numbers. Figure 4.27 displays some typical instantaneous visualization photographs obtained from particle and dye visualizations in the water tunnel. The visualization studies indicate that the region between the first and the second cylinders contains two standing vortices. The flow in this region therefore resembles cavity flow. Violent vortex shedding occurs over the second cylinder. The asymmetry caused by this shedding process induces a periodic disturbance in the flow over the first gap. Consequently, there is periodic spillover of fluid from the first gap. The shedding over the second or rather the first two cylinders turns the flow sharply and attaches it periodically onto the third cylinder. A schematic representation of the flowfield is shown in figure 4.28.

Wake flows as well as cavity flows contain random and organized elements. The organization usually consists of large-scale structures and is due to the rolling up of free shear layers which emanate from separations. The organized motion brings freestream fluid into the wake or cavity. As a result, an increase in the organization in such flows should result in an increase in heat transfer. It has indeed been indicated to be so by some researchers [Lebouche and Martin, 1986;

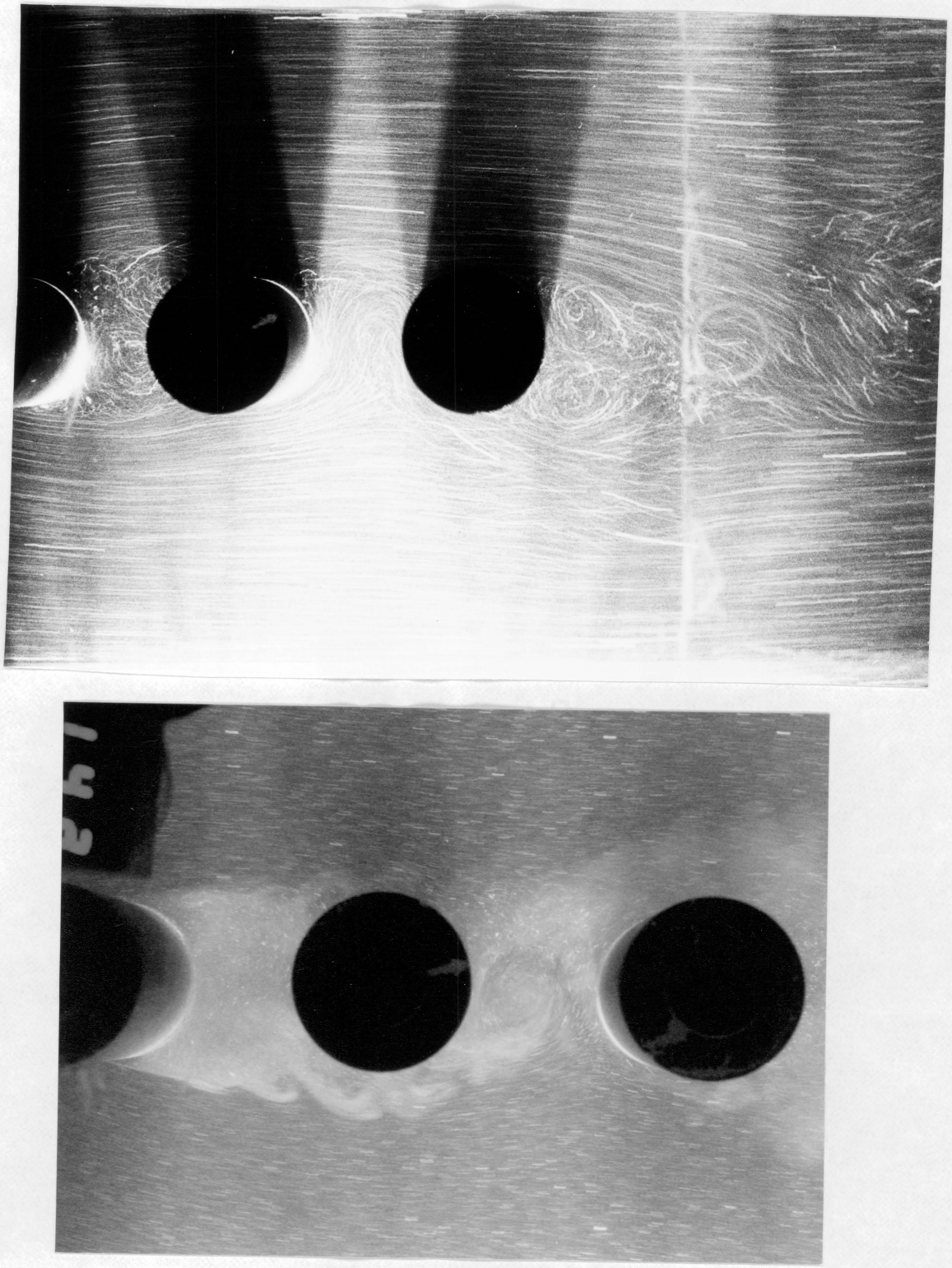

Figure 4.27a Instantaneous flow visualization photographs

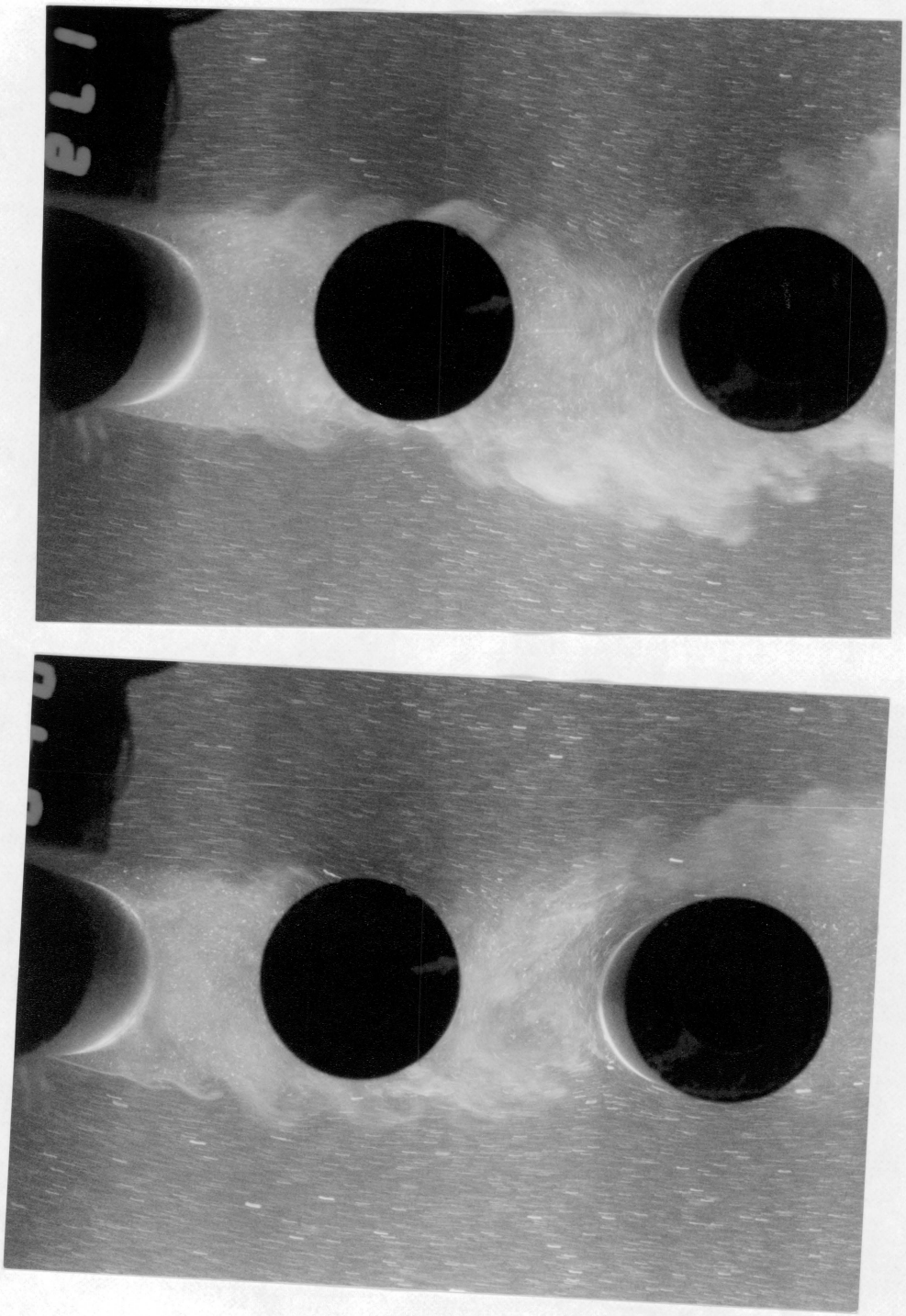

Figure 4.27b Instantaneous flow visualization photographs

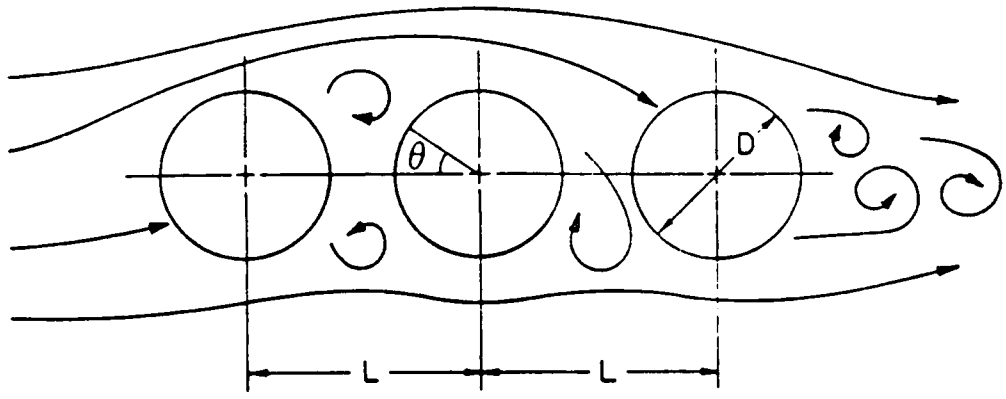

Figure 4.28 Schematic representation of the flow field

Vandenberghe et al., 1986]. It is expected that organization in wake and cavity flows will increase when freestream is pulsed at frequencies which induce lock-on. The level of such activity in the wake or cavity can be inspected by frequency spectra of velocity, skin friction and pressure. Figure 4.29 shows frequency data obtained with a hot-wire probe positioned at the level of the top of the cylinders in the second gap for steady and pulsed air flow. A Reynolds number of 23,000 and a pitch-to-diameter of 1.1 are used. The organization induced into the gap flow by freestream pulsation is evident from the dominant frequency displayed in figure 4.29b. Also the level of activity in the gap is increased as indicated by the larger amplitude of the dominant frequency spike. Figure 4.30 shows the frequency response of a hot-wire in the wake behind the third cylinder. Here the shedding frequency is seen to have locked on to the subharmonic of the driving frequency. Figure 4.31 shows the power spectra for skin friction and pressure at different locations on the second cylinder for steady and pulsed flow driven at 18 Hz. Unlike those for the single cylinder, the spectra for skin friction in steady flow do not show any dominant frequency at 140 and 180 degree positions. In fact there is no indication of well organized skin friction anywhere around the cylinder for steady flow. Introduction of an organized disturbance in the freestream at 18 Hz changes the entire picture as indicated in the spectra with pulsed flow. The flowfield for multiple cylinders is known to have a strong dependence on the pitch-to-diameter ratio (see e.g. Aiba et al., 1980; Igarashi and Suzuki, 1984). Figures 4.32 and 4.33 show frequency response of pressure and skin friction for the second cylinder at pitch-to-diameter ratios of 2.5 and 1.8,

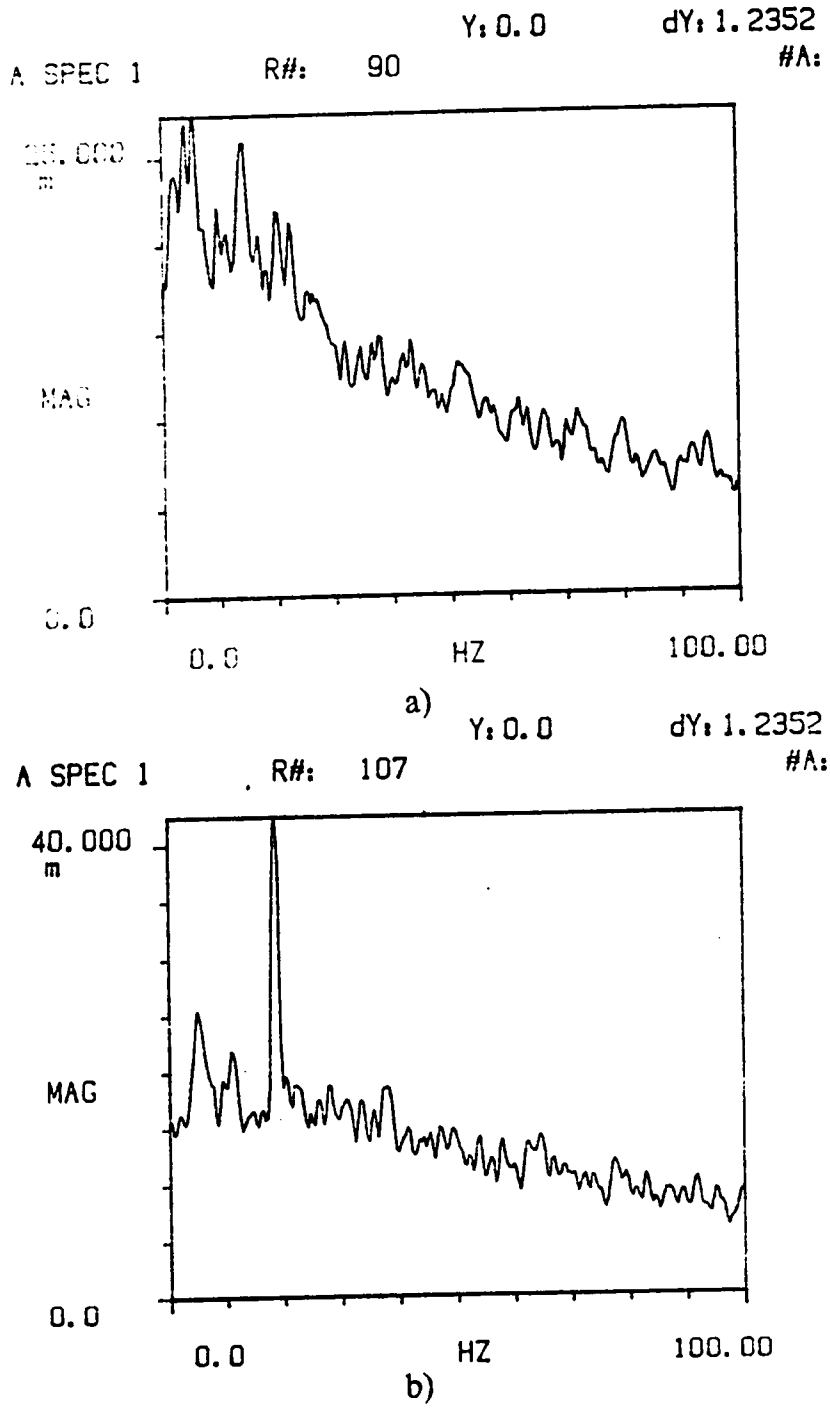

Figure 4.29 Velocity spectra for steady and pulsed air flow above the second cylinder

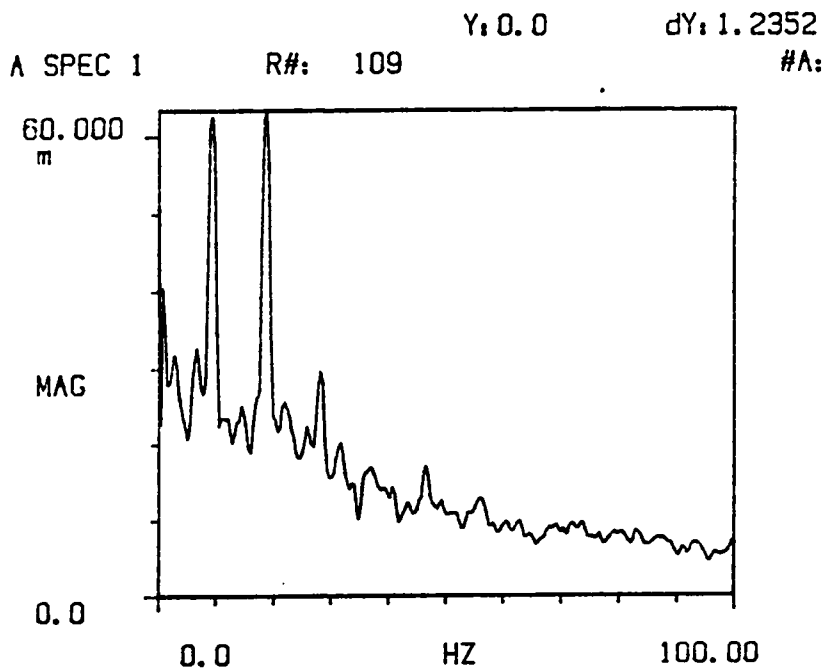

Figure 4.30 Velocity spectrum in the wake of the third cylinder

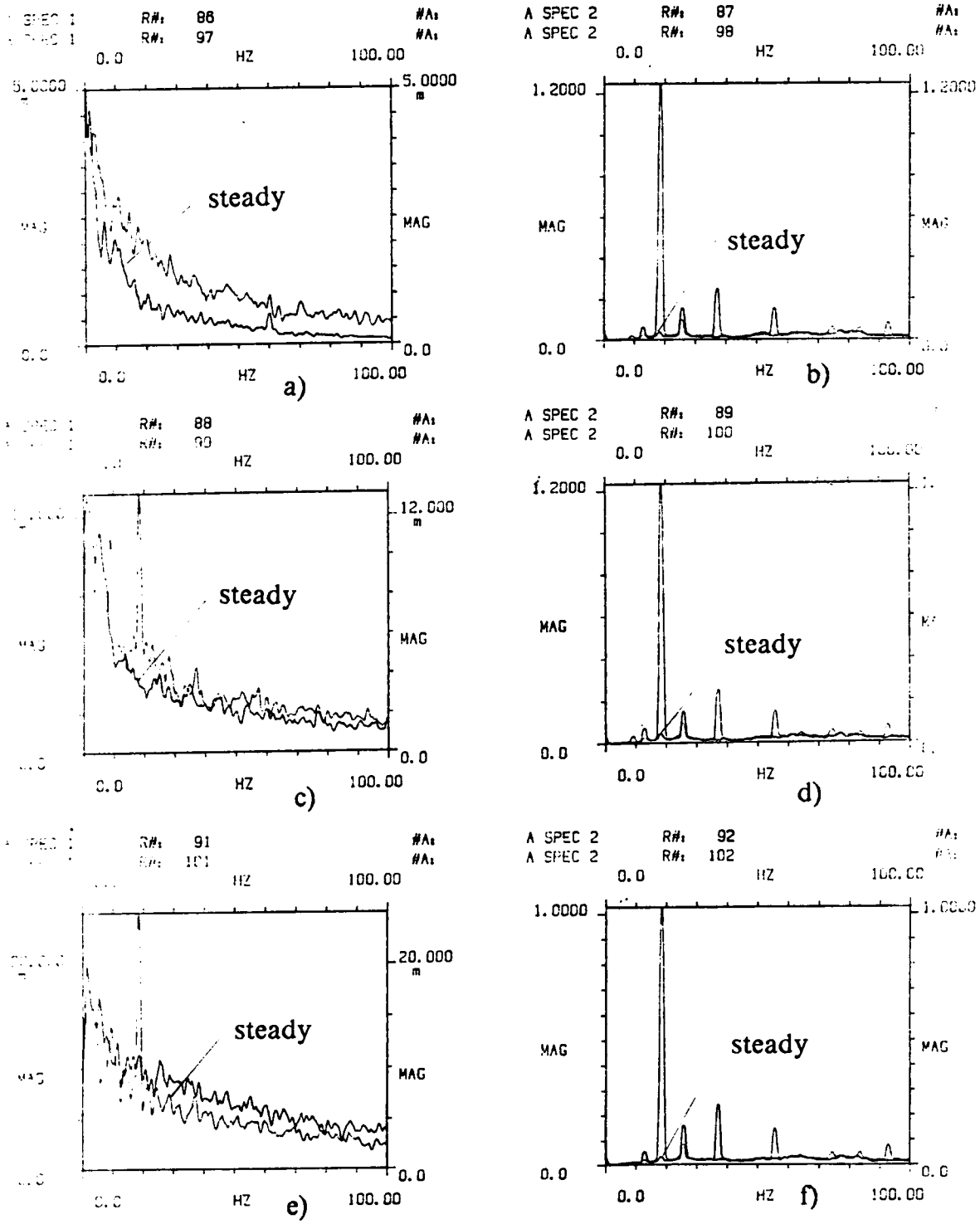

Figure 4.31a Power spectra of skin friction and pressure at different locations on the cylinder with a driving frequency of 18 Hz, P/D = 1.1 and Re = 23,000 a) τ_0 b) p_0 c) τ_{40} d) p_{40} e) τ_{90} f) p_{90}

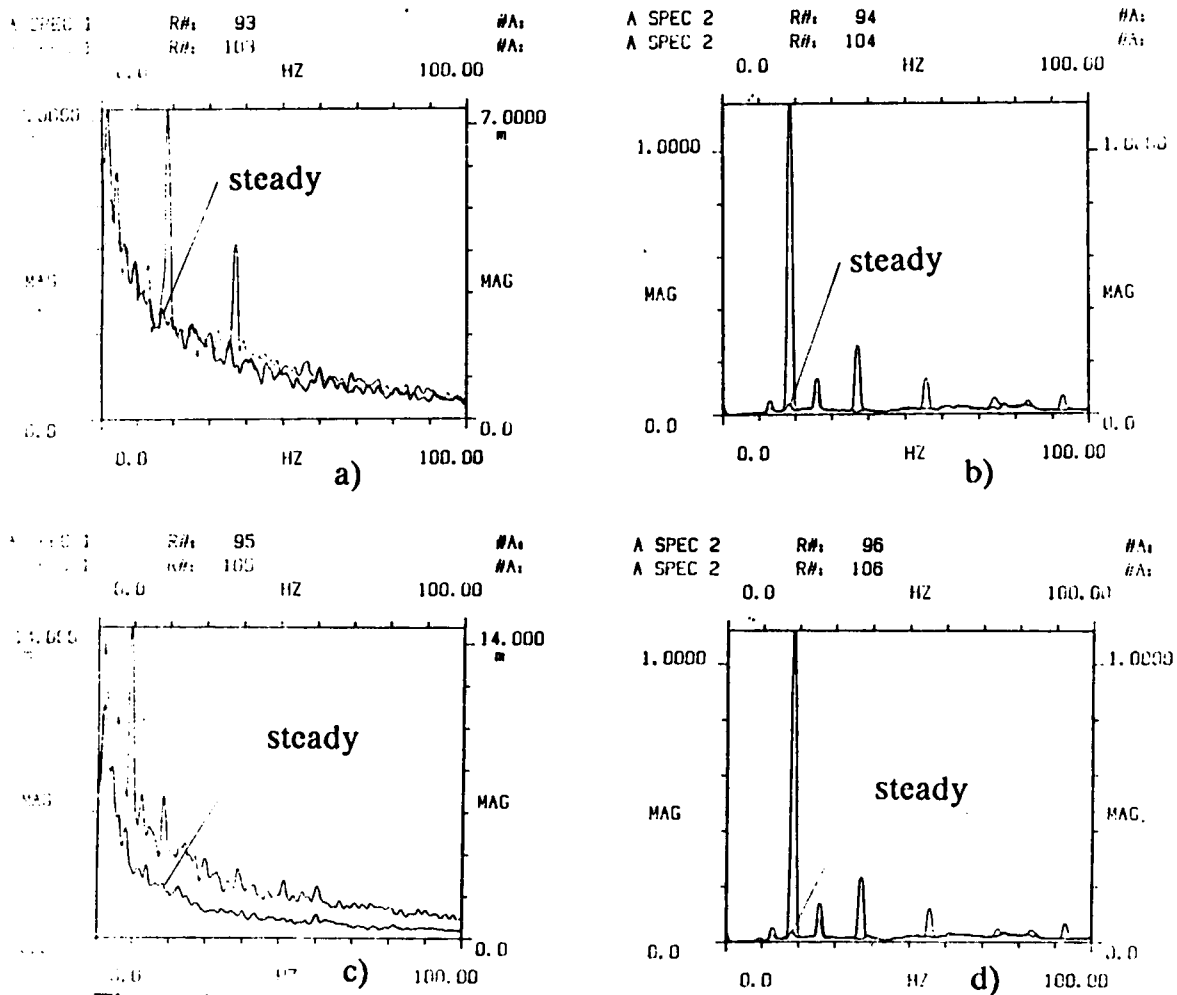

Figure 4.31b Power spectra of skin friction and pressure at different locations on the cylinder with a driving frequency of 18 Hz, P/D = 1.1 and Re = 23,000 a) τ_{140} b) p_{140} c) τ_{180} d) p_{180}

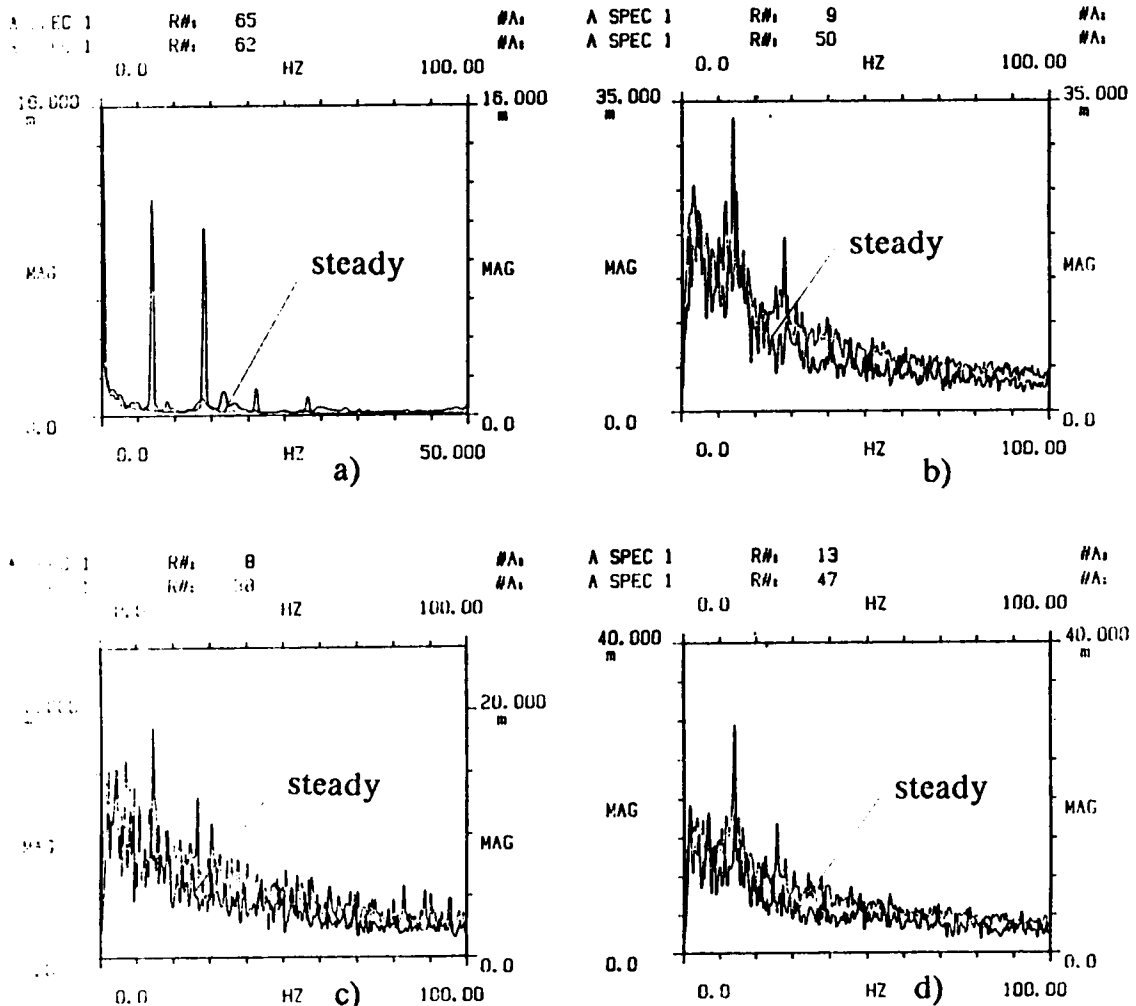

Figure 4.32 Frequency response of pressure and skin friction on the second cylinder at fd = 14 Hz, P/D = 2.5 and Re = 50,000
a) p_{90} b) τ_{40} c) τ_{140} d) τ_{90}

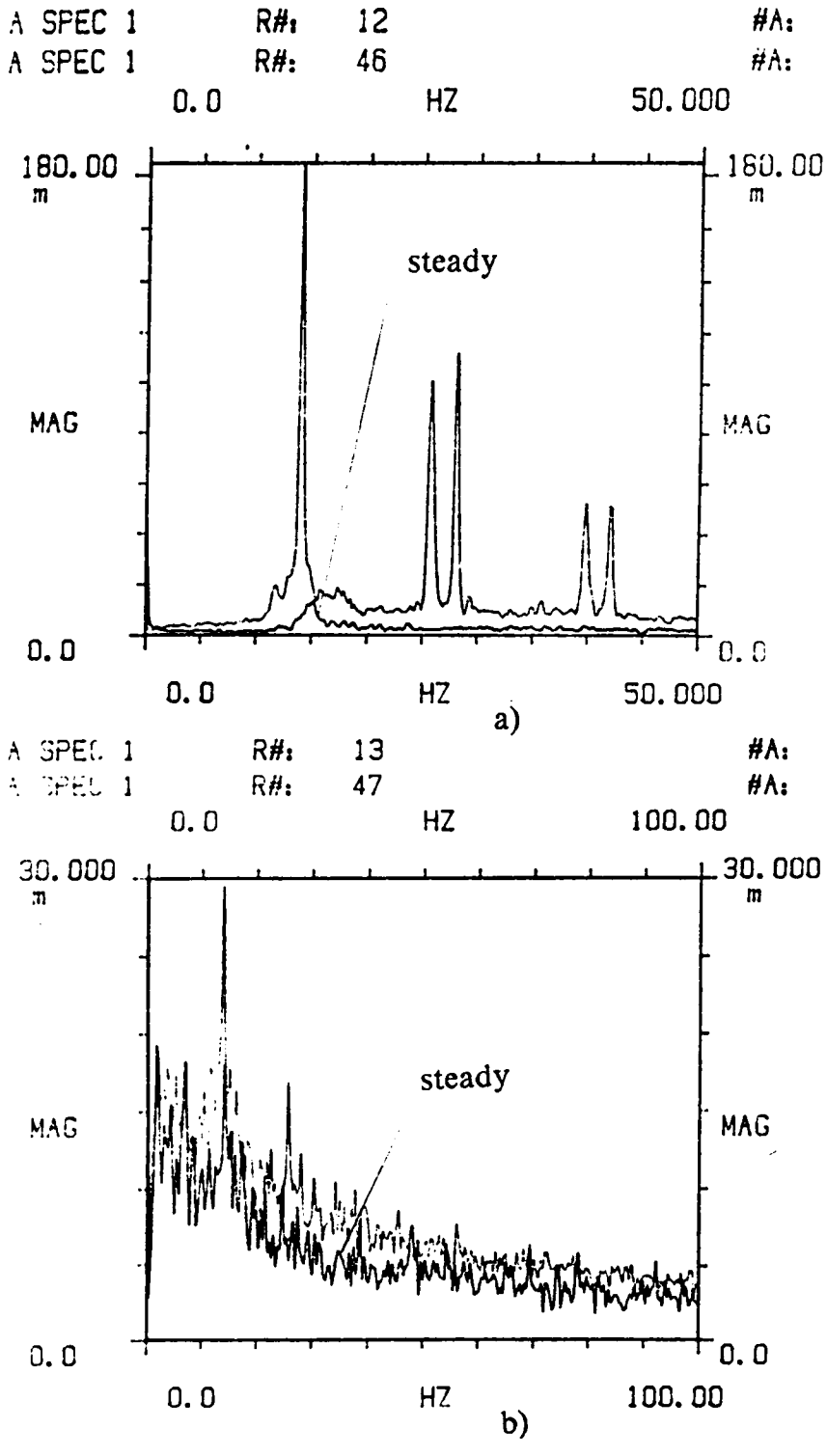

Figure 4.33 Frequency response of pressure and skin friction on the second cylinder at fd = 14 Hz, P/D = 1.8 and Re = 50,000
a) p_{90} b) τ_{90}

respectively. Pulsation of the flow is seen to contribute to some organization in these cases also. However, the magnitude of the locked-on quantity decreases with pulsation. In this range of spacings, therefore, pulsing may result in decreased heat transfer.

Figure 4.34 displays the mean skin-friction coefficient distribution around the second cylinder for different driving frequencies and two different Reynolds numbers. A pitch-to-diameter ratio of 1.8 is used. The shape of the curves in all the cases is similar but no simple correlation between the absolute value of the mean skin friction and the driving frequency is observed. This figure also indicates that the skin-friction coefficient as defined earlier is lower for lower Reynolds number. On physical grounds, we know that the first lobe in this figure represents negative skin friction. The trough displayed, therefore, actually should be close to zero for all these curves. This arises because of the directional insensitivity of the skin friction gauge. Skin friction data for flow past three cylinders is not available for comparison.

Figure 4.35 shows the rms of fluctuation of the coefficient of skin friction around the second cylinder for the various cases mentioned above. The plot of rms of the fluctuation of skin friction versus position on the cylinder displays a shape somewhat similar to the mean skin-friction coefficient distribution. The rms values of skin friction are found to be proportional to their respective mean skin friction values.

Figure 4.36 shows the static pressure distribution around the second cylinder for a pitch-to-diameter ratio of 1.8. Driving frequencies of 0, 10, 14 and

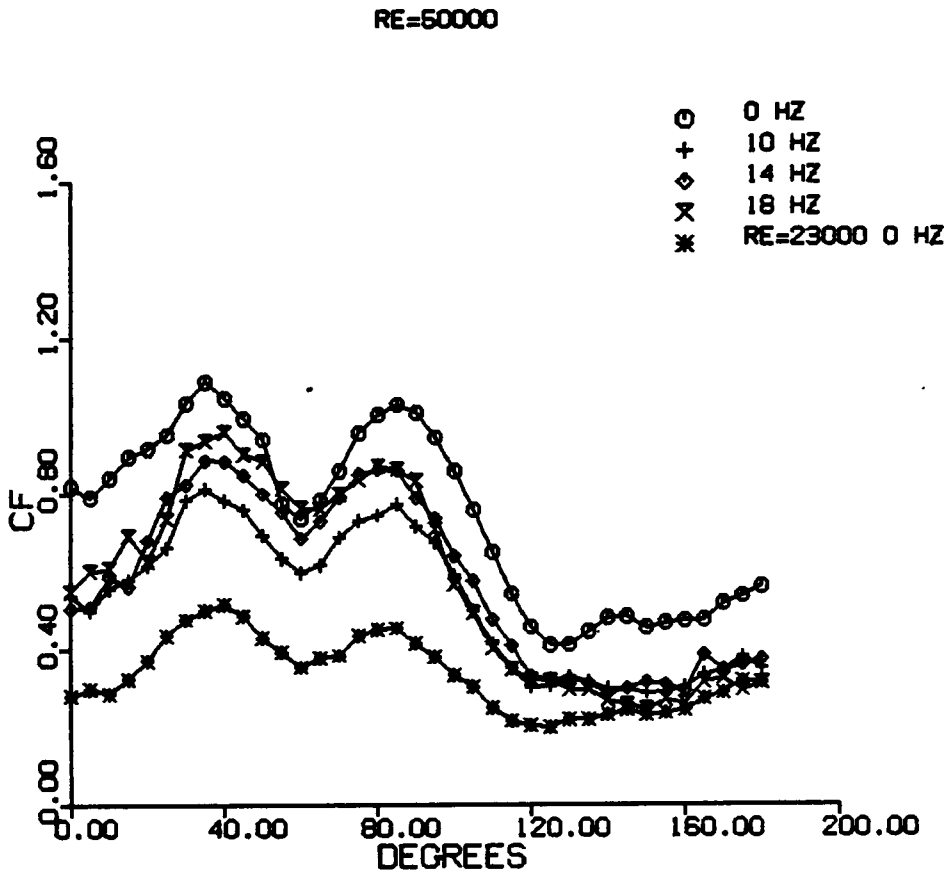

Figure 4.34 Distribution of mean skin friction around the second cylinder for P/D = 1.8

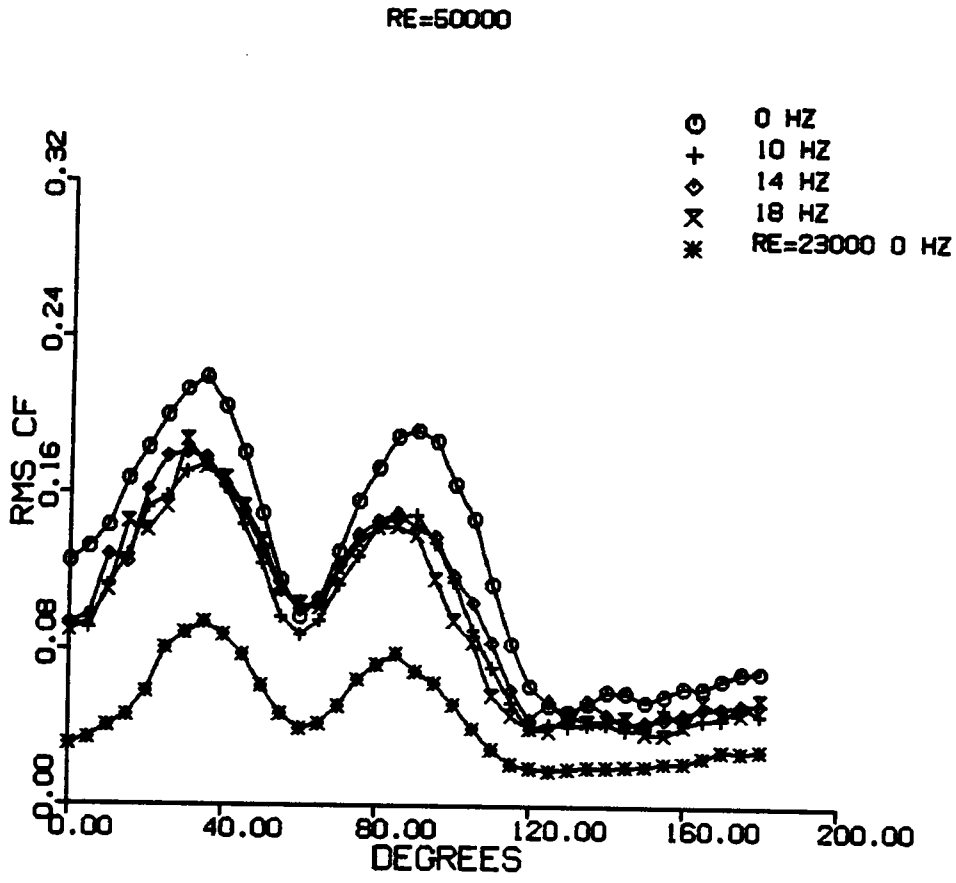

Figure 4.35 Distribution of rms of skin friction fluctuation around the second cylinder for P/D = 1.8

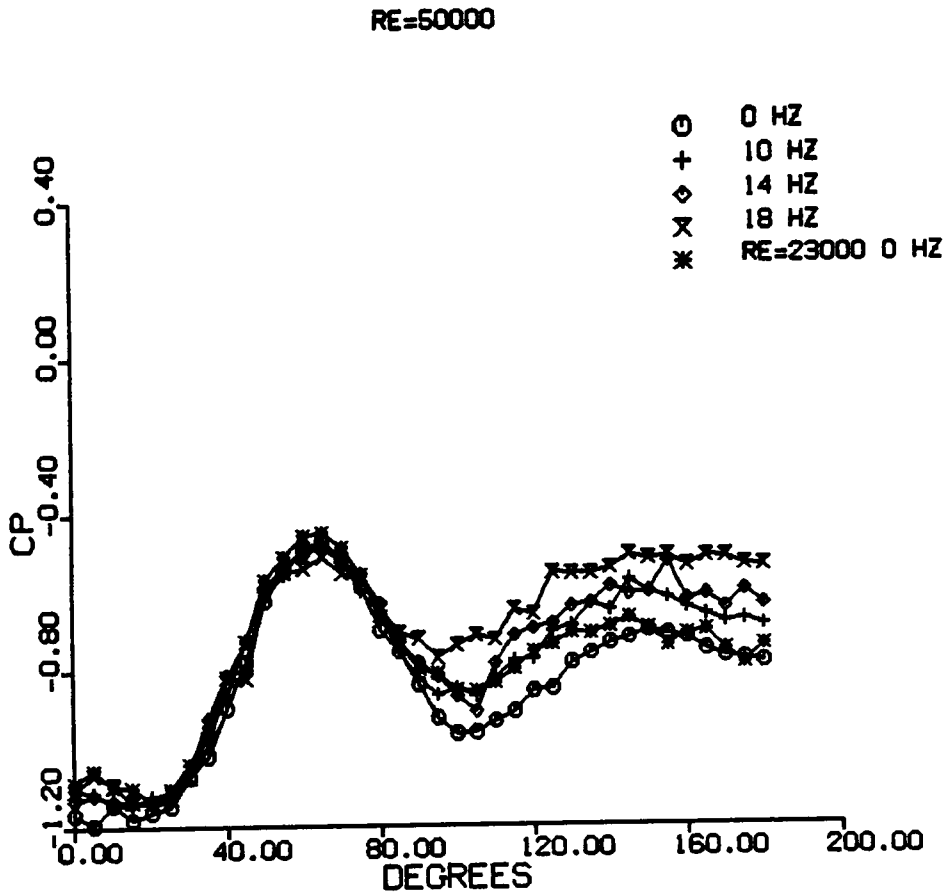

Figure 4.36 Distribution of static pressure around the second cylinder for P/D = 1.8

18 Hz with a Reynolds number of 49,000 and steady flow with a Reynolds number of 23,000 are considered. The maximum value of the coefficient of pressure lies between the 60 and 70 degree locations. Igarashi and Suzuki's [1984] results for steady flow at Re = 21,800 and P/D = 2.06 indicate a similar location for maximum pressure coefficient. It is clearly seen that the flow stagnates in the mean at about 60 to 65 degrees. This corroborates the skin friction estimate of a zero value at about this point. The shape of the static pressure distribution for steady flow also matches with that obtained by Igarashi and Suzuki for Re 21,800 and P/D = 2.06. Distribution of absolute values of the coefficient of static pressure for a pitch to diameter of 1.8 is not available for comparison. The effect of pulsation frequency on the coefficient of pressure is more pronounced in the separation region and the pressure coefficient in this region is lower for higher frequencies of pulsation. The net flow resistance or C_d for the second cylinder as indicated in the following chapter can be expected to decrease from this observation.

Figure 4.37 shows the distribution of rms of fluctuating pressure around the second cylinder for a pitch-to-diameter ratio of 1.8. The rms of fluctuating pressure increases proportionately with the driving frequency.

Recirculating cavity flows were achieved with a tightly packed configuration of cylinders at P/D of 1.1. Figure 4.38 shows the distribution of coefficient of skin friction around the second cylinder for this spacing and at Reynolds numbers of 50,000 and 23,000. Steady freestream and freestream pulsed at 10 and 18 Hz are considered. The frequency at which the shedding

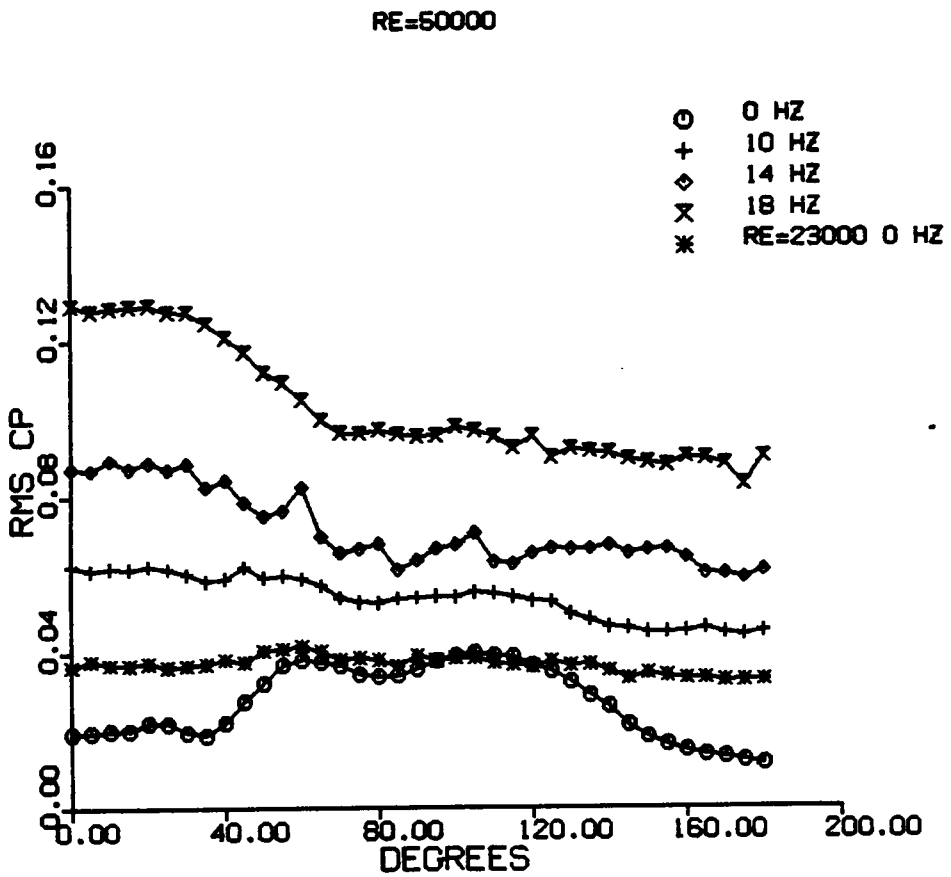

Figure 4.37 Distribution of rms of pressure fluctuation around the second cylinder for P/D = 1.8

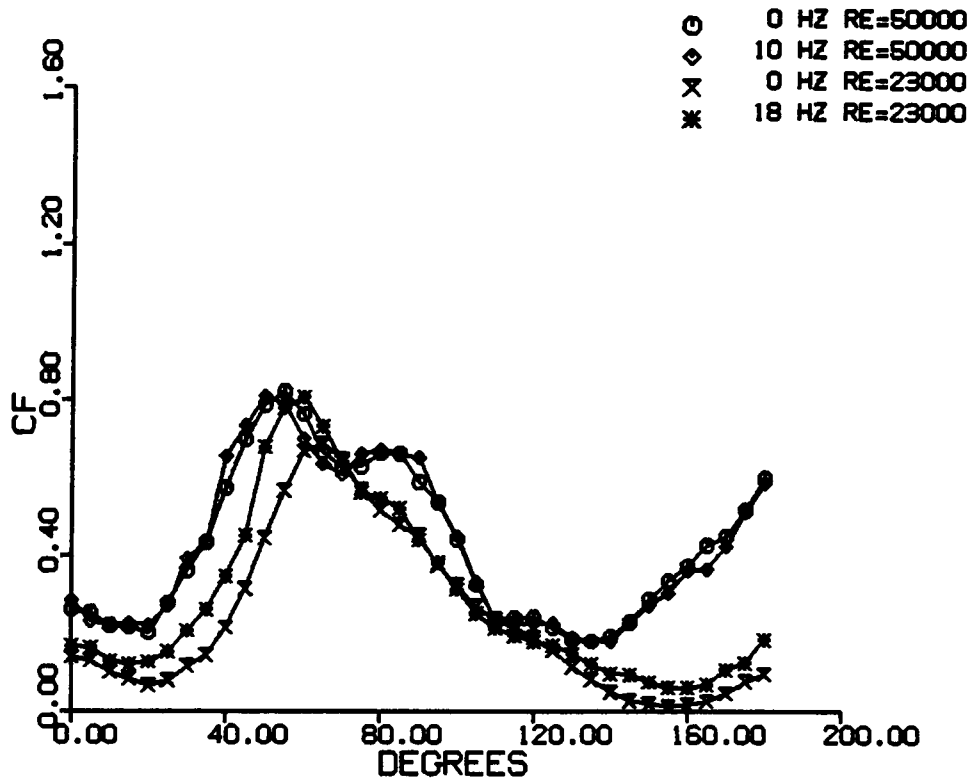

Figure 4.38 Distribution of mean skin friction around the second cylinder for P/D = 1.1

locks with the subharmonic of the driving for Re = 23,000 is equal to 18 Hz. The effect of pulsation on mean skin friction does not have a set trend. The shape of the curve and the absolute values of the coefficient of skin friction at Re = 50,000 do not differ much for steady flow and pulsed flow at 10 Hz. However, for a driving frequency of 18 Hz the absolute value of the coefficient of skin friction at Re = 23,000 is noticeably higher in the front and back portions of the cylinder. At a Reynolds number of 50,000, the effect of pulsation is observed to be more pronounced at a P/D of 1.8.

Figure 4.39 shows the distribution of rms of the skin friction around the second cylinder for the different conditions of freestream. The shape of the rms of skin friction curve is again somewhat similar to the shape of the corresponding mean skin friction curve. The rms of fluctuation of skin friction is observed to be higher for lower Re. The magnitude of rms of skin friction is lower compared to that for a P/D of 1.8.

Pressure distributions around the second cylinder for a pitch to diameter ratio of 1.1 and Reynolds numbers of 50,000 and 23,000 are shown in figure 4.40. The pattern of the steady flow curve for Re = 23,000 is similar to Igarashi and Suzuki's [1984] results for a pitch-to-diameter ratio of 1.18 and a Reynolds number of 26,200. Unlike the case with a pitch to diameter ratio of 1.8, pulsation at 10 Hz for Re = 50,000 does not change the distribution of the coefficient of pressure much. But a driving frequency of 18 Hz at Re = 23,000 increases the coefficient of pressure appreciably from 55 degrees onwards.

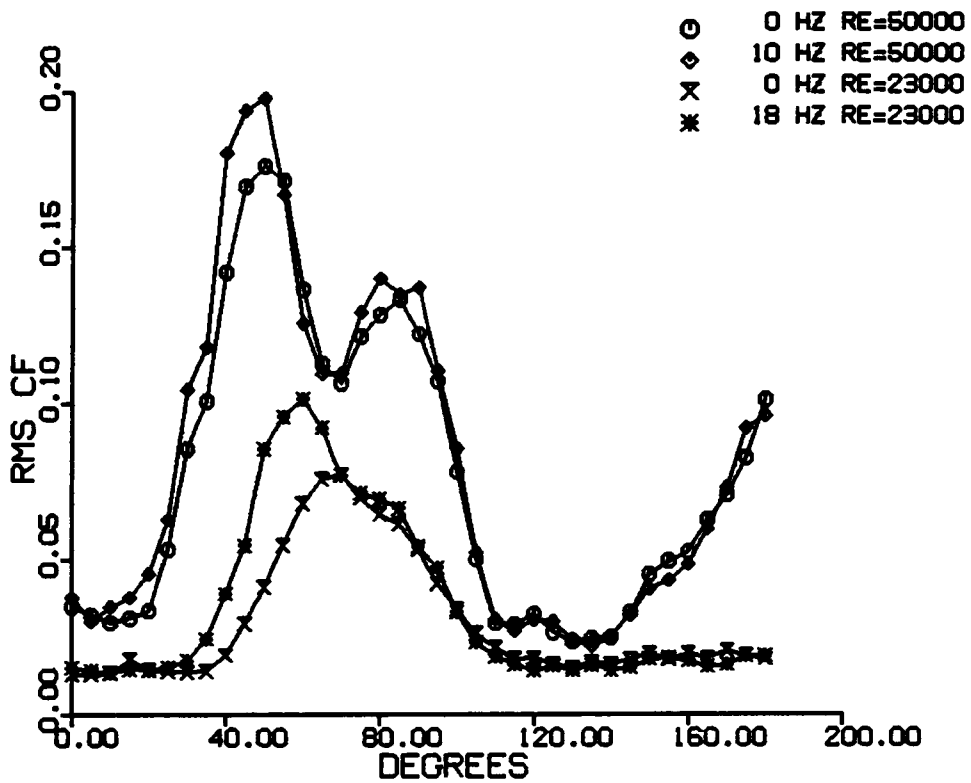

Figure 4.39 Distribution of rms of skin friction fluctuation around the second cylinder for P/D = 1.1

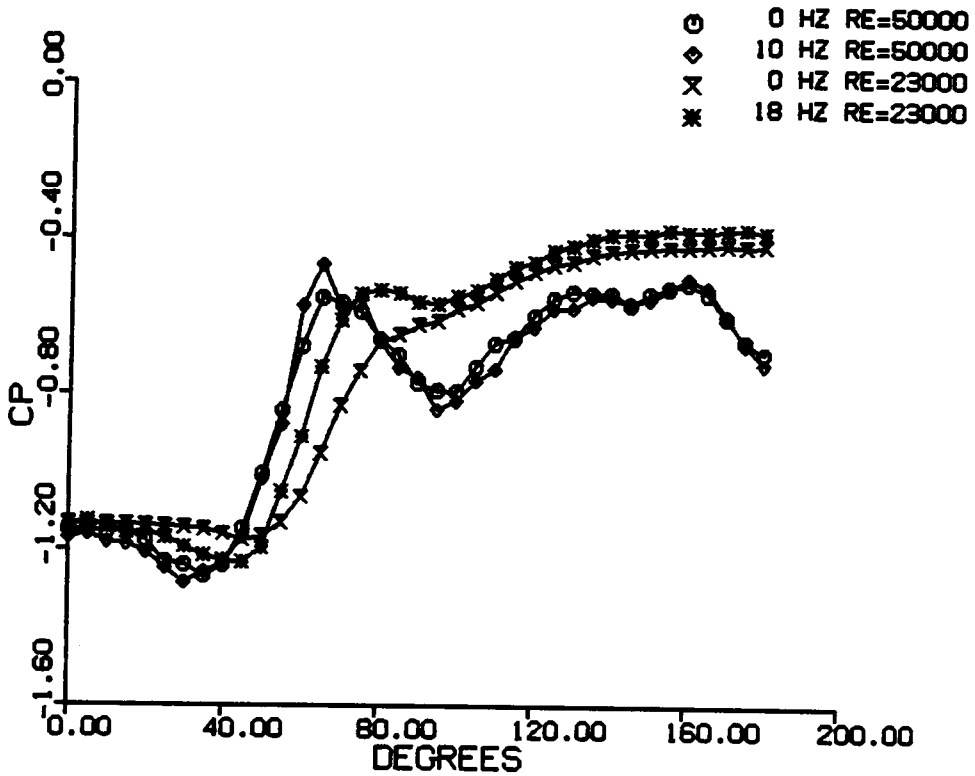

Figure 4.40 Distribution of static pressure around the second cylinder for P/D = 1.8

Figure 4.41 shows the distribution of the rms of pressure fluctuation around the second cylinder. The rms of pressure fluctuation is seen to increase with the increase in the driving frequency as for other cases discussed earlier.

4.4 FLOW PAST A PENTAD OF CYLINDERS

Figure 4.42 shows the shedding frequency content of the LDV signal behind the third cylinder. A pitch-to-diameter ratio of 1.8 and a Reynolds number of 22,000 were employed. The Strouhal number corresponding to the shedding frequency is 0.14 which is slightly lower than the value in the three-cylinder case of 0.16. Ishigai and Nishikawa [1975] found the Strouhal number to be slightly below 0.12 for a pitch-to-diameter ratio of 2.0 and approximately 0.16 for a pitch to diameter ratio of 1.5. They point out that the Strouhal number changes drastically for pitch to dimeter ratios between 1.5 and 2.0. The Strouhal number observed lies between these two values. The velocity spectrum in the first gap does not show any dominant frequency which indicates that flow in this gap behaves like cavity flow. The dominant frequency, when there is one, has the same value for all the gaps. The dominant frequency is inescapable when the probe is away from the center of the gap and there does not seem to be any drastic change in the Strouhal frequency as indicated by Ishigai and Nishikawa.

Results of a lock-on study are presented in figure 4.43. A Reynolds number of 17,200 and a pitch-to-diameter ratio of 1.8 were employed. The figure exhibits

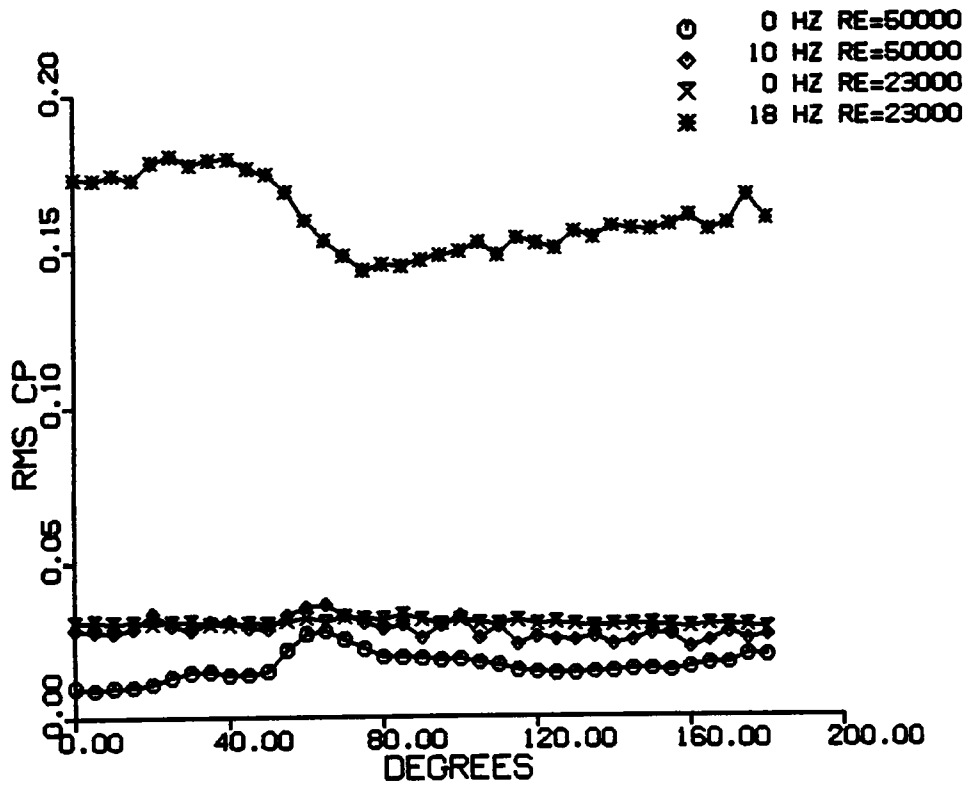

Figure 4.41 Distribution of rms of pressure fluctuation around the second cylinder for P/D = 1.1

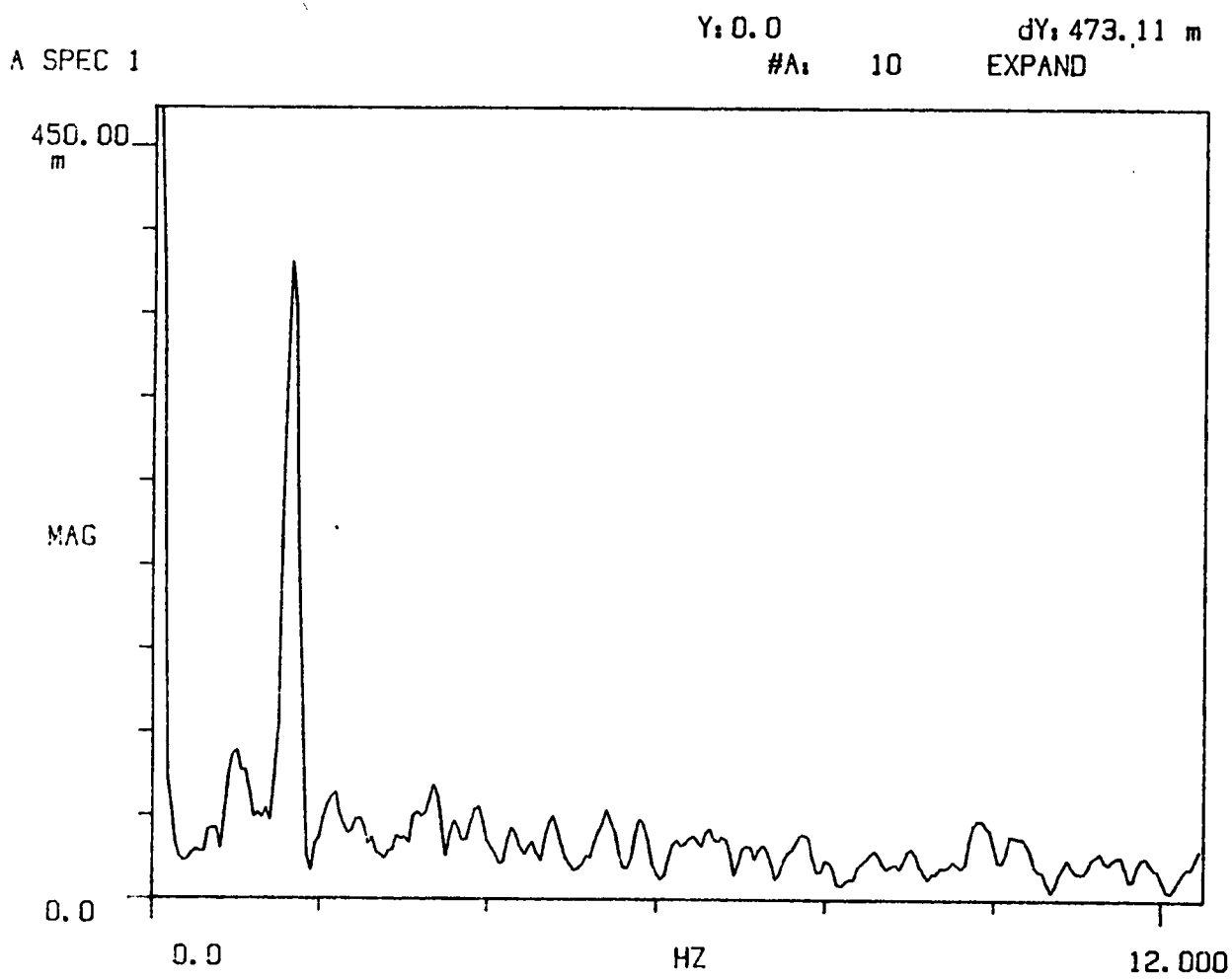

Figure 4.42 Frequency content of LDV signal behind the third cylinder

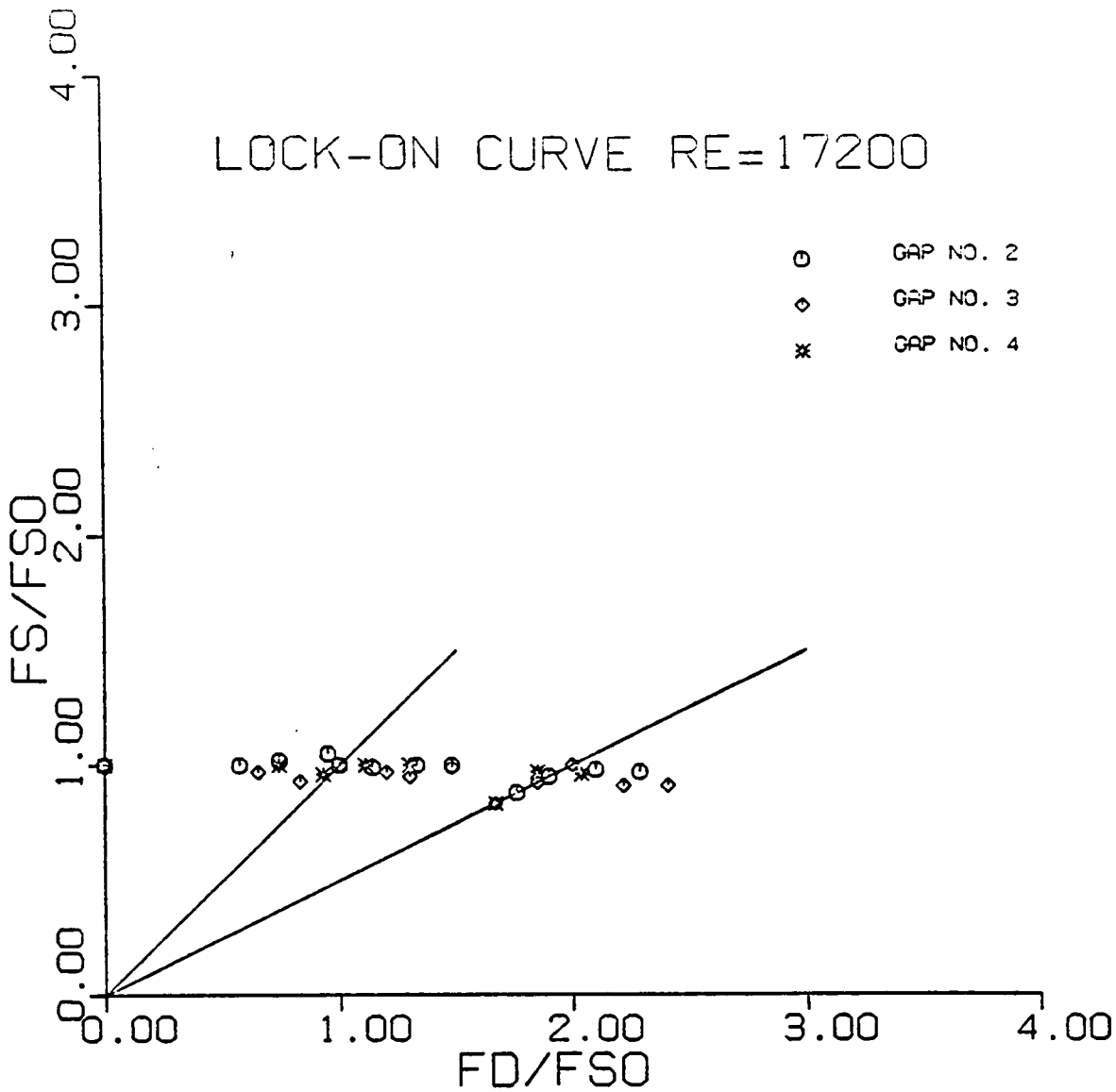

Figure 4.43 Lock on curve for the cavity regions

a well defined lock-on to the subharmonic of the driving frequency in all of the three cases. Hence, driving at twice the shedding frequency is expected to activate and organize the shedding characteristics of the flow in the gaps, which in turn could result in increased heat transfer rates. Figure 4.44 shows lock-on curves for the third gap at different Reynolds numbers. Lock-on is observed again at the subharmonic of the driving frequency for Reynolds numbers of 17,200 and 47,200. Away from the center of the gap, the flowfield is smoother owing to the organized shedding. A power spectrum of the velocity fluctuation in the center of the gap is shown in figure 4.45. As expected, the flow in this region does not show organization and there is a lot of turbulence. Figure 4.46 shows the plot of mean velocity vectors for the third gap. No velocity data could be found in the literature for comparison.

Figure 4.47 displays some typical instantaneous flow visualization photographs. Flow was visualized using particles and dyes. The flow visualization indicates that the first gap contains two standing vortices and the flow in this region resembles cavity flow. Vortices are shed from all the cylinders except the first. Vortices shed from an intermediate cylinder reattach onto the next cylinder alternately at the top and the bottom. A schematic representation of the flowfield is shown in figure 4.48. It can be observed that the velocity data obtained agree with the results of flow visualization.

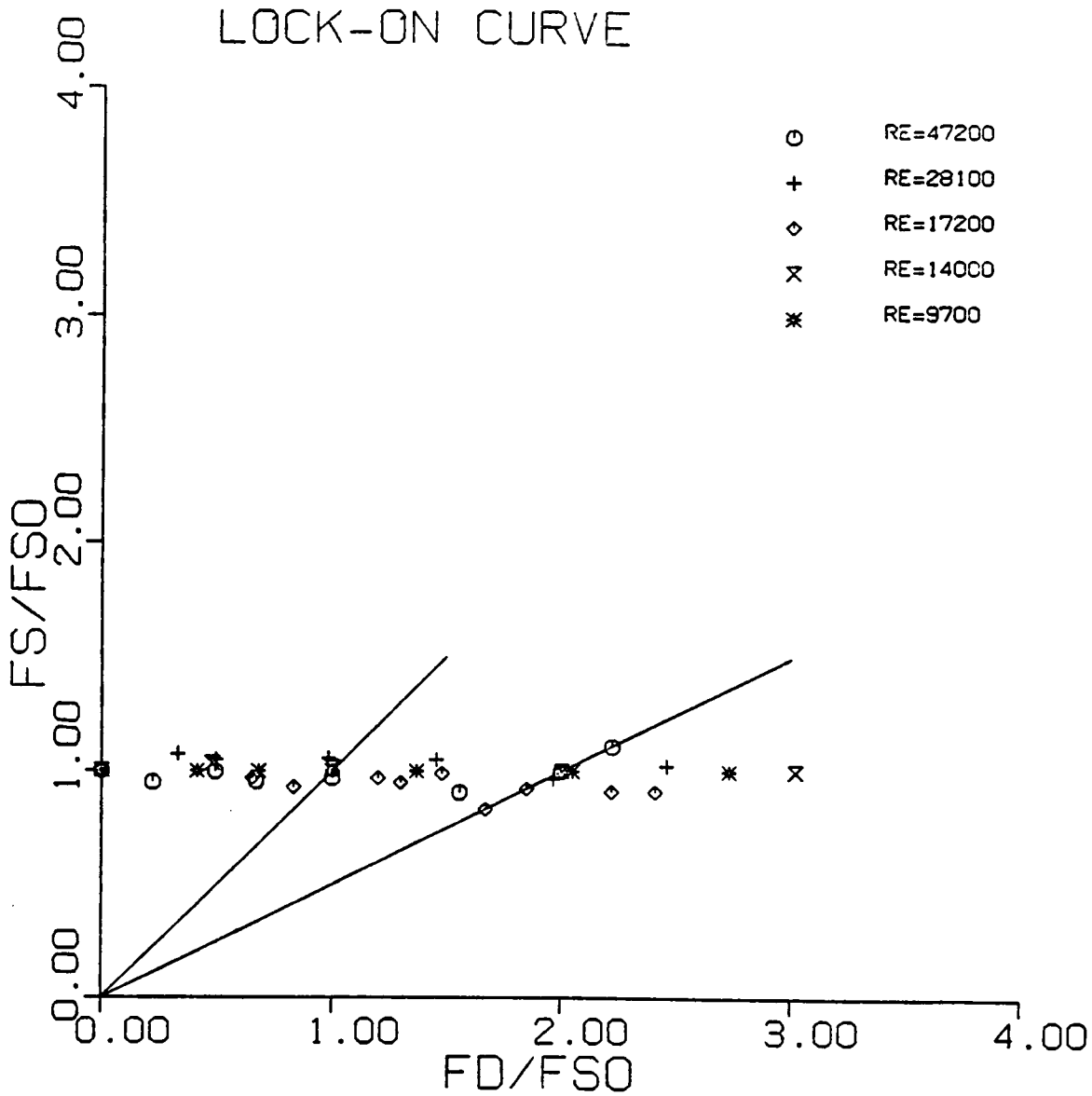

Figure 4.44 Lock-on curve at various Re for the third gap

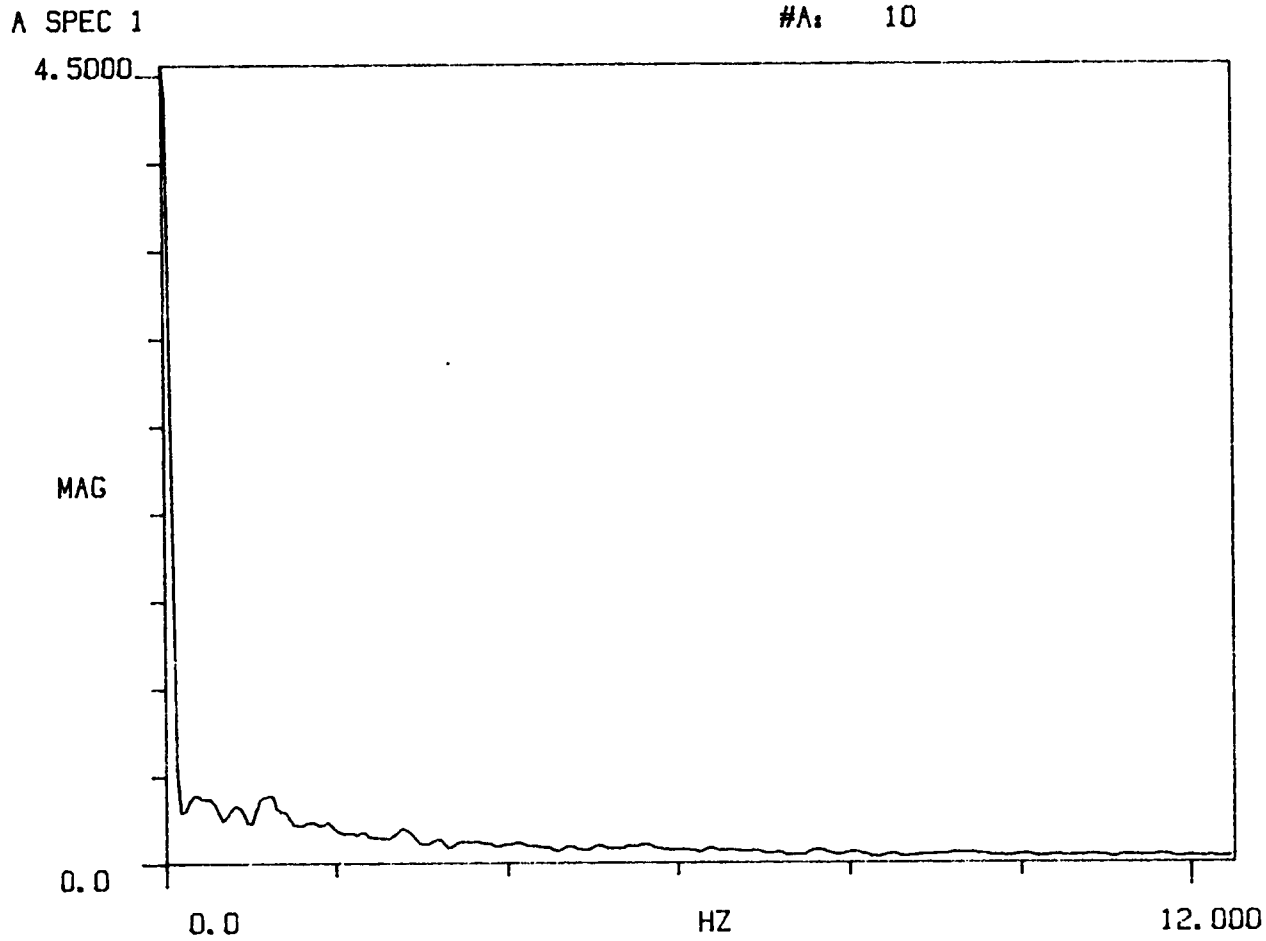

Figure 4.45 Power spectrum of velocity fluctuation in the center of the third gap

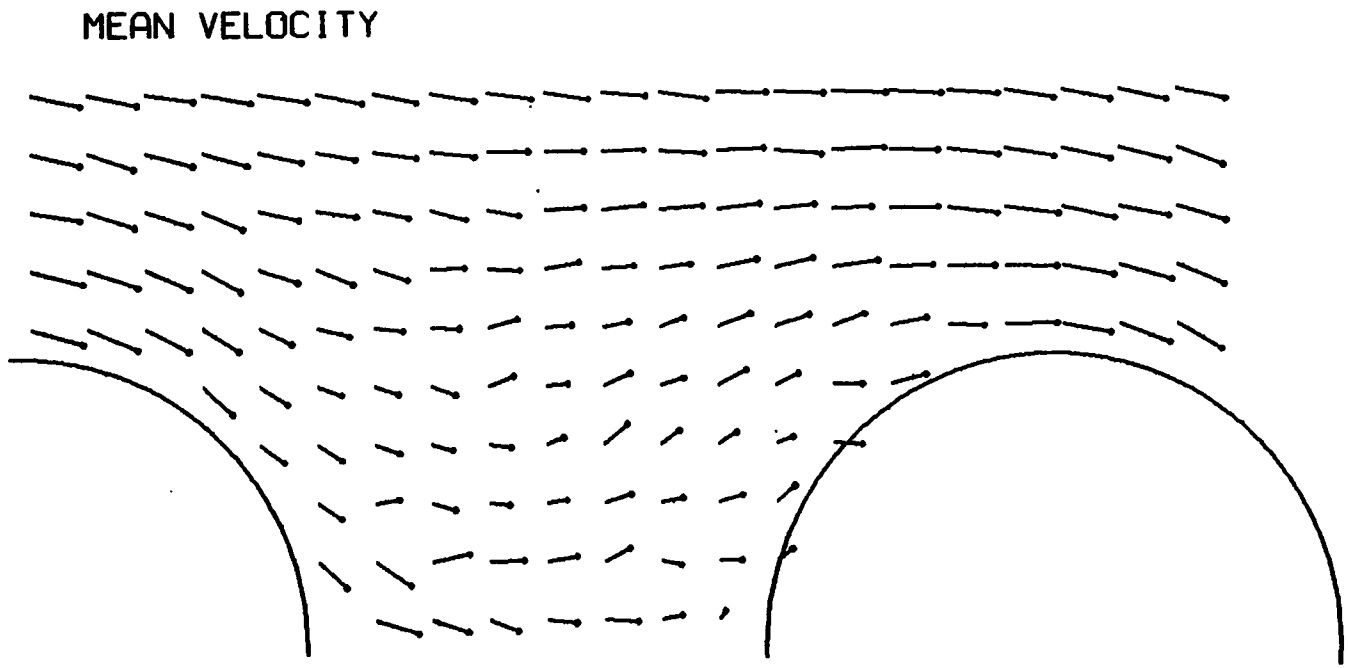

Figure 4.46 Mean velocity vectors for the third gap

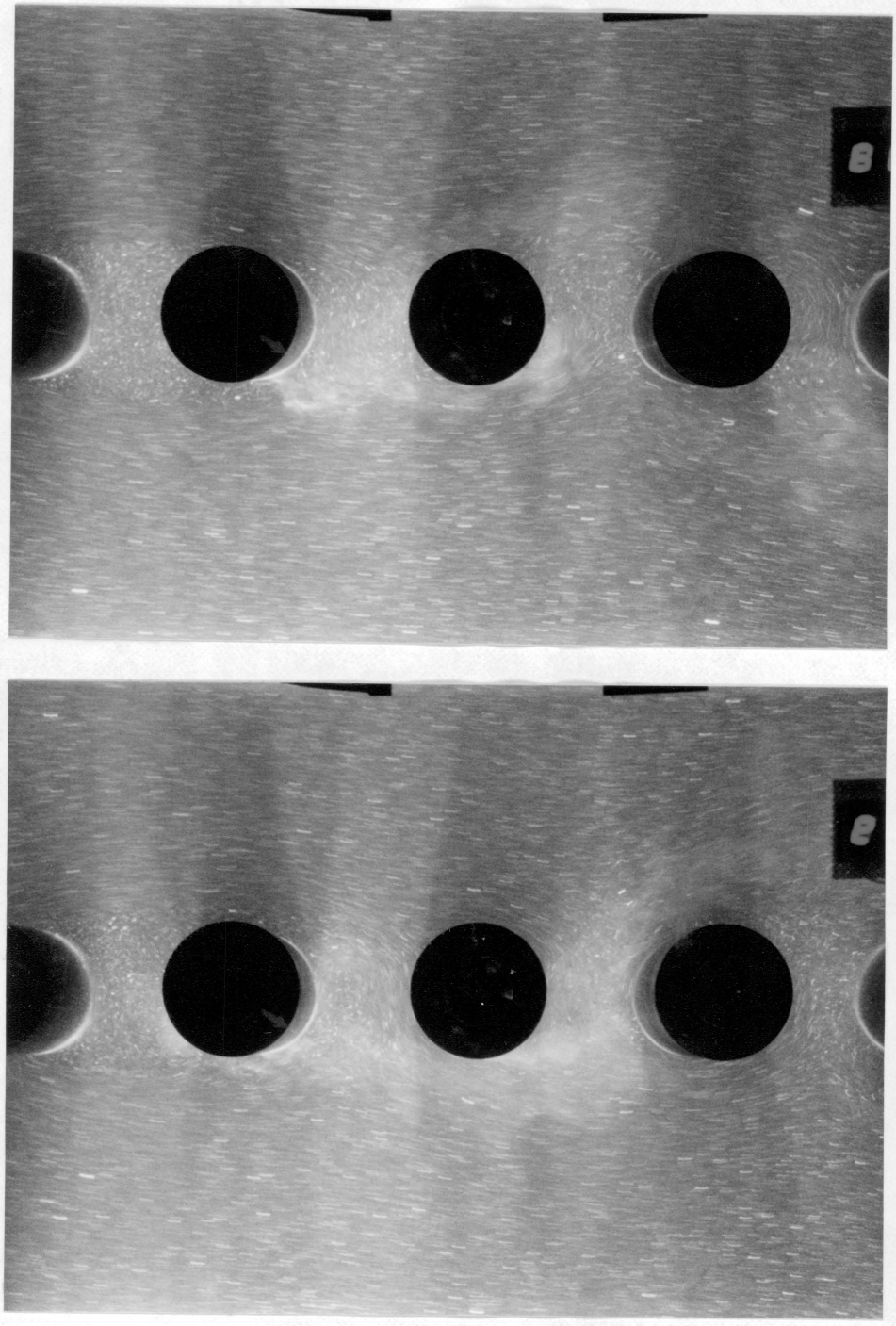

Figure 4.47a Typical instantaneous flow visualization photographs

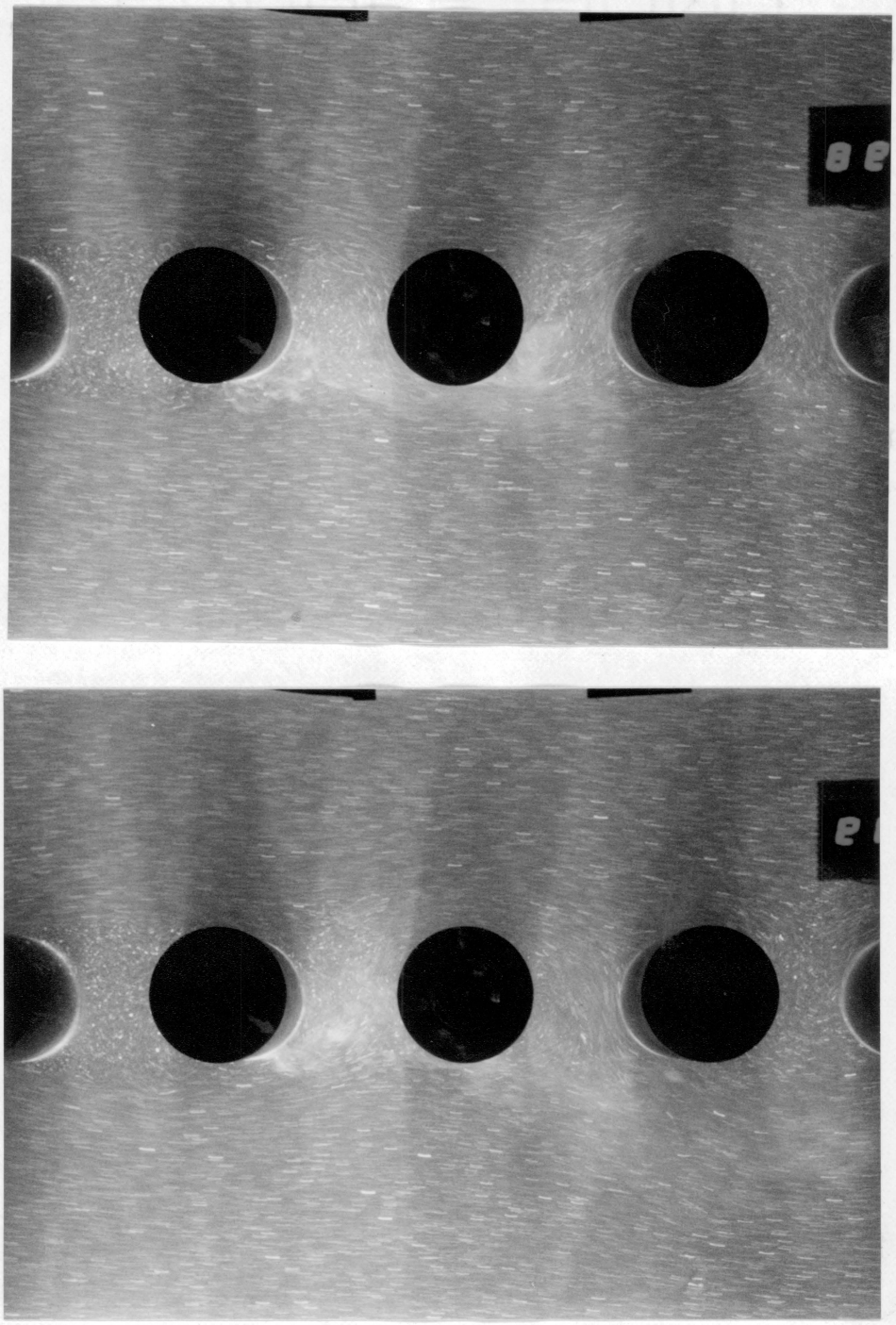

Figure 4.47b Typical instantaneous flow visualization photographs

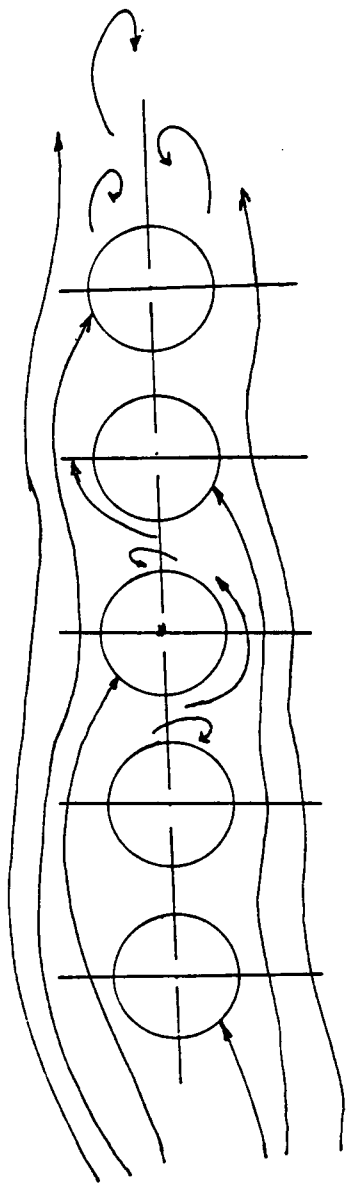

Figure 4.48 Schematic of the flow field for five cylinders (P/D = 1.8)

CHAPTER V

THEORY AND FINITE ELEMENT ANALYSIS

5.1 INTRODUCTION

Flow past a single cylinder is of fundamental importance in aerodynamics and hydrodynamics. The hydrodynamic and heat transfer characteristics of fluid flow around multiple cylinders are of interest in the design of heat exchangers, boilers, condensers, nuclear reactors etc.. The Navier-Stokes equations governing viscous flows are highly nonlinear. An analytical solution of the Navier-Stokes equations is possible only for a few cases of very simple configurations. A number of researchers have numerically solved the Navier-Stokes equations for the flow past a single cylinder numerically. Finite difference methods have been employed to calculate flow past a single cylinder. Finite element analysis has recently gained popularity. Despite the availability of modern powerful computers, the time-dependent solutions of the Navier-Stokes equations for flow past cylinders is still very expensive and different techniques are being sought continuously for better efficiency. The amount of computer time involved in obtaining vortex shedding from a circular cylinder virtually necessitates the use

of supercomputers. High-Reynolds-number flows pose additional difficulty owing to the need for very refined grids near the cylinder walls.

In this chapter, the finite element method as applied to the problem of fluid mechanics and heat transfer of flow past cylinders is discussed. A single cylinder, three and five cylinders in a row and in-line and staggered bundles of cylinders in cross flow are considered. Because of the insufficient time allotted on the CRAY computer, the time dependent problems reported here are only a part of an ongoing research.

5.2 SURVEY OF LITERATURE

Numerical analysis of flow past a single cylinder has been carried out by numerous researchers. Finite-difference analyses include solutions of the boundary layer equations, the potential flow equation and the Navier-Stokes equations. Solutions of the Navier-Stokes equations for flow past a single cylinder have been presented by Kawaguti [1953], Son and Hanratty [1969], Dennis and Chang [1970], Jordan and Fromm [1972], Swanson and Spalding [1978], Kawamura and Kuwahara [1984]. Finite difference solution of flow past three and five cylinders in a row is not available. Some numerical studies using the finite difference method for fluid flow and heat transfer across a bundle of cylinders have appeared recently. LeFeuvre [1973] obtained a finite-difference solution for an in-line bank with uniform tube wall temperature. Launder and Massey [1978] obtained a finite-difference solution for an inner row of staggered

tube bank with the assumption of uniform wall heat flux. Fujii et al. [1984] used the one-step-forward half-step-backward iteration hybrid finite difference method to solve the stream function-vorticity and energy equations for a five row in-line tube bank. Antonopoulos [1985] used a finite difference method to solve the transport equations in curvilinear coordinates for turbulent inclined flow past an interior region of a tube bank.

The finite element method allows suitable representation of the complicated geometry of multiple cylinders without having to use curvilinear coordinates or mapping. Moreover, proper boundary conditions of the flow can be imposed in a natural way. Finite-element simulations of flow past a single cylinder have been presented by Kawahara and Hirano [1983], Gresho et al. [1984], Brooks and Hughes [1982], Benque et al. [1983], Smith and Brebbia [1977], Glowinski et al. [1978] and Bristeau et al. [1978]. Penalty-finite-elemnet analyses of fluid flow and heat transfer around in-line and staggered bundles of cylinders have been presented by the auther's group [Dhaubhadel et al., 1986A, Dhaubhadel et al., 1986B]. The detailed results are included in chapter 6.

5.3 GOVERNING EQUATIONS

For two-dimensional laminar flow of an incompressible fluid with negligible viscous dissipation, the Navier-Stokes equations and the energy equation can be written as

$$\frac{\partial u}{\partial t} + u\frac{\partial u}{\partial x} + v\frac{\partial u}{\partial y} = 2\nu\frac{\partial^2 u}{\partial x^2} + \nu\frac{\partial}{\partial y}\left(\frac{\partial u}{\partial y} + \frac{\partial v}{\partial x}\right) - \frac{1}{\rho}\frac{\partial p}{\partial x} + \frac{1}{\rho}f_x \qquad [5.3.1]$$

$$\frac{\partial v}{\partial t} + u\frac{\partial v}{\partial x} + v\frac{\partial v}{\partial y} = \nu\frac{\partial}{\partial x}\left(\frac{\partial u}{\partial y} + \frac{\partial v}{\partial x}\right) + 2\nu\frac{\partial^2 v}{\partial y^2} - \frac{1}{\rho}\frac{\partial p}{\partial y} + \frac{1}{\rho}f_y \qquad [5.3.2]$$

$$\frac{\partial u}{\partial x} + \frac{\partial v}{\partial y} = 0 \qquad [5.3.3]$$

$$\frac{\partial T}{\partial t} + u\frac{\partial T}{\partial x} + v\frac{\partial T}{\partial y} = \alpha\left(\frac{\partial^2 T}{\partial x^2} + \frac{\partial^2 T}{\partial y^2}\right) \qquad [5.3.4]$$

where (u,v), p, (f_x, f_y), ρ , ν, T and α denote the velocity components, pressure, body force components, density, kinematic viscosity, temperature and coefficient of diffusivity, respectively. These equations are nondimensionalized using the characteristic variables as below:

$$u^* = \frac{u}{u_\infty}, x^* = \frac{x}{L}, y^* = \frac{y}{L}, p^* = \frac{p}{\rho u_\infty^2}$$

$$f^* = \frac{f}{\rho u_\infty^2}, T^* = \frac{T - T_{in}}{T_w - T_{in}} = \theta \qquad [5.3.5]$$

where, u_∞ = characteristic velocity

L = characteristic length, taken as the diameter of cylinder

T_w = wall temperature

T_{in} = temperature at inlet

The equations in nondimensional form become

$$\frac{\partial u}{\partial t} + u\frac{\partial u}{\partial x} + v\frac{\partial u}{\partial y} = \frac{2}{Re}\frac{\partial^2 u}{\partial x^2} + \frac{1}{Re}\frac{\partial}{\partial y}\left(\frac{\partial u}{\partial y} + \frac{\partial v}{\partial x}\right) - \frac{1}{\rho}\frac{\partial p}{\partial x} + \frac{1}{\rho}f_x \quad [5.3.6]$$

$$\frac{\partial v}{\partial t} + u\frac{\partial v}{\partial x} + v\frac{\partial v}{\partial y} = \frac{1}{Re}\frac{\partial}{\partial x}\left(\frac{\partial u}{\partial y} + \frac{\partial v}{\partial x}\right) + \frac{2}{Re}\frac{\partial^2 v}{\partial y^2} - \frac{1}{\rho}\frac{\partial p}{\partial y} + \frac{1}{\rho}f_y \quad [5.3.7]$$

$$\frac{\partial u}{\partial x} + \frac{\partial v}{\partial y} = 0 \quad [5.3.8]$$

$$\frac{\partial \theta}{\partial t} + u\frac{\partial \theta}{\partial x} + v\frac{\partial \theta}{\partial y} = \frac{1}{RePr}\left(\frac{\partial^2 \theta}{\partial x^2} + \frac{\partial^2 \theta}{\partial y^2}\right) \quad [5.3.9]$$

where the asterisks have been omitted for brevity; Re denotes the Reynolds number, $\mathrm{Re} = \frac{U_\infty}{\nu}L$ and Pr denotes the Prandtl number, $\mathrm{Pr} = \frac{\nu}{\alpha}$

The equation for the stream function $\overline{\psi}$,

$$-\nabla^2\overline{\psi} = \zeta \quad [5.3.10]$$

with appropriate boundary conditions is solved to obtain the streamlines. Here $\zeta = \left(\frac{\partial u}{\partial y} - \frac{\partial v}{\partial x}\right)$ denotes the vorticity, which is post-computed from the velocity field.

5.4 VARIATIONAL FORMULATION AND PENALTY FINITE ELEMENT MODEL

Because the continuity equation does not contain the pressure term, it can be viewed as a constraint on the velocity field given by the momentum equations. The variational problem associated with the penalty function method [see Reddy 1982a, 1982b, 1983] corresponding to equations (5.3.6-5.3.8) is formulated as follows

$$0 = \int_{\Omega^e}[w_1(u\frac{\partial u}{\partial x} + v\frac{\partial u}{\partial y}) + \frac{2}{Re}\frac{\partial w_1}{\partial x} + \frac{1}{Re}\frac{\partial w_1}{\partial y}(\frac{\partial u}{\partial y} + \frac{\partial v}{\partial x}) - w_1 f_y]dxdy$$

$$+ \int_{\Omega^e}\gamma\frac{\partial w_1}{\partial x}(\frac{\partial u}{\partial x} + \frac{\partial v}{\partial y})dxdy$$

$$- \int_{\Gamma^e}w_1[(\frac{2}{Re}\frac{\partial u}{\partial x} - P)n_x + \frac{1}{Re}(\frac{\partial u}{\partial y} + \frac{\partial v}{\partial x})n_y]ds \qquad [5.4.1]$$

$$0 = \int_{\Omega^e}[w_2(u\frac{\partial v}{\partial x} + v\frac{\partial v}{\partial y}) + \frac{1}{Re}\frac{\partial w_2}{\partial x}(\frac{\partial u}{\partial y} + \frac{\partial v}{\partial x}) + \frac{2}{Re}\frac{\partial w_2}{\partial y}\frac{\partial v}{\partial y} - w_2 f_y]dxdy$$

$$+ \int_{\Omega^e}\gamma\frac{\partial w_2}{\partial y}(\frac{\partial u}{\partial x} + \frac{\partial v}{\partial y})dxdy$$

$$- \int_{\Gamma^e}w_2 + \frac{1}{Re}(\frac{\partial u}{\partial y} + \frac{\partial v}{\partial x})n_x + [(\frac{2}{Re}\frac{\partial v}{\partial y} - P)n_y]ds \qquad [5.4.2]$$

where ω is the problem domain with boundary γ, superscript e indicates that the quantities are for a typical finite element, w_1 and w_2 are the weight functions

associated with u and v, respectively, γ is the penalty parameter, n_x and n_y are direction cosines. The coefficients of w_1 and w_2 in the boundary integrals of equations (5.4.1) and (5.4.2) are denoted by t_x and t_y, respectively. The variational formulation of energy and stream function-vorticity equations are given by

$$0 = \int_{\Omega^e}\left[w_3\left(u\frac{\partial\theta}{\partial x} + v\frac{\partial\theta}{\partial y}\right) + \frac{1}{RePr}\left(\frac{\partial w_3}{\partial x}\frac{\partial\theta}{\partial x} + \frac{\partial w_3}{\partial y}\frac{\partial\theta}{\partial y}\right)\right]dxdy$$

$$- \int_{\Gamma^e} w_3\left(\frac{\partial\theta}{\partial x}n_x + \frac{\partial\theta}{\partial y}n_y\right)ds \qquad [5.4.3]$$

$$0 = \int_{\Omega^e}\left(\frac{\partial w_4}{\partial x}\frac{\partial\overline{\psi}}{\partial x} + \frac{\partial w_4}{\partial y}\frac{\partial\overline{\psi}}{\partial y} - w_4\zeta\right)dxdy$$

$$- \int_{\Gamma^e} w_4\left(\frac{\partial\overline{\psi}}{\partial x}n_x + \frac{\partial\overline{\psi}}{\partial y}n_y\right)ds \qquad [5.4.4]$$

where w_3 and w_4 denote the weight functions associated with θ and $\overline{\psi}$, respectively.

Let the dependent variables u, v, θ and $\overline{\psi}$ be interpolated over a typical element by expressions of the form,

$$u = \sum_{j=1}^{n} u_j\psi_j, \quad v = \sum_{j=1}^{n} v_j\psi_j,$$

$$\theta = \sum_{j=1}^{n} \theta_j\psi_j, \quad \overline{\psi} = \sum_{j=1}^{n} \overline{\psi}_j\psi_j \qquad [5.4.5]$$

where ψ_j are the finite-element interpolation functions, u_j , v_j, θ_j and $\overline{\psi}_j$ are the nodal values of u, v, θ and $\overline{\psi}$, respectively and n denotes the number of nodes in the element.

Substituting equation (5.4.5) into the variational equations (5.4.1) and (5.4.2), we obtain

$$\sum_{j=1}^{n} \overline{K}_{ij}^{11} u_j + \sum_{j=1}^{n} \overline{K}_{ij}^{12} v_j - F_i^1 = 0, i = 1, 2, \ldots\ldots, n \qquad [5.4.6]$$

$$\sum_{j=1}^{n} \overline{K}_{ij}^{21} u_j + \sum_{j=1}^{n} \overline{K}_{ij}^{22} v_j - F_i^2 = 0, i = 1, 2, \ldots\ldots, n \qquad [5.4.7]$$

or, in matrix form we have

$$\begin{bmatrix} [\overline{K}^{11}] & [\overline{K}^{12}] \\ [\overline{K}^{12}] & [\overline{K}^{22}] \end{bmatrix} \begin{Bmatrix} u \\ v \end{Bmatrix} = \begin{Bmatrix} F_1 \\ F_2 \end{Bmatrix} \qquad [5.4.8]$$

Equations (5.4.3) and (5.4.4) similarly can be written in matrix form as follows

$$[K^I]\{\theta\} = \{F_\theta\} \qquad [5.4.9]$$

$$[K^{II}]\{\overline{\psi}\} = \{F_{\overline{\psi}}\} \qquad [5.4.10]$$

where,

$$[\overline{K}^{11}] = [K^{11}] + [G] + \gamma[S^{11}]$$

$$[\overline{K}^{12}] = [K^{12}] + \gamma[S^{12}]$$

$$[\bar{K}^{21}] = [K^{21}] + \gamma[S^{21}]$$

$$[\bar{K}^{22}] = [K^{22}] + [G] + \gamma[S^{22}]$$

$$[K^{11}] = \frac{2}{Re}[S^{11}] + \frac{1}{Re}[S^{22}]$$

$$G_{ij} = \int_{\Omega^e} \psi_i (u_o \frac{\partial \psi_j}{\partial x} + v_o \frac{\partial \psi_j}{\partial y}) dxdy$$

$$S_{ij}^{11} = \int_{\Omega^e} \frac{\partial \psi_i}{\partial x} \frac{\partial \psi_j}{\partial x} dxdy$$

$$S_{ij}^{22} = \int_{\Omega^e} \frac{\partial \psi_i}{\partial y} \frac{\partial \psi_j}{\partial y} dxdy$$

$$[K^{12}] = [K^{21}]^T = \frac{1}{Re}[S^{12}]^T$$

$$S_{ij}^{12} = \int_{\Omega^e} \frac{\partial \psi_i}{\partial x} \frac{\partial \psi_j}{\partial y} dxdy$$

$$[K^{22}] = [S^{11}] + \frac{2}{Re}[S^{22}]$$

$$F_i^1 = \int_{\Omega^e} f_x \psi_i dxdy + \int_{\Gamma^e} t_x \psi_i ds$$

$$F_i^2 = \int_{\Omega^e} f_y \psi_i dxdy + \int_{\Gamma^e} t_y \psi_i ds$$

$$[K^I] = \frac{1}{RePr}\{[S^{11}] + [S^{22}]\} + [G]$$

$$F_i^{\theta} = \int_{\Gamma_e} \psi_i t_\theta ds$$

$$[K^{II}] = [S^{11}] + [S^{22}]$$

$$F_i^{\overline{\psi}} = -\int_{\Omega_e} \psi_i \zeta dx dy + \int_{\Gamma_e} \psi_i t_{\overline{\psi}} ds \qquad [5.4.11]$$

and where u_o and v_o are velocities from a previous iteration.

From convergence and stability considerations (see Reddy, 1986) reduced integration technique is to be used to evaluate the penalty terms (i.e. coefficients of γ). For the bilinear element (n = 4) used in the present investigation, a 2 × 2 Gauss quadrature is used to evaluate all coefficient matrices except the penalty terms, for which a 1 × 1 quadrature is employed. Because of the presence of the convective terms, the coefficient matrices for the Navier-Stokes equations are not symmetric and an iterative procedure is required to handle the nonlinear convective terms. For the first iteration, the velocity field is set to zero everywhere, except at the boundaries, where boundary conditions are employed. The solution of the assembled equations (5.4.8) is obtained after specifying the known velocity (and gradient) boundary conditions by direct (Picard type) iteration. Convergence is assumed when the Euclidian norm for the velocities computed for two consecutive iterations is less than an error tolerance of 0.01 percent. The converged velocity field is used to solve the temperature equation (5.4.9) explicitly. Vorticity (velocity gradients) is computed from the velocity field

and subsequently, Poisson's equation for the stream-function (equation 5.4.10) is also solved.

CHAPTER VI

NUMERICAL RESULTS AND DISCUSSION

6.1 INTRODUCTION

Five cases of flow past cylinders are investigated by the Penalty Finite Element Method which is described in the previous chapter. Because of insufficient computer time currently available, unsteady cases could not be completed. Thus the results presented are mostly for steady two-dimensional laminar flows. The results are divided into five sections according to the type of the problem. The first section covers the flow past a single cylinder. The second section is on flow past three cylinders. The third section deals with flow past five cylinders in a row. The last two sections are devoted to the case of in-line and staggered bundles of cylinders in cross flow. Comparison with numerical and experimental results is made wherever possible.

6.2 FLOW PAST A SINGLE CYLINDER

A steady symmetric solution of flow past a cylinder at a Reynolds number of 100 is obtained. This problem was undertaken as a test case for a quick check

on the algorithm and no effort was made to study vortex shedding. Figure 6.1 shows the finite element and the boundary conditions. Figure 6.2 displays the velocity vectors for the flow field. Two symmetric vortices are seen in the back of the cylinder. Separation takes place around 110 degrees from the stagnation point. Location of separation point can also be judged from the skin friction and pressure distributions around the cylinder as shown in figures 6.3 and 6.4 respectively. The skin-friction coefficient has a value of zero at separation for the steady flow. The skin friction and pressure values agree well with the results of Brooks and Hughes [1982]. The coefficient of skin friction multiplied by the square root of Reynolds number has a higher peak value compared to the experimental result shown in figure 4.7. This is because of a lower Reynolds number used in the numerical analysis and the point of separation on the cylinder is further downstream for a lower Reynolds number. The distribution of coefficient of pressure has a pattern similar to the experimental result in figure 4.9. Figure 6.5 shows the distribution of local Nusselt number around the cylinder.

6.3 FLOW PAST A TRIAD OF CYLINDERS

Steady flow past three in-line cylinders with a pitch-to-diameter ratio of 1.8 is solved for a Reynolds number of 100. The time dependent problem was attempted for a Reynolds number of 10,000. The finite element mesh and the boundary conditions used are shown in figure 6.6. The velocity vector field

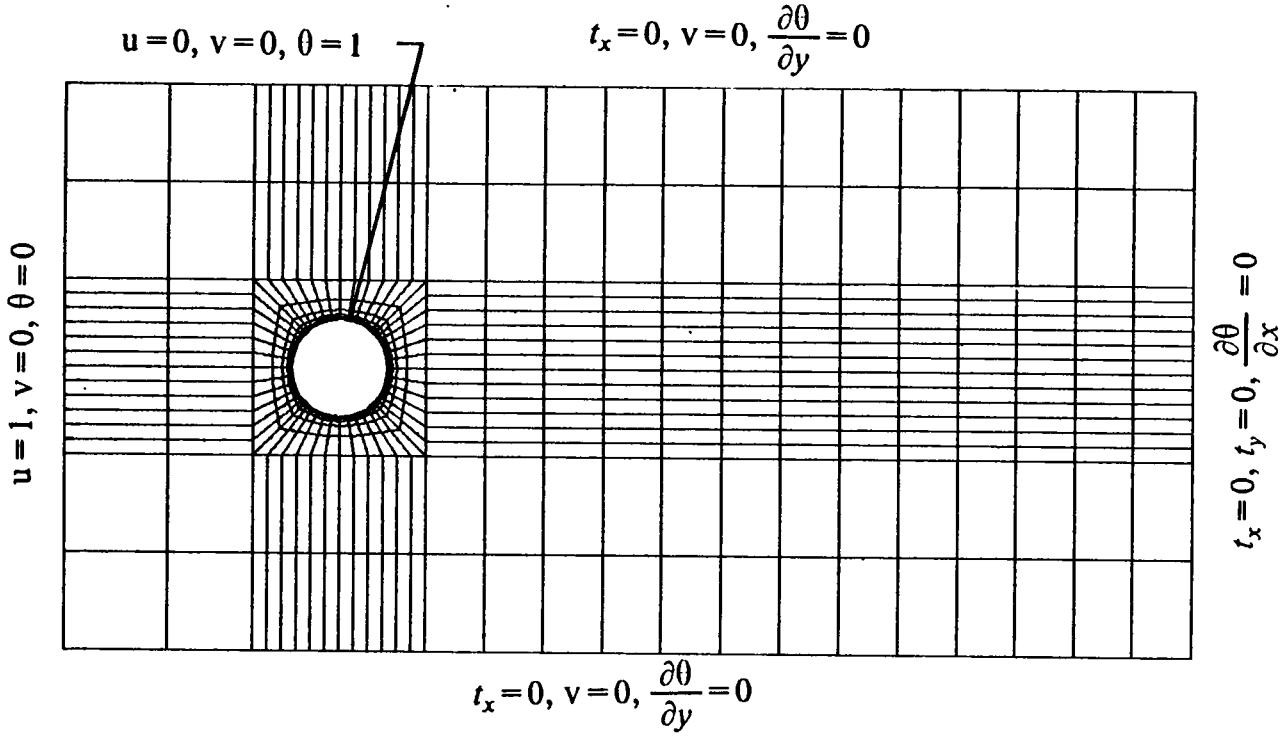

Figure 6.1 Finite element mesh and boundary conditions for flow past a single cylinder

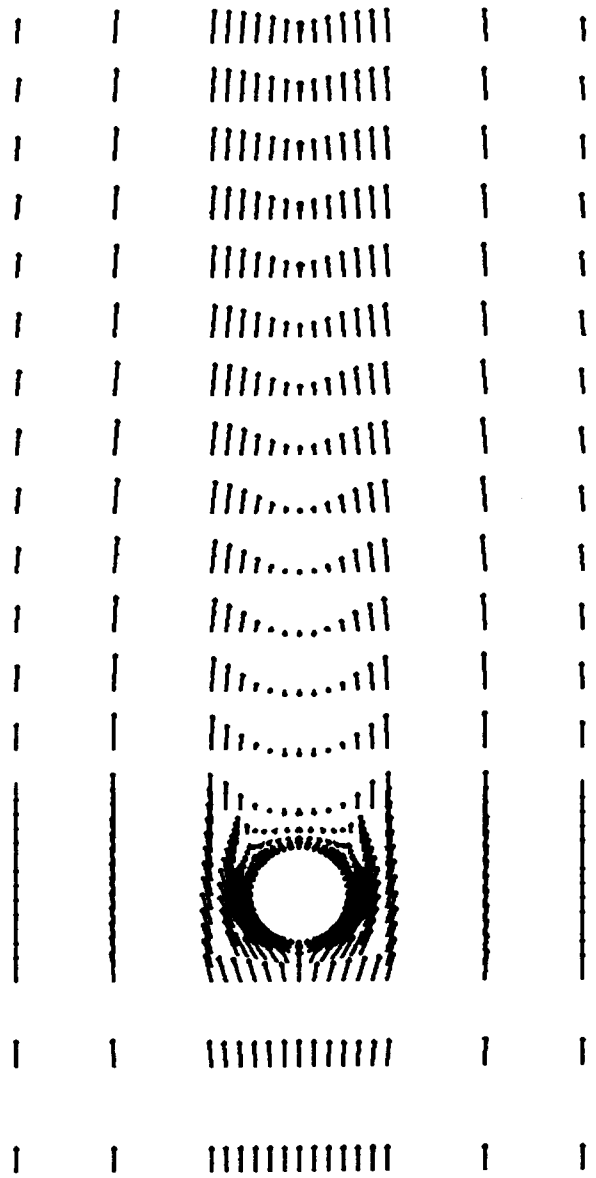

Figure 6.2 Velocity vectors for flow past a single cylinder, Re = 100

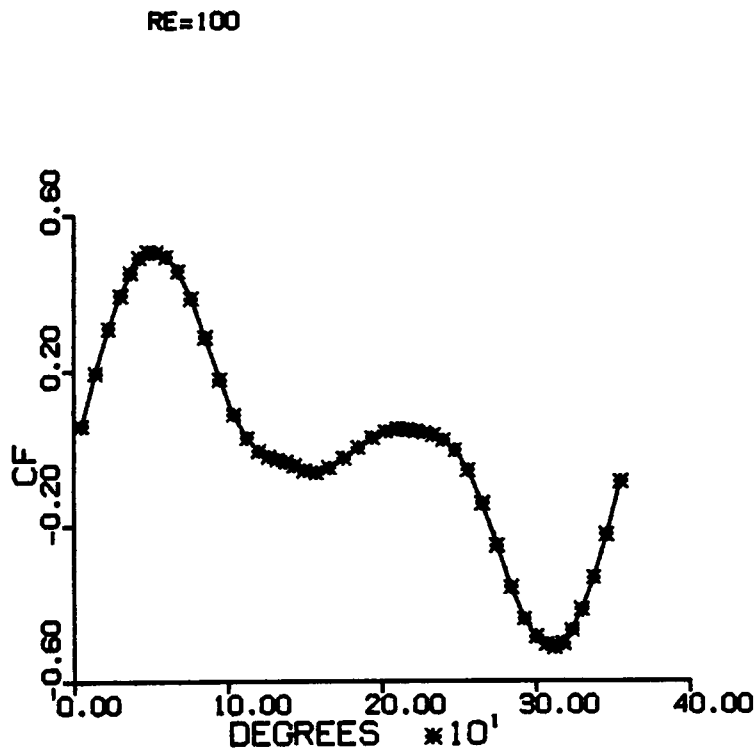

Figure 6.3 Skin friction distribution for flow past a single cylinder

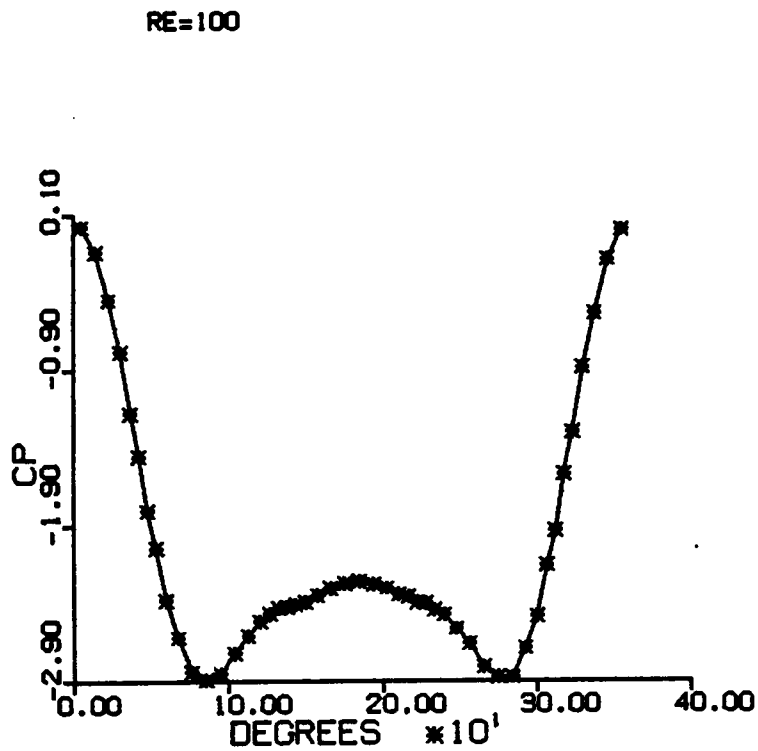

Figure 6.4 Pressure distribution for flow past a single cylinder

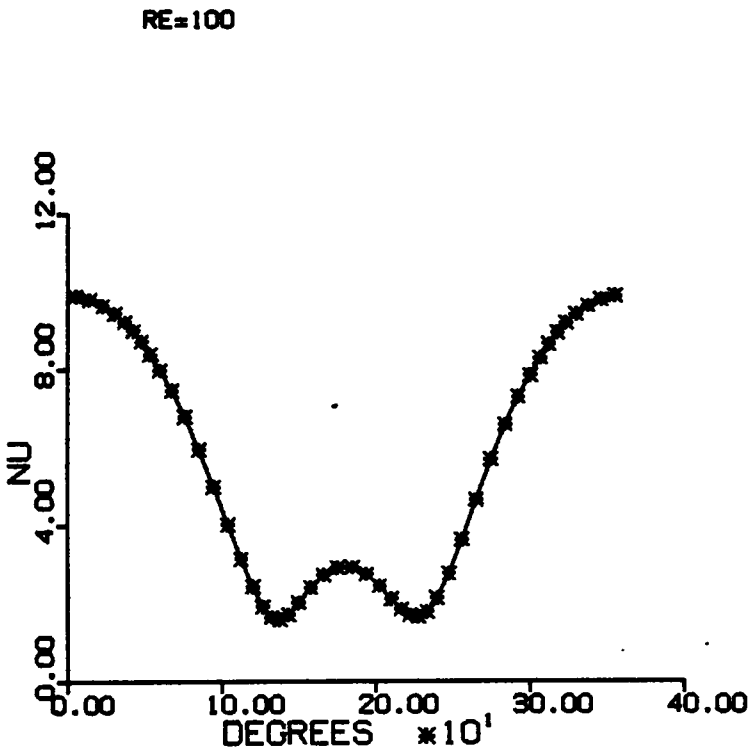

Figure 6.5 Local Nusselt number distribution for flow past a single cylinder

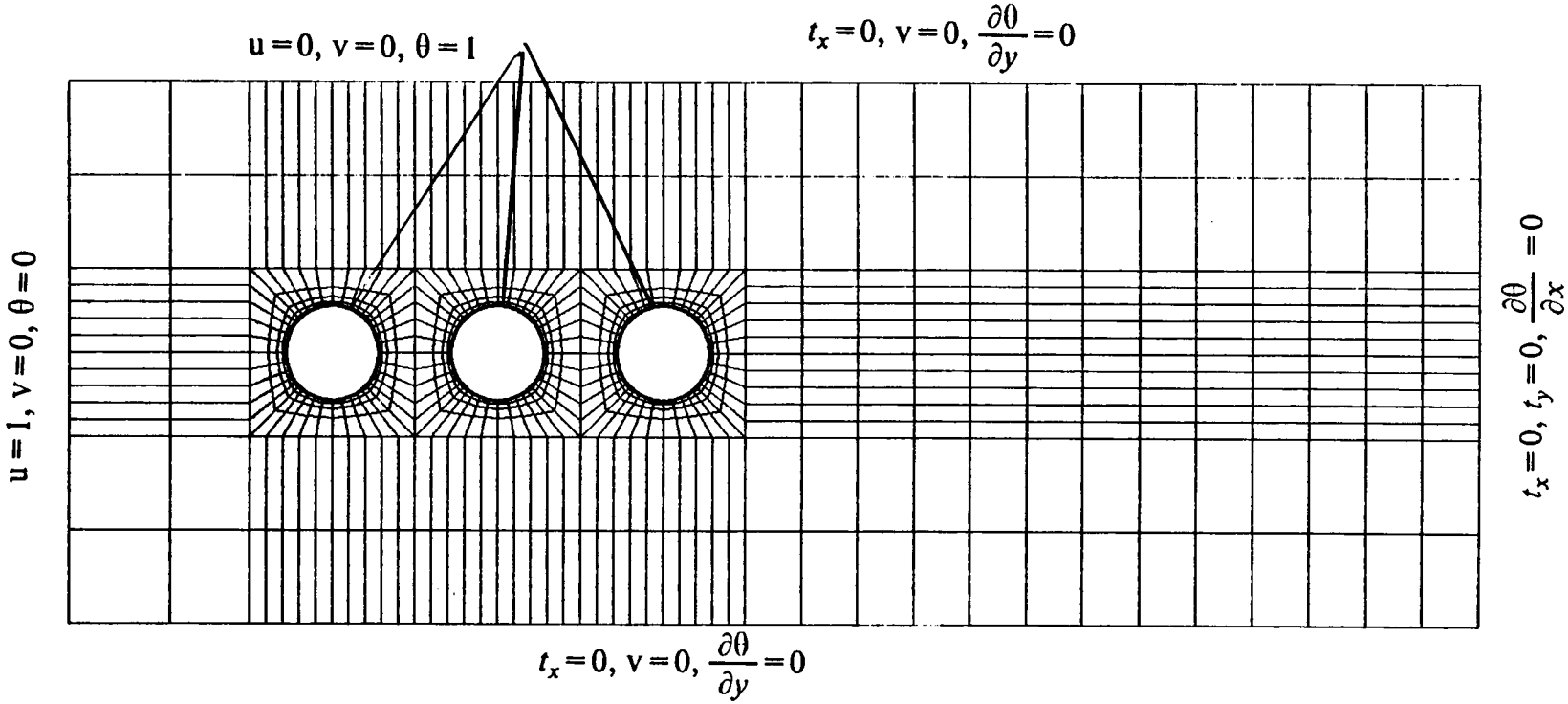

Figure 6.6 Finite element mesh and boundary conditions for flow past a triad of cylinders

obtained for the steady case is shown in figure 6.7. A typical run of the steady case at a Reynolds number of 100 takes approximately 50 seconds on CRAY-XMP. In the unsteady case at Reynolds number of 10,000, an artificial plate boundary near the top of the third cylinder was used with a view to trigger the shedding of vortices. The steady symmetric velocity field for Reynolds number of 100 shown in figure 6.7 was used as the initial condition. Figure 6.8 displays the velocity vector field after 2 time steps of 0.1. The artificial plate boundary was removed after 10 time steps. Figure 6.9 shows the velocity vectors obtained after the next 10 time steps. For a Reynolds number of 10,000 and 15 time steps each of 0.1 time units, the computer time (CPU + I/O) taken on CRAY-XMP was approximately 80 minutes and a lot more computer time would be needed before the formation of vortex shedding from the second cylinder can be observed. This problem is expected to be taken up soon with the availability of more computer time on the CRAY's. Figures 6.10, 6.11 and 6.12 show, respectively, the pressure distribution, the skin friction distribution and the Nusselt number distribution around the three cylinders at Re = 100.

6.4 FLOW PAST A PENTAD OF CYLINDERS

This problem is similar to the three cylinder case discussed above. Addition of two more cylinders requires more storage and hence more computational time. Figure 6.13 shows the finite element mesh and the boundary conditions. Figure 6.14 displays the velocity vectors for a steady flow at a

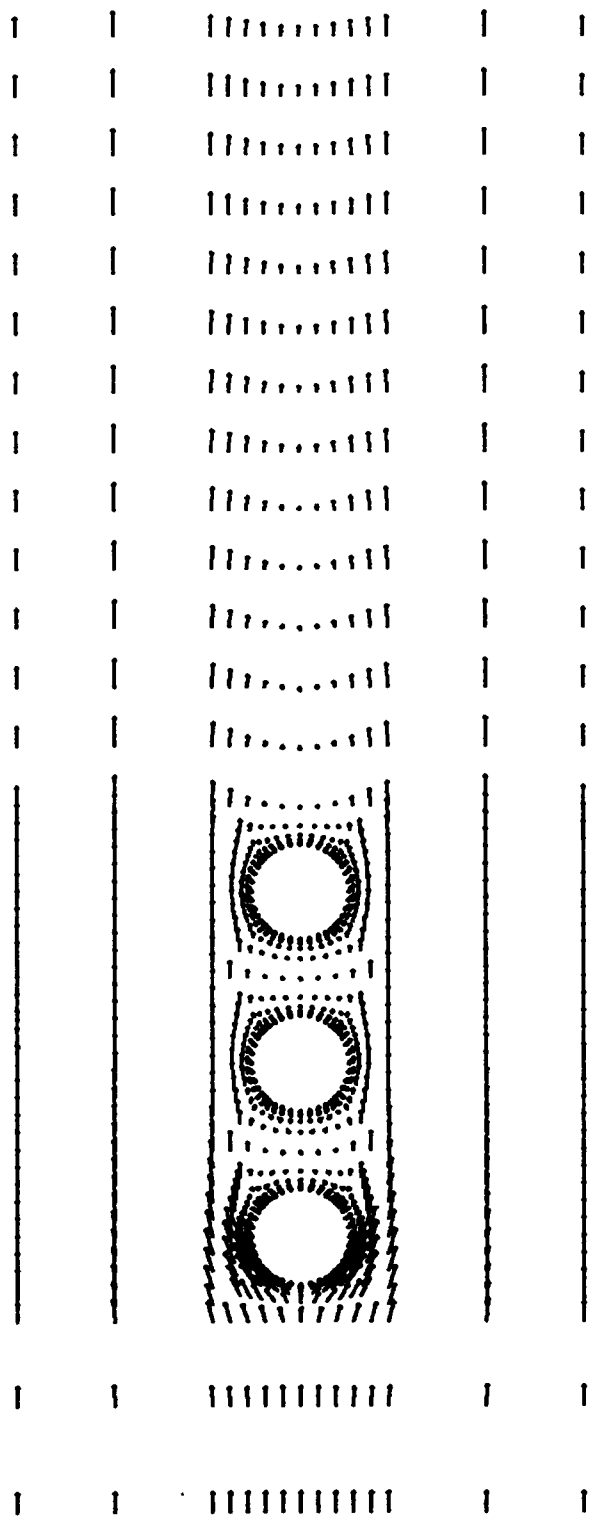

Figure 6.7 Velocity vectors for steady flow past a triad of cylinders at Re = 100

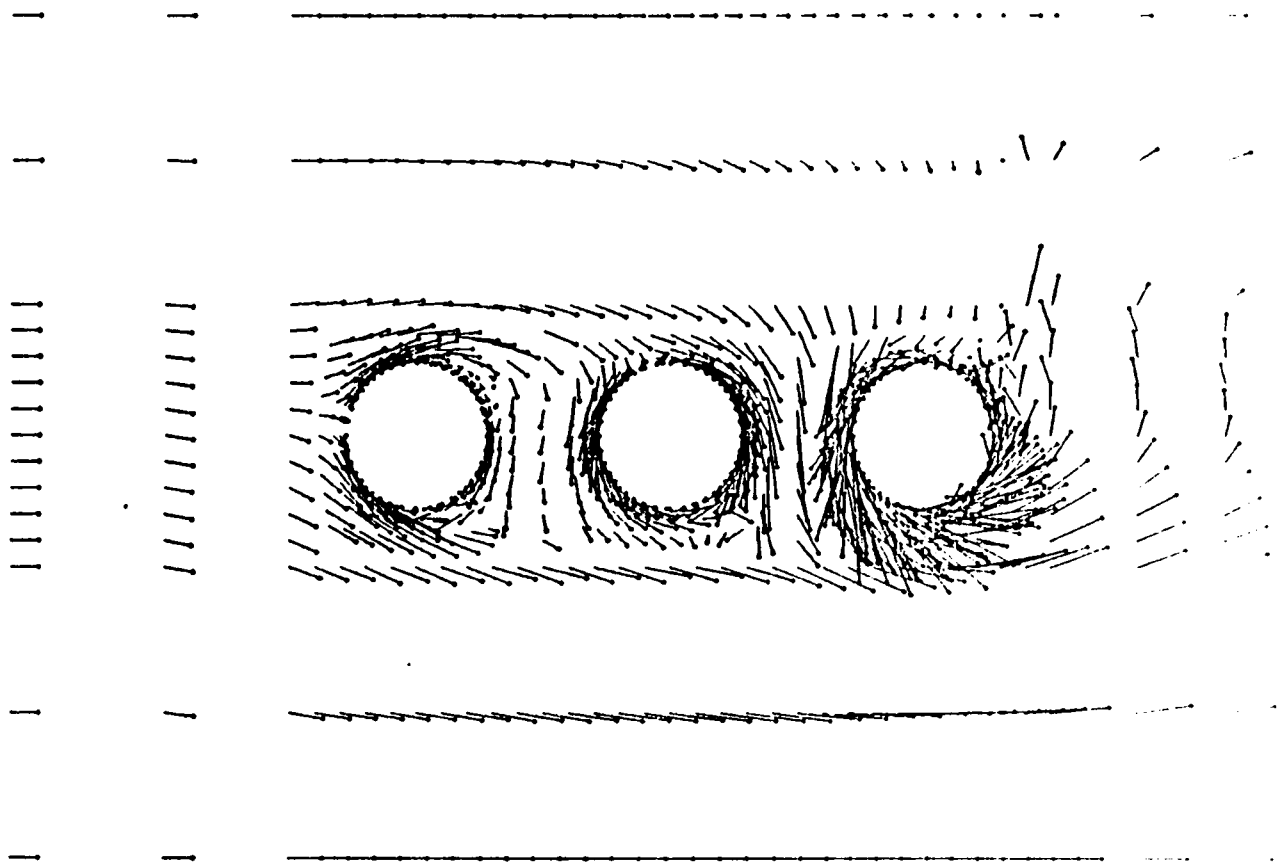

Figure 6.8 Velocity vectors for unsteady flow past a triad of cylinders at Re = 10000, time = 0.2 with plate boundary intact

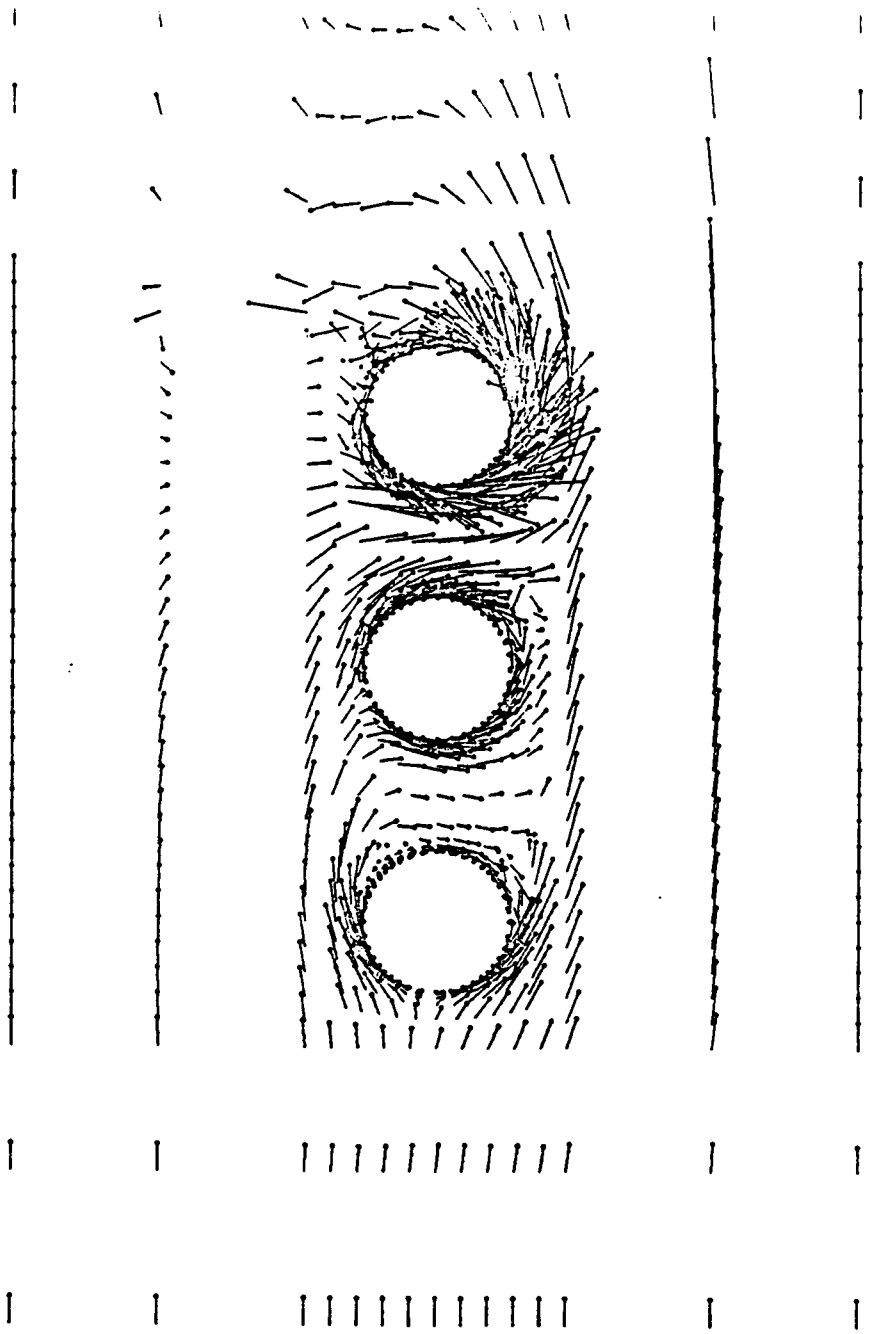

Figure 6.9 Velocity vectors for unsteady flow past a triad of cylinders at Re = 10000, time = 1.0

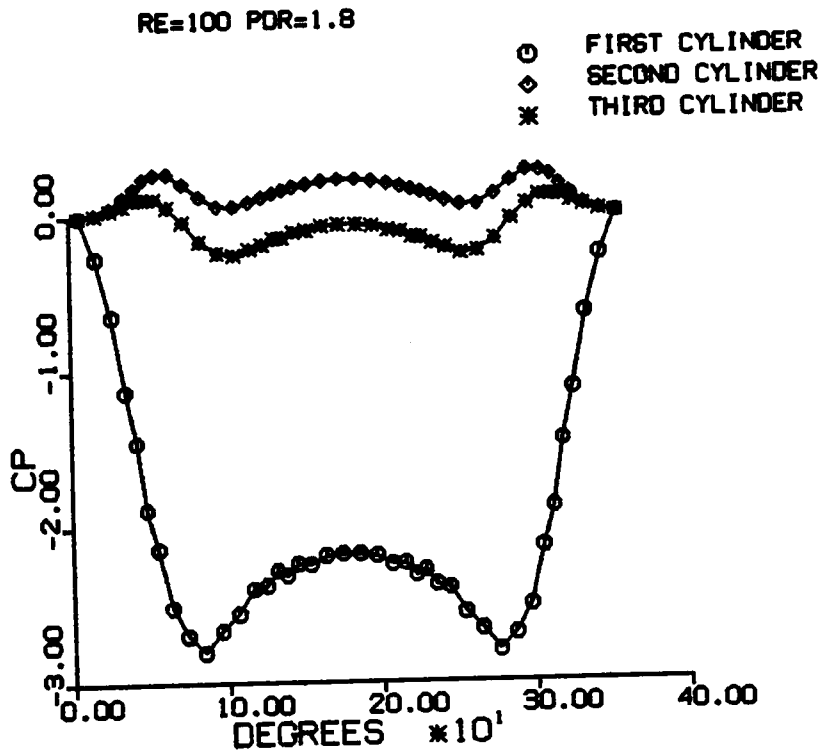

Figure 6.10 Pressure distribution for steady flow past a triad of cylinders, Re = 100

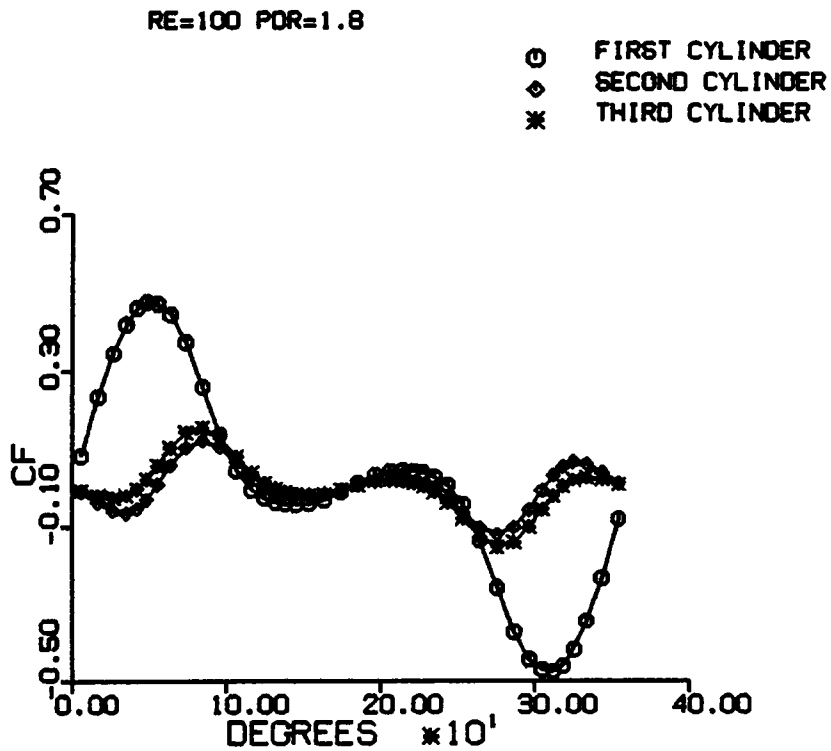

Figure 6.11 Skin friction distribution for steady flow past a triad of cylinders, Re = 100

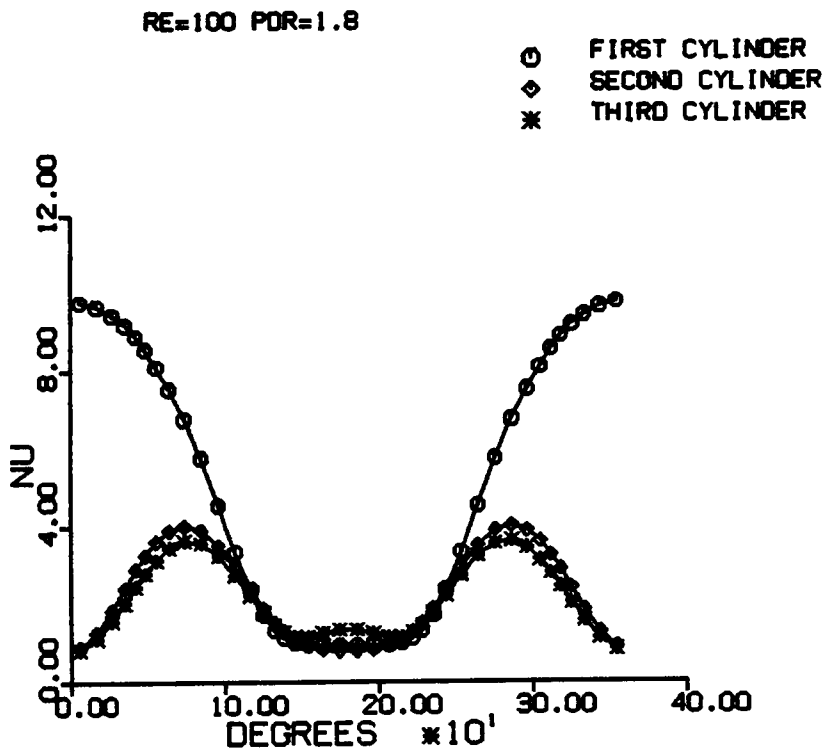

Figure 6.12 Local Nusselt number distribution for flow past a triad of cylinders

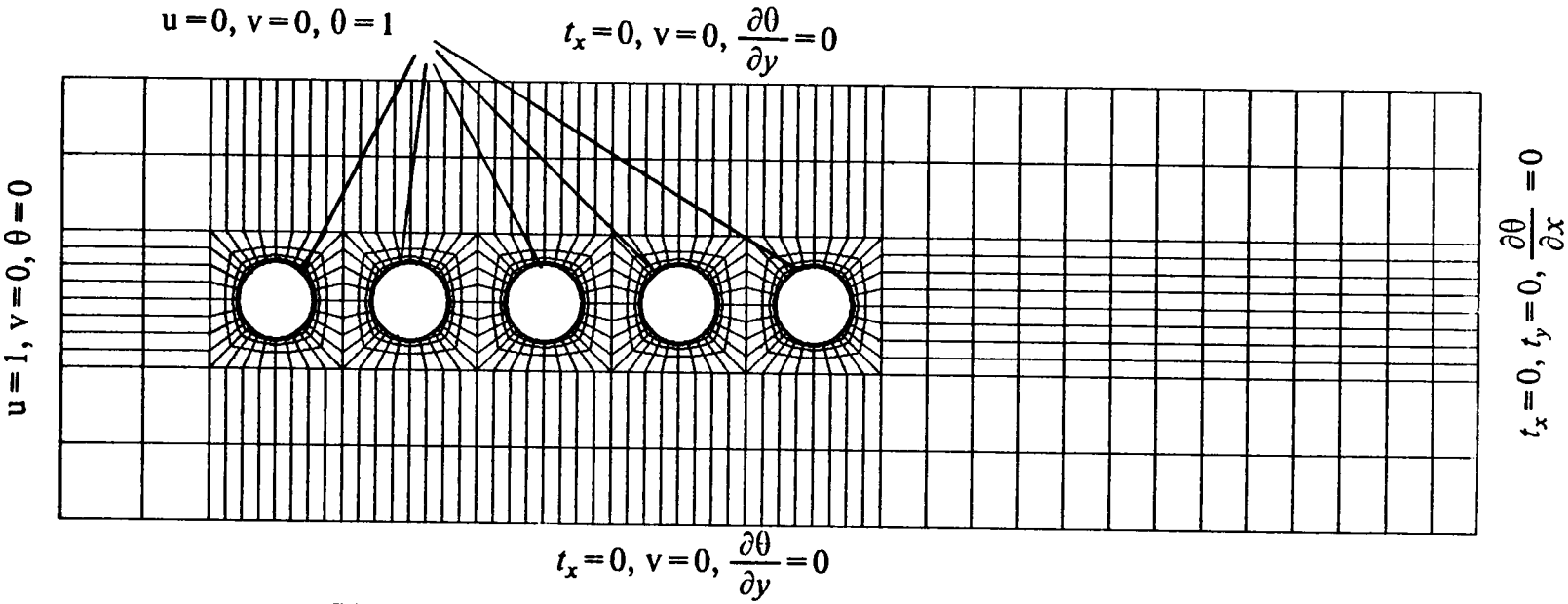

Figure 6.13 Finite element mesh and boundary conditions for flow past a pentad of cylinders

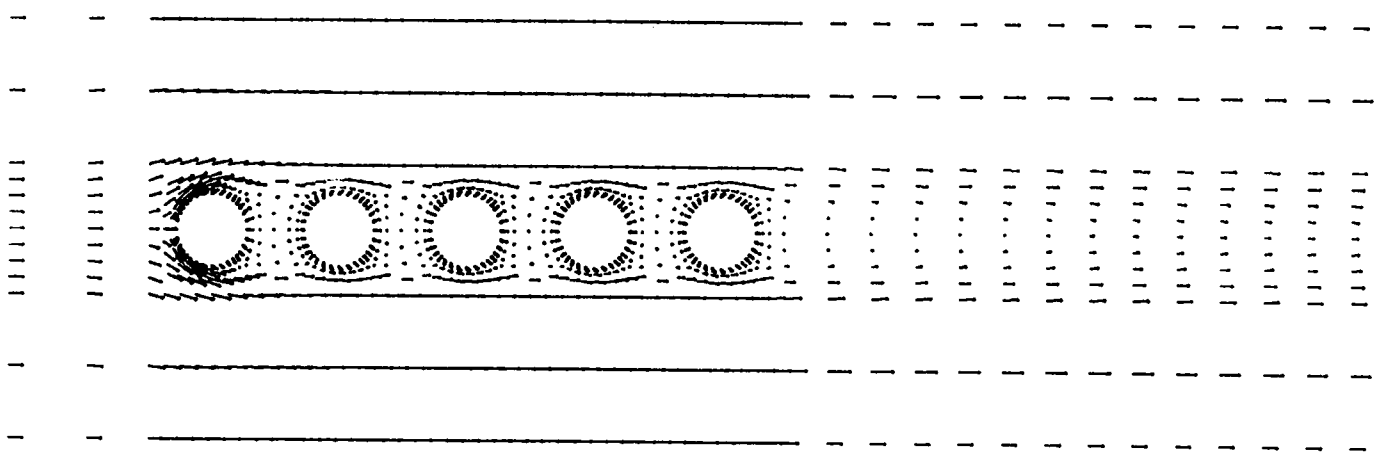

Figure 6.14 Velocity vectors for steady flow past a pentad of cylinders at Re = 100

Reynolds number of 100. The point of separation and the point of reattachment are around 130 and 40 degrees, respectively from the front stagnation point. Figure 6.15 and figure 6.16 show the pressure distribution and the skin friction distribution around the cylinders, respectively. Figure 6.17 displays the local Nusselt number distribution around the five cylinders.

6.5 FLOW PAST IN-LINE BUNDLES OF CYLINDERS

Figure 6.18a depicts the physical model of flow past a five-row deep bundle of heated (or cooled) cylinders. The computational domain is the region enclosed by the thick dotted line ACDB. Figure 6.18b shows computational domain for an infinite bundle of cylinders. The boundary conditions are indicated in figures 6.19a and 6.19b. In the infinite bundle case, a periodic boundary condition with regard to velocity is applied both at the inlet and the outlet of the computational domain. In other words, the velocities obtained from previous iteration along the symmetry line of the computational domain (see figure 6.18b) are taken as boundary conditions for both the inlet and the outlet. For temperature boundary conditions at the inlet and the outlet, the normalized temperatures obtained at sections 1-1 and 2-2 in figure 6.18a are used. The finite-element meshes for each case are shown in figures 6.20a and 6.20b. The finite-element meshes are automatically generated and are designed to capture the boundary layer effects near the cylinder walls, as well as the separating shear layers.

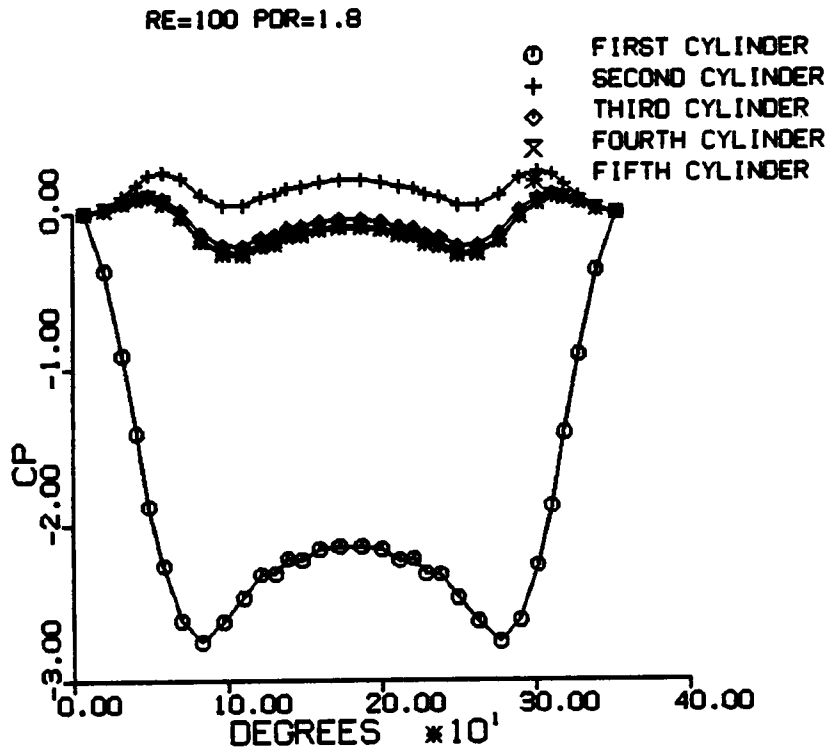

Figure 6.15 Pressure distribution for steady flow past a pentad of cylinders, Re = 100

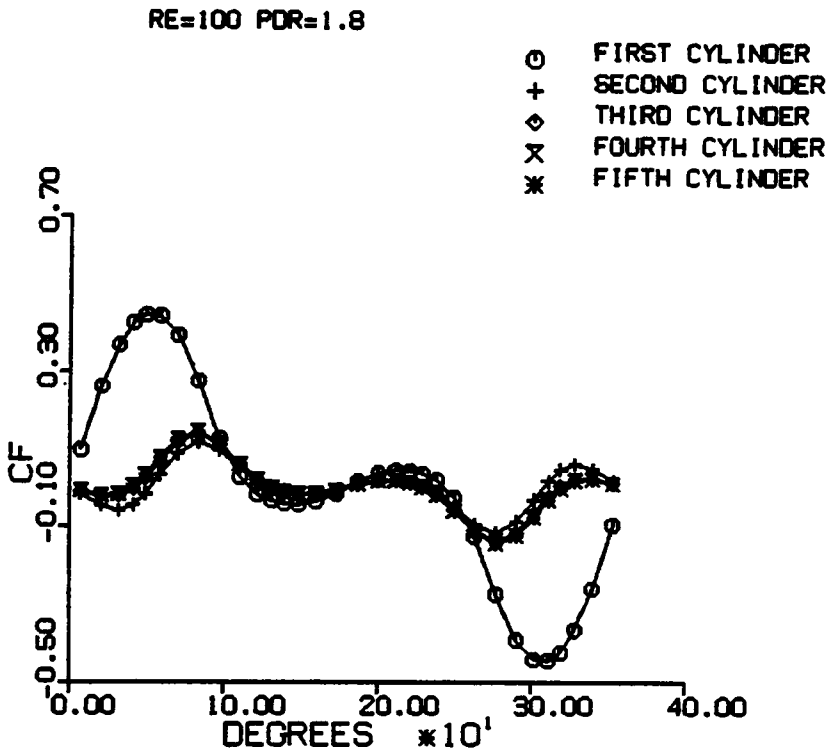

Figure 6.16 Skin friction distribution for steady flow past a pentad of cylinders, Re = 100

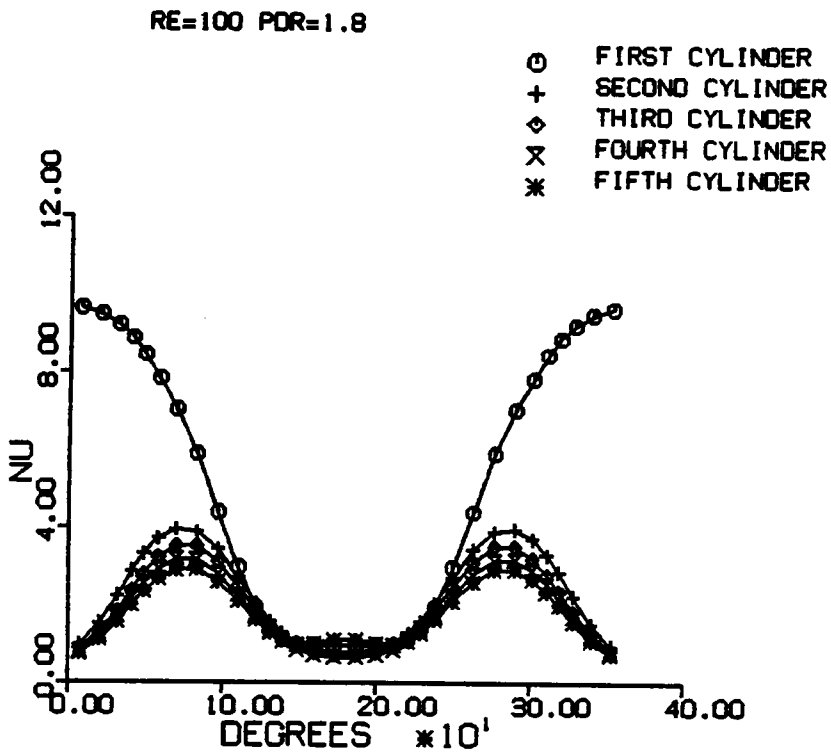

Figure 6.17 Local Nusselt number distribution for flow past a pentad of cylinders

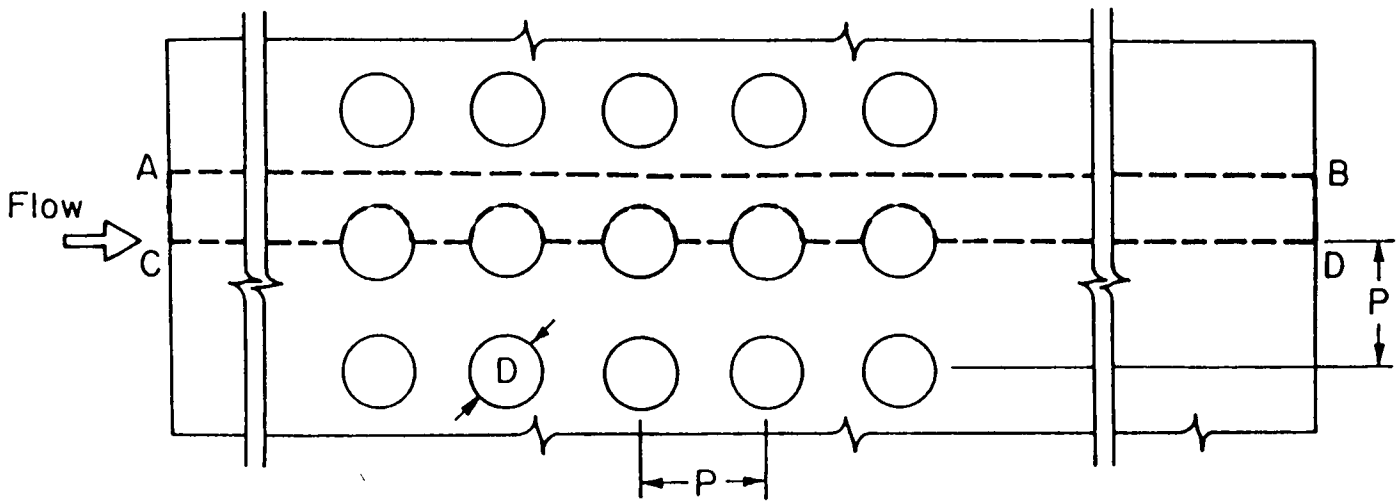

Figure 6.18a Physical model of flow past a five-row deep bundle of in-line cylinders

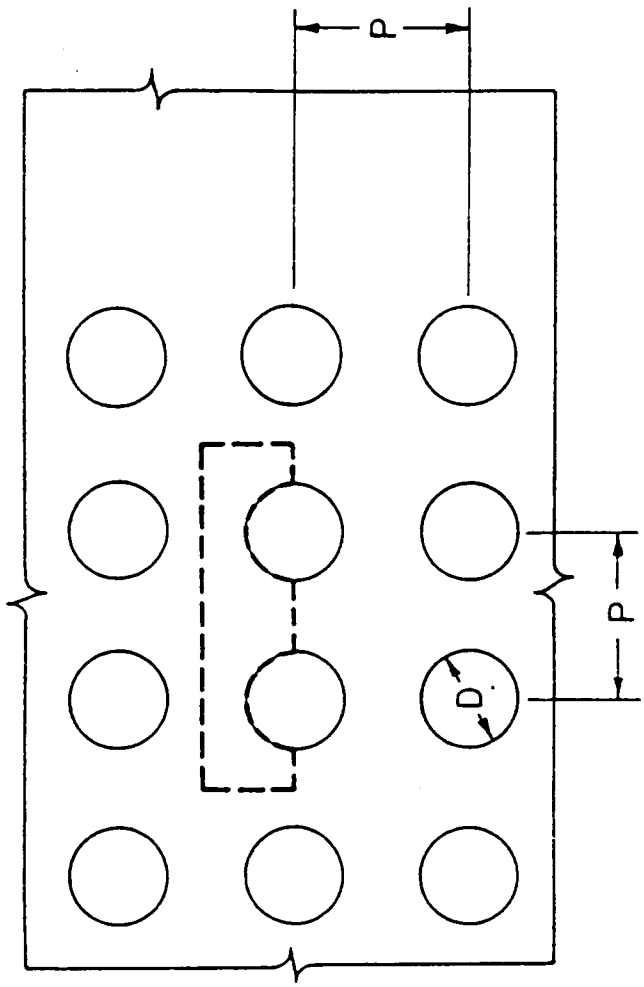

Figure 6.18b Computational domain for an infinite bundle of in-line cylinders

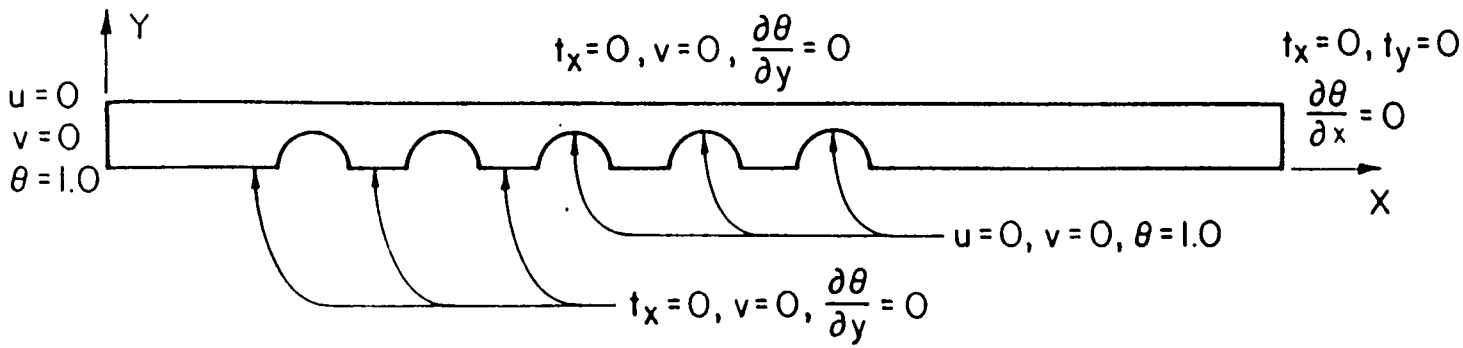

Figure 6.19a Boundary conditions for finite-row in-line bundle of cylinders

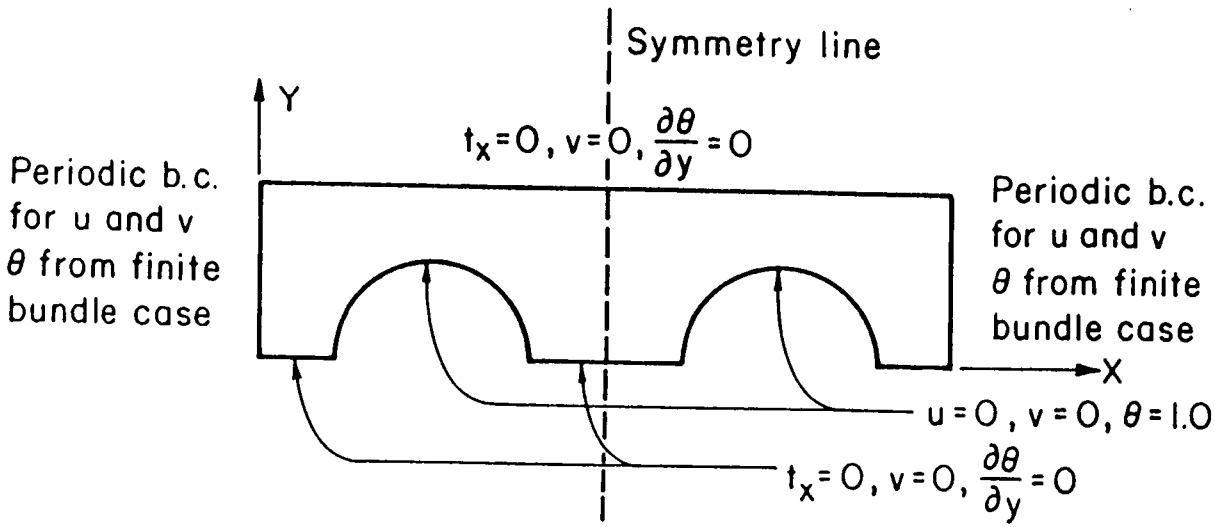

Figure 6.19b Boundary conditions for an infinite bundle of in-line cylinders

Figure 6.20a Finite-element mesh for five-row in-line bundle of cylinders

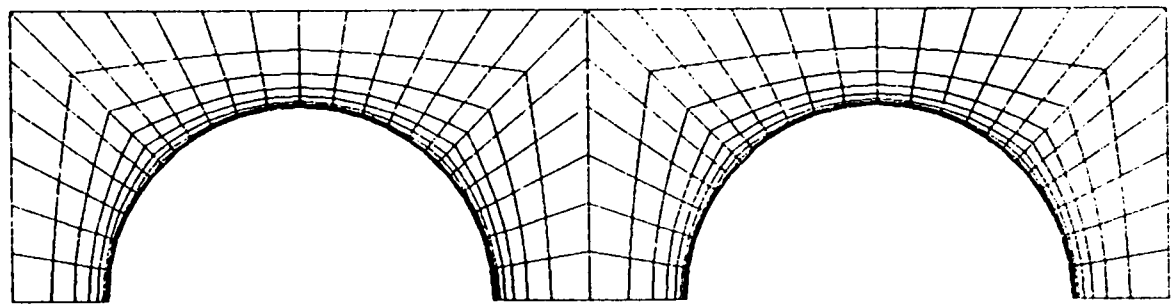

Figure 6.20b Finite-element mesh for an infinite bundle of in-line cylinders

Velocity vectors at Re = 300 for five rows of an in-line cylinder bank and for an inner row of an infinite bundle are shown in figures 6.21a and 6.21b, respectively, for a pitch-to-diameter ratio of 1.8. Here Re is the Reynolds number based on velocity at minimum flow cross section. The velocity field in the gaps between adjacent cylinders (figure 6.21a) indicates that the flow after the second is almost fully developed. The difference between velocity field around the third and the fourth cylinders is 1.8 percent in Euclidian norm for the Re = 300 case. This is also evidenced by almost identical velocity field found for the infinite bundle in figure 6.21b. The velocity field around the fourth cylinder and the velocity field around a cylinder of the infinite bundle have a difference of 1.2 percent in Euclidian norm for Re = 300. The flow field is similar for various Re in the range Re = 100 - 600 studied. The gaps between cylinders contain strongly recirculating regions. A pair of elongated vortices are present behind the fifth row.

Figures 6.22a, 6.22b, 6.22c and 6.22d show examples of streamlines, isovorticity lines, isobars and isotherms for flow across a five-row deep bundle of cylinders. The streamlines and isovorticity lines again indicate an almost fully developed flow pattern in the region behind the second row and in front of the last row. Pressure contours (isobars) display the drop of pressure along the flow direction. The temperature contours (isotherms) for the space between the third and the fourth row in the five-row bundle case and for the infinite bundle match well. The isotherms, isobars, isovorticity and streamlines are qualitatively similar for different Re in the range 100 - 600.

Figure 6.21a Velocity vectors for five-row in-line bundle of cylinders, Re = 300, P/D = 1.8

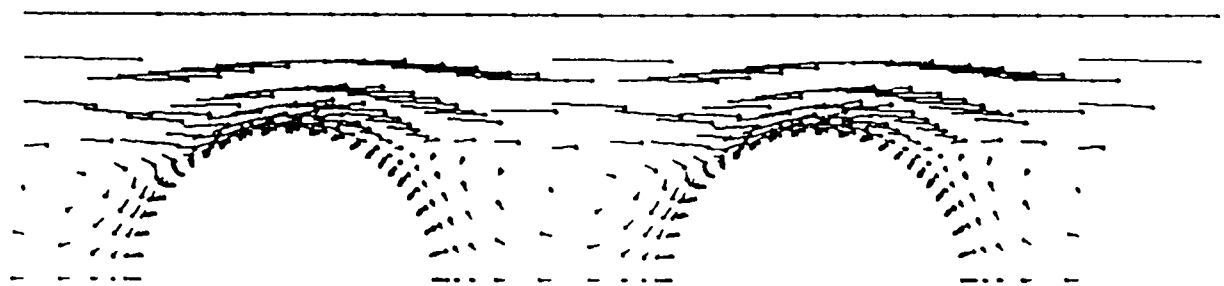

Figure 6.21b Velocity vectors for an infinite bundle of in-line cylinders, Re = 300, P/D = 1.8

Figure 6.22a Streamlines for five-row in-line bundle of cylinders, Re = 300, P/D = 1.8

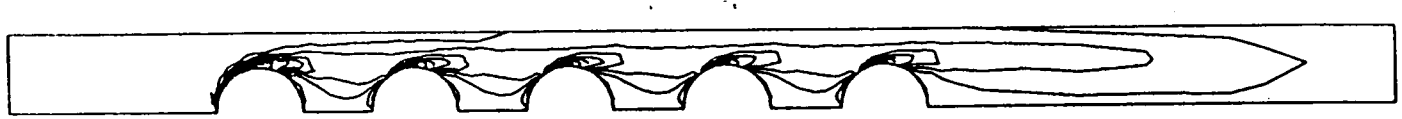

Figure 6.22b Isovorticity lines for five-row in-line bundle of cylinders , Re = 300, P/D = 1.8

Figure 6.22c Isotherms for five-row in-line bundle of cylinders, Re = 300, P/D = 1.8

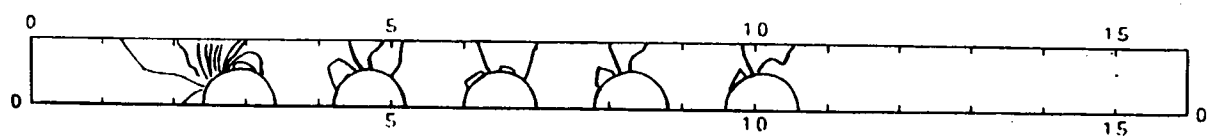

Figure 6.22d Isobars for five-row in-line bundle of cylinders, Re = 300, P/D = 1.8

Figures 6.23a, 6.23b and 6.23c show distributions of local heat transfer coefficient around cylinders. The abcisca in these graphs is the angle from the front stagnation point. The Nusselt number Nu is based on the difference in wall temperature T_w and bulk temperature T_b at the minimum flow cross section as a representative temperature difference $\mathrm{Nu} = \dfrac{T_w - T_{in}}{T_w - T_b} \dfrac{\partial\theta}{\partial r}\Big|_{r=R}$ where T_{in} = inlet temperature and r = radial coordinate. For the five-row deep bundle, the local Nusselt number distribution has the same form on all cylinders except for the front half of the first row and the rear half of the last row. The maximum Nu for the first occurs at 60 degrees and for the rest of the rows at 70 degrees, which is in agreement with Fujii et al. [1984], but the maximum value itself does not change until beyond Re = 200. The pattern of Nu distributions for Re = 250 and higher is similar to the one shown in figure 6.23b. It can be seen in figures 6.23b and 6.23c that for higher pitch-to-diameter ratio the coefficient of heat transfer is lower. The results of LeFeuvre [1973] for Re = 100 and the results for second row of Fujii et al. [1984] are shown in figure 6.23a for comparison. For the fully developed case of an infinite bundle, the Nu distribution in figure 6.23d is nearly the same as for the 4th row in figure 6.23b.

Figures 6.24a, 6.24b and 6.24c show typical distributions of skin friction coefficients around the cylinders. Except for the first cylinder, there are two zero skin friction points for each cylinder above the center line, signifying a reattachment point and a separation point. The reattachment point near the middle of the first quadrant moves from 40 degrees to 55 degrees as Re is increased from 100 to 600. The point of separation moves from 130 degrees to 110

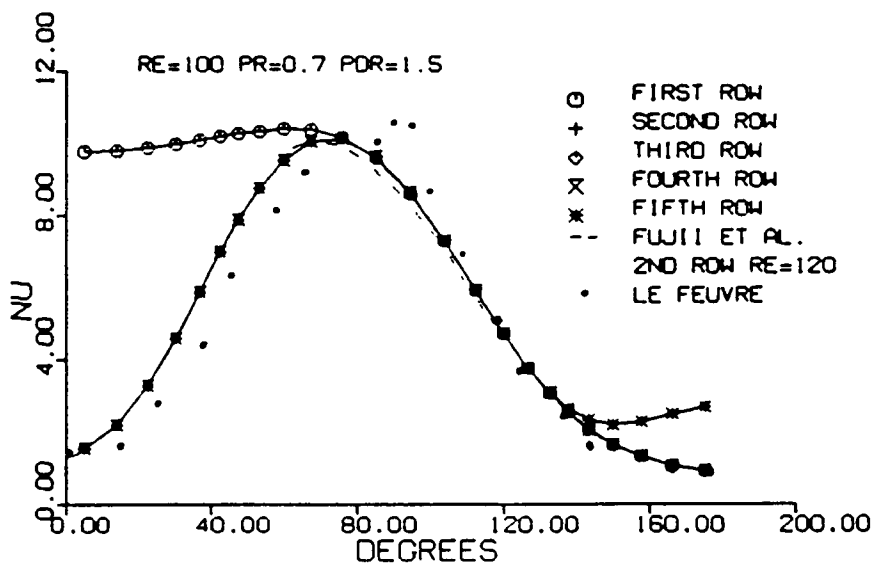

Figure 6.23a Comparison of Nusselt number distributions with other numerical results for a five-row deep bundle of in-line cylinders, Re = 100, P/D = 1.5

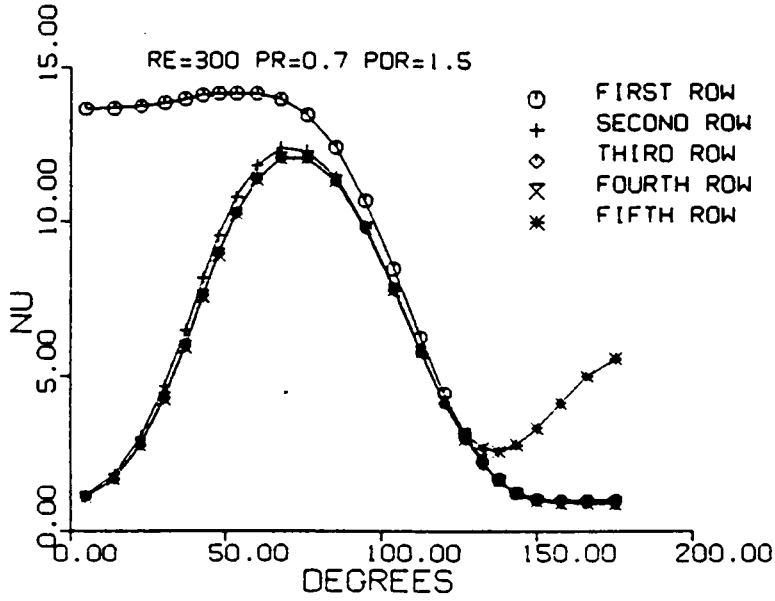

Figure 6.23b Nusselt number distributions for a five-row deep bundle of in-line cylinders, Re = 300, P/D = 1.5

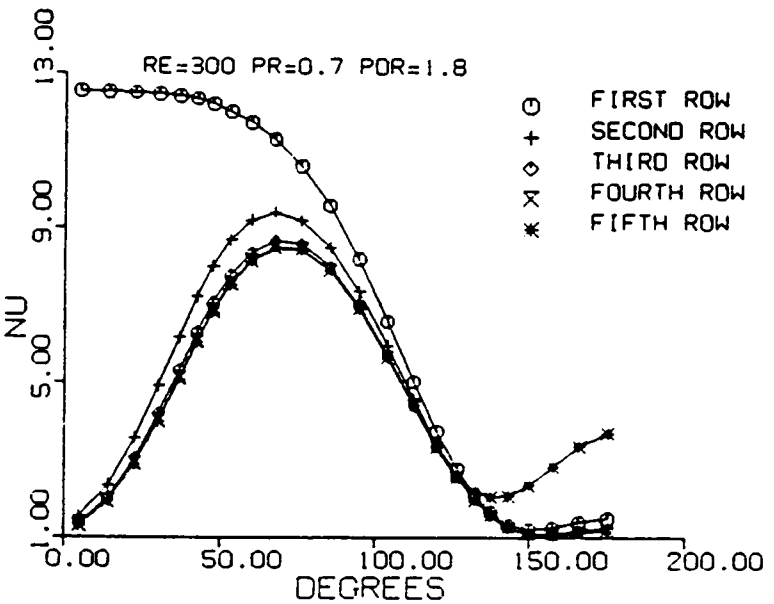

Figure 6.23c Nusselt number distributions for a five-row deep bundle of in-line cylinders, Re = 300, P/D = 1.8

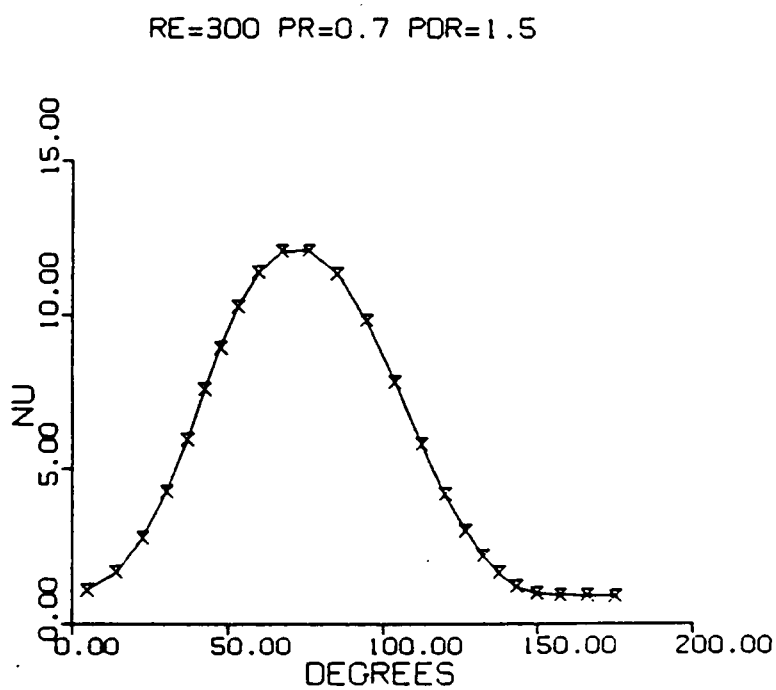

Figure 6.23d Nusselt number distribution around an interior cylinder in an infinite bundle of in-line cylinders,

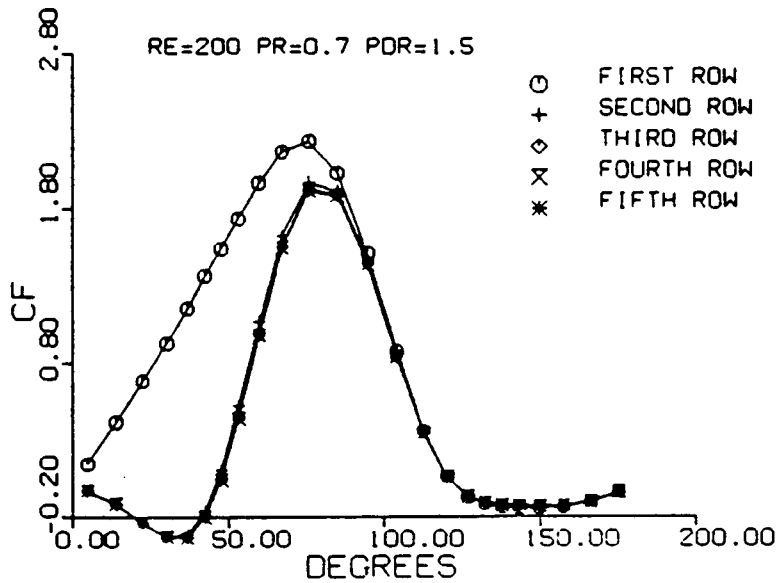

Figure 6.24a Skin friction distributions around cylinders for a five-row deep bundle of in-line cylinders, Re = 200, P/D = 1.5

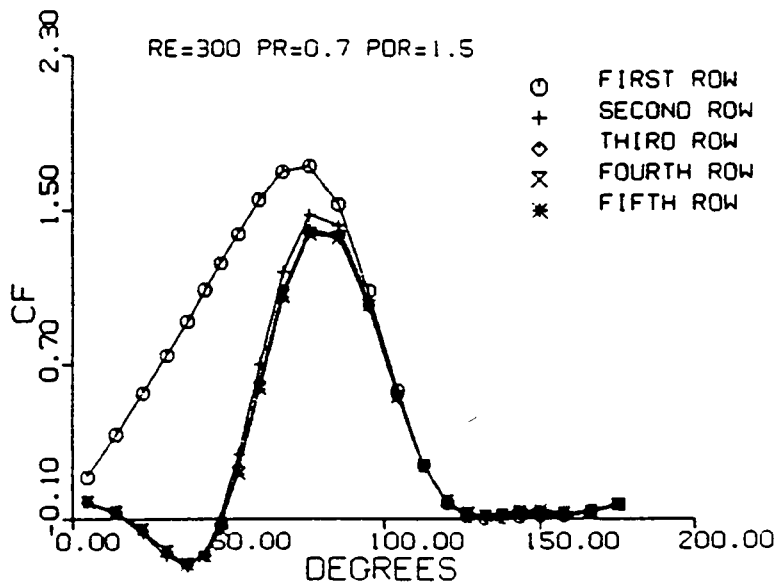

Figure 6.24b Skin friction distributions around cylinders for a five-row deep bundle of in-line cylinders, Re = 300, P/D = 1.5

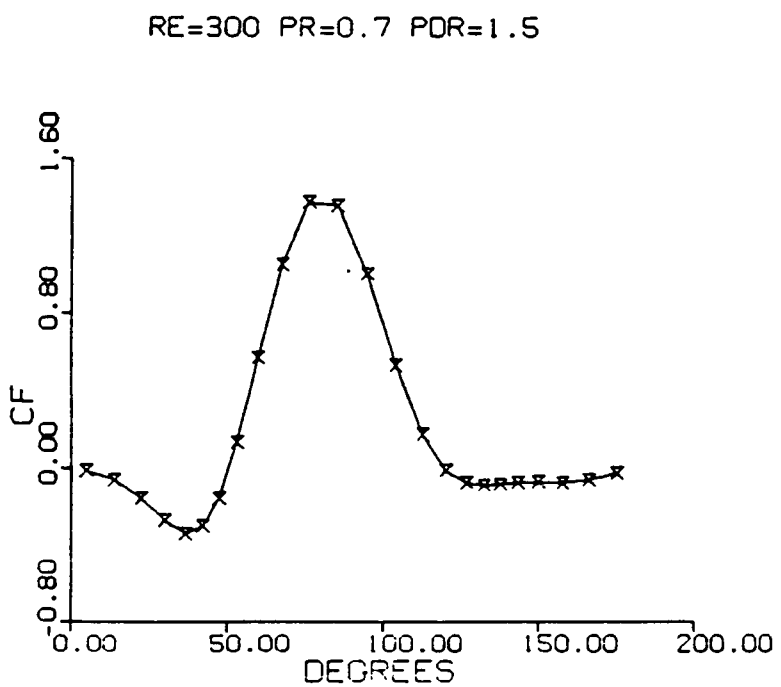

Figure 6.24c Skin friction distribution around an interior cylinder in an infinite bundle of in-line cylinders, Re = 300, P/D = 1.5

degrees when Re increases from 100 to 600. The shift in the location of the points of reattachment and separation is responsible for increased heat transfer at higher Re. For any particular Re, the reattachment point and the separation point have approximately the same angular positions for all rows of cylinders. Skin friction distributions for the infinite bundle case in figure 6.24c is nearly the same as for the fourth row in figure 6.24a.

Figures 6.25a and 6.25b show the comparison of the results on averaged heat transfer coefficients with experimental results of Bergelin et al. [1950,1952] for pitch-to-diameter ratios (P/D) of 1.5 and 1.25, respectively. Results of Fujii et al. [1984] for a P/D of 1.5 and Antonopoulos [1985] for a P/D of 1.25 are also shown. The averaged Nusselt number Nu_{lm} is based on log mean temperature difference defined by $\Delta t_{lm} = \dfrac{(T_w - T_{in}) - (T_w - T_{out})}{\ln[(T_w - T_{in})/(T_w - T_{out})]}$. The present results are in good agreement with experimental works of Bergelin et al..

Figures 6.26a and 6.26b show pressure distributions, $C_p = \dfrac{P - P_{in}}{1/2\rho u_{in}^2}$ along the top (AB) and the bottom (CD) lines of the computational domain for Re = 100 and P/D ratios of 1.5 and 1.8 respectively. The pressure distribution for the first row is almost identical with that of a single cylinder. From the second row onwards, the pressure drop from one row to the next is almost uniform, which is consistent with the flow field shown in figure 6.21a. Fujii et al. found that there was a discrepancy in the pressures at the top and the bottom of their computational domain far downstream behind the fifth row. They attribute this to a calculation error. In the present method, a pressure recovery behind the fifth row brings pressures along the top and the bottom lines to the same value which

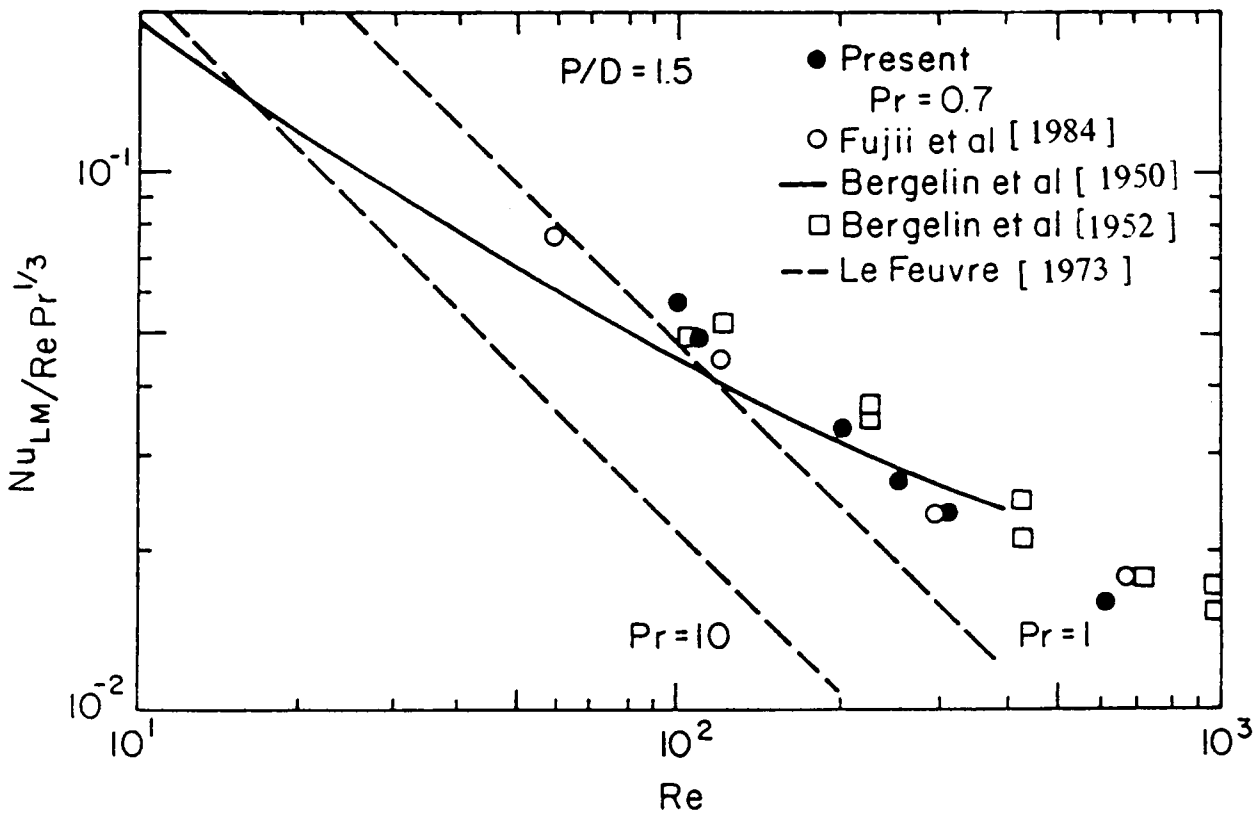

Figure 6.25a Comparison of averaged heat transfer coefficient with experimental and other numerical results, in-line P/D = 1.5

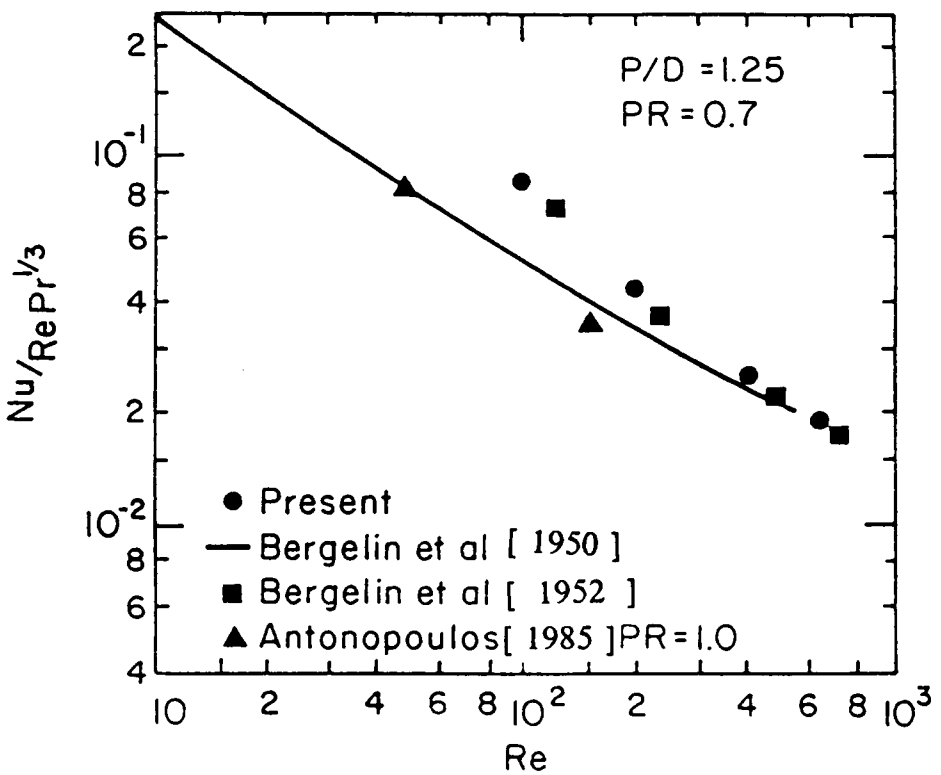

Figure 6.25b Comparison of averaged heat transfer coefficient with experimental and other numerical results, in-line P/D = 1.25

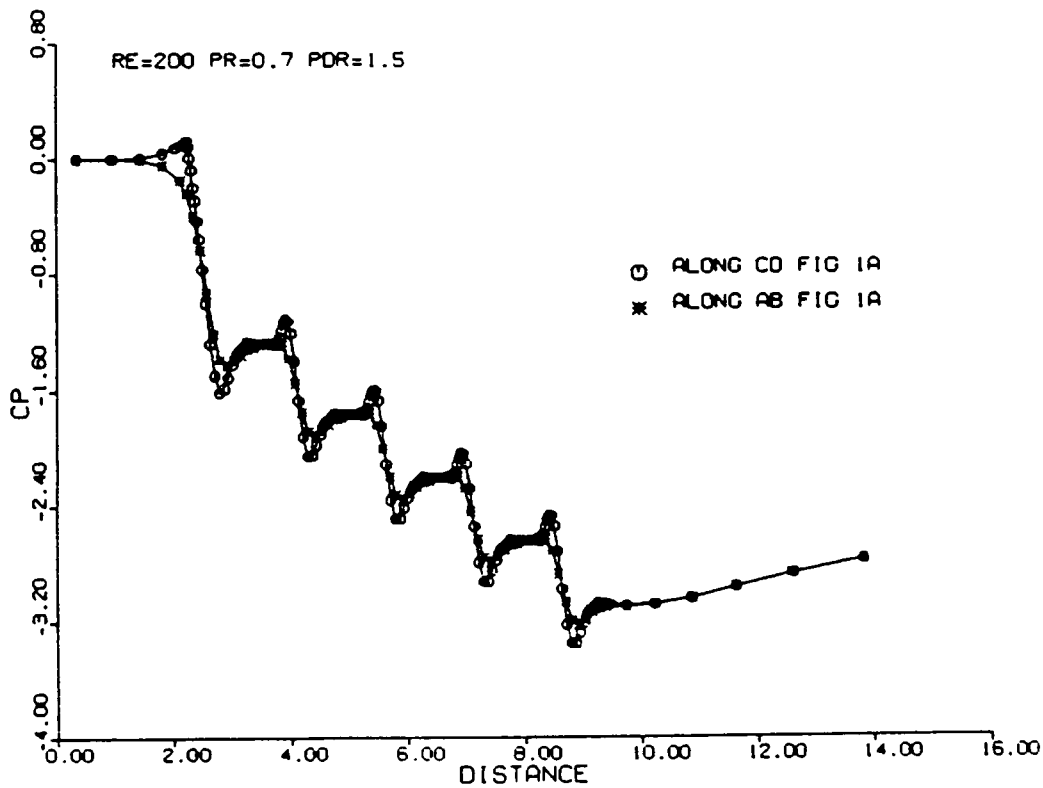

Figure 6.26a Distributions of coefficients of pressure for five-row deep in-line bundle of cylinders, Re = 200, P/D = 1.5

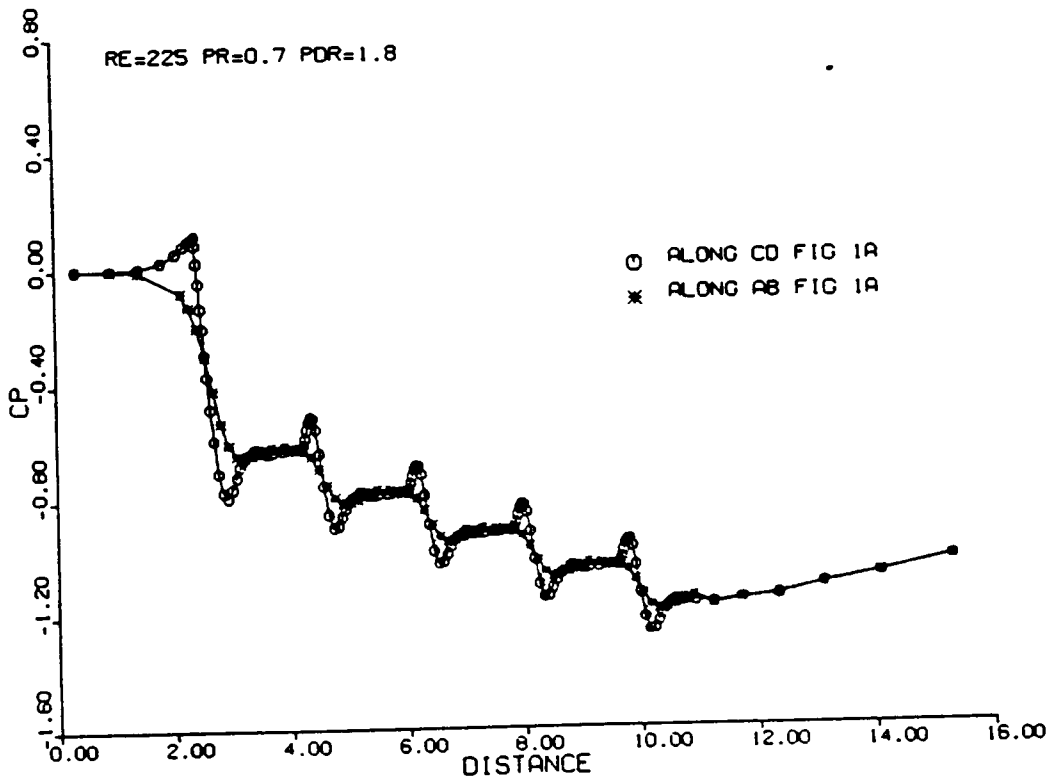

Figure 6.26b Distributions of coefficients of pressure for five-row deep in-line bundle of cylinders, Re = 225, P/D = 1.8

is to be expected. From figures 6.26a and 6.26b it can be seen that with higher P/D ratio, the pressure drop across any one row is lower.

Figure 6.27 shows the drag coefficient defined as $C_d = \frac{\Delta P}{2n\rho u_m^2}$ versus Re in comparison with experimental results (10 row case) of Bergelin et al. [1950,1952] and numerical results of Fujii et al. [1984] and LeFeuvre [1973]. The present results are in good agreement with the experimental results of Bergelin et al. as well as the numerical results of Fujii et al. and LeFeuvre.

6.6 FLOW PAST STAGGERED BUNDLES OF CYLINDERS

The physical model of flow around five-row deep (finite) staggered bundles of cylinders in three different configurations are shown in figures 6.28a, 6.28b and 6.28c. The computational domain is shown by thick dotted line in figure 6.28a. The boundary conditions are indicated in figure 6.29. Figure 6.30 shows a typical finite-element mesh used. The finite-element mesh including the boundary conditions are generated by the computer program for any number of rows in a bundle with the minimum of input parameters. This mesh is designed in a way which provides a denser mesh along the boundary layers and the separated free shear layers. The thickness of an element increases in geometrical proportion away from the cylinder surface so that a sufficient number of points falls inside the boundary layer for the Reynolds number considered. This assures reasonable resolution of boundary-layer effects near the cylinder walls. The finite-element mesh for the five-row deep bundle of cylinders used in this study

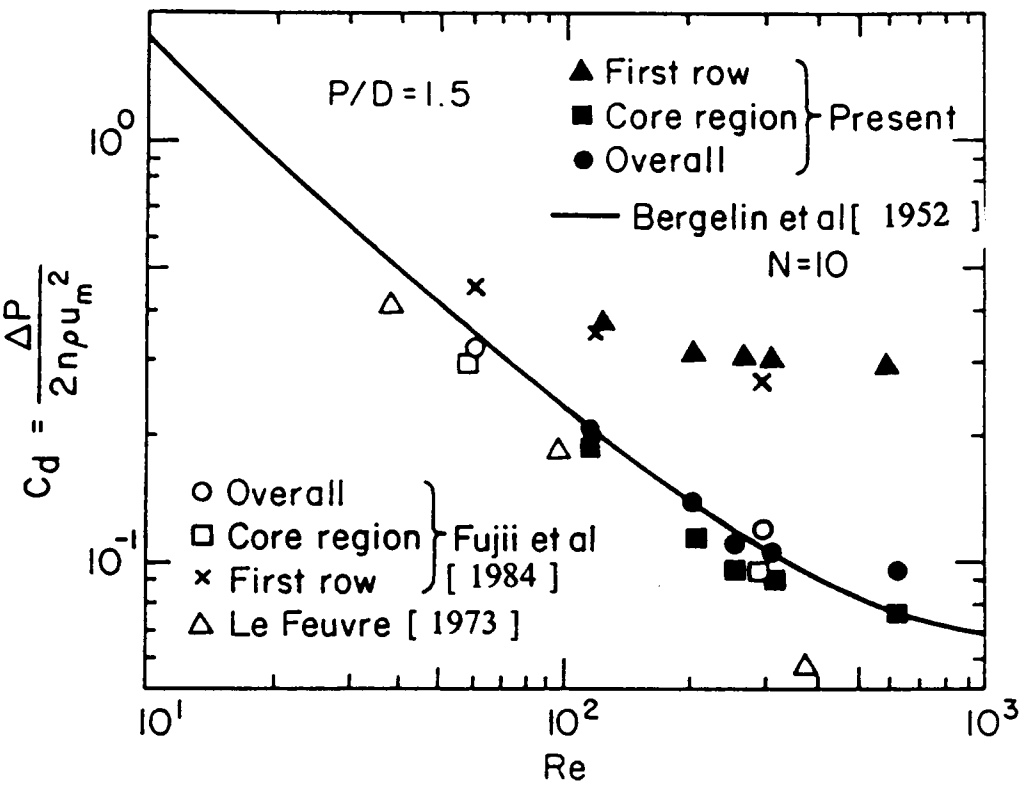

Figure 6.27 Drag coefficients for five-row deep in-line bundle of cylinders

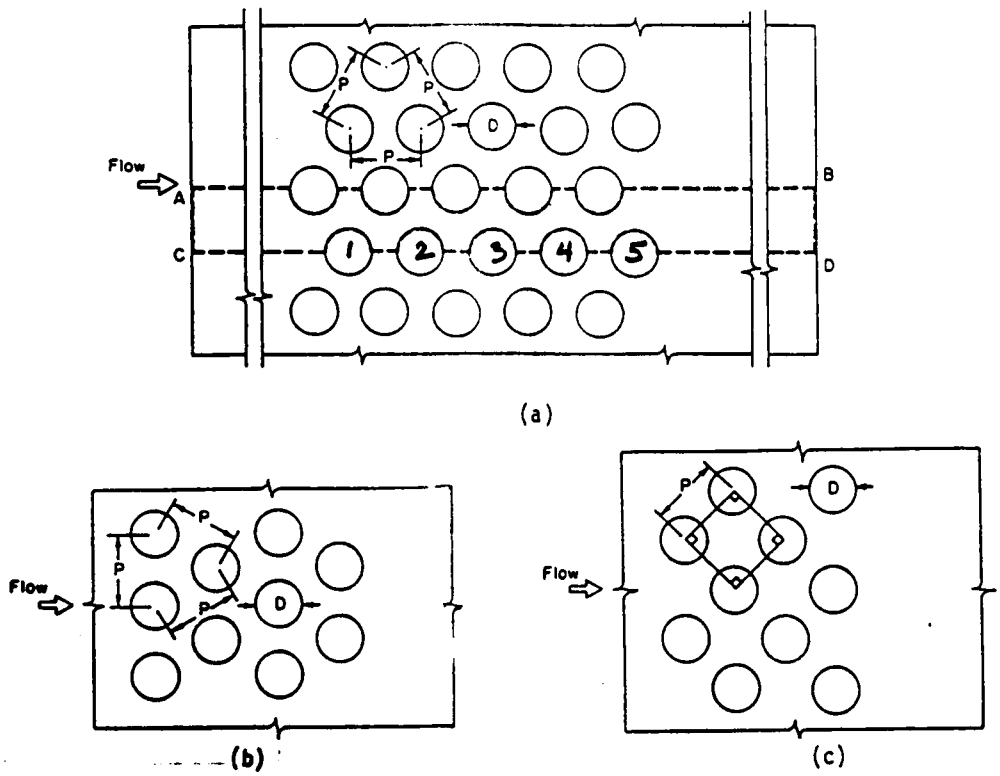

Figure 6.28 Physical model and computational domain of a five-row deep staggered bundle of cylinders (a) cylinders in equilateral arrangement (b) cylinders in equilateral arrangement turned at 90° with respect to free stream as compared to (a) (c) cylinders in staggered square arrangement

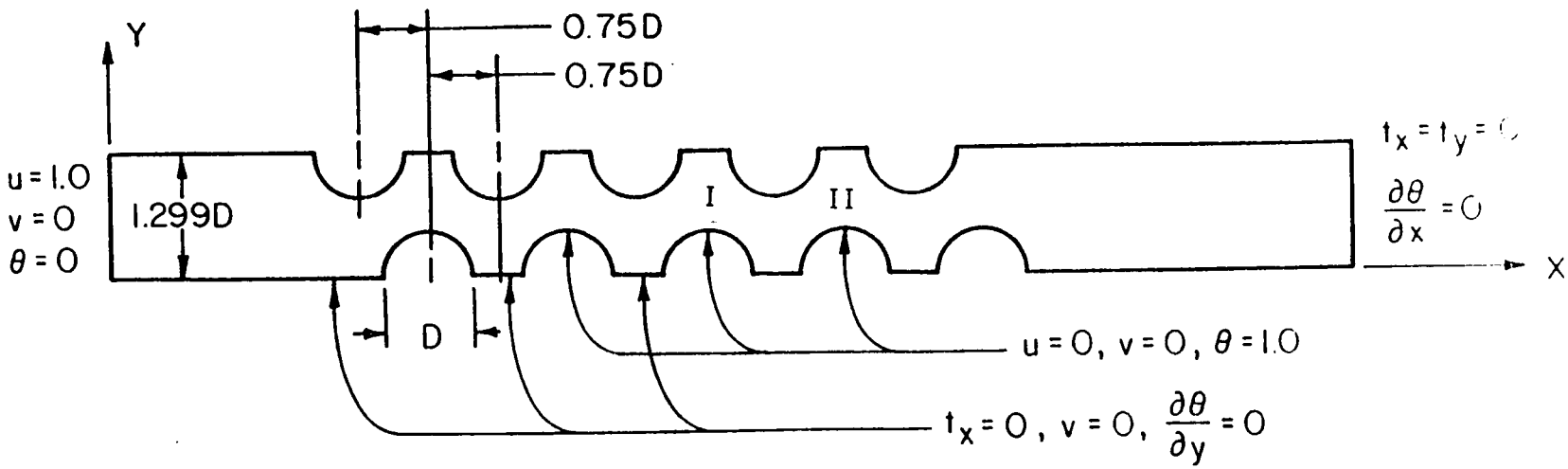

Figure 6.29 Boundary conditions for a five-row deep staggered bundle of cylinders

a.

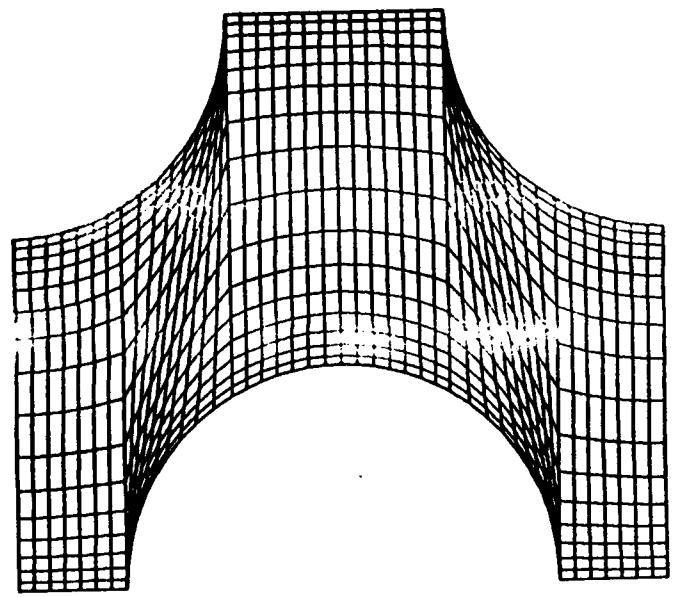

b.

Figure 6.30 Finite-element mesh for the staggered bundle of cylinders

(figure 6.30) has 4811 nodes and 4512 elements. The computations were carried out on CRAY-XMP computer. A typical run took 190 seconds.

Typical velocity vector fields for flow across the cylinders is shown in figure 6.31. These are for a Reynolds number based on velocity at minimum cross section of 200 and P/D of 1.5 for the case of figure 6.28a. The velocity field after the third cylinder indicates almost fully developed flow. The difference in velocity field in regions I and II in figure 6.29 is 0.85 percent in Euclidian norm. The flow field in each of the three configurations is similar for different Reynolds number in the range studied. Reattachment occurs at 40 degrees on the front of the cylinders and separation point lies near 130 degrees from the stagnation point in the case of the triangular arrangement of cylinders shown in figure 6.28a. Recirculating flow is trapped between cylinders which appears to be similar to cavity flows.

Figures 6.32a, 6.32b and 6.32c show examples of isotherms, isobars and isovorticity lines. The overall pattern of contours in all the cases remain similar for different Reynolds numbers and pitch-to-diameter ratios. When dissipation is negligible, the equations governing the fields of temperature and vorticity are identical. As a consequence, the isotherms and isovorticity lines have similar patterns as can be seen from figures 6.32a and 6.32c. The isobars in turn indicate a uniform pressure in the cavity regions and a characteristic bulge in the neighborhood of reattachment.

Figures 6.33a, 6.33b and 6.33c show the distribution of skin friction coefficient ($C_f = \frac{\tau}{1/2\rho U_\infty^2}$) for a line of cylinders in the configuration of figure

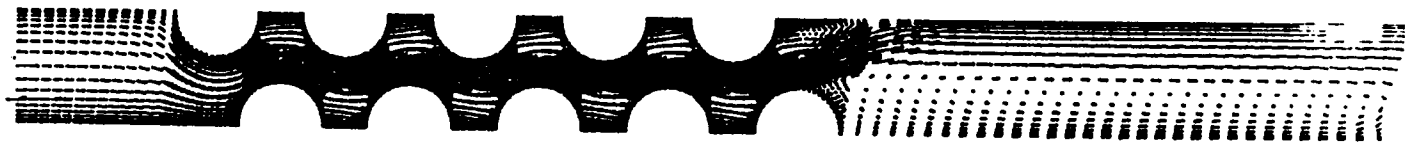

a.

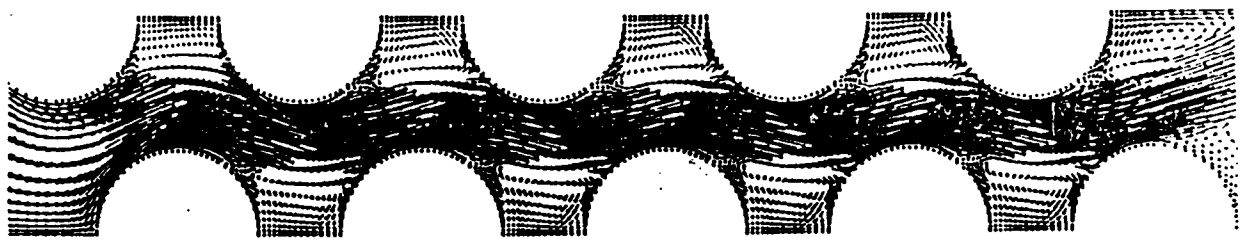

b.

Figure 6.31 a. Velocity vectors for five-row deep staggered bundle of cylinders in figure 6.28a Re = 200 and P/D = 1.5
b. Enlarged view of velocity vectors in the different regions

Figure 6.32a Isotherms for five-row-deep bundle of cylinders in figure 6.28a, Re = 200, P/D = 1.5 and PR = 0.7

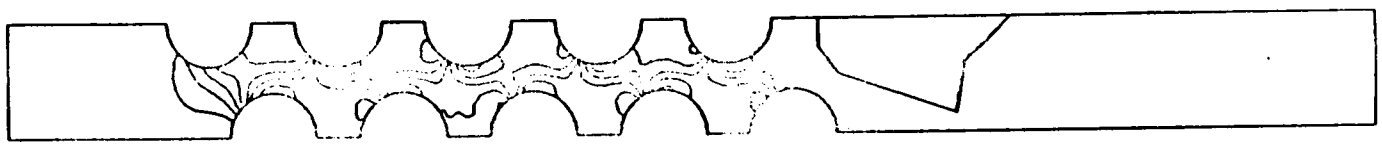

Figure 6.32b Isobars for five-row deep bundle of cylinders in figure 6.28a
Re = 200, P/D = 1.5

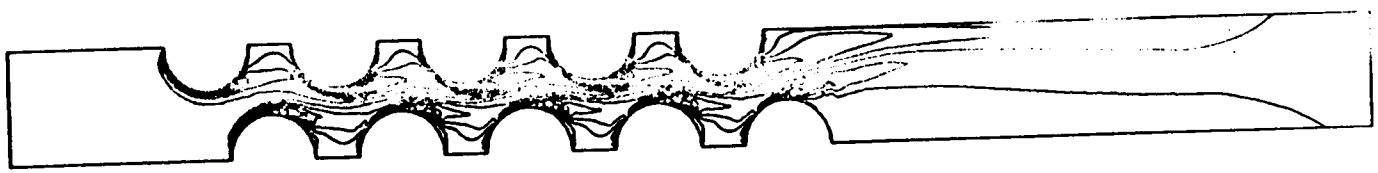

Figure 6.32c Isovorticity lines for five-row-deep bundle of cylinders in figure 6.28a; Re = 200, P/D = 1.5

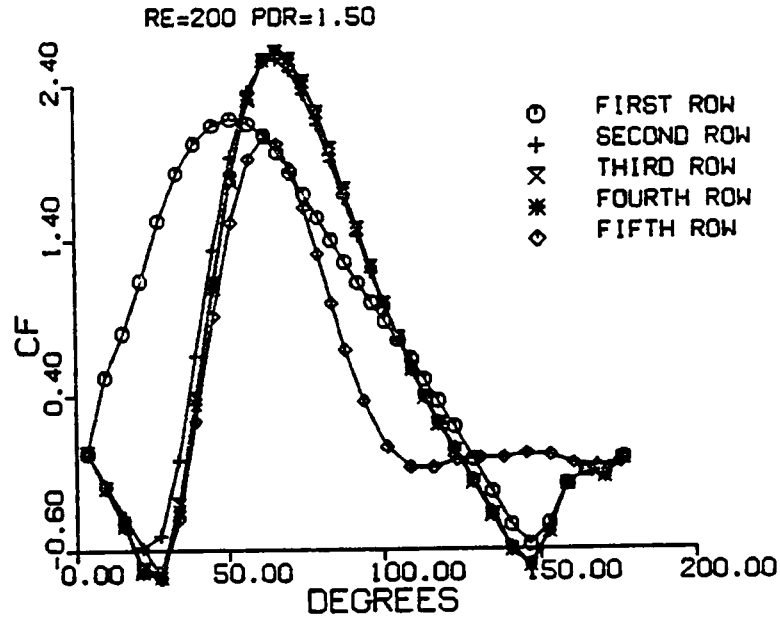

Figure 6.33a Distributions of skin friction coefficient around the cylinders for a five-row deep staggered bundle of cylinders in figure 6.28a, Re = 200, P/D = 1.5

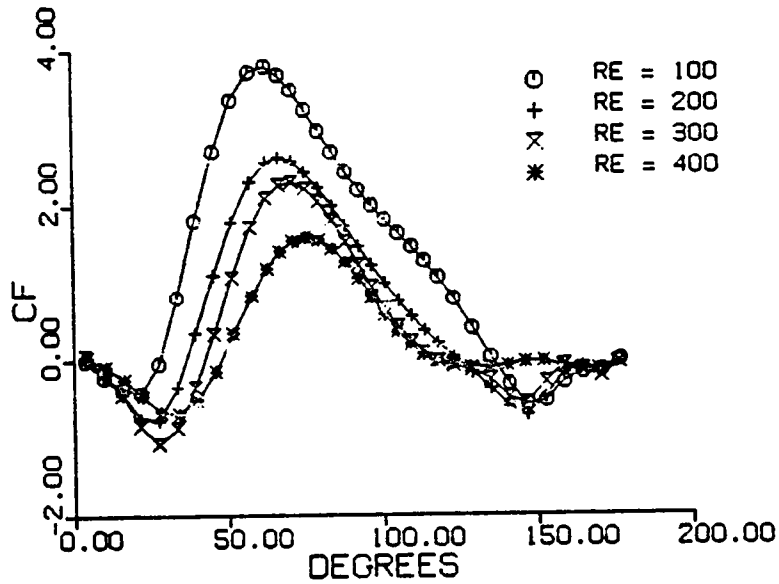

Figure 6.33b Distributions of skin friction coefficient around the bottom fourth cylinder in figure 6.28a for different Reynolds numbers, P/D = 1.5

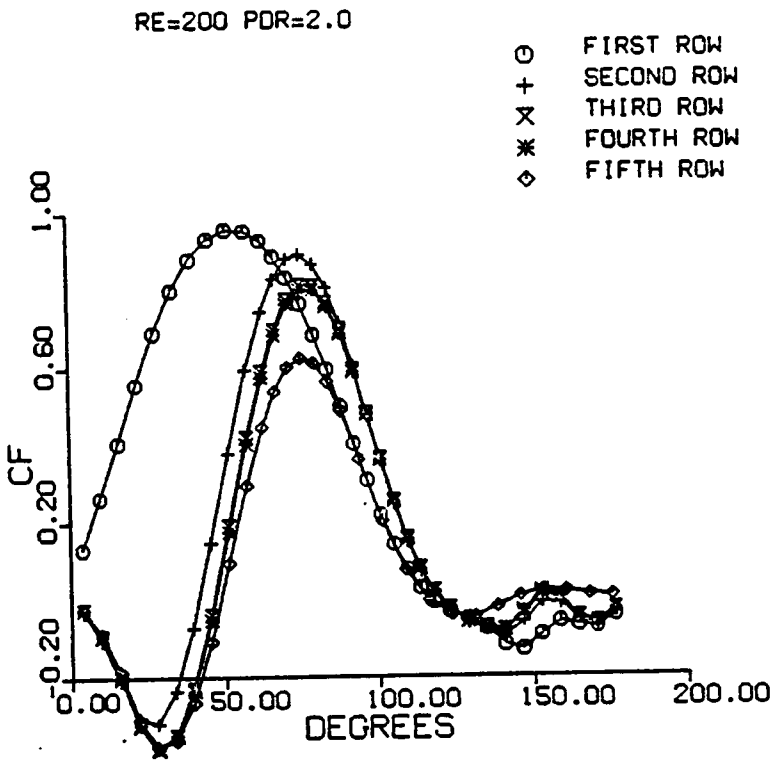

Figure 6.33c Distributions of skin friction coefficient around the cylinders for a five-row deep staggered bundle of cylinders in figure 6.28a, Re = 200, P/D = 2.0

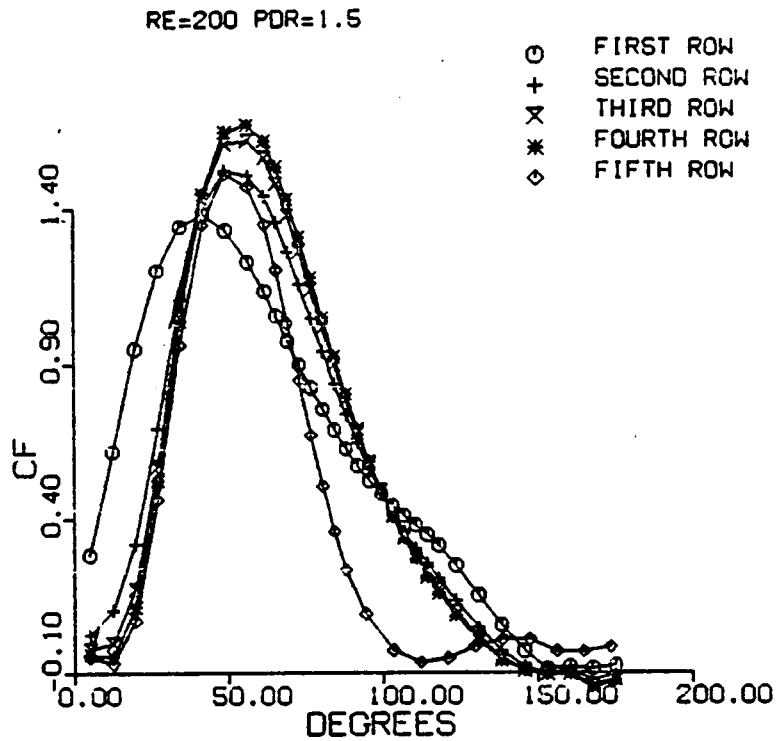

Figure 6.33d Distributions of skin friction coefficient around the cylinders for a five-row deep staggered bundle of cylinders in figure 6.28c, Re = 200, P/D = 1.5

6.28a. The point of reattachment (C_f = 0) is near 40 degrees from the front stagnation point for all cylinders after the front one. The point of separation (C_f = 0) occurs near 130 degrees from the front stagnation point. Figure 6.33b shows the distribution of skin friction coefficient for the fourth cylinder at different values of Reynolds numbers. The point of reattachment moves from 30 degrees to 50 degrees and the separation point moves from 135 degrees to 110 degrees as the Reynolds number is increased from 100 to 400. For a particular Reynolds number, the point of reattachment and point of separation have approximately the same angular positions for all cylinders. Figure 6.33c gives the skin friction coefficient distribution around the cylinders for a P/D of 2.0. Figure 6.33d shows the skin friction coefficient around the cylinders for the case of the staggered square arrangement of figure 6.33c.

Figure 6.34a shows the distribution of pressure coefficient ($C_p = \frac{p - p_s}{1/2\rho U_\infty^2}$) for the bottom five cylinders in the computational domain of figure 6.28a. The pressure distribution for the first row is similar to the pressure distribution for a single cylinder except for the kink near 150 degrees which is near the point of minimum local Nusselt number and also the point of minimum coefficient of skin friction. The pressure drop from one row to the next for the middle rows is almost uniform. Pressure distribution for the third and the fourth row are almost identical indicating that the flows around them are nearly the same. The distribution of pressure coefficient for the fourth cylinder at different Reynolds numbers is shown in figure 6.34b. The pressure coefficient is higher for higher Reynolds number and the pressure drop across a cylinder is higher for lower

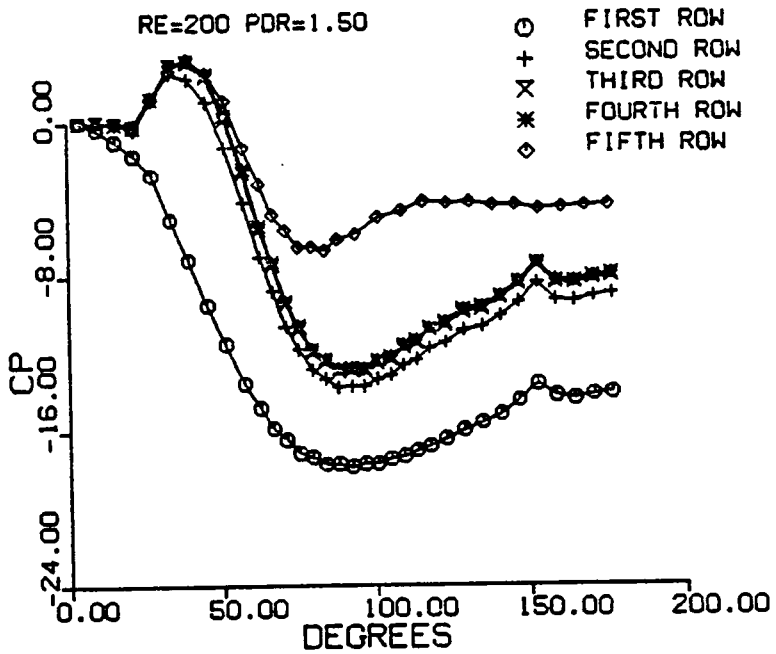

Figure 6.34a Distributions of coefficient of pressure around the cylinders for a five-row deep staggered bundle of cylinders in figure 6.28a, Re = 200, P/D = 1.5

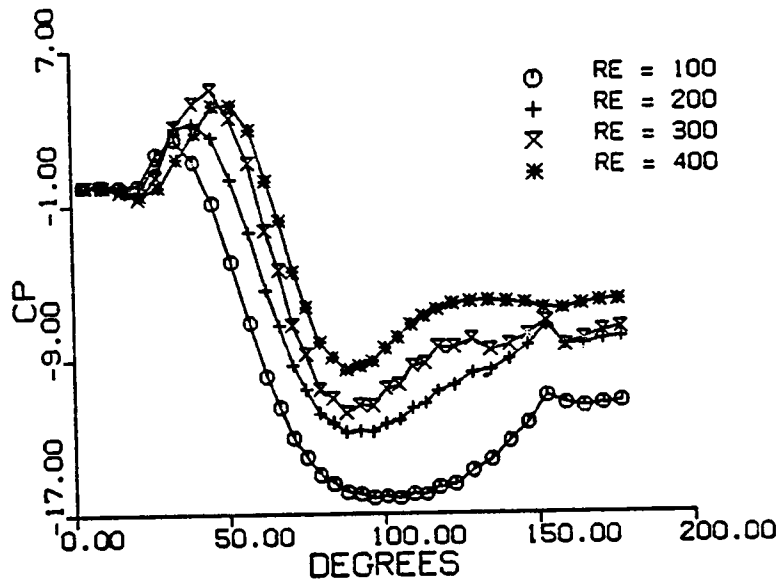

Figure 6.34b Distributions of coefficient of pressure around the bottom fourth cylinder in figure 6.28a for different Reynolds numbers, P/D = 1.5

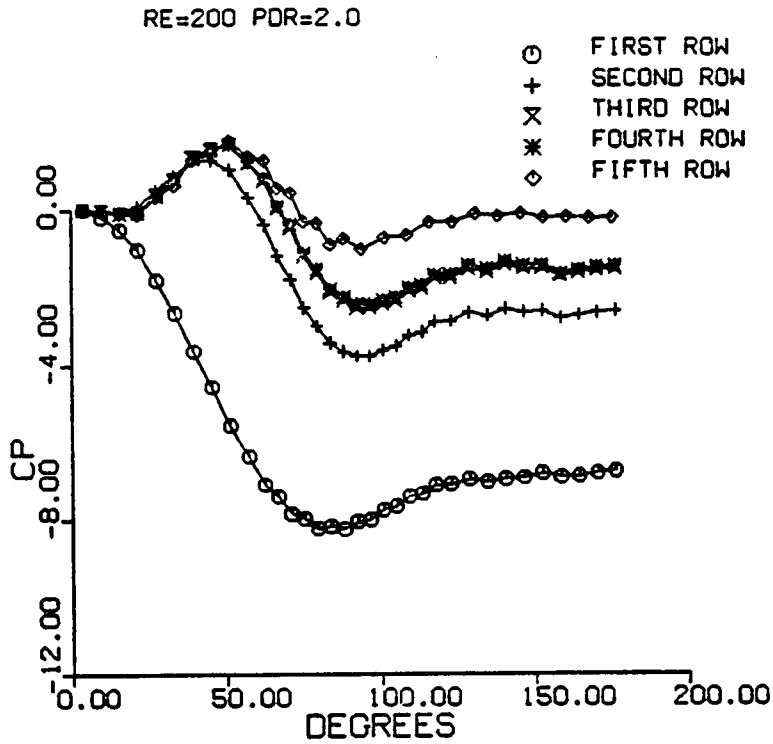

Figure 6.34c Distributions of coefficient of pressure around the cylinders for a five-row deep staggered bundle of cylinders in figure 6.28a, Re = 200, P/D = 2.0

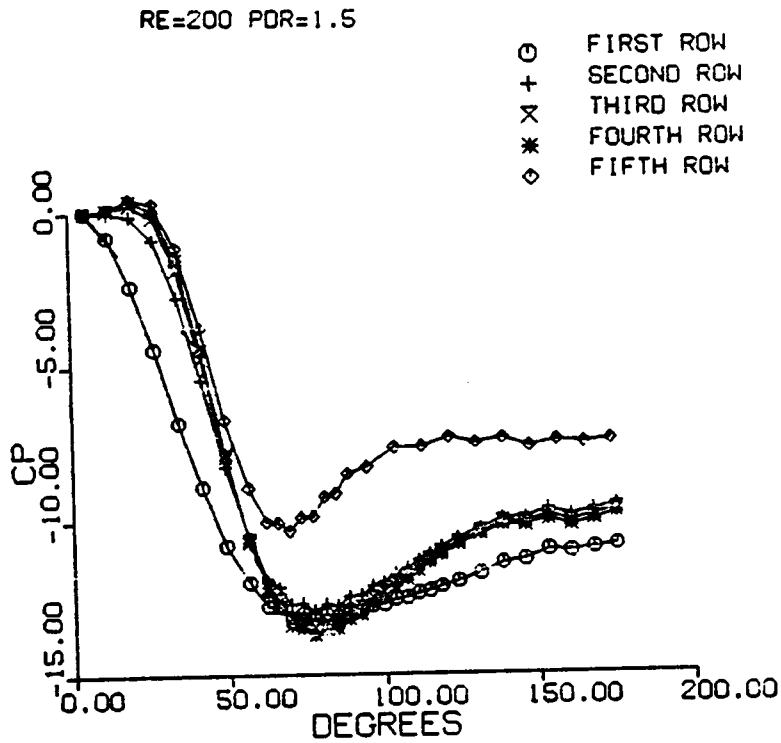

Figure 6.34d Distributions of coefficient of pressure around the cylinders for a five-row deep staggered bundle of cylinders in figure 6.28c, Re = 200, P/D = 1.5

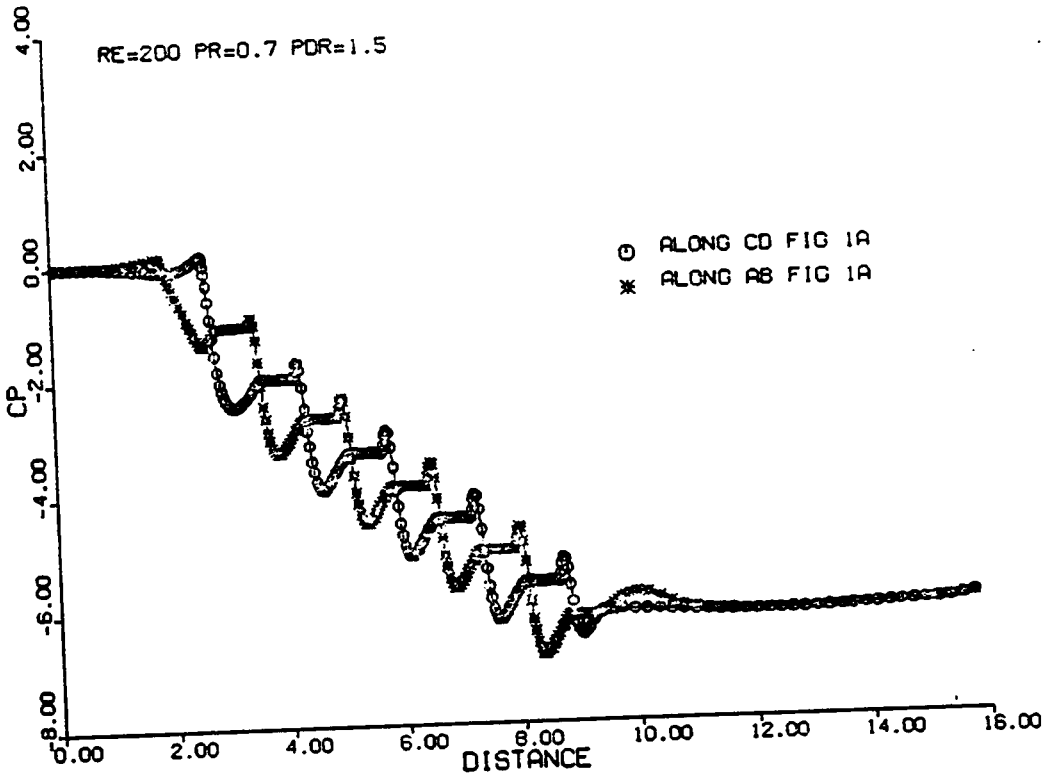

Figure 6.34e Streamwise distribution of coefficient of pressure along lines AB and CD in figure 6.28a

Reynolds number. Figure 6.34c shows the distribution of the coefficient of pressure around the cylinders for a P/D of 2. As can be seen from figures 6.34a and 6.34c, for a higher P/D the pressure drop across a cylinder is lower for the same Reynolds number. Figure 6.34d gives the pressure coefficients for the cylinders in figure 6.28c. Figure 6.34e shows a typical pressure distribution ($C_p = \frac{p - p_{in}}{1/2\rho U_\infty^2}$) along the top AB and the bottom CD lines of figure 6.28a for Re = 200 and P/D = 1.5.

Distribution of local heat transfer coefficient around the five cylinders (figure 6.28a) are shown in figures 6.35a, 6.35b and 6.35c. The Nusselt number Nu is again based on the difference in the wall temperature and the bulk temperature along the vertical line through the center of the cylinder under consideration.

The local Nusselt number distribution has the same form for all the cylinders except the front and last cylinders. The local Nusselt number distribution shows only a small change for the middle rows. The maximum Nusselt number for the bottom line of cylinders in figure 6.28a occurs near 60 degrees except for the front cylinder for which the maximum occurs at near 25 degrees. Figure 6.35b shows the local Nusselt number distribution for the fourth row bottom cylinder at different Reynolds numbers. It is seen that although the average heat transfer coefficient increases with higher Reynolds numbers the local heat transfer coefficient is not higher everywhere around the cylinder. Figure 6.35c gives the distribution of local Nusselt number for a P/D of 2.0. From figures 6.35a and 6.35c it can be seen that the coefficient of heat transfer decreases with

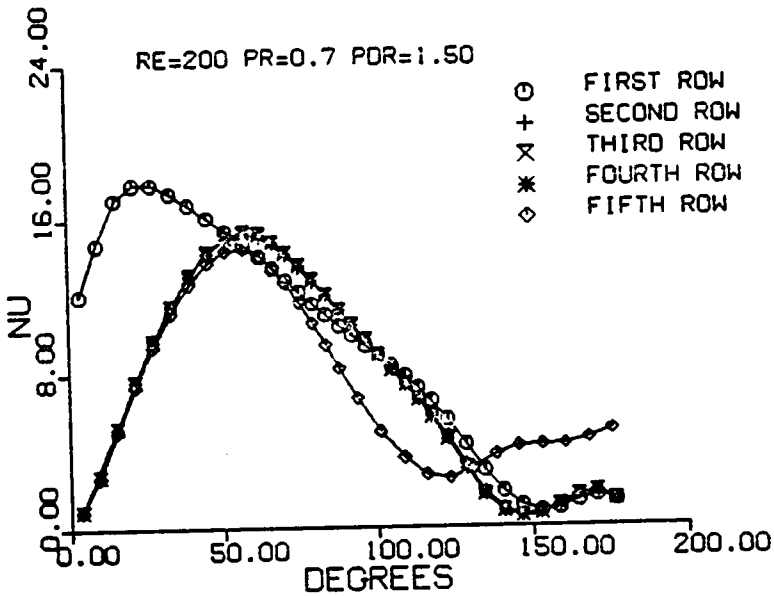

Figure 6.35a Distributions of local heat transfer coefficient around the cylinders for a five-row deep staggered bundle of cylinders in figure 6.28a, Re = 200, P/D = 1.5

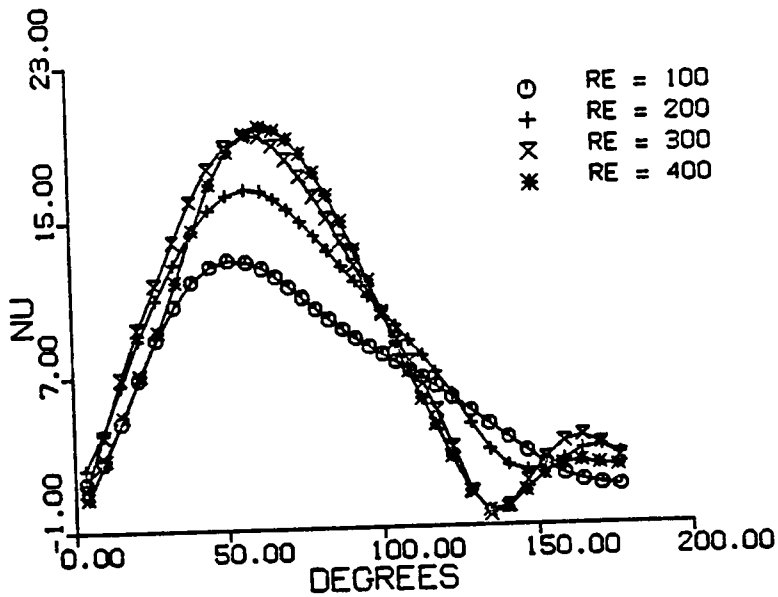

Figure 6.35b Distributions of local heat transfer coefficient around the bottom fourth cylinder in figure 6.28a for different Reynolds numbers, P/D = 1.5

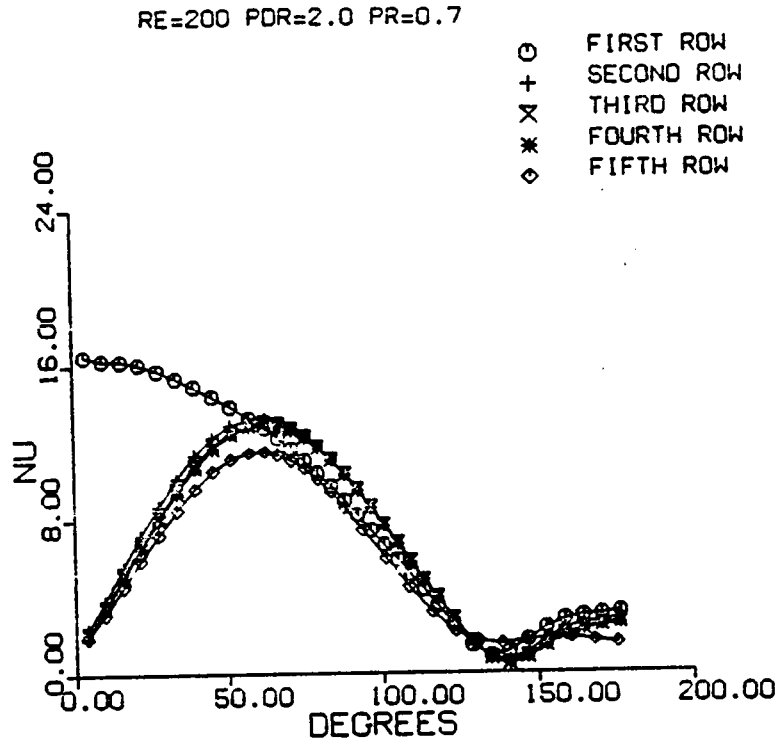

Figure 6.35c Distributions of local heat transfer coefficient around the cylinders for a five-row deep staggered bundle of cylinders in figure 6.28a, Re = 200, P/D = 2.0

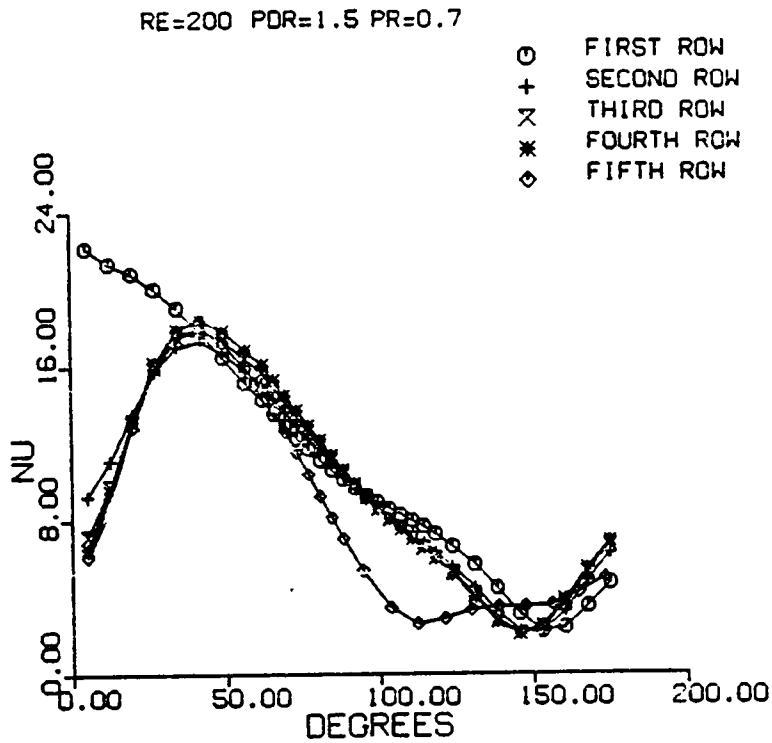

Figure 6.35d Distributions of local heat transfer coefficient around the cylinders for a five-row deep staggered bundle of cylinders in figure 6.28c, Re = 200, P/D = 1.5

the increase of P/D. In other words more compact cylinders at these Reynolds numbers will improve heat transfer characteristics but will lead to larger pressure drops and therefore higher flow resistance. Figure 6.35d shows the distribution of local heat transfer coefficient around the cylinders for the staggered square arrangement.

Figure 6.36 shows the averaged heat transfer coefficients for a P/D of 1.5 for the three cases of staggered bundles of cylinders. The experimental results of Bergelin et al. [1952] and the numerical results of Antonopoulos [1985] are also shown for comparison. The present results are in fairly good agreement with the experimental results of Bergelin et al. and the numerical results of Antonopoulos.

The drag coefficients ($C_d = \frac{p - p_{in}}{1/2\rho U_\infty^2}$) for different Reynolds numbers are shown in figure 6.37 for the case of figure 6.28a. The results of Bergelin et al. [1952] and Antonopoulos [1985] are shown for comparison. The present results predict slightly higher values of the drag coefficients as compared to the results of Bergelin et al. and Antonopoulos.

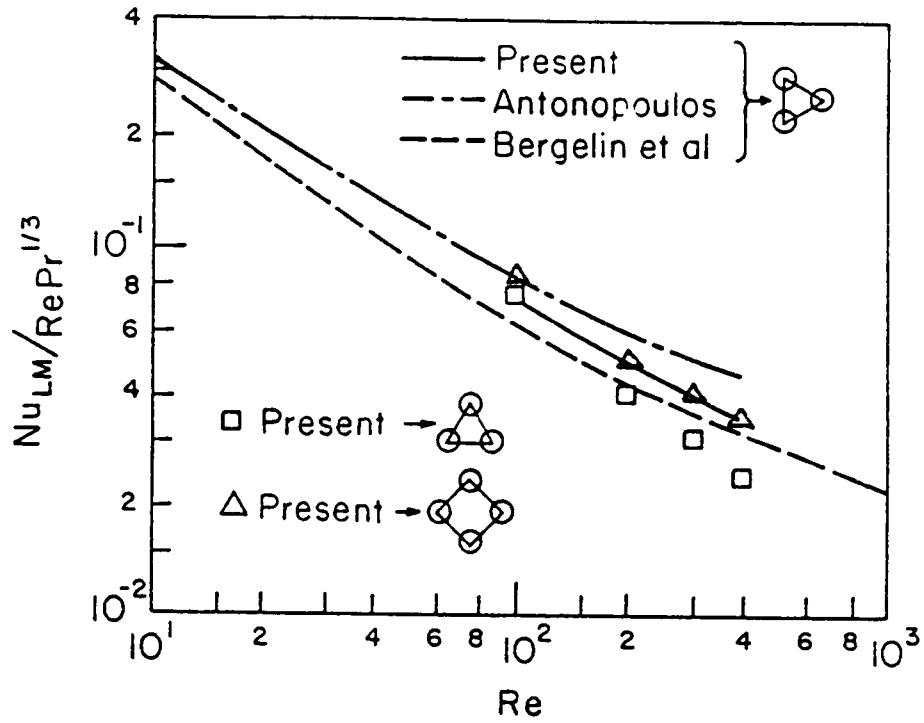

Figure 6.36 Comparison of averaged heat transfer coefficient with experimental and numerical results; P/D = 1.5

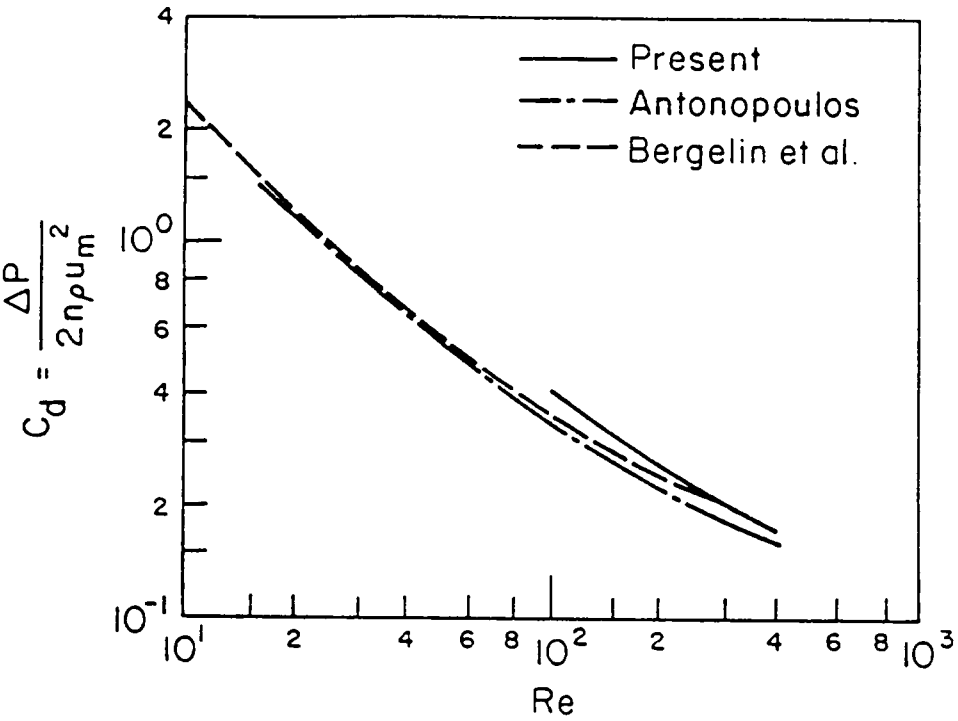

Figure 6.37 Drag coefficient for five row deep staggered bundle of cylinders in figure 6.28b

CHAPTER VII

CONCLUSIONS AND RECOMMENDATIONS

The main purpose of this investigation has been the study of the hydrodynamic interaction between bluff bodies. Circular cylinders were employed because they accomodate repeatability and are appealing to numerical analysis due to their simple shapes. Moreover, practical applications of flow past cylinders are numerous, as stated earlier. The present investigation provides experimental and numerical results which are useful in the understanding of flows past single and multiple cylinders. The experimental results include time-domain and frequency-domain data on velocity, skin friction, pressure, lift and drag for steady as well as pulsed flows. Simultaneous measurements of the different fluid dynamic quantities under identical conditions provide a more complete picture of steady and oscillatory flows past a cylinder. Results of an extensive flow visualization coupled with the detailed measurements have provided new important information on flow past in-line cylinders. Instantaneous velocity fields in the regions between cylinders have been obtained with the use of a sophisticated LDV data acquisition system. A powerful numerical method has been applied to solve the Navier-Stokes and energy equations for flow past multiple cylinders in different configurations.

Flow past a single cylinder exhibits a region from near the point of separation to around the 120 degree position where no organization of skin friction is seen for steady or pulsed flow. The magnitude of the mean skin friction and the rms of fluctuation of skin friction varies with the frequency of pulsation of the freestream. The static pressure at a point around the cylinder for pulsed flow is higher than the steady flow value when the skin friction is lower than the corresponding steady flow value and vice versa. In steady flow, the rms of fluctuation of pressure has a maximum value near the point of separation which is in agreement with other available data. Pressure fluctuations increase in proportion to driving frequency. When the free stream is pulsed at near twice the shedding frequency, the shedding frequency locks on to the subharmonic of the driving frequency.

Massive wakes of bluff bodies contain low-level energy scattered in a wide spectrum of frequencies. However, the free shear layers released at separation usually introduce some organization which appears in the form of large vortical structures. In the present study, we found that for a pitch-to-diameter ratio of 1.8, such structures are trapped in the first cavity of a triad, but they are freely shed from the second cavity. Apparently this phenomenon is independent of the effects of the wake of the last cylinder. This was tested and verified by use of a splitter plate. The shedding in multiple cylinders can be captured more easily by externally imposed disturbances as compared to shedding over a single cylinder. Such wake capture or lock-on induces an increase in the organization in the wakes and cavities, which in turn affect the heat transfer characteristics. The skin

friction distribution around the second cylinder displays a uniform shape at different driving frequencies and the rms of fluctuating skin friction is proportional to the mean skin friction. Pressure on the second cylinder around the separated region increases significantly with pulsation of the freestream at $P/D = 1.8$ and this results in a decrease in the flow resistance. For $P/D = 1.1$, however, the pressure on the cylinder in the separated region decreases with the pulsation. The rms of pressure fluctuation increases proportionately with the driving frequency irrespective of P/D ratio.

For flow past a pentad of cylinders, flow in the first gap again resembles cavity flow with two standing vortices. Vortices shed from an intermediate cylinder reattach onto the next cylinder alternately at the top and the bottom. Frequency of this shedding remains constant for all the gaps. Near the center of a gap there is no organization and the flow in this region is turbulent. Lock-on occurs again at the subharmonic of the driving frequency.

Forcing the shedding of flows has been a common exercise for single cylinders but was never attempted for multiple cylinders. Our results indicate that it is possible to lock the shedding process on the subharmonic of a driving frequency. The organization of the cavity flow is then increased.

A basic hypothesis of the present effort was that increased organization in a separated region can be detected by measurements on the surface of the body. It was in fact proved that a skin friction gauge can provide a clear indication on the organized activities of a wake. This is not true, as expected, for pressure transducers which pick up signals of phenomena that do not necessarily occur

next to the body surface. This discovery leads to another hypothesis that improved organization of wake flow implies better mixing of fluid with the free stream, which in turn results in increase of the heat transfer in the separated flow region. In the present study we provide information on the organization of the wakes, both in steady and pulsed flows. In sister studies [VandenBerghe, 1985; Gundappa, 1986] it was indeed proved that heat transfer increases exactly in the regions and for the parameters indicated by the present study.

Unlike earlier contributions, the present study is not confined to global characteristics or single point measurements of only a few quanties. It provides distributions along the entire periphery of cylinders as well as over preassigned grids of measurements in the flow. Moreover, the numerical studies generate similar detailed distributions which provide a complete picture of the physical phenomenon.

A penalty finite element method to solve the 2-D Navier-Stokes and energy equations is presented. This method is applied to flow across a single cylinder and multiple cylinders in different configurations. The advantage over finite difference methods is that in the present case irregular geometries and boundary conditions are well represented.

The method presented is readily available for a parametric study whereby the geometrical parameters, the Reynolds and Prandtl numbers, can be varied to provide comparative information. The finite element analysis generates important integral characteristics, like overall flow resistance or heat transfer. Detailed local distributions of the various fluid dynamic quantities are also obtained. We could

not find computational time data to compare with but it is believed that the present method will be slower than some efficient finite difference methods.

In the case of both in-line and staggered bundles of cylinders, the averaged heat transfer coefficients and friction factor results are in good agreement with available experimental results. The local distribution of skin friction, pressure and heat transfer coefficients are consistent with the flow characteristics indicated by velocity field vectors, streamlines, isovorticity lines, isobars and isotherms. For higher pitch to diameter ratio, the pressure drop across any one row decreases and the coefficient of heat transfer also decreases. In the range of Reynolds number studied, the staggered square arrangement gives a higher value of the averaged heat transfer coefficient as compared to the in-line and the equilateral triangular arrangements.

The effect of organized pulsation on flow past bundles of cylinders is an area for future studies. We are in the process of making these studies and results may be expected sometime in the near future. Numerical solution of time-dependent problems for high Reynolds number flows in complex geometries is another challenging area. The extension to three-dimensional flows in complex domains is also recommended. We have been working for sometime on the numerical modelling of three-dimensional flow past perpendicular arrangement of cylinders and results may soon be forthcoming.

REFERENCES

Achenbach, E., "Distribution of Local Pressure and Skin Friction around a Circular Cylinder in Cross Flow up to Re = 5,000,000", *J. Fluid Mechanics*, Vol. 34, pp. 625-639, 1968.

Achenbach, E., "Total and Local Heat Transfer and Pressure Drop of Staggered and In-line Tube Bundles", *Heat Exchangers, Thermal-Hydraulic Fundamentals and Design*, eds. Kakac, Bergles and Mayinger, Hemisphere Publishing Co., Washington DC, 1981.

Aiba, S., H. Tsuchida and T. Ota, "Heat Transfer Around Tubes in In-line Tube Banks", *Bulletin of JSME*, Vol. 25, No. 204, pp. 919-926, June 1982.

Aiba, S., H. Tsuchida and T. Ota, "Heat Transfer around a Tube in a Bank", *Bulletin of JSME*, Vol. 23, No. 181, July 1980.

Andraka, C. E. and T. E. Diller, "Heat Transfer Distribution Around a Circular Cylinder in Pulsating Crossflow", ASME Paper No. 85-GT-67, 1985.

Antonopoulos, K. A., "Heat Transfer in Tube Assemblies Under Conditions of Laminar Axial, Transverse and Inclined Flow", *International Journal of Heat and Fluid Flow*, Vol. 6, pp. 193-204, 1985.

Arie, M., M. Kiya, M. Moriya and H. Mori, "Pressure Fluctuations on the Surface of Two Circular Cylinders in Tandem Arrangement", *J. Fluids Engineering, Trans. ASME*, Vol. 105, pp. 161-167, 1983.

Bellhouse, B. J. and D. L. Schultz, "Determination of Mean and Dynamic Skin Friction, Separation and Transition in Low-Speed Flow with a Thin-Film Heated Element", *J. Fluid Mechanics*, Vol. 24, Part 2, pp. 379-400, 1966.

Benque, J. P., P. Esposito and G. Labadie, "New Decomposition Finite Element Methods for the Stokes Problem and the Navier-Stokes Equations", *Proc. of the Third International Conference on Numerical Methods in Laminar and Turbulent Flow*, pp. 563-563, August 1983.

Bergelin, O. P., G. A. Brown, H. L. Hull and F. W. Sullivan, "Heat Transfer and Fluid Friction During Viscous Flow Across Bank of Tubes - III. A Study of Tube Spacing and Tube Size", *Trans. ASME*, Vol. 72, pp. 881-888, 1950.

Bergelin, O. P., G. A. Brown and S. C. Doberstein, "Heat Transfer and Fluid Friction During Flow Across Banks of Tubes - IV. A Study of the Transition Zone Between Viscous and Turbulent Flow", *Trans.* ASME, Vol. 74, pp 953-960, 1952.

Borell, G. K., B. K. Kim, W. Ekhaml, T. E. Diller, and D. P. Telionis, "Pressure and Heat Transfer Measurements Around a Circular Cylinder in Pulsating Crossflows," *Proc. of ASME Fluid Engr. Conf.*, Feb. 1984.

Bristeau, M., R. Glowinski, J. Periaux, P. Perrier, O. Pironneau and G. Poirier, "Application of Optimal Control and Finite Element Methods to the Calculation of Transonic Flows and Viscous Incompressible Flows", Research Report No. 294, Institute de Recherche d'Informtique et d'Automatique, Le-Chesuay, France, 1978.

Brooks, A. N. and T. J. R. Hughes, "Streamline Upwind/Petrov-Galerkin Formulations for Convection Dominated Flows with Particular Emphasis on the Navier-Stokes Equations", *Computer Methods in Applied Mechanics and Engineering*, Vol. 32, pp. 199-259, 1982.

Brunn, H. H., "Interpretation of Hot-wire Probe Signals in Subsonic Air Flows", *VKI LS 96*, 1977.

Comte-Bellot, G., "The Physical Background for Hot-Film Anemometry", *Turbulence in Liquids*, eds. Patterson and Zakin, pp. 1-13, 1975.

Comte-Bellot, G., "Hot-wire Anemometry", *An. Rev. Fluid Mech.*, Vol.8, pp. 209-231, 1976.

Dennis, S. C. R. and G. Z. Chang, "Numerical Solutions for Steady Flows Past a Circular Cylinder at Reynolds Numbers up to 100", *J. Fluid Mech.*, Vol. 37, 1959.

Dhaubhadel, M. N., J. N. Reddy and D. P. Telionis, "Penalty Finite-Element Analysis of Coupled Fluid Flow anf Heat Transfer for In-line Bundle of Cylinders in Cross Flow", *Int. J. of Nonlinear Mechanics*, in press, 1986A.

Dhaubhadel, M. N., J. N. Reddy and D. P. Telionis, "Finite-Element Analysis of Fluid Flow anf Heat Transfer for Staggered Bundle of Cylinders in Cross Flow", submitted for publication in the *Int. J. of Num. Meth. in Fluids*, 1986B.

Drain, L. E., *The Laser Doppler Technique*, John Wiley & Sons, 1980.

Durst, F., A. Melling and J. H. Whitelaw, *Principles and Practice of Laser-Doppler Anemometry*, Academic Press, London, 1976.

Durst, F., "Laser Doppler Anemometry in Single and Two Phase Flows-- a Review", *Advanced Measurement Techniques in Fluid Dynamics*, VKI LS 96, 1977.

Farell, C., S. Carrasquel, O. Guven and V. C. Patel, "Effect of Wind-Tunnel Walls on the Flow Past Circular Cylinders and Cooling Tower Models", *Trans. ASME*, Paper No. 76WA/FE-20, pp. 470-479, 1977.

Fujii, M., T. Fujii and T. Nagata, "A Numerical Analysis of Laminar Flow and Heat Transfer of Air to In-line Tube Bank", *Numerical Heat Transfer*, Vol.7, pp. 89-102, 1984.

Glowinski, R., B. Mantel, J. Periaux and O. Pironneau, "H^{-1} Least Squares Method for the Navier-Stokes Equations", *Numerical Meth. in Laminar and Turbulent Flow*, Proc. of the First Int. Conf., Swansea, UK, 1978.

Gresho, P. M., S. T. Chan, R. L. Lee and C. D. Upson, "A Modified Finite Element Method for Solving the Time Dependent Incompressible Navier-Stokes Equations", *Journal of Numerical Method in Fluids*, Vol. 4, pp. 619-640, 1984.

Gundappa, M., Ph.D. Dissertation, VPISU, 1986.

Hiwada, M., I. Mabuchi and H. Yanagihara, "Fluid Flow and Heat Transfer Around Two Circular Cylinders", *Bulletin of the JSME*, Vol. 25, No. 209, 1982.

Igarashi, T., "Characteristics of the Flow around Two Circular Cylinders Arranged in Tandem", *Bulletin JSME*, Vol. 27, No. 233, pp. 2380-2387, 1984.

Igarashi, T. and K. Suzuki, "Characteristics of the Flow around Three Circular Cylinders Arranged in Line", *Bulletin of the JSME*, Vol. 27, No. 233, pp. 2397-2404, 1984.

Ishigai, S. and E. Nishikawa, "Experimental Study of Structure of Gas Flow in Tube Banks with Tube Axes Normal to Flow", *Bulletin of the JSME*, Vol. 18, No. 119, pp. 528-535, 1975.

Jones, G. S., "Measurement and Visualization of Vortex Shedding--Natural and Forced", M.S. Thesis, VPISU, 1980.

Jordan, S. and J. Fromm, "Oscillatory Drag, Lift and Torque on a Circular Cylinder in a Uniform Flow", *Phys. Fluids*, Vol. 15, 1972.

Karniadakis, G. E., B. B. Mikic and A. T. Patera, "Unsteady Heat Transfer from a Cylinder in Cross Flow; A Direct Numerical Simulation", *Proc. of the Eighth Int. Heat Transfer Conf.*, Vol. 2, pp. 429-434, 1986.

Kawaguti, M., "Numerical Solution of the Navier-Stokes Equations for the Flow around a Circular Cylinder at Reynolds Number 40", *J. Phys. Soc. Japan*, Vol. 8, 1953.

Kawahara, M. and H. Hirano, "A Finite Element Method for High Reynolds Number Viscous Fluid Flow Using Two Step Explicit Scheme", *International Journal of Numerical Methods in Fluids*, Vol. 3, pp. 137-163, 1983.

Kawamura, T. and K. Kuwahara, "Computation of High Reynolds Number Flow Around a Circular Cylinder wiyh Surface Roughness", AIAA-84-0340, January 1984.

Kestin, J., P. F. Meader and H. H. Sogin, "The influence of Turbulence on the Transfer of Heat to Cylinders near the Stagnation Point", *Z. Agneu. Math. Phys.*, Vol. 12, pp. 115-132, 1969.

Kim, B. K., G. J. Borell, M. S. Cramer, T. E. Diller, and D. P. Telionis, "Pulsating Flow and Heat Transfer Over a Circular Cylinder," *Proc. Symp. on Nonlinear Problems in Energy Engr.*, DOE CONF-830313, 1983.

Koromilas, C. A., "Experimental Investigation of Unsteady Separation", Ph.D. Dissertation, VPISU, 1978.

Kostic, Z. G. and S. N. Oka, "Fluid Flow and Heat Transfer with Two Cylinders in Cross Flow", *Int. J. of Heat and Mass Transfer*, Vol. 15, pp. 279-299, 1972.

Kostic, Z. and S. Oka,"Fluid Flow and Convection Heat Transfer in Boundary Layer on Smooth Cylindrical Surface of a Tube in a Tube Bank in a Crossflow", *Heat and Mass Transfer in Boundary Layers*, Vol. 1, pp. 451-458, 1972.

Launder, B. E. and T. H. Massey, "Numerical Predictions of Viscous Flow and Heat Transfer in Tube Banks", *Journal of Heat Transfer*, Vol. 100, pp. 565-571, 1978.

Lebouche, M. and M. Martin, "Convection Forcee Autour du Cylindre; Sensibilite aux Pulsations de L'Ecoulement Externe", *International Journal of Heat and Mass Transfer*, Vol. 1825, pp. 1161-1175, 1975.

LeFeuvre, R. F., "Laminar and Turbulent Forced Convection Processes Through In-line Tube Banks", Imperial College London, Mech. Eng. Dept., HTS/74/5, 1973.

Lomas, C. G., *Fundamentals of Hot Wire Anemometry*, Cambridge University Press, 1986.

Mathioulakis, D., "Vorticity Shedding over Two Dimensional Bodies", Ph.D. Dissertation, VPISU, 1985.

Meier, H. U., H. P. Kreplin and L. W. Fang, "Experimental Study of Two- and Three-Dimensional Boundary Layer Separation", *Unsteady Turbulent Shear Flows*, Eds. Michel, Cousteix and Houdeville, Springer-Verlag, N. Y., pp. 87-99, 1981.

Mezaris, T. B., "Visualization and LDV Measurements of Separating Oscillatory Laminar Flows", M.S. Thesis, VPISU, 1979.

Morgan, V. T., "The Overall Convective Heat Transfer from Smooth Circular Cylinders", *Advances in Heat Transfer*, Vol. II, Academic Press, pp. 199-264, 1975

Pfiefer, H., "Measurements in Gas Flows and Flames", VKI LS 1981-3, 1981.

Poling, D. R., "Airfoil Response to Periodic Disturbances--The Unsteady Kutta Condition", Ph.D. Dissertation, VPISU, 1985.

Reddy, J. N., "On Penalty Function Methods in the Finite Element Analysis of Flow Problems", *Int. J. of Numerical Methods in Fluids*, Vol. 2, pp. 151-171, 1982.

Reddy, J. N., "Penalty-Finite-Element Analysis of 3-D Navier-Stokes Equations", *Computer Methods in Applied Mechanics and Engineering*, Vol. 35, pp. 87-106, 1982.

Reddy, J. N., "Penalty-Finite Element Methods in Conduction and Convection Heat Transfer", *Numerical Methods in Heat Transfer*, Vol. II, pp. 145-177, 1983.

Reddy, J. N., *Applied Functional Analysis and Variational Methods in Engineering*, McGraw-Hill, New York, 1986.

Reddy, J. N., *An Introduction to the Finite Element Method*, McGraw-Hill, New York, 1984.

Roshko. A., "Experiments on the Flow Past a Circular Cylinder at very High Reynolds Numbers," *J. Fluid Mech.*, Vol. 10, pp. 345-356, 1961.

Savkar, S. D., "A Survey of Flow Induced Vibrations of Cylindrical Arrays in Crossflow", ASME Paper No. 76-WA/FE-21, 1976.

Saxena, V. C. and A. D. K. Laird, "Heat Transfer from a Cylinder Oscillating in a Cross-Flow", *J. Heat Transfer, Trans. ASME*, Vol. 100, pp.684-689, 1978.

Scheiman, J. and J. D. Brooks, "Comparison of Experimental and Theoretical Turbulence Reduction from Screens, Honeycomb and Honeycomb-Screen Combinations", AIAA-80-0433R, 1980.

Smith, S. L. and C. A. Brebbia, "Improved Stability Techniques for the Solution of Navier-Stokes Equations", *Appl. Math. Modelling*, Vol. 1, pp. 227-234, 1977.

Son, J. S. and T. J. Hanratty, "Velocity Gradients at the Wall for Flow Around a Cylinder at Reynolds Numbers from 5,000 to 50,000", *Journal of Fluid Mechanics*, Vol. 35, Part 2, pp. 353-368, 1969.

Son, J. S. and T. J. Hanratty, "Numerical Solution for the Flow around a Circular Cylinder at Reynolds Numbers of 40, 200 and 500", *Journal of Fluid Mechanics*, Vol. 35, Part 2, pp. 369-386, 1969.

Swanson, J. and M. Spaulding, "Three Dimensional Numerical Model of Vortex Shedding behind a Cylinder", *Nonsteady Fluid Dynamics*, ASME, 1978.

Tavakoli, T., B. K. Kim, G. J. Borell, T. E. Diller, and and D. P. Telionis, "Design and Evaluation of a Pulsating Flow Wind Tunnel", VPI-E-83-41, 1983.

Telionis, D. P., D. Mathioulakis, B. K. Kim and G. S. Jones, "Calibration of the ESM Water Tunnel" to appear as VPISU report, 1984.

VandenBerghe, T., M. N. Dhaubhadel, T. E. Diller and D. P. Telionis, "Pulsating Flow and Heat Transfer Over Multiple Cylinders", *Proc. of the Third Symp. on Energy Engineering Sciences*, DOE CONF-8510176, pp. 240-247, Oct. 1985.

VandenBerghe, T. M., "Heat Transfer from In-line and Perpendicular Arrangements of Cylinders in Steady and Pulsating Crossflow", M. S. Thesis, VPISU, 1985.

West, G. S. and C. J. Apelt, "The Effects of Tunnel Blockage and Aspect Ratio on the Mean Flow Past a Cicular Cylinder with Reynolds Numbers between 10,000 and 100,000", *Journal of Fluid Mechanics*, Vol. 114, pp. 361-377, 1982.

Zdravkovich, M. M., "Review of Flow Interference Between Two Circular Cylinders in Various Arrangements", *Trans. of the ASME*, pp. 618-633, 1977.

Zukauskas, A.,"Heat Transfer from Tubes in Cross Flow", *Adv. Heat Transfer*, Vol. 8, pp. 93-160, 1972.

Zukauskas, A., V. I. Katinas and E. E. Perednis, "Average Heat Transfer Coefficients of Tube Bundles in Flows of Viscous Fluids at Angles of Attack", *Heat Transfer-Soviet Research*, Vol. 15, No. 2, 1983.

APPENDIX A

LDV DATA ACQUISITION PROGRAM

Glossary of terms:

T1998, C1998, I1998 : Subroutines used for digital data acquisition supplied by TSI and modified for this work.
DX, DY, NX and NY : Step size in mm and total number of steps to be executed in each of the X- and Y-directions to confirm to a preselected grid system.
CONSTX, CONSTY : Calibration constants for X-LVDT and Y-LVDT transducers.
IFIRST : Begining channel number, Rest of the channel numbers become IFIRST + 1, IFIRST + 2 etc.
PERIOD : Time between two consecutive data points.
NE : Number of points per ensemble.
MS : Numbers of ensembles.
ISTEPX : Number of pulses sent to horizontal stepping motor for traversing a distance of DX.
ISTEPy : Number of pulses sent to vertical stepping motor for traversing a distance of DY.
IDIRX : Direction of horizontal traverse = 1 for downstream and = 4 for upstream.
IDIRY : Direction of vertical traverse = 1 for downward and = 4 for upward.
VOLTX : Voltage output from LVDT-X corresponding to X-location of the measuring volume.
VOLTY : Voltage output from LVDT-Y corresponding to Y-location of the measuring volume.
IBUF : Array used to temporarily store the digital data.
X1, X2 and X3 : Arrays containing voltages (0-5.12V) corresponding to the data stored in IBUF(,1), IBUF(,2) and IBUF(,3) respectively.
BA(,n) : Array in which Xn data are stored.

Subroutines :
GETSTR : specifies the name of the data file. Name of the data file is an alphanumeric string of upto 14 charaters.
OPEN : opens the data file specified by GETSTR.
XRATE, CLOCKA : activate the clock such that there is one A/D conversion every PERIOD.
IPOKE(*A,B) : assigns the number B to the memory location of address A. For instance the digital-out module of the MINC has 171262 as its address and D/A converter has the address 171066.
IADINP : reads the voltage from the LVDT's.
T1998 : data acquisition routine for 1000 real data points.
SETBUF, RLSBUF : define the buffer array where the data are stored.
ADSWP : activates the A/D converter. Conversion for each channel is started simultaneously by an external trigger.
IWTBUF : wait for the buffer to be available. When buffer is available save data.
BOUNDS : calculates the maximum and minimum values of a set.

GRINIT, GRREGN, GRAPHS : plot data on the screen.
VTCLR : Clears the screen.
STPSWP : stops the data acquisition process
CLOSE : closes the data file.

PROGRAM LISTING :

```
      PROGRAM CAVITY
      EXTERNAL T1998,C1998,GTDMA,I1998
      INTEGER*2 INFO(40),IBUF(1024,1),IGINFO(30),FNAME(15)
      REAL*4 X1(512),X2(512),X3(512),BA(512,3),X11(512)
      TYPE 100
100    FORMAT('$INPUT DX = = >')
      ACCEPT *,DX
      TYPE 101
101    FORMAT('$INPUT DY = = >')
      ACCEPT *,DY
      TYPE 102
102    FORMAT('$INPUT NX = = >')
      ACCEPT *,NX
      TYPE 103
103    FORMAT('$INPUT NY = = >')
      ACCEPT *,NY
      TYPE 104
104    FORMAT('$INPUT CONSTX = = >')
      ACCEPT *,CONSTX
      TYPE 105
105    FORMAT('$INPUT CONSTY = = >')
      ACCEPT *,CONSTY
      CALL IPOKE("44,IPEEK("44),OR,"100)
      TYPE 106
106    FORMAT('$INPUT MAXIMUM NUMBER OF MEASUREMENTS = = >')
      ACCEPT *,MMAX
      TYPE 107
107    FORMAT('$ENTER BEGINING CHANNEL NUMBER = = >')
      ACCEPT *,IFIRST
      TYPE 108
108    FORMAT('$ENTER INTER SAMPLE INTERVAL IN SEC = = >')
      ACCEPT *,PERIOD
      TYPE 109
109    FORMAT('$ENTER NUMBER OF POINTS PER SAMPLE = = >')
      ACCEPT *,NE
      DO 122 I=1,NE
      DO 122 J=1,3
122    BA(I,J)=0.
      DO 130 I=1,NE
130    X11(I)=I*PERIOD
      TYPE 110
110    FORMAT('$ENTER NUMBER OF ENSEMBLES = = >')
      ACCEPT *,MS
      TYPE 111
111    FORMAT('$ENTER FILESPEC OF DATA FILE = = >')
      CALL GETSTR(5,FNAME,14,EFLG)
      OPEN (NAME=FNAME,TYPE='NEW',UNIT=10)
      TYPE 112
112    FORMAT('$INPUT INDEX OF POSITION; INITIAL=1 = = >')
```

```
      ACCEPT *,MPAR
      CALL XRATE(PERIOD,IRATE,IPRE)
      CALL CLOCKA(IRATE,IPRE,IND)
      IF(IND.EQ.0) STOP 'CLOCKA ERROR'
      ISTEPY=IFIX(ABS(DY)*80.)
      ISTEPX=IFIX(ABS(DX)*250.)
      DO 1 IX=1,NX
      DO 2 JY=1,NY
       IF(JY.EQ.1) GO TO 25
      IDIRY=4
      CALL IPOKE("171066,4095)
      DO 3 K=1,ISTEPY
      CALL IPOKE("171262,IDIRY)
      DO 4 KK = 1,150
4     CONTINUE
      CALL IPOKE("171262,0)
      DO 3 M = 1,10
3     CONTINUE
25    CALL IADINP(,4,IVALY)
      VOLTY=(IVALY-2048)*0.0025
      IF(JY.EQ.1) VOLTY0=VOLTY
      IF(JY.EQ.1) GO TO 21
      YLVDT=(-VOLTY+VOLTY0)/CONSTY
      DIFFY=(JY-1)*DY-YLVDT
      WRITE(7,777) DIFFY,YLVDT,VOLTY,VOLTY0
777    FORMAT(4F10.5)
      IF(ABS(DIFFY).LT.0.01) GO TO 21
      IDIRY=1
      IF(DIFFY.GT.0) IDIRY=4
      ISTEPDY=IFIX(ABS(DIFFY)*80)
      CALL IPOKE("171066,4095)
      DO 23 JJ=1,ISTEPDY
      CALL IPOKE("171262,IDIRY)
      DO 24 KK=1,150
24    CONTINUE
      CALL IPOKE("171262,0)
      DO 23 KK=1,10
23    CONTINUE
      GO TO 25
21    CONTINUE
C     INITIALIZE BUFFER SYSTEM
C     DELAY LOOP
55    TYPE 35
35    FORMAT('$DELAY LOOP STARTED')
      DO 230 I1=1,80
      DO 230 I2=1,80
      DO 230 I3=1,80
230    CONTINUE
      TYPE 36
36    FORMAT('$DELAY LOOP FINISHED')
C     T1998 IS A MODIFIED VERSION OF TSI SUPPLIED DIGITAL
C     DATA ACQUISITION ROUTINE USED TO GET 1000 REAL TIME
C     DATA POINTS. T1998 ALSO CALLS TSI'S C1998 AND I1998.
      CALL T1998
      MP=3*NE
C     START A/D CONVERSION WITH EXTERNAL TRIGGER
```

```
      ML=MS*NE
      PAR4=1./FLOAT(ML)
      DCV=0.
      DCV2=0.
      DCV3=0.
      DO 150 J=1,MS
      CALL SETIBF(INFO,IND,,IBUF(1,1))
      CALL RLSBUF(INFO,IND,0)
      CALL ADSWP(INFO,MP,1,256,,,,IFIRST,3)
      WRITE(7,27) J,IX,JY
27     FORMAT(10X,3I5)
C     WAIT FOR BUFFER OR CARRIAGE RETURN. IF BUFFER BECOMES
C     AVAILABLE, SAVE THE DATA.
      WRITE(7,40) INFO(1)
      CALL IWTBUF(INFO,,IBUFN,IND)
      WRITE(7,40) IND
      PAR1=1./FLOAT(J)
      PAR2=FLOAT(J-1)/FLOAT(J)
      IF(ITTINR().GE.0) GO TO 510
      DO 16 I=1,NE
      V1=((IBUF(I*3-2,IBUFN+1).AND."7777)-2048)*.0025
      X1(I)=V1*PAR1+BA(I,1)*PAR2
      BA(I,1)=X1(I)
      V2=((IBUF(I*3-1,IBUFN+1).AND."7777)-2048)*.0025
      X2(I)=V2*PAR1+BA(I,2)*PAR2
      BA(I,2)=X2(I)
      V3=((IBUF(I*3,IBUFN+1).AND."7777)-2048)*.0025
      X3(I)=V3*PAR1+BA(I,3)*PAR2
      BA(I,3)=X3(I)
      DCV=DCV+V1*PAR4
      DCV2=DCV2+V2*PAR4
      DCV3=DCV3+V3*PAR4
      SUMSQ1=SUMSQ1+V1*V1
      SUMSQ2=SUMSQ2+V2*V2
      SUMSQ3=SUMSQ3+V3*V3
16     CONTINUE
150    CONTINUE
      RMS1=SQRT(SUMSQ1/FLOAT(ML))
      RMS2=SQRT(SUMSQ2/FLOAT(ML))
      RMS3=SQRT(SUMSQ3/FLOAT(ML))
40     FORMAT(I5)
      CALL BOUNDS(1,BA(1,1),VMAX1,VMIN1,NE)
      CALL BOUNDS(1,BA(1,2),VMAX2,VMIN2,NE)
      CALL BOUNDS(1,BA(1,3),VMAX3,VMIN3,NE)
      DU1=VMAX1-VMIN1
      DU2=VMAX2-VMIN2
      DU3=VMAX3-VMIN3
      WRITE(10,503) DCV,DCV2,DCV3,DU1,DU2,DU3,VMAX1,VMAX2,VMAX3
      WRITE(10,504) DCV,DCV2,DCV3
      WRITE(10,502) RMS1,RMS2,RMS3,MPAR,IX,JY,IDIRX,IDIRY
      WRITE(10,501) (BA(I,1),I=5,NE,5)
      WRITE(10,501) (BA(I,2),I=5,NE,5)
      WRITE(10,501) (BA(I,3),I=5,NE,5)
501    FORMAT(1X,8F8.4)
502    FORMAT(3F10.5,5I6)
503    FORMAT(1X,9F7.4)
```

```
504    FORMAT(3F10.5)
C     PLOT RESULTS
      CALL GRINIT(IGINFO)
      CALL GRREGN(IGINFO,0,1)
      CALL GRAPHS(IGINFO,,X11,BA(1,1),NE,,0)
      CALL GRREGN(IGINFO,1,2)
      CALL GRAPHS(IGINFO,,X11,BA(1,2),NE,,1)
C     DELAY LOOP OF ABOUT 5 SECONDS
      DO 43 I1 = 1,60
      DO 43 I2 = 1,60
      DO 43 I3 = 1,60
43     CONTINUE
C     ERASE THE SCREN
      CALL VTCLR
      WRITE(7,502) MPAR
      WRITE(7,501) DCV,DCV2,DCV3,DU1,DU2,DU3
2      CONTINUE
      YMAX = (NY-1)*DY
      IDIRY = 1
      IYMAX = IFIX(ABS(YMAX)*80.)
      CALL IPOKE("171066,4095)
      DO 300 K = 1,IYMAX
      CALL IPOKE("171262,IDIRY)
      DO 301 KK = 1,150
301    CONTINUE
      CALL IPOKE("171262,0)
      DO 300 KJ = 1,10
300    CONTINUE
225    CALL IADINP(,4,IVALY)
      VOLTY = (IVALY-2048)*.0025
      YLVDT = (-VOLTY + VOLTY0)/CONSTY
      DIFFY = 0.0-YLVDT
      WRITE(7,777) DIFFY,YLVDT,VOLTY,VOLTY0
      IF(ABS(DIFFY).LT..01) GO TO 221
      IDIRY = 1
      IF(DIFFY.GT.0.) IDIRY = 4
      ISTEPDY = IFIX(ABS(DIFFY)*80.)
      CALL IPOKE("171066,4095)
      DO 223 JJ = 1,ISTEPDY
      CALL IPOKE("171262,IDIRY)
      DO 224 KK = 1,150
224    CONTINUE
      CALL IPOKE("171262,0)
      DO 223 KK = 1,10
223    CONTINUE
      GO TO 225
221    CONTINUE
      IDIRX = 4
      CALL IPOKE("171066,0)
      DO 5 IJ = 1,ISTEPX
      CALL IPOKE("171262,IDIRX)
      DO 6 IK = 1,150
 6    CONTINUE
      CALL IPOKE("171262,0)
      DO 5 JK = 1,10
5      CONTINUE
```

```
26     CALL IADINP(,5,IVALX)
       VOLTX = (IVALX-2048)*0.0025
       IF(IX.EQ.1) VOLTX0 = VOLTX
       IF(IX.EQ.1) GO TO 22
       XLVDT = (-VOLTX + VOLTX0)/CONSTX
       DIFFX = (IX-1)*DX-XLVDT
       WRITE(7,777) DIFFX,XLVDT,VOLTX,VOLTX0
       IF(ABS(DIFFX).LT.0.01) GO TO 22
       IDIRX = 1
       IF(DIFFX.GT.0.) IDIRX = 4
       ISTEPDX = IFIX(ABS(DIFFX)*250)
       CALL IPOKE("171066,0)
       DO 280 IJ = 1,ISTEPDX
       CALL IPOKE("171262,IDIRX)
       DO 28 IKK = 1,150
28     CONTINUE
       DO 280 IJJ = 1,10
280    CONTINUE
       GO TO 26
22     CONTINUE
 1     CONTINUE
510    CALL STPSWP(INFO,,IND)
       CLOSE(UNIT = 10)
       STOP
       END
```

APPENDIX B

DATA ACQUISITION PROGRAM FOR PRESSURE AND SHEAR STRESS MEASUREMENTS

```
10 CLS:CLEAR 250:PRINT@256,"DATA AQUISITION SYSTEM ONLINE"
20 POKE 16916,2:'      PROTECT SCROLLING CLOCK
30 POKE 16419,196
40 PRINT@320,"MODIFIED VERSION - VANDENBERGHE AND
  ANDRAKA'S DATA ACQUISITION PROGRAMME"
42 PRINT@448,"THIS PROGRAMME READS ACRMS AND DC 0-10 VOLTS
  ON FOUR CHANNELS "
50 INPUT"<ENTER> TO CONTINUE";G$
51 CLS
60 GOSUB  1000              'GOTO SETUP ROUTINE
70 CLS:PRINT @99,USING"POSITION=  ####.## DEGREES";
  P0/20;:PRINT @256,"ENTER  <M>AN
80 M$=INKEY$ M$="" GOTO80
90 IF LEFT$(M$,1)="R" GOTO 150
100 IF LEFT$(M$,1)="J" GOSUB 2130
110 IF LEFT$(M$,1)="M" GOSUB 2030
120 IF LEFT$(M$,1)="C" GOSUB 2360
130 IF M$="L" GOSUB 8000
135 IF M$="Q" GOTO 180
136 IF M$="S" CMD"I","DO T2400Z"
140 GOTO 70
150 GOSUB 3000 :'      RUN SETUP
160 IF RS=1 GOTO70
170 GOSUB 5050 :'      RUN ROUTINE
180 CLS
190 PRINT"DATA ARE STORED IN THE FOLLOWING FILES:"
200 FOR I=1 TO NG
210 PRINT USING "GAUGE ## IN FILE %        %";I,NM$(I)
220 NEXT I
230 RE=INP(252) OR 16:OUT 236,RE
240 OUT 18,0
241 OPEN "E",1,NM$(1)
242 PRINT#1," 1000   ";TM(1)
243 CLOSE 1
250 INPUT "RUN AGAIN?";G$ G$="Y" GOTO 70
260 POKE 16916,0
270 END
1000 REM *****:SETUP ROUTINE
1010 DIM J%(5000),T1%(64),N1(4),N(4),T(4),TM(35)
1020 DIM NM$(4),GL(4),GAN(4),GD$(4),DS(12,4)
1030 DIM AVG(4),SD(4),TC$(35)
1040 CMD"L","DMACH2/CMD"
1050 DEFUSR1=&HFE00:REM     STEPPER ROUTINE
1060 DEFUSR3=&HFF00:REM     TEMPERATURE ROUTINE
1070 DEFUSR4=&HFE4A:REM     ADC ROUTINE
1080 DEFUSR6=&HFEA4:REM      ADC AVERAGING ROUTINE
```

```
1090 DEFUSR5=&HFDC0:REM       DIRECTORY CHECK ROUTINE
1100 POKE &HFFFF,&HCC
1120 RE=INP(252):RE=RE OR 16:OUT(236),RE
1130 OUT(17),0
1140 OUT(18),0
1170 PRINT @384,;:INPUT"ROTATE CYLINDER TO START AND
   INPUT POSITION OF PROBE #1
1180 P0=P0*20
1190 OUT(17),&HCC
1200 CMD"R"    'TURN ON CLOCK
1210 CLS:PRINT@384,"RESET CLOCK (Y/N)":
1220 G$=INKEY$ G$=""GOTO 1220
1230 IF G$<>"Y" GOTO 1280
1240 PRINT @384,"INPUT HOUR,MIN,SEC: ";:INPUT T(1),T(2),T(3)
1250 FOR I=1 TO 3
1260 POKE 16922-I,T(I)
1270 NEXT I
1280 RETURN
2000 '*******
2010 'MANUAL POSITIONING ROUTINE
2020 '*******
2030 PRINT @256,""
2040 INPUT "NEW POSITION";P:P1=INT(P*20+.5)  '200 ST/REV, 36:1 RATIO
2050 PC%=P1-P0                'CHANGE POSITION
2060 X=USR1(PC%)                'ROTATE TUBE
2070 P0=P1                   'NEW POSITION
2080 PRINT @99, USING "POSITION=  ####.## DEGREES";P0/20
2090 GOTO 2560          'EXIT
2100 '*******
2110 'JOG ROUTINE
2120 '*******
2130 SJ=1:DI=0
2140 SJ=1
2150 PRINT @256,"FUNCTIONS:";TAB(40);
   "CURRENT CONDITIONS:":PRINT "   0 TO END JO
2160 GOTO 2250
2170 JO$=""
2180 PRINT @593,"";CHR$(30);:JO$=INKEY$ JO$=""GOTO 2180
2190 IF JO$="0"GOTO 2560
2200 IF JO$="L" INPUT JO$
2210 IF JO$="."LET DI=DI+1:GOTO 2250
2220 IF VAL(JO$)>.5 LET SJ=VAL(JO$):GOTO 2250
2230 PC%=((-1)[DI)*SJ
2240 GOTO2290
2250 IF (-1)[DI>=0 PRINT @424, "POSITIVE DIRECTION";
2260 IF (-1)[DI<0 PRINT @424, "NEGATIVE DIRECTION";
2270 PRINT @488, USING "SPEED=  #### STEPS/CYCLE";SJ;
2280 GOTO 2170
2290 P0=P0+PC%
2300 X=USR1(PC%)
2310 PRINT @99, USING "POSITION=  ####.## DEGREES";P0/20
2320 GOTO2170
2330 '*******
2340 'CALIBRATE ADC AMPS
2350 '*******
2360 CLS:PRINT @384,"CALIBRATE WHAT CHANNEL?(0 TO FINISH)"
```

```
2370 G$=INKEY$:IFG$="" GOTO 2370
2380 CN=VAL(G$):CLS
2390 IF CN>4 GOTO 2360
2400 IF CN=0 RETURN
2410 I=1
2420 RE=INP(252)OR 16
2430 OUT 236,RE
2440 OUT 9,16-CN
2450 J%(I)=INP(12)+256*(INP(13)AND 15)  'GET VALUE
2460 I=I+1 THEN I=1
2470 AV=0              'CLEAR AVERAGE
2480 FOR J=1 TO 8
2490 AV=AV+J%(J)
2500 NEXT J            'GET AVG OF LAST 8
2510 AV=AV/8
2520 PRINT@384,"AMP ";CN;" OUTPUT=";USING"###.####";(2048-AV)/204.8;
2530 PRINT" VOLTS"
2535 G$=INKEY$ G$="V"GOSUB 2551
2540 IF G$<>"" GOTO 2360
2550 GOTO 2440
2551 J%(0)=16-CN:H%=10:X=100
2552 H%=VARPTR(J%(0))
2553 X=USR4(H%)
2554 AVG#=0
2555 FOR IB=0 TO 3:AVG#=AVG#*256+PEEK(&HFFDB-IB)
2556 NEXT IB
2557 PRINT:AVG=AVG#/5000:PRINT USING"AVG=  ##.#### VOLTS";
   (2048-AVG)/204.8
2558 G$="":RETURN
2560 :PRINT @640,"HIT
   Z' TO RESET ZERO; ELSE
ENTER"
2570 Z$=INKEY$ Z$="" GOTO 2570
2580 IF Z$="Z" LET P0=0
2590 RETURN
3000 '*****************************************************
3010 'RUN SETUP ROUTINE
3020 '   -INPUTS SPECIFICATIONS FOR THIS RQN
3030 '*****************************************************
3040 CLS
3050 H%=100
3060 I%=100
3070 X=100
3080 SD=0
3090 AVG=0
3100 WT=1
3110 RS=0
3200 CLS:POKE 16916,2
3210 INPUT"INPUT NO. CHANNELS";NG
3260 CLS
3280 POKE 16916,5
3290 PRINT
3300 INPUT"  ENTER TEST # ";NM$(1)
3305 NM$(1)=NM$(1)+"/DAT:1"
3310 IF LEN(NM$(I))<4  NM$(I)="0"+NM$(I):GOTO 3310
3320 NM$(I)="D"+NM$(I)+"/DAT:1"
```

```
3330 I% = VARPTR(NM$(I))
3340 H% = PEEK(I% + 1) + 256*PEEK(I% + 2)-65536
3350 X = USR5(H%)
3360 IF X = 1 PRINT " < ENTER > WHEN PROBLEM SOLVED ";:GOTO 3260
3370 IF X = 2 PRINT"TEST # EXISTS. ";:GOTO 3300
3380 CLS
3430 GAN(I) = 1
3440 INPUT"INPUT FOUR AMPLIFIER GAINS";GW,GX,GY,GZ
3460 POKE 16916,2
3470 CLS
3490 NTC = 1
3500 CLS
3560 CLS
3570 GOTO 3620
3580 FOR I = 3 TO NTC
3590 TC$(I) = CHR$(62 + I)
3600 NEXT I
3610 TC$(1) = "AMBIENT":TC$(2) = "FLOW"
3620 PRINT @256,:INPUT"OSCILATION FREQUENCY (HZ.) = ";FRQ
3630 PRINT @256,:INPUT"OSCILATION AMPLITUDE (%) = ";AMP
3640 PRINT @256,:INPUT"PITOT TUBE READING, (IN. H2O) = ";DP
3650 PRINT @256,:INPUT"BAROMETER PRESSURE (IN HG.) = ";AIRPR
3655 INPUT"INPUT L/D:";LD
3657 INPUT"COMMENTS? ";CM$
3660 CLS
3670 POKE 16916,6
3680 PRINT
3690 PRINT"ENTER NUMBER OF SECTIONS- ":PRINT
   "NEW SECTIONS ARE NEEDED FOR DIFFER
3700 ND = 0
3701 GOTO3710
3703 ND = 5
3704 DS(1,1) = 0:DS(1,2) = -5:DS(1,3) = 14
3705 DS(2,1) = -70:DS(2,2) = -2:DS(2,3) = 5
3706 DS(3,1) = -80:DS(3,2) = -1:DS(3,3) = 10
3707 DS(4,1) = -90:DS(4,2) = -2:DS(4,3) = 5
3708 DS(5,1) = -100:DS(5,2) = -5:DS(5,3) = 17
3709 GOTO3860
3710 INPUT"     TOTAL SECTIONS THIS RUN (-1 = DEFAULT):";ND
3720 IF ND < 1 GOTO3703
3730 CLS
3740 FOR I = 1 TO ND
3750 PRINT "  DATA SECTION #";I
3760 PRINT:INPUT"ENTER START POINT, INCR,
   # OF PTS.:";DS(I,1),DS(I,2),DS(I,3)
3770 PRINT"  STOP FOR HEATER ADJUST AFTER SECTION?(Y/ < N > )"
3780 G$ = INKEY$ G$ = "" GOTO 3780
3790 IF G$ = "Y" DS(I,4) = 1 ELSE DS(I,4) = 0
3800 CLS:NEXT I
3810 POKE 16916,2
3820 CLS
3830 PRINT "RUN SETUP:  ( < Y > /N)"
3840 POKE 16916,4
3850 PRINT
3860 PRINT "   THERE ARE ";NG;" ACTIVE GAUGES"
3870 PRINT
```

```
3880 FOR I=1 TO NG
3890 PRINT " FOR GAUGE ";I;":"
3900 PRINT "   -TYPE= ",GD$(I)
3910 PRINT "   -LOCATION= ";GL(I)
3920 PRINT "   -AMPLIFIER= "GAN(I)
3930 PRINT "   -DATA FILE= "NM$(I)
3940 G$=INKEY$ G$="" GOTO 3940
3950 IF G$="N" PRINT"REENTER":GOTO 3200
3960 POKE16916,0:CLS
3970 NEXT I
3980 PRINT "   -";NTC;" THERMOCOUPLES WILL BE ACTIVE"
3990 PRINT"   -OSC. FREQUENCY= ";FRQ;" HZ."
4000 PRINT"   -OSC. AMPLITUDE= ";AMP;" %"
4010 PRINT"   -PITOT TUBE READS ";DP;" IN. WATER"
4020 PRINT"   -PRINT BAROMETER IS ";AIRPR;" IN. HG."
4030 G$=INKEY$ G$="" GOTO 4030
4040 IF G$="N" PRINT "REENTER":GOTO 3200
4050 CLS
4060 PRINT" RUN POSITIONS (DEGREES) OF REF LOCATION:"
4070 FOR I=1 TO ND
4080 FOR J=1 TO DS(I,3)
4090 PRINT DS(I,1)+(J-1)*DS(I,2);",";
4100 NEXT J
4110 PRINT
4120 IF DS(I,4)=1 PRINT"PAUSE FOR HEATERS" ELSE PRINT "CONTINUE"
4130 NEXTI
4140 G$=INKEY$ G$="" GOTO 4140
4150 IF G$="N" PRINT"REENTER":GOTO 3200
4160 CLS:PRINT"THERMOCOUPLE ASSIGNMENTS:"
4170 FOR I=1 TO NTC STEP 3
4180 PRINT USING "%  % IS IN ##  ;
    %  % IS IN ##  ;  %  % IS IN ##";TC$(I),I,TC
4190 'PRINT TC$(I);" IS IN ";I;"     ;     ";TC$(I+1);" IS IN ";I+1
4200 NEXT I
4210 G$=INKEY$ G$=""GOTO 4210
4220 IF G$="N" PRINT "REENTER":GOTO 3200
4230 POKE 16916,2:CLS:POKE 16916,3
4240 PRINT
4250 CLS
4260 RE=INP(252) OR 16:OUT 236,RE
4270 OUT 18,&H80              'HOLD SET ON TC AMPL.
4275 FOR IR=1 TO 1500:NEXT IR:              'DELAY FOR TC AMP
4280 GOSUB 9000              'CHECK FOR SWITCH POSITIONS
4290 CLS:PRINT"FORMATING FILES ON DISK"
4300 NP=0
4310 FOR ID=1 TO ND
4320 NP=NP+DS(ID,3)
4330 NEXT ID
4335 INPUT"STORE RUN INFORMATION?";JZ$ JZ$="N" :GOTO4470
4336 OPEN"O",1,NM$(1)
4337 PRINTNM$(1)
4345 IF NS<1 LET NS=1
4350 ID=1
4356 GOTO4415
4357 GOTO4390
4360 OPEN "R",1,NM$(ID)
```

```
4370 PUT 1,NS
4380 CLOSE
4390 CLS:PRINT"STORING RUN INFORMATION"
4401 CLOSE1
4410 OPEN "O",1,NM$(1)
4412 PRINT NM$(1)
4415 PRINT#1,MID$(NM$(1),1,5)
4430 PRINT#1,FRQ;AMP;DP;AIRPR;LD
4435 PRINT#1,GW;GX;GY;GZ
4439 PRINT#1,"COMMENTS: ";CM$
4440 PRINT#1,"ABOVE DATA:FILE NAME,FREQ,AMP,PITOT TUBE,P,L/D"
4441 PRINT#1,"AND GAIN ON CH#1-4"
4443 PRINT#1,"BELOW DATA:POS,TEMP,VDC CH#1-4,VACRMS CH#1-4"
4455 G$="B"
4456 CLOSE 1
4460 TI=6:GOSUB 6550
4470 REM
4480 CLS:RETURN
4490 REM
5000 '************************************************
5010 '
5020 '       RUN ROUTINE
5030 '
5040 '************************************************
5050 FOR I=1 TO ND
5060 P1=DS(I,1)*20
5070 PC%=P1-P0
5080 CLS:PRINT"MOVING TO FIRST LOCATION"
5090 X=USR1(PC%)       'MOVE TO FIRST LOCATION
5100 P0=P1
5110 PRINT @99,USING"POSITION= ####.## DEGREES";P0/20
5120 FOR J=1 TO DS(I,3)
5130 GOSUB 6030        'WAIT ROUTINE
5140 TI=INT(.8167+3.8767*NTC+.5)
5150 GOSUB 6550
5160 CLS:PRINT"READING ";NTC;" THERMOCOUPLES"
5170 POLD=P0
5180 T1%(0)=NTC
5190 H%=VARPTR(T1%(0))
5200 X=USR3(H%)        'GET THERMOCOUPLE READINGS
5210 FOR IT=1 TO T1%(0)
5220 TM(IT)=(T1%(2*IT-1)+100*T1%(2*IT))/10
5230 NEXT IT
5240 FOR IA=1 TO NG
5250 CLS:PRINT"READING HEAT TRANSFER GAUGE ";IA
5255 RE=INP(252)OR16:OUT 236,RE:FOR ID=1 TO 50:NEXT ID
5260 J%(0)=16-IA
5270 H%=VARPTR(J%(0))
5280 X=USR4(H%)        'ADC ROUTINE, PASS CHANNEL NUMBER
5285 TI=5:GOSUB 6550
5290 GOSUB7500
5440 NEXT IA
5460 PC%=DS(I,2)*20
5470 X=USR1(PC%)
5480 P0=P0+PC%
5490 PRINT @99,USING"POSITION= ####.## DEGREES";P0/20
```

```
5500 NEXT J
5510 NEXT I
5520 WT=0
5530 GOSUB 6030
5540 PC%=1
5550 IF PEEK(&HFFFF)=&HCC RETURN
5560 X=USR1(PC%)
5570 P0=P0+1
5580 GOTO 5550
6000 '*****************************************
6010 '   WAIT AND STORAGE ROUTINE
6020 '*****************************************
6030 NP1=0
6040 IF I>ID GOTO 6130
6080 FOR ID=I TO ND
6084 NP1=NP1+DS(ID,3)
6085 IF NP1<0 LET NP1=0
6090 IF DS(ID,4)=1 LET ID=ND
6095 NEXT ID
6096 NP1=NP1-J+1
6100 TI=INT(NP1*(WT+3.5+(NTC-1)*3.95+NG*5))
6105 IF NG>1 LET TI=TI+NG*15*NP1
6110 GOSUB 6560
6115 PRINT @00,USING"EST. NEXT HEATER ADJUST AT ##:##:##";
   N(3);N(2);N(1);
6120 TI=WT:GOSUB 6600:N1(1)=N(1):N1(2)=N(2):N1(3)=N(3):N1(4)=N(4)
6130 CLS:PRINT" IN WAIT AND STORAGE ROUTINE"
6140 PRINT
6160 IF WT>0 PRINT " NEXT DATA AT ";
   N(3);":";N(2);":";N(1):ELSE PRINT "FINAL ST
6170 IF I=1 AND J=1 GOTO 6271
6199 FORJY=1TO5:PRINT:NEXTJY
6200 FORJY=1TO4:PRINTAVG(JY);:NEXT JY:PRINTTM(1)
6202 FORJY=1TO4:PRINTSD(JY);:NEXT JY:PRINT""
6204 OPEN"E",1,NM$(1)
6205 PRINT#1,PO/20;TM(I):PRINTPO/20,TM(I)
6206 FORJY=1TO4:PRINT#1,AVG(JY);:NEXTJY:PRINT#1,""
6208 FORJY=1TO4:PRINT#1,SD(JY);:NEXTJY:PRINT#1,""
6265 CLOSE 1
6268 FORJY=1TO4:AVG(JY)=0:SD(JY)=0:NEXTJY
6270 TI=INT(2.55*NG+.5):GOSUB 6550
6271 NT#=N1(4)
6272 FOR IW=3 TO 1 STEP -1
6273 NT#=NT#*100+N1(IW)
6274 NEXT IW
6275 PT#=PEEK(16923)        :                    'DATE
6280 FOR IW=3 TO 1 STEP-1
6290 'IF N1(IW)>PEEK(16918+IW)GOTO6290
6291 PT#=PT#*100+PEEK(16918+IW)
6300 NEXT IW
6305 IF NT#>PT# GOTO 6275
6310 RETURN
6550 '******RESET CLOCK AFTER DELAYS******
6551 GOSUB 6560:FOR ITC=1 TO 3:POKE 16918+ITC,N(ITC):NEXT ITC
6553 RETURN
6560 '*********CLOCK ADJUST ROUTINE********
```

```
6565 T(4)=PEEK(16923)
6570 T(3)=PEEK(16921)
6580 T(2)=PEEK(16920)
6590 T(1)=PEEK(16919)
6600 N(1)=T(1)+TI
6602 N(2)=T(2):N(3)=T(3):N(4)=T(4)
6610 FOR ITC=1 TO 2
6620 IF N(ITC)<60 GOTO 6650
6630 N(ITC)=N(ITC)-60:N(ITC+1)=N(ITC+1)+1
6640 GOTO 6620
6650 NEXT ITC
6655 IF N(3)>23 LET N(3)=N(3)-24:N(4)=N(4)+1
6660 RETURN
7000 CLS
7010 PRINT"*******ADJUST HEATER W/ MANUAL TC BOX*******"
7020 INPUT"TURN SELECT BOX TO
   OFF', <ENTER>";G$
7030 RE=INP(252) OR 16:OUT 236,RE
7040 OUT 18,0
7050 POKE16916,3:CLS
7060 PRINT" REMAINING POINTS ARE:"
7070 FOR IR=I+1 TO ND
7080 FOR IJ=1 TO DS(IR,3)
7090 PRINT DS(IR,1)+DS(IR,2)*(IJ-1);",";
7100 NEXT IJ
7110 PRINT
7120 IF DS(IR,4)=1 PRINT"PAUSE FOR HEATER" ELSE PRINT"CONTINUE"
7130 NEXT IR
7140 PRINT @896,CHR$(255):P1=P1/20:PRINT @896,;
   :INPUT"ENTER DESIRED HEATER ADJUS
7150 RE=INP(252) OR 16:OUT 236,RE
7160 IF P1=999 P1=0:INPUT"TURN BOX TO
OFF',REPLACE PLUGS";G$:OUT 18,&H80:POKE 16916,2:CLS:RETURN
7170 IF P1>500 GOTO 7140
7180 P1=P1*20
7190 PC%=P1-P0
7200 X=USR1(PC%)
7210 P0=P1
7220 PRINT @99,USING"POSITION= ####.## DEGREES";P0/20
7230 GOTO 7140
7500 PRINT @512,"AVERAGING HEAT TRANSFER VALUES"
7510 AVG#=0
7520 FOR IB=0 TO 3
7530 AVG#=AVG#*256#+PEEK(&HFFDB-IB)
7540 NEXTIB
7550 AVG=AVG#/5000
7560 J%(0)=VARPTR(AVG)
7570 H%=VARPTR(J%(0))
7580 X=USR6(H%)
7590 FOR IB=0 TO 3
7600 H%=VARPTR(SD)
7610 POKE H%+IB,PEEK(&HFFDC+IB)
7620 NEXT IB
7630 AVG(IA)=(2048-AVG)/204.8
7640 SD(IA)=SQR(SD/5000)/204.8
7650 TI=14:GOSUB 6550
```

```
7655 PRINT @512,CHR$(255)
7658 FORJY=1TO4:PRINTAVG(JY),SD(JY):NEXTJY
7660 RETURN
8000 '*********************************************
8010 '    DISK READ PROGRAM
8020 '*********************************************
8025 CMD"D:1":ON ERROR GOTO 8030
8030 INPUT NM$:OPEN "I",1,NM$
8035 INPUT"PRINTER?";P$ P$="Y" THENCMD"Z","ON"
8040 INPUT#1, G$,GD$
8045 PRINT G$
8050 PRINT GD$
8060 INPUT#1,GL,GAN,NTC,FRQ,AMP,DP,AIRPR,NP
8070 PRINT "GL=";GL,"GAN=";GAN,"NTC=";NTC
8080 PRINT "THERMOCOUPLE ASSIGNMENTS:"
8090 FOR I=1 TO NTC
8100 INPUT#1,TC$
8110 PRINT USING"%  % IS IN ##";TC$,I
8120 NEXTI
8130 INPUT#1,PS,AVG,SD
8140 FOR I=1 TO NTC
8150 INPUT#1,TM(I)
8160 NEXT I
8170 PRINT USING "AT POS=####.# DEG,
   AVG=###.## V, SD=##.#### V";PS,AVG,SD
8180 PRINT"TEMPS:"
8185 PRINT TM(1),TM(2)
8190 FOR I=3 TO NTC STEP 4:FOR J=I TO I+3
   :PRINT USING "###.# ";TM(J);:NEXT J:PRI
8200 IF EOF(1)=0 GOTO 8130
8210 CLOSE
8220 CMD"Z","OFF"
8230 INPUT G$:RETURN
9000 '*************************************************************
9010 '*  ABSENT-MINDED EXPERIMENTOR CHECK ROUTINE                 *
9020 '*************************************************************
9030 '**CHECK AMPLIFIER ZEROING SWITCH
9035 FOR IC=1 TO  NG:CN=IC
9040 RE=INP(252) OR 16:OUT 236,RE
9050 OUT 9,16-CN
9060 J%=INP(12)+256*(INP(13) AND 15)
9070 VO=(2048-J%)/204.8
9090 PRINT"CH#";IC;"=";VO
9110 NEXT IC
9120 '**CHECK TC READOUT PLUG
9130 T1%(0)=3
9140 H%=VARPTR(T1%(0))
9150 X=USR3(H%)
9160 FOR IT=1 TO 3
9170 TM(IT)=(T1%(2*IT-1)+100*T1%(2*IT))/10
9180 NEXT IT
9200 IFTM(1)<20:GOTO9240
9210 RETURN
9240 PRINT @256,:INPUT"CHECK TC READOUT WIRING";G$
9250 IF G$="B" RETURN ELSE GOTO 9130
```

APPENDIX C

COMPUTERS USED

CRAY'S: The CRAY's used are located in Lawrence Livermore National Laboratory in California. CRAY X-MP is a multiprocessor with two CPU's each of which are nominally about 1.2 times faster than the CRAY 1's. CRAY X-MP is a vector processing machine and carries 2 million words of memory. The latest addition to the NMFECC (National Magnetic Fusion Energy Computing Center) is a CRAY 2 with four CPU's and 65 million words of memory. Currently 2 Gegabytes of online storage is available. This is expected to go up to 40 Gegabytes when on full service. A typical program runs at the order of 50 MFLOPS.

HP 5420A Digital Signal Analyzer: This is a very handy 2-channel digital FFT spectrum analyzer. It provides time domain and frequency domain analysis of analog signal from DC to 25 KHz. Analog signal is input through the HP 54410 A/D converter. Antialiasing is provided by a HP 54470 digital filter. Both internal and external trigger modes are possible.

IBM 3090 : This is the mainframe computer at VPI. It is considered to be a class VI or supercomputer. Its features include:

64 MB of shared central storage

64 MB of extended storage

32 integrated data channels

A high-speed memory cache of 64 KB

Two central processors

64-bit wide data paths

Faster floating point operation algorithms

Special circuitry for loop control

18.5-nanosecond cycle time

MINC: The Modular INstrument Computer is a labotatory computer system which can be used for computation, monitoring and control of experiments and data acquisition. It consists of the central processing unit and memory, diagostic/loader module, IEEE bus interface cable, serial ASCII controller, A/D converter, dual multiplexer, preamplifier, clock, D/A converter, digital input module and digital output module.

MASSCOMP 560: This equipment operates under a real time UNIX system and provides the capability of high speed, 16-channel real time data sampling and processing. It has 1 MB RAM, 1 MB floppy disk, 27 MB Winchester disk, 1 MHz 16-channel A/D, 8-channel simultaneous sample/hold, 500 KHz 4-channel A/D, 16 lines of parallel digital I/O.

The vita has been removed from the scanned document